Department of Electronic and Electrical Engineering
UNIVERSITY COLLEGE LONDON

PULSED LASER DEPOSITION OF ELECTRONIC MATERIALS

SASSON AMIRHAGHI

A thesis submitted to the University of London in fulfilment for the degree of Doctor of Philosophy.

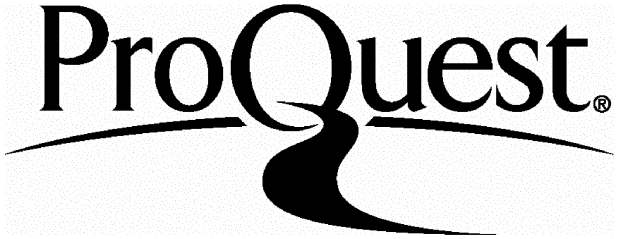

to my late Father

Abstract

The technique of pulsed laser deposition (PLD) which has been studied since the development of high power lasers, offers numerous advantages over other thin film techniques which include, film stoichiometry close to that of the source target material, low contamination levels, high deposition rate and dissociative evaporation. This project involves the use of PLD to grow thin films of oxide materials and investigate the deposition parameters involved. During the course of the project characterization techniques such as x-ray diffraction, scanning electron microscopy, transmission electron microscopy, and low temperature resistance measurements were utilized.

High temperature superconductor oxides (HTSC) based on copper and rare alkaline earths are chemically and structurally complex materials in which the preservation of stoichiometry is essential. Thus PLD is an attractive deposition method for producing such materials in thin film form. In order to grow HTSC films on commercially desirable substrates such as silicon, an inter-mediate buffer layer is required to avoid the detrimental problems of chemical interaction and/or interdiffusion during high temperature annealing processes.

The *in-situ* growth of high quality CeO_2 thin films used as buffer layers is highly dependent on the deposition conditions. In this project a number of parameters such as substrate temperature, oxygen partial pressure, film thickness, choice of laser (wavelength) and the target surface are investigated. Single crystal wafers of Si(100) and Si(111) together with sapphire and Corning glass 7059 were used as substrates. The possibility of growing multilayers with a gradual change in lattice constant to ensure better lattice matching to the top layer(s) is shown by depositing a film of CeO_2 doped with La over an undoped CeO_2 film. The growth of cuprates such as $YBa_2Cu_3O_{7-\delta}$ on Si with CeO_2 as a buffer layer is also shown. The preparation of the electron doped cuprate, $Nd_{2-x}Ce_xCuO_{4-y}$, ($0.13<x<0.18$ and $y\approx0.04$), in bulk and thin film form is studied. A number of parameters involved in producing highly textured single phase thin films of this material by *in-situ* and *ex-situ* growth on MgO single crystal substrates are examined. The effect of varying the Ce concentration on crystal dimensions of the bulk material is also investigated. Thin films of ZnO are widely used in electronic device technology as optically transparent materials exhibiting large piezoelectric and piezooptic effects when highly textured. In this project a number of parameters involved in growing ZnO films on Si and Corning glass 7059 are examined.

Acknowledgements

I am indebted to a number of people who have been a tremendous help throughout the course of this project and deserve thanks for doing so.

Many thanks go to:

Dr. S.Tarling, Mr. M.Vickers and Dr. P.Barnes, Department of Crystallography, Birkbeck College for allowing the use of the x-ray diffractometer.

Dr. I.Wood, Department of Geology, UCL, for the x-ray diffraction measurements and Rietveld refinement.

Prof. C.Humphreys and E.Beithal, Department of Material Science and Metallurgy, University of Cambridge, for the transmission electron microscopy studies.

Dr. F.Saba, Department of Materials, Imperial College of Science, Technology and Medicine, for the Energy Dispersive X-ray analysis

Dr. J.A.Kilner and Dr.Y.H.Li, Department of Materials, Imperial College of Science, Technology and Medicine for the transmission electron microscopy studies.

Dr. D.Jedamzig and Mr. S.Zammatio, GEC Hirst Research Laboratories, for the low temperature resistance measurements.

Mr. K.Reeves, Institute of Archeology, UCL, for the Electron-Probe Micro-Analysis.

Mr. M.Gillett, A.Gorrod, T.Hamer, A.Drury and J.Van Sickle , the workshop team at the department, for always letting me jump the queue for job requests.

Mrs.M.Small, Mrs.M.Karia and Mrs M.Goldstein, the secretarial team at the department, for being immensely kind and helpful.

My friends and colleagues at the department for sharing with me memorable periods of laughter, quarrel, discussion, sympathy and celebration.

The Science and Engineering Research Council, and British Telecom. for the CASE studentship.

I would like to tender my sincere gratitude to Dr. Frank Beech, Dr. Glenn Tyrrell, and Dr. Valentin Craciun, firstly, for their kind patience in proof-reading my thesis and their invaluable comments and suggestions, and secondly, for their assistance while performing the experiments.

I am deeply grateful to my supervisor, Dr. Ian Boyd, for taking me on in the first place. His advice, support, criticism and encouragement greatly contributed towards the success of this project. I am thankful to him for being particularly understanding during my period of depression.

Above all, I would like to thank my mother for being so patient and providing all the confidence and encouragement which was much needed throughout these years, and my late father for his solid support during the first few years of this project. His memory continued and keeps on being a great source of inspiration.

Table of Contents

Chapter 1

Introduction

Modern electronic technology utilizes thin films of a vast range of materials that display a diverse range of properties ranging from dielectric to semiconductivity, metallic, degenerate semiconductivity, and more recently high transition temperature superconductivity. The materials deposited cover a wide spectrum of complexity ranging from simple elementary metals to highly complex ceramics. In all cases the deposited film must be of uniform thickness and controlled stoichiometry. Thin films can be deposited using physical or chemical methods, with each technique having its own advantages and drawbacks.

The technique of pulsed laser deposition, PLD, has been studied since the development of high power lasers a quarter of a century ago [1], and since then it has been successfully used in the deposition of high quality dielectric films, highly crystalline semiconducting layers, metals, and recently high temperature superconductor, HTSC, thin films. Apart from a simple experimental set-up, the technique offers numerous advantages which include, film stoichiometry close to that of the target, low contamination levels, and controllable deposition rates.

The discovery of superconductivity at around 30 K in oxides based on copper and rare alkaline earths in 1986 [2] was a breakthrough which ignited a worldwide interest in the search for superconducting compounds containing Cu-O planes. Since then many new superconducting oxides have been discovered, with ever increasing chemical and structural complexity; the highest transition temperature to date being 133 K [3]. The discovery of superconductivity at ≈20 K in electron doped cuprates $Ln_{2-x}Ce_xCuO_{4-y}$ (Ln= Pr, Sm, Nd) proved the assumption that hole-doped CuO-layers are a crucial pre-requisite for HTSC to be premature.

Recently the use of single crystal silicon as a substrate for the growth of HTSC thin films has attracted interest due to its high degree of structural perfection, accessibility, purity, low cost, and less restricted substrate size. However an intermediate buffer layer between the superconducting film and the substrate is generally necessary to avoid the problem of chemical interaction and/or interdiffusion during high temperature annealing processes. This layer would then become the substrate for HTSC film deposition and it is therefore crucial that it has a smooth and flat surface. A major disadvantage of PLD is that the film surface contains a number of particulates which can affect the quality of the superconducting film deposited over it. This problem can be minimized by optimising the deposition conditions.

Although the technique of PLD owes its revival to the discovery of HTSC, it has also been extensively used in the deposition of other materials, particularly oxides. Apart from the deposition of intermediate buffer oxide layers between HTSC and silicon, PLD has also been proved to be a well established technique for the growth of oxides used as optical coatings, gas sensors, etc.

The aim of this project is to deposit thin films of electronic materials by PLD and optimise the parameters involved. Materials investigated include CeO_2, a promising candidate for usage as a buffer layer between HTSC and silicon, $Nd_{2-x}Ce_xCuO_{4-y}$, an intriguing material widely studied due to its electron doped nature as a superconductor, and ZnO which is attracting considerable interest due to its piezoelectric characteristics and being a prime candidate for usage as a transparent conductive film in optical devices.

The layout of this thesis is as follows:

In chapter 2 the growth of thin films is described in terms of the various steps involved during the initial stages of film growth, starting from the arrival of atoms, followed by nucleation, clustering of individual nuclei, and finally filling in of the network spacings. The three basic modes of growth i.e. layer growth, island growth, and a combination of the first two, are outlined. The concept of film crystallinity, including epitaxial growth is briefly discussed. Finally a number of thin film deposition techniques other than PLD are described at an introductory level.

We then progress in chapter 3 to a discussion on PLD as a thin film deposition technique. In the beginning of this chapter the advantages and drawbacks of the technique are outlined. This is followed by sections that highlight the physical processes involved during ablation, namely, laser - target interaction, plasma formation and expansion and the effect of these processes on film growth. One drawback to this process is that the plume containing the species for film growth is highly one-directional; the effect that this angular distribution has on film growth is briefly outlined.

Chapter 4 starts with an introduction to superconductivity and the properties of the conventional low temperature superconductors. The recently discovered high temperature superconducting cuprates are then discussed. The thin film growth of HTSC using PLD is then described with detailed reference to the case of $YBa_2Cu_3O_{7-\delta}$, which is the most commonly investigated HTSC material and is thus somewhat of a testbed system. Finally a brief discussion on the basic requirements for the growth of HTSC films on single crystal oxide substrates and silicon is presented.

In chapter 5 a brief review of the experimental techniques used to characterize the films grown in this thesis is presented.

In chapter 6 the results obtained from the growth of CeO_2 thin films on silicon, glass and sapphire using PLD are presented. The effect that deposition parameters such as oxygen partial pressure, substrate temperature, film thickness, laser wavelength etc have on film growth are systematically investigated. The possibility of engineering a graded sequence of lattice constants via doping and the use of CeO_2 as a buffer layer between HTSC and silicon is demonstrated.

Chapter 7 begins by a discussion of the basic properties of $Nd_{2-x}Ce_xCuO_{4-y}$. A description of the preparation and characterization of bulk pellets made from this material during the course of this project is then outlined. The systematic approach taken to produce highly oriented films of the desired stoichiometry using both *ex-situ* and *in-situ* growth is presented.

Finally in chapter 8, the growth of ZnO thin films using PLD is described. The parameters involved during the deposition are investigated and their effect on film growth are presented and discussed. This includes the effect on lattice constant which reflects whether the film is under strain - an important factor for a piezoelectric material.

References

[1] H.M.Smith and A.F.Turner, *Appl. Opt.*, **4**, p147, (1965).

[2] J.G.Bednorz and K.A.Müller, *Z. Phys. B*, **64**, p189, (1986).

[3] A.Schilling, M.Cantoni, J.D.Guo and H.R.Ott, *Nature*, **363**, p56, (1993).

Chapter 2

Growth and Deposition of Thin Films

In order to approach the technique of pulsed laser deposition (PLD) objectively it is important to discuss the growth of thin films in general and describe other deposition methods (both of a chemical and physical nature). In this chapter the processes involved during the growth of thin films together with the modes of growth and the crystallinity and orientation of the grown film are highlighted. Thin film deposition methods other than PLD are briefly described.

2.1 Nucleation and growth of thin films

The application of thin films in the fabrication of modern electronic circuits is a fast growing industry and the subject of intensive research. These films provide conducting regions within the device, electrical insulation between metals and semiconductors, anti-reflection coatings and windows to various optical devices, protection coating to environment, etc. Deposited films must be of uniform thickness and controlled composition which can also be reproducible and inexpensive.

In this section the basic processes involved during thin film formation together with the main types of growth and crystal orientation are briefly described. A detailed discussion can be found in a number of excellent books written on this subject of which references [1] and [2] are two examples.

2.1.1 Basic processes on the substrate

Processes involved during the initial stages of film growth are shown in figure 2.1.

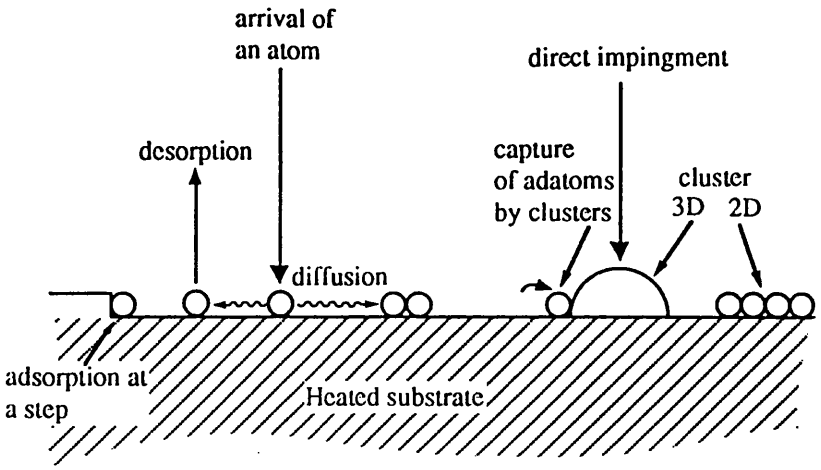

***Figure 2.1** Basic processes on the substrate surface [3].*

The individual steps concerning the growth of a thin film from a gas phase include the arrival and sticking of the vapour components on to the surface, surface migration of the adsorbed species, nucleation of the species, clustering of individual nuclei into interconnecting islands, and finally filling in of the network spacings, before uniform layers can be formed. Some films may be 10's to 100's of nm thick before the completion of this final stage. Nucleation can often be influenced by the presence of various surface structures, such as point defects, or crystal dislocations and other imperfections. A number of common defects frequently encountered in thin films is illustrated in figure 2.2.

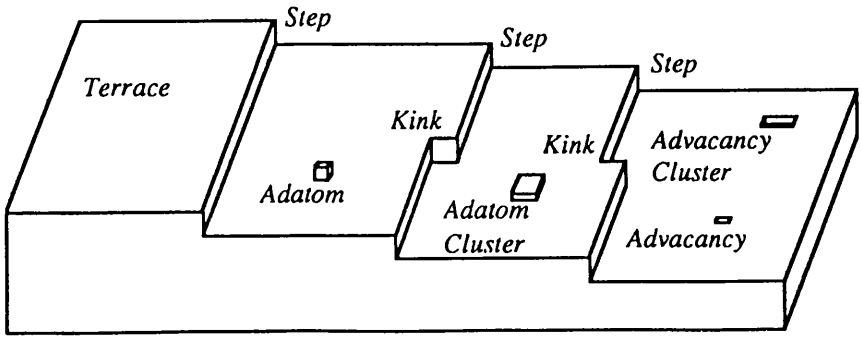

***Figure 2.2** Microstructural features common in thin films [4].*

At low to medium temperatures, the dominant microstructural features are terraces, steps and kinks. Terraces can be considered as planar defects in a bulk three-dimensional crystal. Separating terraces of different heights are ledges, or steps, which are line defects on a two-dimensional surface. Along these steps there may also be kinks, which are point defects on one-dimensional steps. Microstructural features such as adatoms and advacancies, either isolated or clustered into two dimensional islands, become important at higher temperature. Here the terms, low, medium or high temperatures are purely relative, and actual values depend on the material and growth conditions.

In the early stages of thin film growth atoms arrive at the substrate and are adsorbed with a surface concentration *n(t)*. The adatoms diffuse on the substrate surface as [3],

$$\langle x^2 \rangle = 2D.t \qquad (2.1)$$

where $\langle x^2 \rangle$ is the average value of the diffusion distance after diffusion time *t*. *D* is the diffusion constant given by [3],

$$D = D_o \exp(\frac{-E_d}{k_B T_s}) \qquad (2.2)$$

where E_d is the activation energy for diffusion, k_B the Boltzmann constant, T_s the substrate temperature, and $D_o = a_o . \nu_d$ with ν_d being the vibration frequency of adatoms and a_o the distance of one jump.

After an average time τ_A, some of the adatoms desorb into the vacuum at a desorption rate given by [3],

$$R_{des} = \frac{n}{\tau_A} \qquad (2.3)$$

The ratio of (adsorbed rate)/(arrival rate) is known as the "sticking coefficient" which is used frequently in the description of film growth. If *R* is the arrival rate, the differential sticking coefficient $\beta(t)$ is given by [3],

$$\beta(t) = \frac{R - R_{des}(t)}{R} = 1 - \frac{n(t)}{R.\tau_A} \qquad (2.4)$$

The integral sticking coefficient, $\alpha(t)$ is the average value in time t [3],

$$\alpha(t) = \frac{1}{t}\int_0^t \beta(t')d(t') \qquad (2.5)$$

If the arrival rate is constant, an adsorption-desorption equilibrium exists for a short period of time (three dimensional growth at high T_s) whereby [3],

$$n = \text{constant}, \quad \frac{dn}{dt} = R - \frac{n}{\tau_A} = 0 \text{ or } n = R.\tau_A \qquad (2.6)$$

$\beta(t)$ will be zero in this case.

2.1.2 Modes of growth

There are three basic modes of growth which depend on the interactions between the atoms of the substrate and the atoms of the deposit. These are briefly described below and are also shown in figure 2.3.

(a)- Layer growth (LG): This is a two-dimensional (2-D) mode of growth whereby the interaction energy between the atoms of the deposit and the atoms of the substrate (adhesion) is greater than that between the atoms of the deposit themselves (cohesion). A complete layer is grown first before the next layer is allowed to form. It is also known as the Frank-v.d.Merwe mode of growth.

(b)- Island growth (IG): This is a three-dimensional (3-D) mode of growth which takes place from the beginning of condensation. Here the interaction energy between the atoms of the deposit themselves (cohesion) is larger than that between the atoms of the deposit and the atoms of the substrate (adhesion). It is also known as the Volmer-Weber mode of growth.

(c)- Under certain conditions (eg. lattice distortions due to lattice mismatch), the Stranski-Krastonov mode of growth (SKG) may prevail in which one or several monolayers are initially formed followed by three dimensional clusters (islands) growing on top of them.

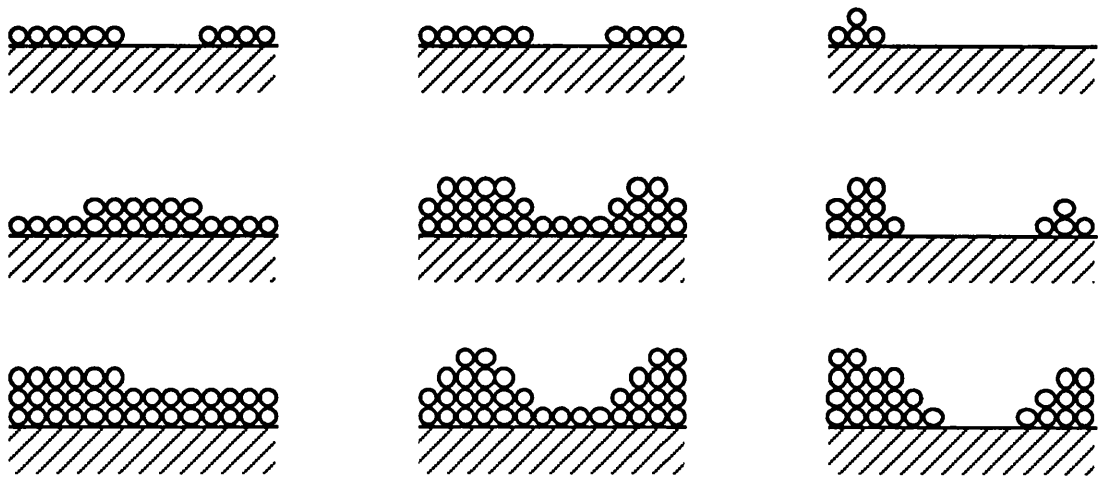

Figure 2.3 *Schematic diagram showing different modes of growth. (a) Layer growth (LG), (b) Stranski-Krastonov growth (SKG), and (c) island growth (IG) [3].*

Layer or island growth takes place depending on the relations between the surface tension of the substrate, γ_B, the surface tension of the deposit, γ_A, and the interfacial tension between the substrate and the deposit, γ^*,

For island growth [3]	IG	$\gamma_B < \gamma_A + \gamma^*$	(2.7)
For layer growth [3]	LG	$\gamma_B \geq \gamma_A + \gamma^*$	(2.8)

The mode of growth also depends on the ratio between the vapour pressure of the vapour beam and the vapour pressure of the deposit at the substrate temperature, known as supersaturation, ξ. Eqns 2.7 and 2.8 are thus modified to [3],

For island growth	IG	$\gamma_B < \gamma_A + \gamma^* - (k_B.T_s.\ln\xi)/\text{const.}$	(2.9)
For layer growth	LG	$\gamma_B \geq \gamma_A + \gamma^* - (k_B.T_s.\ln\xi)/\text{const.}$	(2.10)

A transition from 3-D to 2-D growth is possible with increasing supersaturation, or a transition from 2-D to 3-D growth is possible with decreasing T_s .

2.1.3 Crystallinity and orientation of thin films

The nature of the substrate, substrate temperature, deposition rate and film material determine whether the film can grow with amorphous, polycrystalline textured or single crystal structures. In general raising the adatom mobility (eg. by raising the substrate temperature) causes an increase in grain size of the film. Defects or impurities on the surface can reduce the mobility of adatoms. Metastable phases and special structures may be formed during the initial stages of growth which are not found in bulk. These phases disappear with increasing film thickness. Under ideal conditions the film grown on a single crystal substrate is formed as a single crystal which inter-relates with the substrate. This is known as "epitaxy", a complex phenomena with no theory to predict its formation from the physical properties of film and substrate.

For 2-D layer growth perfect lattice matching is not totally crucial for epitaxy since with a low misfit a thin deposit layer fits to the substrate by strain. The strain energy however increases with thickness until at a "critical thickness" misfit dislocations are introduced to decrease this energy. The lattice parameters for a thicker film are thus closer to that of the bulk. If the misfit between the film and the deposit is large, a "coincidence lattice" is believed to be formed which relaxes near the interface. In this case an m number of thin film atoms can grow on an n number of substrate atoms with little misfit, compensated by strain and misfit dislocations.

In the case of 3-D island growth, the islands not only diffuse laterally on the surface of the substrate but rotate as well. Rotation continues until the island reaches an epitaxial position with respect to the substrate. However it has been shown experimentally that generally a good lattice matching between the film and the substrate does not play a decisive role for epitaxial growth. Also it has been found that for every deposition rate a critical temperature exist above which epitaxial growth occurs. As the deposition rate increases so does the critical temperature.

2.2 Thin film growth techniques

Thin film technology has developed over the past twenty years to become an important area of material science. The motivation for deposition of thin films is now obvious when one considers such varied issues as the complexity and drive for miniaturisation of the modern microelectronics community, the protective and optical coatings industry and the need for conservation of expensive and limited material resources. A number of excellent treatises on thin film technology are available and the interested reader is referred to them for information beyond the scope of this thesis (eg. [1,2,4]).

Thin film deposition can be considered as a combination of three processes. Firstly, the transport of a flux of atoms, molecules or ions to a substrate surface. Secondly, the consideration of energetic processes of incoming species and their heats of condensation/formation on the surface. The final processes concern the periodicity of the growing film, its topography and structural orientation at a micro-crystalline level.

A number of diverse techniques are well advanced and have been successfully applied for the thin film growth of electronic materials for many years. These may be conveniently divided into physical vapour deposition (PVD) and chemical vapour deposition (CVD) methods. Within these divisions, the most commonly used techniques are:

(a) Physical vapour deposition (PVD):
  (i) Sputter deposition
  (ii) Thermal/electron beam evaporation
  (iii) Flash evaporation
  (iv) Molecular beam epitaxy (MBE)
  (v) Pulsed laser deposition (PLD)

(b) Chemical vapour deposition (CVD):
  (i) Metallo-organic CVD (MO-CVD)
  (ii) Plasma-assisted CVD (PA-CVD)

All PVD techniques are carried out in vacuum. The principal reason for this is that the growth species are produced by some physical excitation process ie thermal, electron beam, ion or laser. Upon vaporisation the evaporant must retain its inherent energy, and its transport to the substrate should be uniform i.e. in a straight line. By using vacuum technology, the number of intermolecular collisions between the incoming species can be reduced so that the mean free path of the evaporant is greater than the dimensions of the deposition chamber. The minimum vacuum required for molecular flow of this type can be calculated from simple gas kinetic theory. For air at room temperature the mean free path, λ, is approximated by [5],

$$\lambda = \frac{6.4 \times 10^{-3}}{P} \quad \text{cm} \qquad (2.11)$$

where P is pressure in mbar. Thus at $1x10^{-6}$ mbar λ is $6.4x10^{3}$ cm while at $1x10^{-3}$ mbar λ is only 6.4 cm.

It is convenient to separate the wide vacuum spectrum used in PVD into ranges:

low to rough vacuum	1013 mbar (atmosphere)-few mbar
medium vacuum	a few mbar-10^{-3} mbar
high vacuum (HV)	10^{-3} mbar-10^{-7} mbar
ultra-high vacuum (UHV)	below 10^{-7} mbar

At low to rough vacuum, the flow of gas is viscous with turbulent flow occurring close to atmospheric pressure and laminar (layered) flow at a few mbar. At high vacuum, the flow is molecular and hence atoms move without collision or mutual constraints. Flow in this regime is generally random and λ is much greater than the chamber dimensions. The intermediate flow region exists at medium vacuum conditions and marks a transition between laminar and molecular flow. The regime of ultra-high vacuum is useful when control of impurities at a small percentage of a monolayer is required.

A brief description of techniques other than PLD is given in the following section to create a clearer insight into the advantages and drawbacks of using PLD, which is described in detail in chapter 3.

2.2.1 Physical vapour deposition techniques other than PLD

2.2.1.1 Sputter deposition

The principle of sputtering is based on the production of particles (neutrals and ions) that are emitted from a target as a result of collision of energetic high-mass ions (most typically argon). Once the bombardment energy exceeds the bond energy of a solid (by three or four times), atoms will be knocked loose, providing a source of atomized material. A plasma can be created in the inert gas (typically argon) by passing either a dc or ac electrical current through it. When dc is used most of the region between the anode (substrate) and the cathode (target) is filled with a glow discharge, in which roughly equal number of ions and electrons maintain a constant voltage. A dark region appears close to the cathode where there is a shortage of electrons and a surplus of ions. In this region the ions are accelerated towards the cathode. Since the target serves as the cathode it is essential that it electrically conductive, therefore dc sputtering is not suitable for insulating materials.

In depositing insulating materials an rf discharge is generated between the target and the vacuum chamber itself. If an rf power is applied to two electrodes, the voltage drop is strongly and inversely proportional to the area of the electrodes. Thus the target is the small electrode which is capacitively coupled to the power supply (the capacitor is required to prevent shortening out the discharge through the power supply).

Sputtering can be assisted by employing a partial pressure of a reactive gas such as oxygen in which case the process is frequently referred to as reactive sputtering. Through momentum transfer, atoms near the surface of the target material become volatile and are transported as a vapour towards the substrate. The vapour interacts with the reactive gas en-route and grows as a film on the substrate.

Occasionally the argon ions are either produced in a separate ion source and directed towards the target, (ion-beam sputtering), or a magnetron-assisted plasma is created in front of the target plate where the argon gas is ionized and these ions are directed towards the target surface by the applied magnetic field, (magnetron sputtering).

Film area-coverage is dictated by the size of the target and the film surface is generally smoother than films produced by PLD or flash evaporation but not as smooth as films produced by molecular beam epitaxy.

In depositing complex materials such as high temperature superconductors, HTSC, a major drawback with sputtering is that in most cases the film composition does not reflect the target composition. To solve this problem either the target composition is adjusted to account for losses of certain elements, or a multi-source set-up with adjusted sputtering rates is utilized. Also in the usual geometry where the substrate faces the target it has been found that negative oxygen ions produced in the sputtering plasma causes a backsputtering effect on the substrate that etches the growing film, depleting it of some elements more than others. An off-axis geometry is thus used, with the disadvantage that the deposition rate is reduced by almost an order of magnitude.

2.2.1.2 Thermal/electron-beam evaporation

Evaporation is performed using either a resistance-heated source (thermal evaporation), or by directing an electron beam onto the source (e-beam evaporation).

In the case of thermal evaporation the source can be either a filament (eg. tungsten for evaporating aluminium), a resistive boat (eg. molybdenum for evaporating gold) or an inductively heated crucible (usually boron nitride). The technique is one the simplest PVD methods but there is a high risk of contamination from the crucible.

For e-beam evaporation, a thermionic filament supplies the current to the beam, and the electrons are accelerated by an electric field to strike the surface of the material to be evaporated (known as charge), held in a water cooled hearth. Thus the risk of contamination from the crucible can be avoided. To prevent impurities from the filament to reach the charge, a magnetic field bends the e-beam path thus screening the impurities. A disadvantage of this process is the generation of x-rays by the e-beam which can penetrate the surface layers causing damage. This can be repaired by subsequent annealing.

A disadvantage of evaporation emerges when alloys are to be deposited. When an alloy is melted, the various components will have different vapour pressures and thus different evaporation rates. Using multiple sources facilitates co-evaporation to produce films of complex materials such as HTSC, however the precise control of film stoichiometry is difficult.

2.2.1.3 Flash evaporation

In this case a batch of material is evaporated instantly and the process is repeated until the desired film thickness is deposited. This is particularly useful for the deposition of multi-element materials. In the case of HTSC for example, the powder which is made from a sintered bulk superconducting material is located in a feed mechanism that drops a predetermined amount of matter onto the evaporation source and is evaporated instantly [6].

The disadvantages of using this technique are that often the films are not exactly of the same composition as the source material and that contamination resulting from interaction with the evaporation source is also highly possible. Superconducting films deposited using this method require a post-annealing treatment since the relatively short exposure time during deposition does not allow enough incorporation of oxygen when depositing in an oxygen ambient [6].

2.2.1.4 Molecular beam epitaxy (MBE)

MBE is an epitaxial process involving the reaction of one or more thermal beams of atoms or molecules with a crystalline surface under UHV conditions. This technique is in several respects similar to co-evaporation except that the deposition is carried out mostly sequentially rather than simultaneously. The molecular beams are produced by evaporation or sublimation from heated liquids or solids contained in crucibles known as Knudsen cells or effusion ovens. A distinct characteristic of MBE is the extremely low background pressure (UHV) which apart from providing a cleaner growth environment, allows the application of certain analysis techniques such as reflection high-energy electron diffraction (RHEED), Auger electron spectroscopy (AES), X-ray

photoelectron spectroscopy (XPS) etc. to track film characteristics on a monolayer basis during growth. At the pressures used in MBE, collision-free beams from various sources interact chemically on the substrate to form an epitaxial film. Films of precisely controllable atomic layers and without any macroparticles can be produced, however due to its comparably low deposition rate and high maintainence costs, MBE is not an economically practical technique.

2.2.2 Chemical vapour deposition techniques

In the basic set-up most CVD processes employ a deposition chamber (usually hot-walled) in which a mixture of gases are introduced (with or without an additional carrier gas) from evaporation sources located outside the chamber, whereby they decompose and interact on the heated substrate surface and thus form the film. Deposition is often conducted at low pressures (at ≈1 mbar) to improve film thickness uniformity and increase deposition rate. CVD reactions occur at elevated temperatures, requiring heating of the substrates. In a "hot-walled" reactor, the walls of the chamber are heated up and heat is transmitted to the substrates which is thus maintained at a lower temperature. In a "cold-walled" configuration, the substrates are heated more directly by resistive heating, rf induction, or heating lamps.

The major advantages of using CVD are the ability to homogeneously deposit films over large areas at relatively high deposition rates. The control of film stoichiometry is however determined empirically by adjusting the gas flow of each individual vapour source. A single-source approach in which the vapour is produced from a single source of mixed composition outside the deposition chamber may be more feasible.

Metallo-organic (MO) CVD is by far the most widely used technique. For the deposition of HTSC films oxygen is supplied via the carrier gas. By using a plasma near the substrate the deposition temperature can be reduced [1]. Also it has been demonstrated that by replacing O_2 with N_2O not only lower deposition temperatures are accessed but also the deposition rate is enhanced by a factor of 2 [7].

2.3 Summary

The basic processes involved during the initial nucleation and growth of thin films were briefly described. It was explained that depending on whether the interaction between the atoms of the deposit and the atoms of the substrate is greater or smaller than the interaction between the atoms of the deposit themselves, a layered or an island mode of growth is obtained, and under certain conditions a combination of these two results. It was shown that the nature of the substrate, the film material, and the deposition parameters determine the degree of film crystallinity, and that epitaxial growth does not necessarily depend upon perfect lattice matching of the film and the substrate. A number of the more popular physical (other than PLD) and chemical thin film deposition techniques were outlined.

References

[1] J.L.Vossen and W.Kern (eds.), *"Thin Film Processes"*, Academic Press, New York, (1978).

[2] K.L.Chopra, *"Thin Film Phenomena"*, McGraw Hill, USA, (1969).

[3] K.Reichelt, *Vacuum*, **38**, 12, p1083, (1988).

[4] J.Y.Tsao, *"Materials fundamentals of molecular beam epitaxy"*, Academic Press, Boston, (1993).

[5] N.Harris, *"Modern Vacuum Practice"*, McGraw Hill, UK, (1989).

[6] C.Stoessel, R.F.Bunshah, S.Prakash and H.R.Fetterman, *J. of Supercon*, **6**, 1, p1, (1993).

[7] T.Tsuruoka, H.Takahashi, R.Kawasaki and H.Abe, *Jpn. J. Appl. Phys.*, **28**, L1800, (1989).

Chapter 3

Pulsed Laser Deposition

This chapter surveys the pulsed laser deposition (PLD) technique and provides analysis on why it has found popular acceptance as a method for the deposition of complex thin films structures. A key objective is to highlight the physical processes that operate in the laser ablation process and their effect on film growth. In particular, the central processes that concern the interaction of laser radiation with matter, the mechanism of removal of target material, the development of an ablation plasma and its condensation on a heated substrate into a highly oriented crystalline film of similar stoichiometry to the original target material will be discussed. In several cases reference is made to the PLD of high T_c superconducting materials; this is described in detail in chapter 4.

3.1 PLD as a thin film deposition technique

Since the first demonstration of the laser in the 1960s a diverse range of wavelengths have been accessed by solid state and gas lasers. These have already found a wide range of practical applications that range from boring vias and holes in semiconductor devices to performing delicate laser eye surgery [1]. The application of lasers, most particularly using the PLD technique for the growth of thin films, is an active area of research. In this section the application of the PLD technique to the growth of thin films of advanced materials is discussed. It should be noted that in the literature PLD is often also referred to by a variety of different names, eg. laser evaporation, laser sputtering, laser ablation deposition etc.

The first demonstration of the technique was that of Smith and Turner who in 1965 used a ruby laser to deposit films of simple elementary and binary materials on various

substrates [2]. This initial breakthrough was not followed up by immediate applications until the discovery of high T_c superconductors in 1986 [3]. It was the great potential of these and other complex oxides that led to the search for deposition methods that could produce them in thin film form that resulted in a re-evaluation of the PLD technique. The ability to transfer source materials to the substrate whilst retaining stoichiometry allowed the thin film growth of metals, dielectrics, semiconducting and superconducting materials.

The role of the laser in PLD is to provide an external source of energy to vaporize materials which are contained within a vacuum environment. This vapour (at high laser fluences) manifests itself as a plume and is used as a source of material to grow films. A simple experimental set-up is shown in figure 3.1.

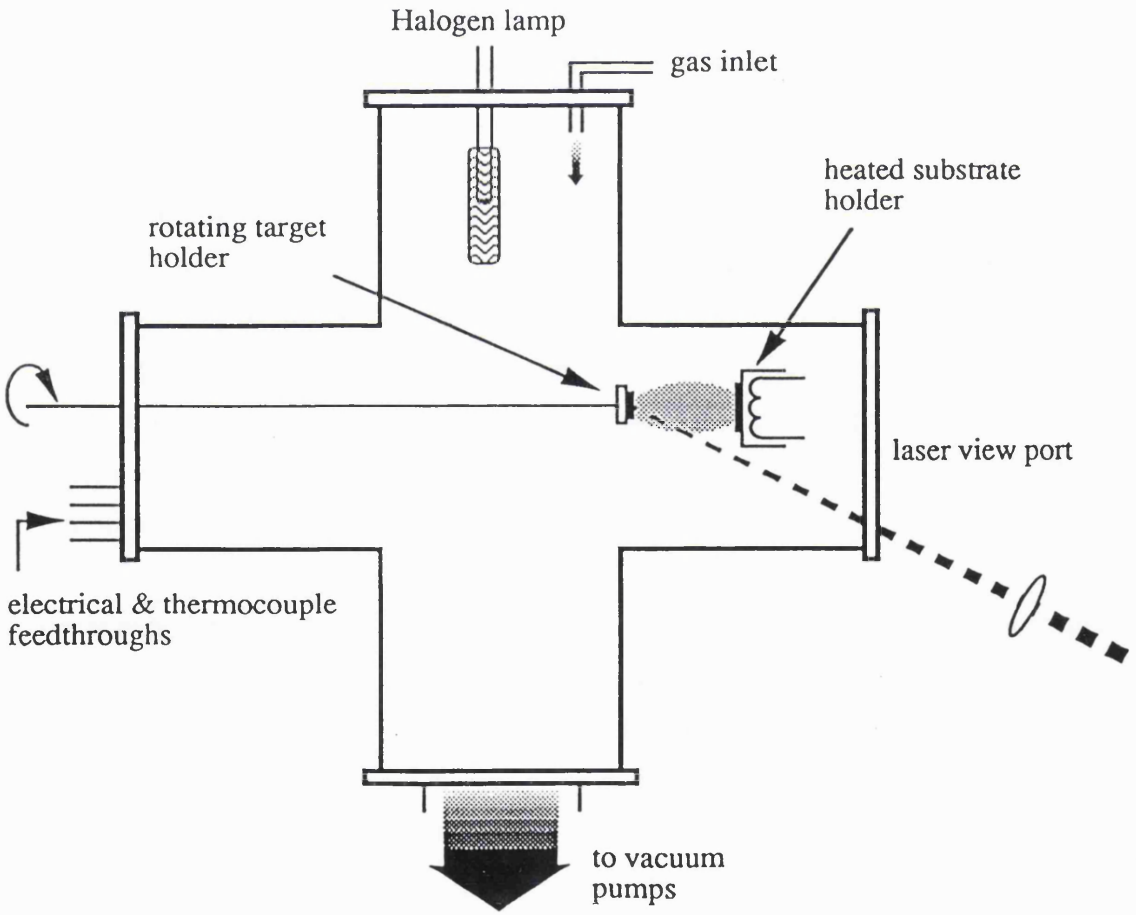

Figure 3.1 *The experimental set-up used in this project for pulsed laser deposition.*

This typically consists of a reaction chamber containing a rotatable target holder and a heated substrate holder. The laser beam is directed into the chamber via suitable laser optics. As with other PVD techniques the chamber is maintained under vacuum to enhance the mean free path of the evaporants and allow a better degree of purity. PLD can also be performed in a reactive atmosphere eg. O_2 or N_2O, by maintaining a partial pressure of the reactive agent which can be introduced through a gas inlet. The ablated species react with the gas phase before they condense on the substrate.

The target material to be ablated is in the form of a compressed pellet (cold pressed or hot pressed) of fine polycrystalline powder, a shaped metal plate or a single crystal. The target is usually rotated in order to reduce the exposure of any one area of the pellet to repetitive laser irradiation and thus decrease the chance of deep crater formation. In some cases the laser beam is rastered i.e. scanned horizontally on the target (normally computer controlled) to utilize a greater portion of the pellet and to cover a larger area on the substrate.

The uniformity of film thickness is directly proportional to the distance between the target and the substrate. A larger separation generally results in more uniform films, however this is at the expense of a lower deposition rate which is more pronounced when high partial pressures are involved as in the case of reactive deposition. It should be noted that there are a number of other factors such as the laser spot size and the laser energy density which affect the angular profile of evaporants and thus thin film uniformity.

Laser radiation provides the energy to cause physical reactions. When continuous wave (CW) radiation or long pulses are employed conventional thermal evaporation is expected to occur which is not desirable in the case of multi-component materials whereby the transfer of stoichiometry from target to substrate is of paramount importance. However when short pulses (<50 ns) are utilized, the ablated material is identical in composition to that of the target. This transfer without a change in the phase constituents is referred to as *congruent evaporation.*

The relative advantages and drawbacks of the PLD technique can be summarized in table 3.1.

***Table 3.1** Advantages and disadvantages of the PLD technique.*

Advantages	Disadvantages
(a) transfer of target stoichiometry to the substrate. (b) generation of species with high kinetic energy. (c) control of deposition rate. (d) purity of source material. (e) limited heat radiation from the source. (f) dissociative evaporation.	(a) poor film thickness uniformity. (b) formation of particulates on the film surface. (c) degradation of optical components.

These are explained in more detail as follows:

(i)-Advantages

(a)-The ability to reproduce target stoichiometry in the deposited film - congruent evaporation. This arises from the rapid heating and cooling cycles on the target (a cycle is typically a few milliseconds), which for a complex material allows all the constituents to evaporate within a period that is shorter than the time taken for the individual components to diffuse over a dimension greater than the thermal diffusion length [4].

(b)-Hyperthermal neutral species with very high kinetic energy can be generated. Deposition of hyperthermal neutrals can enhance the adatom mobility and thus the film quality. Depending on the atomic mass, kinetic energies in the range of 5-40 eV are generated [5]. This can be compared to the typical kinetic energies available from different deposition techniques, as shown in figure 3.2. For magnetron sputtering there are also high energy (100-1000 eV) ions in the plasma which can lead to substrate damage. For PLD the ions in the laser plume usually have energies which are below the damage threshold of $\approx$100 eV [5-7].

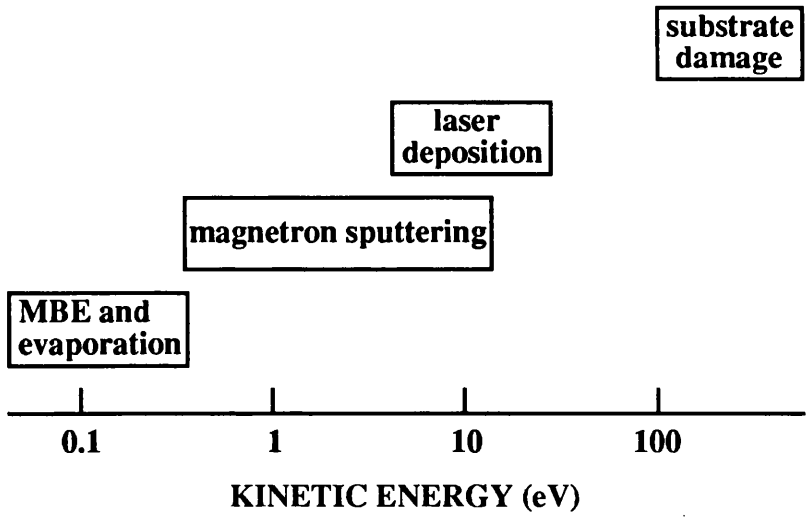

Figure 3.2 *Comparison of the typical atomic kinetic energies for various deposition techniques [5].*

(c)-Deposition rate can be varied from low to high (< 1 Å/s to $>10^6$ Å/s) with accurate controllability. This is desirable for the growth of multilayers, particularly superlattices. It has been shown that in the growth of YBCO films by PLD a low deposition rate (1.8 Å/s) would result in films with pinholes due to incomplete coalescence while at a high deposition rate (150 Å/s) coalescence will be complete but misoriented grains or "out-growths" would nucleate [8]. An optimal deposition rate would thus lie somewhere in between the two extremes. Also for very high instantaneous deposition rates the heat of condensation released during film deposition will accumulate in the thin surface layer and act as an effective local heat source [4]. High quality epitaxial films were produced by Gaponov et al. [9] by depositing thin layers of PbSe on substrates held at 20°C at a high deposition rate of 10 Å/s.

(d)-Target materials form their own crucibles during ablation, thus the purity of the source material can be preserved and any contamination effect due to the reaction of source material with the crucible at high temperatures can be prevented.

(e)-Laser ablating sources radiate considerably less heat than conventional sources such as the ones used in thermal evaporation due to the small size of the evaporating volume and the shorter radiation time in pulsed laser heating. This is particularly advantageous for thin films deposited on temperature sensitive substrates. Also less target material is

consumed due to local heating (limited by the laser spot) which makes the technique attractive for the deposition of thin films made of highly precious materials.

(f)-Dissociative evaporation due to the extremely high surface temperatures. Certain elements which are normally produced in a molecular or polymeric form in conventional evaporation techniques can be produced in atomic forms when PLD is used. For example in the thermal evaporation of GaAs or CdTe, Ga atoms and As_2 molecules, or Cd atoms and Te_2 molecules are produced upon heating. However due to the very high surface temperatures in PLD, GaAs or CdTe dissociate into Ga atoms and As atoms, or Cd atoms and Te atoms [4]. This would result in a more precise transfer of target stoichiometry. Dissociative evaporation is therefore linked to or complements the subject of target stoichiometry preservation described in (a).

(ii)-Disadvantages

(a)-The area of uniform film thickness coverage is usually low (1-2 cm^2). Higher film coverage can be achieved by increasing the distance between target and substrate and/or scanning the laser beam over a rotating target of large diameter. However, these approaches have the disadvantage of lowering the deposition rate. Also the spot size and the energy density of the laser are effective in defining film thickness uniformity.

(b)-The existence of microscopic particles on the film surface, produced by the transfer from target, can deteriorate film quality and morphology. This will be described in detail later in this chapter.

(c)-Degradation of optical components, coating of laser beam optics with ablating material. Coating of optics, particularly the laser viewport, would result in the attenuation of the laser radiation reaching the target. A number of geometries and methods have been used to reduce the coating of view ports. One is to direct the laser beam on to the target via a mirror inside the chamber [10]. The degradation of mirror reflectivity is slower than the loss of transmission through the viewport. Also heating of optical components reduces the coating rate due to their lower sticking coefficient at high temperatures [10]. Another approach is the flow of inert gas across the viewport and inside the chamber to deflect the evaporants.

In the following sections the physical phenomena underlying the technique of PLD are outlined and discussed.

3.2 The laser ablation process

As yet the exact mechanism associated with PLD is not fully understood, however there are a number of theories and models that provide a clearer insight into the ablation process of which some are fully quantified and some are fair approximations. The interaction of the laser beam with the bulk target may be considered as a number of stages as represented in figure 3.3.

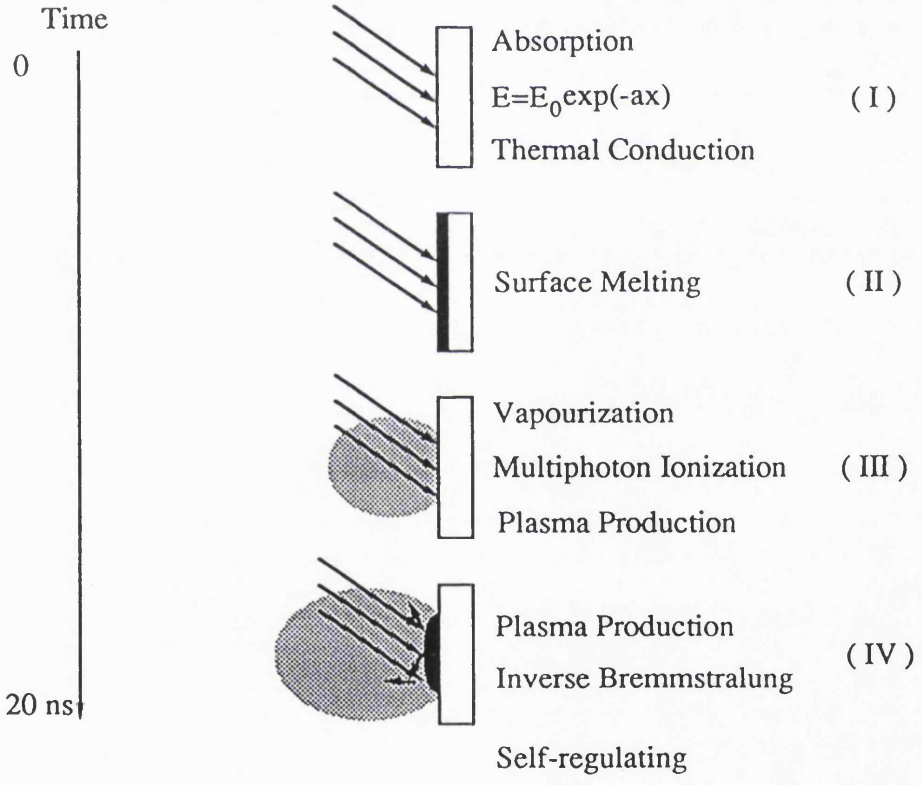

***Figure 3.3** Number of stages involved during laser target interaction.*

The ablation process has been divided into regions which occur within the time-scale of a laser pulse (in this case 20 ns);

3.2.a Absorption/conduction and surface melting (regimes I & II):

At the impact of laser light with the target surface, the energy of the photons are absorbed and transformed into heat leading to a rapid increase of surface temperature. Heat conduction into the target results in an increase in thickness of the heated layer. At a time τ_h after the onset of laser irradiation the thickness of the heated layer is of the order of $\sqrt{2D\tau_h}$, where D is the thermal diffusivity defined as $(\sigma/\rho c)$ where σ is the thermal conductivity, ρ is the mass density and c is the heat capacity of the target material. For a laser pulse of duration τ_p, at normal incidence on a target material with absorption coefficient α, two limiting cases may be described:

(a) When thermal diffusion length is much larger than optical absorption length, i.e., when $\alpha^{-1} << \sqrt{2D\tau_p}$. In this case heat conduction dominates over optical absorption and the temperature induced within a layer of thickness $\sqrt{2D\tau_p}$ is given by [11,17],

$$T=2(1-R)\Phi\tau_p/C_v\rho\sqrt{\pi}2D\tau_p \qquad (3.1)$$

where R is the reflectivity, Φ the laser power density, C_v the specific heat, and ρ the mass density. The dimensions of the laser spot can be neglected for a short pulse duration (< 1 μs) [17]. As can be seen in eqn. 3.1, the temperature rise is proportional to Φ and $(\tau_p)^{1/2}$. Heat diffuses into the material and the heating rate is proportional to $(\tau_p)^{-1/2}$, and thus for a given laser power density the heating rate is greater at shorter pulse widths.

(b) When thermal diffusion length is much smaller than optical absorption length, i.e., when $\alpha^{-1} >> \sqrt{2D\tau_p}$. In this case and an exponential temperature dependence is obtained and at a depth, z, below the target surface this temperature is given by [4,11],

$$T(z)=(1-R)\Phi\alpha\exp(-\alpha z)\tau_p/C_v\rho \qquad (3.2)$$

Again the temperature rises linearly with Φ, however the heating rate is independent of τ_p and the maximum temperature is directly proportional to it.

Equations 3.1 and 3.2 are only approximations and they do not account for any temperature dependence of the physical constants and the latent heat involved due to phase transitions. The temperature estimates can be an order of magnitude away from the values obtained using these equations [11]. Also since α varies with wavelength (α increases at lower wavelengths), both of these regimes, particularly the second case, are strongly influenced by the laser wavelength used.

Material removal is observed only above a certain threshold fluence, Φ_{th}, known as ablation threshold (sometimes also referred to as evaporation threshold). Φ_{th} is equal to the total fluence required to thermally evaporate the target material, Φ_{total}, plus conduction losses by the target and absorption losses by the plasma, and its value is strongly dependent on the pulse duration and the laser wavelength used. Φ_{total} is equal to the amount of fluence required to thermally melt the irradiated target material, Φ_m, plus the additional fluence needed to thermally evaporate the melted region, Φ_e. By assuming that all the laser light energy is transferred to the target atoms and transformed into heat energy, Φ_m and Φ_e are given by [11],

$$\Phi_m = \rho_s \frac{C_s(T_m - T_r) + L_m}{(1 - R_s)\alpha_s} \qquad (3.3)$$

$$\Phi_e = \rho_m \frac{C_m(T_e - T_m) + L_e}{(1 - R_m)\alpha_m} \qquad (3.4)$$

whereby in the solid form, ρ_s is the mass density, C_s is the temperature-averaged specific heat, and α_s is the temperature-averaged absorption coefficient. T_m is the melting temperature, T_r is the room temperature, and L_m is the latent heat of melting. For equation 3.4, symbols have the same meaning but they refer to the melt-to-evaporate phase transition.

This rationale has been extended by Nakamiya et al. [12], whom using the one dimensional heat flow model [13], calculated the energy density required to reach the melting and ablation (material removal) temperatures on a $YBa_2Cu_3O_{7-\delta}$ target surface using an excimer laser (λ=248 nm, τ=10-50 ns), as shown in figure 3.4.

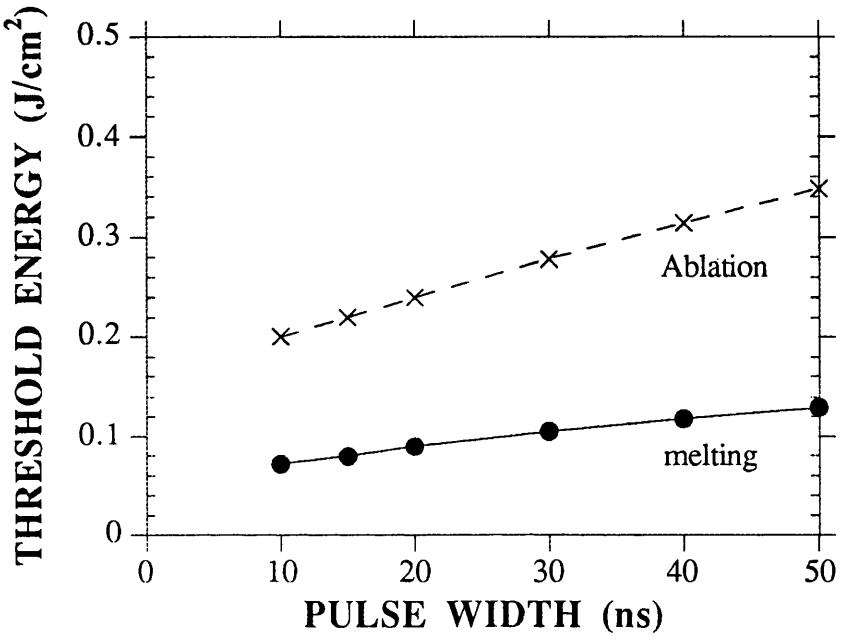

Figure 3.3 *The laser energy density required to reach the melting and ablation temperatures on a $YBa_2Cu_3O_{7-\delta}$ bulk surface for a pulse width of 10-50 ns [12].*

At a pulse width of 15 ns the melting and ablation thresholds were 0.08 J/cm^2 and 0.22 J/cm^2 respectively. This was in good agreement with their experimental results (examining the surface of the $YBa_2Cu_3O_{7-\delta}$ targets using scanning electron microscpy after laser irradiation) in which melting and ablation thresholds of 0.07 J/cm^3 and 0.2-0.27 J/cm^2 were observed respectively.

Craciun et al. [14] using computer simulation studied the temperature distribution inside a laser ablated target of ZnO (melting point = 2300 K, boiling point = 2500 K, [15]). The absorption coefficient of ZnO at 532 nm was taken as 10^4 cm^{-1} at room temperature which increased to $8x10^4$ cm^{-1} as the material approached melting point, while at 248 nm the absorption coefficient was taken as $3.3x10^5$ cm^{-1} at room temperature, increased to $5x10^5$ cm^{-1} at 1200 K, and remained constant up to the melting point. A laser energy density of 3 J/cm^2 was assumed. In the case of excimer laser radiation (λ =248 nm, τ =20 ns), it was shown that at the start of the laser pulse the temperature on the target surface increased sharply with time and reached the melting point in ≈2.5 ns and the boiling point in ≈5 ns. At 5 ns, the melted region was

≈30 nm thick. As the radiation continued more material was removed, such that within the period of 20 ns, a depth of ≈150 nm inside the target reached the boiling temperature. In the case of a frequency doubled Nd:YAG laser (λ =532 nm, τ =4 ns), at the onset of the laser pulse, the temperature at the target surface again increased sharply, however due the higher absorption length at this wavelength, at a depth of up to ≈100 nm inside the target the temperature was nearly identical. Melting was reached at ≈3 ns and evaporation started at ≈3.8 ns.

3.2.b Plasma formation and expansion (regimes III & IV):

At power densities just above the evaporation threshold, material removal is by a mechanism similar to thermal evaporation with the velocity of the evaporants being roughly equal to the average thermal velocity. If the crater depth, H, on the target surface is assumed to be linear with the number of pulses, an $H \propto \Phi$ behaviour is resulted which is not a function of laser wavelength since material removal is governed by heat conduction rather than laser absorption [16].

Under the usual conditions for PLD high surface temperatures (2000-3200 K in the case of $YBa_2Cu_3O_{7-\delta}$) are reached, which result in the thermionic emission of positive ions, electrons, as well as neutral atoms and clusters from the surface of the target [1]. This is accessed at laser energy densities much higher than Φ_{th}. In contrast with the thermal evaporation regime, the emitted species attain higher velocities which correspond to kinetic energies in the order of 10-100 eV in the case of excimer-laser-irradiated YBaCuO targets (depending on the mass of individual components) [16]. (The velocities of individual species with different mass can be made to converge by ablating under a high pressure gas - this will be discussed later in chapter 4). The interaction of laser irradiation with the evaporants results in the dissociation of molecular species desorbed from the target. An expanding plasma is produced in the form of a brilliant glow which extends outwards elongating preferentially perpendicular to the target surface.

The evaporated species can be further heated by the absorption of laser radiation. When low densities of electrons and ions are present within the plume, transitions involving

neutral atoms become the main mechanism for absorption. However, for high electron densities, absorption would occur by an inverse Bremsstrahlung process, which involves the absorption of a photon by a free electron. Depending on the electron-ion density, plasma temperature and laser wavelength the laser beam penetrates through the plasma and is absorbed by it. The penetration of the laser beam is also dependent on the plasma frequency, ν_p, which is given by [17],

$$\nu_p = 8.9 \times 10^3 n_e^{1/2} \qquad (3.3)$$

where n_e is the electron density. The value of n_e when the plasma frequency equals the laser frequency is known as the critical electron density and increases with decreasing wavelength. At u.v. wavelengths for instance the value of the critical electron density is close to the concentration of electrons in a solid or liquid, i.e. $\approx 10^{22}$ cm^{-3} [17]. In contrast, for a CO_2 laser (10.6 μm) the value is $\approx 10^{19}$ cm^{-3} and can be accessed at high laser fluences of $\approx 5 \times 10^9$ W/cm^2 [18]. In this case ablation enters a different regime whereby the laser beam is heavily absorbed.

The plasma can be divided into two regions as shown in figure 3.5.

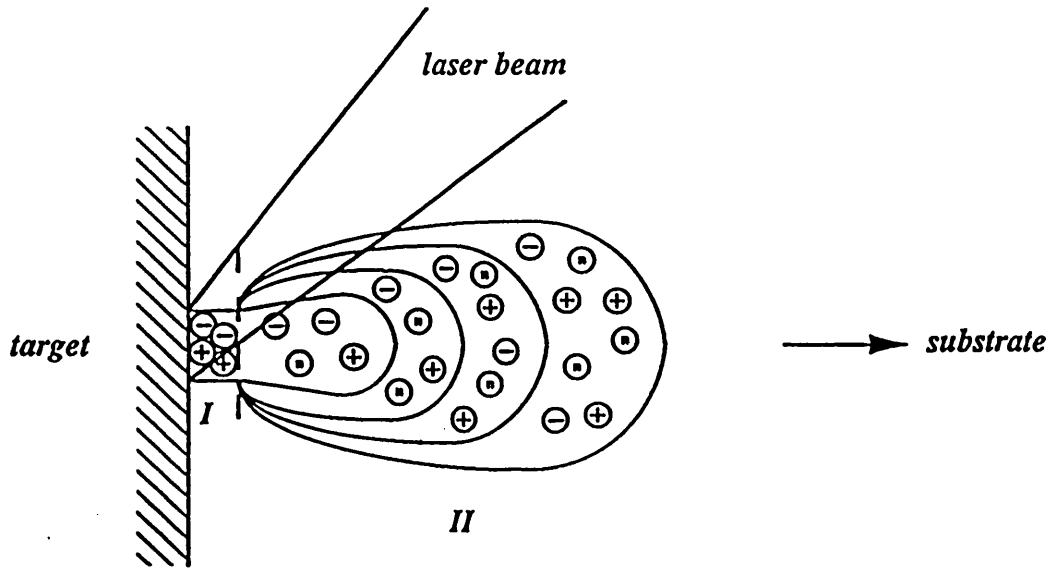

Figure 4.4 Schematic drawing of a plasma: region I - laser absorbing region with a one dimensional plasma flow, region II - non-absorbing region with a three dimensional plasma flow.

In region I (≈1 mm from the target - also the dark area adjacent to the target shown in figure 4.3, regime IV) the plasma can be considered as a high temperature-high pressure layer where the absorption of the laser photons takes place due to high ion densities (the plasma absorption coefficient is proportional to n_i^2, where n_i is the ion density [16,17]) and a one dimensional plasma flow is assumed [18]. However, in region II, the plasma expands with the density and the pressure of the evaporants decreasing and their velocity increasing rapidly in three dimensions with distance from the target and therefore the plasma is transparent to the laser beam.

Using an image-intensified charge coupled detector camera (ICCD), D. Geohegan studied the propagation of the plasma from a $YBa_2Cu_3O_{7-\delta}$ target irradiated with an excimer laser operating at 248 nm with an energy density of 1 J/cm^2, both under vacuum and at an oxygen pressure of 100 mTorr [19]. In both cases the ejected species separate into two components, a near stationary (very slow moving) component stretching out to a distance of ≈1 mm from the target, and a second component expanding one-dimensionally for the first 0.5 μs and then three-dimensionally in a forward-directed manner at a leading edge velocity of 10^6 cm/s. The slow moving region is considered to be the result of gas collisions within the high pressure region leading to a layer with stopped and/or backward moving material, known as the Knudsen layer [20]. Under the oxygen pressure however, the leading edge of the plasma was slowed down in such a way that at ≈2.9 cm away from the target the sharp front nearly halted. This suggested the existence of a shock front as observed earlier by a number of other groups [21-23]. The explanation given by Dyer et al. [21] for such a behaviour is that initially the mass (density) of the ejected particles (driver) is greater than the mass (density) of the driven gas in which the particles propagate through. This situation can be maintained under vacuum, however at high oxygen pressures similar to the case mentioned before, as the plasma expands the mass of the driven gas increases which slows down the driver.

At intermediate power densities of 10^6 - $5x10^8$ W/cm^2 (eg. for a loosely focused Q-switched Nd:YAG or a pulsed Nd:YAG in a free oscillating mode), the evaporated species consist mainly of neutral particles. However collision between atoms results in the formation of neutral clusters [18] together with a few percentage (1-4%) of positive

ions and electrons [4,21]. In this case the non-absorbing plasma results in an $H \propto \ln\Phi$ profile [18].

At higher power densities of > $5x10^8$ W/cm^2 more ions and higher energy clusters (hot clusters) are produced [18]. The electron density near the target surface increases to a level in which the plasma frequency may equal the laser frequency (eg. >10^{19} ions/cm^3 in the case of a CO_2 laser operating at 10.6 μm). The plasma absorption coefficient increases which results in a decrease in evaporation rate. This would lead to a reduction in the plasma absorption coefficient and the ablation process enters a self-regulating regime of periodically absorbing the laser radiation. Since part of the laser energy is used to heat up the plasma, the crater depth is smaller than the cases where low and intermediate energy densities are employed and therefore the highly absorbing plasma leads to an $H \propto \Phi^{5/9}$ behaviour [18].

There are no more particles injected from the target into the plasma once the laser pulse has ended. During the expansion there is a rapid conversion of thermal energy into kinetic energy with the plasma attaining expansion velocities as high as 3-10 times the velocity of sound depending upon the ratio of the heat capacities of the individual particles [16,17]. In a model presented by Singh and Narayan [16,17] the initial dimensions of the plume (when the pulse has terminated) were said to be larger in the transverse direction (Y or $Z \approx$1-4 mm) than in the perpendicular direction ($X \approx$20-100 mm). The expression for plasma dimensions as a function of time showed that highest velocities were in the direction of lowest dimension. In other words the plasma would take an elongated shape in the direction X perpendicular to the target surface. Also if the plasma was initially longer in the Y direction than in the Z direction, the final shape would be longer in the Z direction than in the Y direction. It should be noted that this model did not account for deposition under high reactive gas pressures. Under high vacuum the plume does indeed assume an elongated ellipsoidal shape, however under high pressures ($\approx 10^{-1}$ Torr) a more intense and larger plume is resulted which is not as elongated as in the former case.

3.3 Angular distribution and energy of evaporants

As explained earlier at low power densities, material removal is by a mechanism similar to thermal evaporation and the crater depth on the target (and to a first approximation the deposition rate) increases linearly with power density. The angular distribution of the evaporated material is characterized by a cos θ distribution where θ is the angle between the radial vector and the target normal. In this case the film stoichiometry for compounds is not generally identical to that of the target. This is due to the vapour pressure of the component elements in the compound being different from one another.

However, at high power densities, material removal assumes a ln Φ (non-absorbing plasma) or a $\Phi^{5/9}$ (absorbing plasma) behaviour and is characterized by a highly forward peaked $\cos^n\theta$ (n>>1) distribution super-imposed on a broad $\cos\theta$ distribution. The region on the deposited film corresponding to this highly forward peaked $\cos^n\theta$ distribution possesses a stoichiometry which is generally near identical to that of the target [11,24].

Upon impact with the substrate the kinetic energy of the plasma particles can be completely transformed to enhance lateral mobility and local heating. High laser energy densities lead to plasma particles with high kinetic energy which in turn result in high mobilities and therefore homogeneous layer growth and denser films [18]. Neutral clusters with low kinetic energy remain almost intact once on the surface whereas for larger cluster energies (of the order of the bond strength), local heating 'flattens out' the clusters so that most voids in the film structure disappear as a result of atomic rearrangement [18].

3.4 Particulates

A major drawback to the growth of thin films by PLD is that the deposited film generally contains droplets and outgrowths on its surface. Film smoothness is generally of critical importance in the growth of multi-layer structures. A film grown on top of a base layer follows the surface morphology of the film underneath. A high density of

particulates can also lead to scattering in optical films and thus degrade the coating quality [25]. The physical mechanism for the production of these features has been attributed to a number of factors:

(i)- The presence of trapped gas bubbles underneath the target surface which could rapidly expand during laser-induced heating [4].
(ii)- Superheating of the subsurface layer before the temperature of the surface itself has reached the vaporization value. This is normally the case when high laser wavelengths are employed as will be discussed below [4].
(iii)- The surface roughness of the target which can be improved by polishing the surface prior to deposition and using targets of high homogeneity and density [4].
(iv)- It has been suggested that the shock-front of the plume generated at high pressures produces a sudden change in temperature which results in the formation of clusters (dimensions of the order of 1-2 μm) [26].

Zherikhin et al. [27] classified these features into two distinct types. Type I with a size of $d \geq 1\ \mu m$, d being the average diameter, originate from the laser-target interaction and refer to the ones mentioned above. Particulates of type II usually have $d < 1\ \mu m$ and their density depends on deposition conditions such as substrate temperature and oxygen pressure. Strikovsky et al. [28] divided the types of particulates into large, medium and small ones. The larger type with $d \geq 0.4\ \mu m$ are similar to the type I of Zherikhin et al., the medium type with $0.2 \leq d \leq 0.4\ \mu m$ are not present in the initial plasma flux but arise during its expansion in the background gas and are believed to originate from volume condensation of vapour, and the smaller type with $d < 0.2\ \mu m$ depend on adatom movement and nucleation which are quite similar to the type II mentioned above.

The number of droplets and outgrowths per unit film area can be influenced by the deposition parameters. Extensive studies of the laser wavelength dependent properties of YBaCuO thin films by Koren et al. [29] revealed that the morphology of the films was rough, with large particles resulting from ablation by longer laser wavelengths (mainly the larger ones - type I). In a model presented by Baüerle et al. [30] it was suggested that the maximum temperature during laser - target interaction is obtained at a

distance z_o below the surface. The laser heats up the surface to ablation temperature within a period t_v which is less than the pulse duration τ_p - in the period $t_v < t < \tau_p$, the target is continuously being ablated. This results in the lowering of the maximum temperature to the boiling temperature at the target surface, and in a case of slow heat conduction and finite absorption (accessed at high laser wavelengths, eg. 532 nm), the temperature is effectively higher within a volume inside and adjacent to the target surface, rising from boiling point at the surface and peaking at a distance z_o inside the target. Such a superheating effect can lead to micro-explosions within the melted material with adverse effects on eventual film quality. The temperature rise is not dependent on the absorption coefficient, α, whereas z_o is. For the case of surface absorption (low laser wavelengths, eg. 193 nm),

$$z_0(\alpha \rightarrow \infty) \rightarrow 0 \qquad (3.6)$$

and significant ablation takes place only within the time $0 \leq t \leq \tau_p$. However, in the case of finite absorption, $z_o \neq 0$, and the energy accumulated within the overheated layer of thickness z_o will give rise to material evaporation for times $t > \tau_p$, if the energy dissipation by heat conduction is slower than the ablation process.

The droplet density normalized with respect to the thickness, $\tilde{N}$, is approximately proportional to (i) laser energy at constant spot size, S; (ii) $1/S$ at constant laser energy. The drpolet density, N, is then given by [26],

$$N \propto (\Phi_c\text{-}0.4)(\Phi_e\text{-}1.0)S^2 n_S \qquad (3.7)$$

with n_s the number of pulses and the laser energy density Φ_e>1.0 J/cm^2.

The value 0.4 J/cm^2 represents the threshold energy density for deposition and the value 1.0 J/cm^2 represents the threshold energy density for droplet formation. Thus at a laser energy of ≈1 J/cm^2 the ablation process is already effective but the plasma in front of the target does not become hot enough to remove the droplets from the target.

Blank et al. [31] during the growth of YBaCuO layers on $SrTiO_3$ and YSZ found out that as the film thickness increased, particle density decreased, but particle dimensions increased. These particles were considered to be YBaCuO outgrowths. The outgrowth

density gradually decreased for increasing pulse repetition rates, and decreased when substrate temperature was reduced.

Apart from optimising the deposition conditions there have been a number of other approaches to minimise the problem of particulates. One passive approach is by working with targets of high homogeneity and density [25,32]. It is also common practice to polish the target periodically prior to deposition to free the surface of any features that could potentially be dislodged during evaporation [32]. Another approach, an active one, is based on the fact that particulate velocities are lower than those of the thermal atoms. Lubben et al. [33] measured the average velocity of particles with a size of $d \approx 1\ \mu m$ departing from a laser ablated Ge target to be $\approx 1 \times 10^4$ cm/s (c.f. 3 - 10×10^5 cm/s for neutral Cu species and 1 - 2×10^6 cm/s for Cu^+ ions during ablation of YBaCuO [34]) and found that the velocity of these particles have an inverse relationship with size. A velocity filter can thus be used to stop the slowly moving larger particulates, but to let through the fast atomic and molecular evaporants [32].

By placing the substrate in an off-axis position, i.e. with the substrate normal being perpendicular to the plume, Holzapfel et al. [35] managed to reduce the density of medium size particulates to $\approx 10^5/cm^2$ and avoid the precipitation of larger size particulates altogether. This approach relied on the assumption that for light particles such as atoms, ions and molecules the impact with the dense plasma resulted in these particles being deflected with an appreciable fraction being deposited on the substrate. The larger particulates on the other hand were not affected and bypassed the substrate without deposition. Off-axis deposition had another advantage that the effect of substrate heating by the laser plume could be eliminated. However, the deposition rate was reduced by a factor of 3. R.J.Kennedy [36] studied the above geometry by rotating the substrate through different angles to the target. The optimum angle was 180°, i.e. with the back of the substrate heater facing the target and its centre a distant away from the centre of the target. Another technique which is based on the above mentioned principle whereby light particles are deflected by the plasma but large particles are unaffected, is the spatial separation technique of crossed fluxes [28]. By irradiating two targets positioned at an angle of say 45° to the substrate normal, and by placing a diaphragm opposite the substrate, a significant fraction of the lighter particles finds its

way through the diaphragm and is deposited on the substrate whereas the larger size particles travelling normal to the targets do not reach the substrate.

Vaporization of particulates in their transit from source to the substrate by a second laser beam has also been proposed [37] and experimentally verified [38].The second laser beam traverses the evaporant plume and its pulses are synchronized with the first laser pulses that induce the evaporation from the target. The pulse form the second laser is delayed so that it does not start before the termination of the pulse from the first laser.

Also mechanical/chemical polishing of the deposited YBaCuO films using deionized water with 0.7% HF yielded very smooth films with only the non-homogeneities being attacked by the polishing action [39].

3.5 Summary

In this chapter the advantages and disadvantages of using PLD as a thin film deposition technique have been outlined. The ablation process has been described in terms of laser - target interaction, which results in the production of a plasma whereby in the region adjacent to the target surface a high density of ions and electrons are generated and beyond this an expanding plasma is produced with the density and pressure of the evaporants decreasing rapidly with distance away from the target. Also the angular distribution is characterized by a highly forward peaked $\cos^n\theta$ (n>>1) profile , super-imposed on a broad $\cos\theta$ distribution.

A number of factors that can lead to the generation of particulates on the film surface has been outlined and the deposition parameters and the technical approaches which can be manipulated to minimize these features has been explained.

References

[1] J.Cheung and J.Horwitz, *MRS Bulletin*, **2**, p30, (1992).

[2] H.M.Smith and A.F.Turner, *Appl. Opt.*, **4**, p147, (1965).

[3] J.G.Bednorz and K.A.Müller, *Z. Phys. B*, **64**, p189, (1986).

[4] J.P.Cheung and H.Sankur, *CRC Critical Reviews in Solid State Material Sciences*, **15**, p63, (1988).

[5] H.S.Kwok, *Thin Solid Films*, **218**, p277, (1992).

[6] P.E.Dyer, R.D.Greenough, A.Issa and P.H.Key, *Appl. Phys. Lett.*, **53**, 6, p534, (1988).

[7] J.G.Lunney, J.F.Lawler and R.Aratari, *J. Appl. Phys.*, **74**, 6, p4277, (1993).

[8] C.C.Chang, X.D.Wu, R.Ramesh, X.X.Xi, T.S.Ravi, T.Venkatesan, D.M.Hwang, R.E.Muenchausen, S.Foltyn and N.S.Nogar, *Appl. Phys. Lett.*, **57**, 17, p1814, (1990).

[9] S.V.Gaponov, B.M.Luskin, B.A.Nesterov and N.N.Salashenko, *Sov. Phys. Solid State*, **19**, p1736, (1977).

[10] H.Sankur and J.T.Cheung, *J. Vac. Sci. Technol.* A, **1**, p1806, (1983).

[11] F.Beech and I.W.Boyd, in *Photochemical Processing of Electronic Materials*, edited by I.W.Boyd and R.B.Jackman, Academic Press, New York, p387, (1991).

[12] T.Nakamiya, T.Ikegami and K.Ebihara, *IEEE Trans. on Appl. Supercon.*, **3**, 1, p1057, (1993).

[13] H.S.Carslaw and J.C.Jaeger, *"Conduction of heat in Solids"*, second edition, Clarendon Press, Oxford, (1959).

[14] V.Craciun, D.Craciun, S.Amirhaghi, J.Elders, H.Gardenier and I.W.Boyd, *accepted for presentation at the EMRS Conference*, Strasbourg, May 1994.

[15] O.Madelung (editor), *"Landolt-Bornstein New Series"*, **17b**, Springer Verlag, New York, (1982).

[16] R.K.Singh and J.Narayan, *Phys. Rev. B*, **41**, p8843, (1990).

[17] R.K.Singh, O.W.Holland and J.Narayan, *J. Appl. Phys.*, **68**, 1, p233, (1990).

[18] A.Richter, *Thin Solid Films*, **188**, p275, (1990).

[19] D.B.Geohegan, *Appl. Phys. Lett.*, **60**, 22, p2732, (1992).

[20] R.Kelly and R.W.Dreyfus, *Nuc. Instrum. Methods*, **B32**, p341, (1998).

[21] P.E.Dyer, A.Issa and P.H.Key, *Appl. Phys. Lett.*, **57**, 2, p186, (1990); P.E.Dyer, A.Issa and P.H.Key, *Appl. Surf. Sci.*, **46**, p89, (1990).

[22] K.Scott, J.M.Huntley, W.A.Phillips, J.Clarke and J.E.Field, *Appl. Phys. Lett.*, **57**, 9, p922, (1990).

[23] A.Gupta, B.W.Hussey, A.Kussmaul and A.Semüller, *Appl. Phys. Lett.*, **57**, 22, p2365, (1990).

[24] T.Venkatesan, X.D.Wu, A.Inam and J.B.Wachtman, *Appl. Phys. Lett..*, **52**, 14, p1193, (1988).

[25] H.Sankur, *Thin Solid Films*, **218**, p161, (1992).

[26] J.Folkstra, R.P.J.IJsselsteijn and J.W.M.Hilgenkamp, *Thin Solid Films*, **218**, p304, (1992).

[27] A.Zherikhin, V.Bagratashvili, V.Burimov, E.Sobol, G.Shubnii and A.Sviridov, *Physica C*, **198**, p341, (1992).

[28] M.D.Strikovsky, E.B.Klyuenkov, S.V.Gaponov, J.Schubert and C.A.Copetti, *Appl. Phys. Lett.*, **63**, 8, p1146, (1993).

[29] G.Koren, A.Gupta, R.J.Baseman, M.I.Lutwyche and R.B.Laibowitz, *Appl. Phys. Lett.*, **55**, 23, p2450, (1989).

[30] D.Bäuerle, B.Lukyanchuk, P.Schwab, X.Z.Wang and E.Arenholz, *"Laser Ablation of Electronic Materials: Basic Mechanisms and Applications"*, E.Fogarassy and S.Lazare, Elsevier Science, p39, (1992).

[31] D.H.A.Blank, R.P.J.IJsselsteijn, P.G.Out, H.J.H.Kuiper, J.Flokstra and H.Rogalla, *Mat. Sci. Eng. B.*,**13**, p67, (1992)

[32] T.Venkatesan, X.D.Wu, R.Muenchausen and A.Pique, *MRS Bulletin*, **2**, p54, (1992).

[33] D.Lubben, S.A.Barnett, K.Suzuki, S.Gorbatkin and J.E.Greene, *J. Vac. Sci. Technol. B*, **3**, p968, (1985).

[34] K.L.Saenger, *J. Appl. Phys.*, **66**, 9, p4435, (1989).

[35] B.Holzapfel, B.Roas, L.Schulz, P.Bauer and G.Saemann-Ischenko, *Appl. Phys. Lett.*, **61**, 26, p3178, (1992).

[36] R.B.Kennedy, *Thin Solid Films*, **214**, p223, (1992).

[37] H.Sankur and J.T.Cheung, *Appl. Phys. Lett.*,**56**, p214, (1988).

[38] G.Koren, R.J.Baseman, A.Gupta, M.I.Lutwyche and R.B.Laibowitz, *Appl. Phys. Lett.*, **56**, p2144, (1990).

[39] W.Eidelloth, R.L.Sandstrom and M.M.Plechaty, *Physica C*, **197**, p389, (1992).

Chapter 4

High Temperature Superconductors

In the first two sections of this chapter some of the important properties of the "traditional" low temperature superconductors and the basic physics operating within them are described. This is followed by a brief outline of the recently discovered high temperature superconductors (HTSC) and a short description of the growth of HTSC thin films using the PLD technique. Finally the main requirements for the growth of HTSC thin films on single crystal oxide substrates and silicon are presented.

4.1 Superconductivity

In certain group of materials when cooled the electrical resistance decreases as in metals, but on reaching a temperature known as the critical temperature,T_c , the electrical resistance is lost altogether. They are then said to have passed into the superconducting state (figure 4.1).

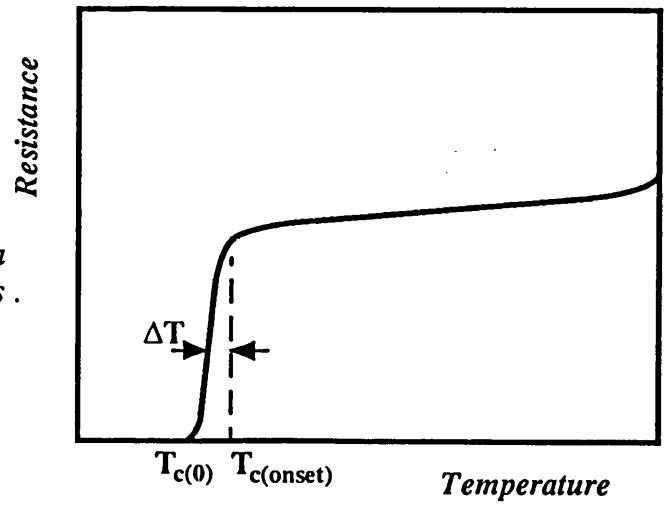

Figure 4.1 Loss of resistance of a superconductor at low temperatures .

Such a material would then have the property that it never has a flux density inside it even when in an applied magnetic field. This is because, whilst in the applied magnetic field, screening currents are generated around the surface of the material which produce a flux density equal and opposite to that applied. This property is known as the *Meissner-Ochsenfeld effect.* The relative permeability, of the material is then, $\mu_r = 0$ and the magnetic susceptibility, $\chi = -1/4\pi$. The screening currents flow within a surface layer, the depth of which is called the *penetration depth,* λ. The flux density consequently does not fall abruptly to zero at the boundary between the normal and superconducting regions but dies away within it.

When a superconductor is cooled below the transition temperature an ordering of some of the conduction electrons occurs, and the material can be regarded as consisting of two interpenetrating electronic fluids, the normal electrons and the super-electrons. The super-electrons in some way possess greater order than the normal electrons, and the degree of order of the superconducting phase can be identified with the density of the superconducting electrons, n_s. This property can change appreciably within a distance known as the *coherence length,* ζ. At the boundary between the normal and superconducting regions the density of superelectrons can rise from zero in the normal region to its density, n_s, in the superconducting region gradually over the distance ζ.

In general ζ and λ are not the same. If $\zeta > \lambda$, then the total free energy is increased close to the boundary between the superconducting and normal regions; hence there is a positive surface energy. If $\zeta < \lambda$, there would therefore be a negative surface energy associated with the boundary.

There are two kinds of superconductors, namely *type-I* and *type-II*. Most of those elements which are superconductors exhibit type-I superconductivity, whereas alloys generally exhibit type-II superconductivity. The two types have many properties in common but show considerable difference in their magnetic behaviour.

As mentioned previously, in an applied magnetic field, resistanceless surface currents circulate so as to cancel the flux density inside. If the strength of the applied magnetic field is increased, the shielding currents must also increase in order to maintain perfect

diamagnetism, until at a certain value of magnetic field, the critical current density is reached by the shielding currents and the metal loses its superconductivity. This is referred to as the *critical magnetic field strength*, H_c. In a type-I superconductor the variation of H_c with temperature is approximated as,

$$H_c \approx H_0 [1-(T/T_c)^2] \qquad (4.1)$$

where H_o is the critical field at absolute zero. The variation with temperature of H_c for a type-I superconductor is shown in figure 4.2.

H_c is also dependent on the size of the body. For example if the thickness of a superconducting film, a, is less than λ, H_c increases in a manner proportional to λ/a.

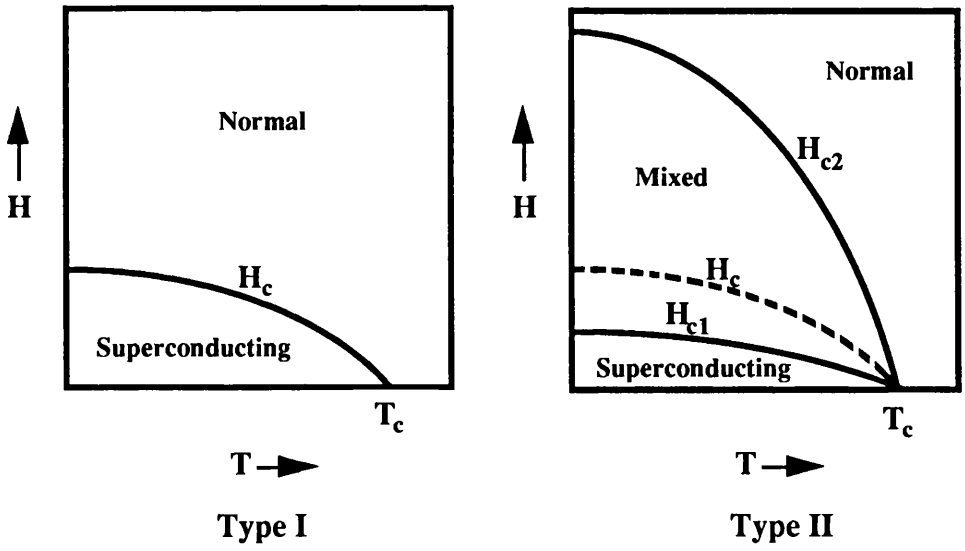

***Figure 4.2** Phase diagram of type-I and type-II superconductors.*

In an increasing magnetic field, once the applied field, H_a reaches a value, $(1-n)H_c$, where n is the demagnetizing factor, the superconducting material splits into normal and superconducting regions. This is known as the *intermediate state*. The magnetic field strength inside the body (the internal field), would remain at H_c until at $H_a = H_c$, it reverts to normal state behaviour. For a body in the shape of a long thin rod and in an applied field parallel to its axis, $n = 0$, and therefore it cannot enter into an intermediate state.

However, in the case of a type-II superconductor, as the applied magnetic field is increased over a certain value known as the *lower critical field,* H_{c1} (which is less than the thermodynamic critical field H_c, or the critical field of an equivalent type-I superconductor), the material enters a *mixed state.* In this condition the favourable configuration (the lowest free energy) is one in which the superconductor is threaded by cylinders of normal material lying parallel to the applied field, known as *vortices.* It should be noted that the mixed state is reached irrespective of the shape (demagnetizing factor) of the material. Because of the mutual interaction the vortices do not lie at random but arrange themselves into a regular periodic array. As the magnetic field is increased further the vortices pack closer together, until at H_{c2}, the *upper critical field,* the material goes into the normal state. This is also shown in figure 4.2.

In a type-I superconductor, ζ is greater than λ, hence there is a positive surface energy associated with the boundary between a normal and a superconducting region. In a type-II superconductor, ζ is less than λ, and the corresponding surface energy is therefore negative. The ratio of λ to ζ is known as the Ginzburg -Landau constant, κ, which is given by,

$$\kappa = \lambda / \zeta \qquad (4.2)$$

A more detailed treatment [1] shows that,

$\kappa < 1/\sqrt{2}$, surface energy positive (type-I)
$\kappa > 1/\sqrt{2}$, surface energy negative (type-II).

Also H_{c1} and H_{c2} can be approximated as ([2] and [3] respectively),

$$H_{c1} \approx \left(\frac{hc}{8\pi e\lambda^2}\right)\ln\kappa \qquad (4.3)$$

$$H_{c2} \approx \frac{hc}{4\pi\mu_o e\zeta^2} \qquad (4.4)$$

In a magnetic field , if a current is passed along a superconductor from some external source, the total current flowing on the surface would be the transport current due to the external source superimposed on the screening currents due to the applied field. The maximum amount of transport current that could be passed along the superconductor without resistance is known as the *critical current* of that piece.

If in the absence of any externally applied magnetic field, a current i is passed along a type-I superconducting wire of radius a, a magnetic field will be generated at the surface of which the strength, H_i is given by,

$$2\pi a H_i = i \qquad (4.5)$$

Now if an external magnetic field is applied in a direction parallel to the axis of the wire it would add vectorially to H_i and the strength H of the resultant field is given by,

$$H^2 = H_a^2 + (i/2\pi a)^2 \qquad (4.6)$$

The critical value i_c of the current occurs when H equals H_c,

$$H_c^2 = H_a^2 + (i_c)^2/4\pi^2 a^2 \qquad (4.7)$$

If the applied field is normal to the axis of the wire, the total field would then be given by,

$$i_c = 2\pi a\,(H_c - 2H_a) \qquad (4.8)$$

Figure 4.3 shows the variation of critical current with the magnetic field applied parallel and perpendicular to a long thin rod of radius a. At the critical current, the wire enters an intermediate state of alternate normal and superconducting regions each of which occupies the full cross-section of the wire. The current passing along the wire now has to flow through the normal regions, so at the critical current the resistance should jump from zero to some fraction of the normal resistance. As the current is increased further the resistance of the wire gradually increases and approaches the full normal resistance asymptotically. In the case of thin films if the thickness, a, is comparable or less than λ, i_c is reduced by a factor $\tanh(a/\lambda)$ in contrast with the increase in H_c.

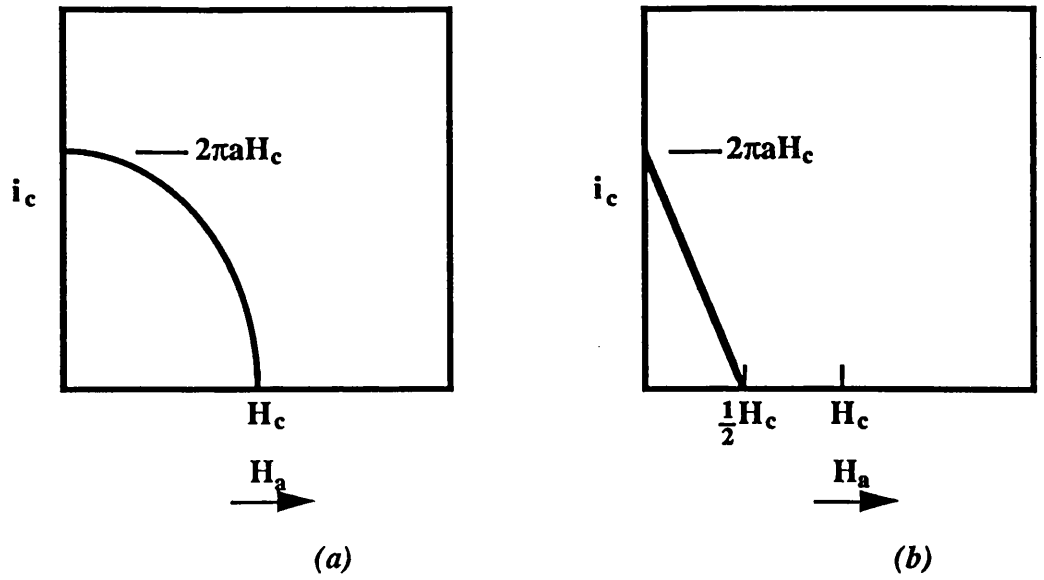

Figure 4.3 *Variation of critical current with magnetic field strength applied (a) parallel, (b) normal, to a long thin rod of radius a.*

In the case of a magnetic field applied at right angle to a type-II superconducting wire, i_c falls linearly with the increasing field, however it does not fall to zero at H_{cl} (c.f. the case of a type-I superconducting wire), but there remains a small i_c, and even above H_{cl} when the material is in the mixed state, there is still some resistanceless current.

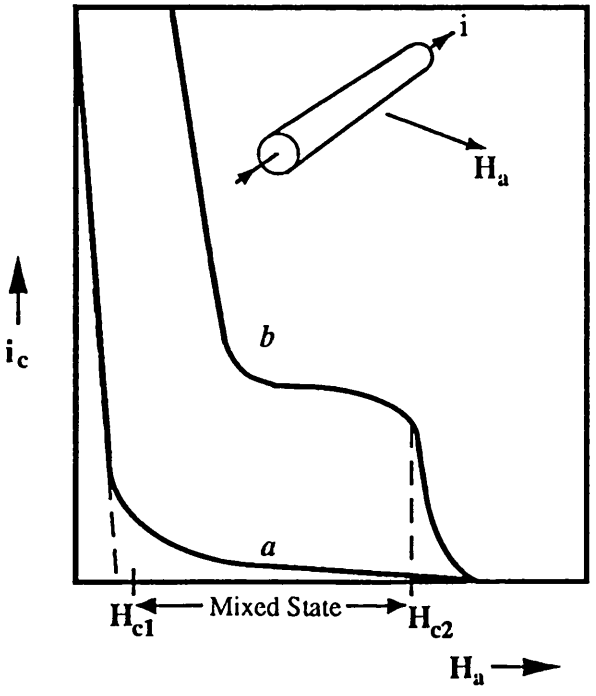

Figure 4.4 *Typical variation of critical currents of wires of (a) highly perfect, (b) imperfect type-II superconductors in transverse applied magnetic field.*

When in a mixed state i_c is completely controlled by the perfection of the material; the more imperfect the material the greater is the i_c. The effect on i_c of an imperfect type II superconducting wire in a transverse applied magnetic field is shown in figure 4.4.

4.2 Microscopic theory of superconductivity

An early step forward in the search for a microscopic theory came when Frölich pointed out that the electron-phonon interaction in a periodic lattice was able to couple two electrons together in such a way that they behaved as if there was a direct interaction between them [1]. This interaction can be thought of as being transmitted by a phonon. One electron emits a phonon which is then immediately absorbed by another.

At absolute zero, the points which represent the momenta of the electrons in three-dimensional momentum space occupy a sphere of radius p_F, known as the "Fermi-sea". This is given by,

$$p_F = (2m\varepsilon_F)^{1/2} \qquad (4.9)$$

where ε_F is the Fermi energy and m the electronic mass.

It was then Cooper who discussed that when two electrons are added to a metal at absolute zero, they are forced by Pauli principle to occupy states with $p > p_F$.and that the energy of an electron before and after emission or absorption of a phonon, ε_1 and ε'_1 respectively, must lie above ε_F. If there is an attraction between them, however weak, they are able to form a bound state so that their total energy is less than $2\varepsilon_F$. This attraction causes scattering of the electrons accompanied by changes in their momenta. If the attraction is an attractive one, the potential energy which results from it is negative. Hence over a period of time during which there are many scattering events, the energy of the two electrons is decreased by the time-average of this negative potential energy, and the amount of this decrease is proportional to the number of scattering events which take place.

The probability of scattering is appreciable only if ε_1-$\varepsilon'_1 \approx h\nu_q$, where ν_q is the frequency of the phonon. The lowest values of ε_1 and ε'_1 which are above ε_F and at the same time satisfy ε_1-$\varepsilon'_1 \approx h\nu_q$ lie within an energy $h\nu_L$ of ε_F, where ν_L is the average phonon frequency typical of the lattice. Also the corresponding p_1 and p'_1 must lie within a range $\Delta_p = mh\nu_L / p_F$ of the Fermi momentum p_F. It turns out that the largest number of allowed scattering processes, yielding the maximum lowering of the energy, is obtained by pairing electrons with equal and opposite spins and momenta. These are known as Cooper pairs. In forming a Cooper pair, the lowering of the potential energy due to the interaction exceeds the amount by which the kinetic energy is in excess of $2\varepsilon_F$.

The great step forward towards a microscopic theory of superconductivity came when Bardeen, Cooper and Schriefer were able to show how Coopers' results could be extended to apply to many interacting electrons. Coopers' results described previously refer to what happens when two additional electrons are added to a metal at absolute zero. It applies equally to the situation whereby a state of lower energy is formed by removing the electrons with p slightly less than p_F from a metal at absolute zero and allowing them to form a Cooper pair. If this can be done for one pair, it can be done for many pairs and lower the energy even further. These Cooper pairs are all in the same quantum state with the same energy.

There is a limit to the number of electrons which can be raised from $p < p_F$ to form Cooper pairs. In order that a pair of electrons may be scattered from ($\mathbf{p}_i\uparrow$, $-\mathbf{p}_i\downarrow$) to ($\mathbf{p}_j\uparrow$, $-\mathbf{p}_j\downarrow$), where $\mathbf{p}_x$ corresponds to electron with momentum $\mathbf{p}$ in state x and the arrow denotes spin up or down, the states ($\mathbf{p}_i\uparrow$, $-\mathbf{p}_i\downarrow$) must first be occupied and the states ($\mathbf{p}_j\uparrow$, $-\mathbf{p}_j\downarrow$) must be empty. There is an optimum arrangement which gives the lowest overall energy and this can be described by specifying the probability h_i of the pair state ($\mathbf{p}_i\uparrow$, $-\mathbf{p}_i\downarrow$) being occupied. This is given by,

$$h_i = \frac{1}{2}\left[1 - \frac{\varepsilon_i - \varepsilon_F}{\{(\varepsilon_i - \varepsilon_F)^2 + \Delta^2\}^{1/2}}\right] \qquad (4.10)$$

where $\varepsilon_i=(p_i)^2/2m$ and positive square root is taken. The quantity Δ which has the dimensions of energy is given by,

$$\Delta = 2h\nu_L \exp[- \{N(\varepsilon_F)V\}^{-1}] \qquad (4.11)$$

where ν_L is the average phonon frequency, $-V$ the matrix element of the scattering interaction and $N(\varepsilon_F)$ is the density of states for electrons at the Fermi energy. Thus the state of lowest energy (the ground state) occurs when all the electrons with momenta within a range $\Delta_p = mh\nu_L/p_F$ about p_F are coupled together in Cooper pairs having opposite momentum and spin.

If the superconductor is excited to a higher state, by raising the temperature or by illuminating it with light of an appropriate wavelength, energy is imparted to the Cooper pairs. The minimum amount of energy required to break up a Cooper pair is 2Δ, known as the energy gap, where Δ is given by eqn 4.11.

The splitting up of a pair results in electrons no longer having equal and opposite momenta. Also decreasing the number of available states to form Cooper pairs reduces the number of scattering events with a corresponding decrease of their binding energy. Hence the total energy of the entire system of electrons increases.

The energy gap decreases as the temperature rises until at the critical temperature, T_c, it falls to zero. T_c is related to the energy gap at absolute zero, $\Delta(0)$, by,

$$2\Delta(0) = 3.5kT_c \qquad (4.12)$$

where k is the Boltzmann's constant. Inserting eqn. 4.12 into eqn.4.11 gives,

$$3.5kT_c = 4h\nu_L \exp[- \{N(\varepsilon_F)V\}^{-1}] \qquad (4.13)$$

Since $\nu_L \propto M^{-1/2}$, where M is the isotopic mass, $T_c \propto M^{-1/2}$. This is known as the isotope effect and is characteristic of a phonon-mediated superconductor.

The great power of the BCS theory is that properties such as critical temperature, T_c, Meissner effect, penetration depth, λ, and coherence length, ζ, can be calculated for superconductors in general.

4.3 High temperature superconductors (HTSC)

A full discussion of the crystal chemistry of the various structural types that display superconductivity is beyond the scope of this thesis. The interested reader is referred to references 4 & 5. This discussion is limited to the most rigorously studied materials with the objective of highlighting some of the basic properties that are apparently common to the cuprate based superconductors.

Following the initial discovery by Bednorz and Müller [6] of superconductivity at 34 K in the La-Ba-Cu-O system several new superconducting cuprates have been discovered having transition temperatures, T_c from 10 K to as high as 133 K [7]. The currently known inorganic HTSC systems are listed in table 4.1 and in figure 4.5 the crystal structures of a number of these systems are shown.

A structural feature common to all these compounds, which belong to the perovskite family shown in figure 4.6(a), is that they contain layers with chemical composition AO_x, where A is the cation and x is 0, 1 or 2, and for $x=2$, the composition is CuO_2 [8]. Generally if oxygen-free layers are absent, $T_c \leq 40$ K. If all types of layers are present, then T_c may be reached to as high as 133 K. Any $x=0$ layers are always bracketed by two $x=2$ layers. There are also layers of composition AO where the oxygen is usually in the centre of the squares formed by the cations. The existence and stacking of the Cu-O planes is critical, since it is the electrical conduction in these planes that gives rise to superconductivity.

HTSC structures are either tetragonal or orthorhombic. They fall into families with different number of "immediately adjacent Cu-O planes". These planes are in turn separated from the next set of Cu-O planes by metal-O "isolation planes".

Table 4.1 *The various high temperature superconducting phases and their corresponding* T_c.

Formula	$\mathbf{T_c}$
$(La_{2-x}Sr_x)CuO_4$	38
$(La_{2-x}Sr_x)CaCu_2O_6$	60
$YBa_2Cu_3O_7$	92
$YBa_2Cu_4O_8$	80
$Y_2Ba_4Cu_7O_{14}$	40
$Bi_2Sr_2CuO_6$	0-20
$Bi_2Sr_2CaCu_2O_8$	85
$Bi_2Sr_2Ca_2Cu_3O_{10}$	110
$TlBa_2CuO_5$	0-50
$TlBa_2CaCu_2O_7$	80
$TlBa_2Ca_2Cu_3O_9$	110
$TlBa_2Ca_3Cu_4O_{11}$	122
$Tl_2Ba_2CuO_6$	0-80
$T_2Ba_2CaCu_2O_8$	108
$Tl_2Ba_2Ca_2Cu_3O_{10}$	125
$(Nd_{2-x-y}Ce_ySr_x)CuO_4$	30
$(Nd_{2-x}Ce_x)CuO_{4-y}$	24
$Sr_{1-x}Nd_xCuO_2$	40
$HgBa_2CuO_{4+\delta}$	94
$HgBa_2Ca_2Cu_3O_{8+\delta}$ (*includes some* $HgBa_2CaCu_2O_{6+\delta}$)	133

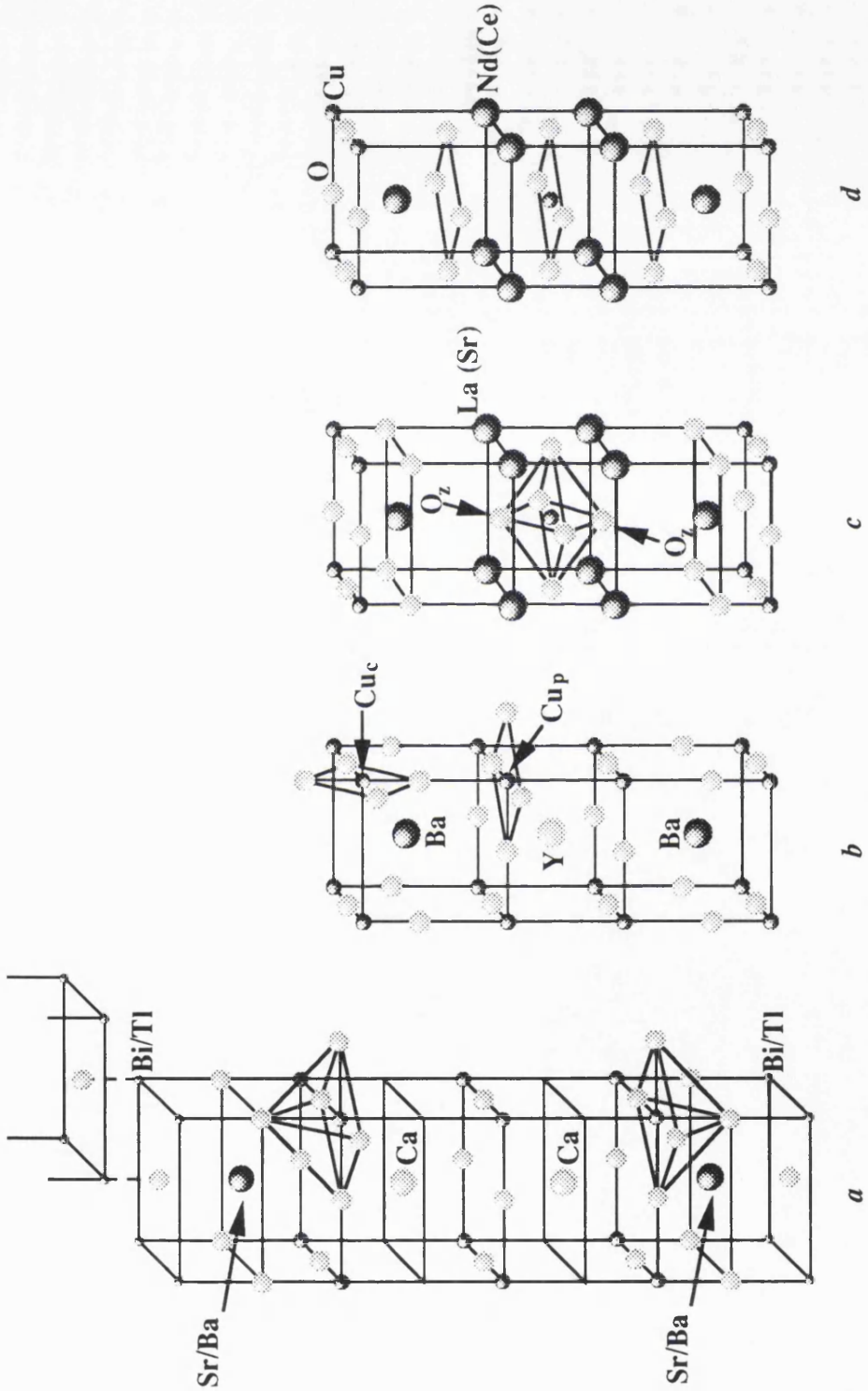

Figure 4.5 *The crystal structures of: (a)- $Tl(Bi)_2Ba(Sr)_2Ca_2Cu_3O_{10}$, (b)- $YBa_2Cu_3O_7$, (c)- $La_{2-x}Sr_xCuO_4$ and (d)- $Nd_{2-x}Ce_xCuO_4$*

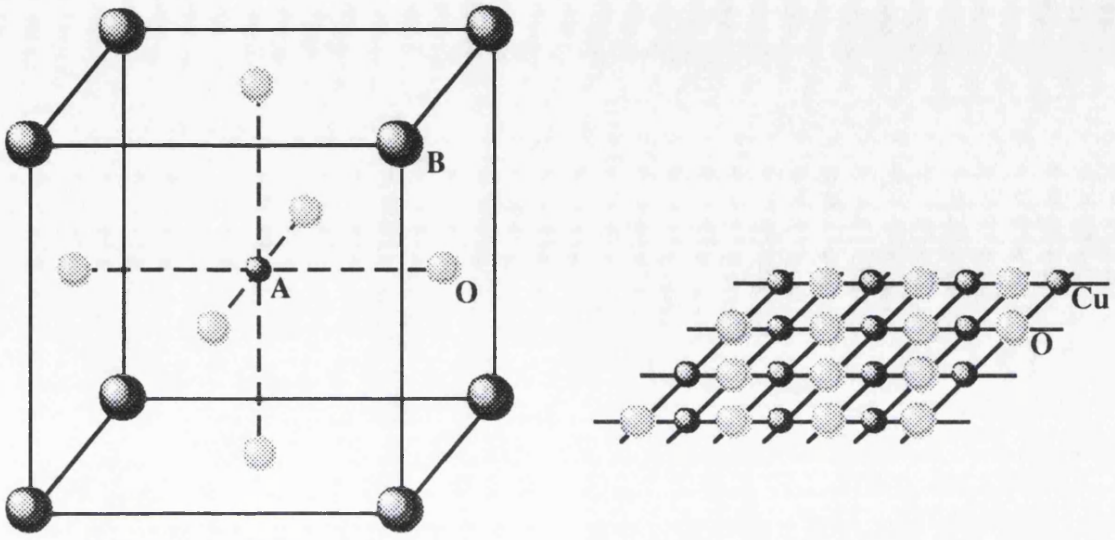

a *b*

Figure 4.6 *The ABO_3 crystal structure of a perovskite (a), and the square-planar bonding of CuO_2 (b).*

The square-planar bonding of Cu to four O atoms can be seen in figure 4.6(b). In all of the HTSC materials, the Cu-O distance is rather short, ≈1.90 Å [4]. However, the Cu-O planes are relatively far apart, for example being ≈6.6 Å in the case of $La_{2-X}Sr_XCuO_4$, figure 4.5(c) [4]. In the case of $YBa_2Cu_3O_7$, figure 4.5(b) the immediately adjacent Cu-O planes are ≈3.2 Å apart while these two Cu-O planes are >8.2 Å from the next two Cu-O planes [4]. For a HTSC crystal such as $Tl_2Ba_2Ca_2Cu_3O_{10}$, there are three immediately adjacent Cu-O planes again separated from each other by ≈3.2 Å, while these planes are separated from the next set by ≈11.6 Å, figure 4.5(a) [4].

Above and below almost all of the Cu atoms there may be an oxygen atom, the apical O_z atom, which is actually part of the metal-O isolation planes since the Cu-O distances are greater than 4.2 Å. For example in the case of the T and T' structures of $La_{2-x}Sr_xCuO_4$ and $Nd_{2-x}Ce_xCuO_{4-y}$, shown in figures 4.5 (c) & (d),there are two O_z atoms, one above and one below the Cu atom in the T structure, and no O_z atom in the T' structure.

In the most well studied of these materials, $YBa_2Cu_3O_7$, there are two different types of Cu atoms, Cu_p for the Cu in the two Cu-O planes, and Cu_c for the Cu on a four-coordinated chain. The occurrence of oxygen atoms, O_c, in the chain causes this material

to be orthorhombic, with the Cu_c-O_c-Cu_c axis defined as the *b*-axis. The Cu_c-O_c distance is 1.94 Å (half of the *b*-axis unit cell length) and the Cu_c-O_z distance is 1.84 Å [4]. Thus the Cu_c atoms are strongly covalently bonded to the four O atoms in a square-planar configuration. The chains not only act as charge reservoirs but also as structural elements.

By removing the O_c atom in the chain the $YBa_2Cu_3O_6$ structure is obtained which results in the Cu_c atoms being two-coordinated in the O_z-Cu_c-O_z sticks and the structure becoming tetragonal. Determining the structure of $YBa_2Cu_3O_{7-\delta}$ with intermediate oxygen content (between 6 and 7) is the subject of considerable research.

For δ=0 to 0.2, T_c is 93 K, but for a smaller oxygen content T_c decreases. At δ=0.75 there is a metal-insulator phase transition with the material becoming tetragonal and antiferromagnetic.

The copper valence in these materials, which can be easily changed by either the removal or uptake of oxygen or by certain cationic substitutions, is a crucial parameter for the appearance of superconductivity. In most of these compounds only those chemical substitutions that lead to an average copper valence greater than 2 can produce super-conductivity [9]. When the valence of copper is 2+, the electrons are localized in a copper-oxygen bond. In some cases when additional oxygen atoms are present in the compound (e.g., Sr in $La_{2-x}Sr_x CuO_4$) further electron can be pulled away from the copper atoms, driving the average valence towards 3+ [10]. The conduction band is then swarmed with electrons leaving regions of positive charged holes. The formation of Cu with a valence greater than 2 (i.e. oxidation of Cu) implies the introduction of a hole charge state. These holes or missing electrons, are the charge carriers in all these cuprate superconductors and they are therefore termed, *p*-type [9]. The holes are believed to reside principally on the Cu-O plane and result in metallic and superconducting behaviour for $x \geq 0.06$ with T_c peaking at ≈38 K for x=0.15. However, for $x > 0.25$ although the material remains a metal (in fact a better electrical conductor at room temperature) it is no longer a superconductor.

A family of superconductors discovered in $Ln_{2-x}Ce_xCuO_{4-y}$ (Ln = Pr,Nd,Sm) by Tokura et al. [11] however has the property that the majority charge carriers are electrons rather than holes and for this reason they are termed *n*-type (the T' structure mentioned earlier and shown in figure 4.5(d)). In this case the reducing atoms (Ce^{4+} in $Ln_{2-x}Ce_xCuO_4$) can add electrons to some of the copper atoms, driving the valence from 2+ to 1+. As in the *p-type* system the electrons are no longer localized and can participate in electrical conduction. *N*-type superconductivity has also been discovered in $Sr_{1-y}Nd_yCuO_2$ [12] with a T_c of ≈40 K. The preparation of this material does not require the reduction step necessary for $Ln_{2-x}Ce_xCuO_{4-y}$. However, an annealing treatment in air at ≈1000°C under a hydrostatic pressure of 25 kbar is needed.

In the insulator phases of all the HTSC materials, the Cu ion magnetic moments order antiferromagnetically at relatively high temperatures. For example in La_2CuO_4, the Neél temperature is T_N ≈340 K and in $YBa_2Cu_3O_6$, T_N ≈500 K, with T_N decreasing rapidly as the metallic phases are approached [2]. In HTSC materials, the coexistence of the antiferromagnetism at temperatures well below T_c is not unusual; the rare earth atoms can magnetically order at much lower temperatures (eg. 2.2 K in $GdBa_2Cu_3O_{3-\delta}$, T_c ≈95 K) with no effect on T_c.

Paired species (electrons or holes) are known to exist in these materials, but the origin of the attractive electron-electron interaction is still debatable particularly in the case of the higher T_c superconductors (>77 K) [2]. Hoen et al. [13] have investigated the isotope effect in YBaCuO and observed a low value of $\alpha \approx 0.02$ ($T_c \propto M^{-\alpha}$, see section 4.2) which is much lower than the expected value of $\alpha \approx 0.5$ observed in the old low temperature superconductors where the electron-electron attraction is due to electron-phonon coupling. This suggests that a new mechanism, other than (or in addition to) the electron-phonon interaction to be responsible for the formation of the pairs.

Given the nature of crystal structures like those shown in figure 4.5, their physical properties show a high degree of anisotropy [14]. As far as the magnetic properties are concerned all HTSC materials are considered to be type-II superconductors [4]. The anisotropy in these structures manifests itself in an anisotropic nature of their magnetic properties. The value of H_{c2} is very high for HTSCs and therefore the coherence length

is quite small. For YBaCuO for instance H_{c2} at 0 K has been estimated to be 670 T and 120 T in the *ab*-plane and along the *c*-axis respectively. The corresponding values for ζ are $\zeta_c(0) \approx 3$ Å and $\zeta_{ab}(0) \approx 16$ Å [4]. Also in NdCeCuO, H_{c2} has been extrapolated to 0 K giving the values of 6.7 T and 137 T along the *c*-axis and in the *ab*-plane respectively, corresponding to values for ζ of $\zeta_c(0) \approx 3.4$ Å and $\zeta_{ab}(0) \approx 70$ Å [4]. For comparison in $Ba_{0.6}K_{0.4}BiO_3$, an isotropic perovskite superconductor, the value of the coherence length has been estimated to be $\zeta(0) \approx 37$ Å, indicating an almost two orders of magnitude increase in the coherence volume when compared to YBaCuO [4].

4.4 Pulsed laser deposition of high temperature superconductors

Several types of lasers have been used for thin film deposition. Pulsed CO_2 lasers have been used for deposition of HTSCs [15]. Very high deposition rates have been demonstrated although films were "bulk like", being polycrystalline and multiphase. Solid state lasers such as pulse Nd:YAG lasers operating at the fundamental (1064 nm), frequency-doubled (532 nm), or higher harmonics (355, 266 nm) have also been used for HTSC thin film deposition [16]. Excimer lasers operating at u.v. wavelengths of 351 nm (XeF), 308 nm (XeCl), 248 nm (KrF) and 193 nm (ArF) are extensively employed [17]. However the most popular laser sources for HTSC thin film deposition are the KrF excimer lasers, since the highest gain and hence the highest pulse energy are available. Although the XeCl laser line gives a slightly lower pulse energy, the gas lifetime is the longest and the HCl precursor is less corrosive to the intracavity optics than F_2.

For a multi-elemental target material, a short optical absorption length (or a large absorption coefficient) at the laser wavelength is desirable in order to deposit enough energy into a sufficiently thin region (surface absorption) so as to guarantee stoichiometric transfer. Typically, this absorption length increases as a function of the wavelength [17]. Eventually it leads to volume absorption, which may cause non-stoichiometric deposition as well as extensive ejection of target material in particulate form, thereby further degrading film properties.

Thin films of all major HTSCs have been produced by PLD, however the majority of work has been done on thin films of YBaCuO. In this section a number of growth parameters involved in growing thin films of YBaCuO are outlined.

Deposition rate and film growth mechanism:

Typically the deposition rate for YBaCuO films by PLD is about 1 Å per pulse. The deposition rate can easily be varied by changing the laser repetition rate as well as the energy density and target to substrate distance. It has been shown that good electrical properties can be obtained even at a deposition rate as high as 150 Å/s [18]. However the crystallinity of these films were inferior to films grown at a low deposition rate.

The target surface is more rapidly modified at low laser energy densities. After long laser exposure, erosion accompanied by shadowing effects lead to cone formation on the target surface [17,19,20]. These cones are tilted towards the laser incidence angle. This results in the pronounced decrease in deposition rate, increase in the number of particulates formed on the substrate and a shift in the angle of the ejected species towards the laser.

It has been observed that with increasing number of laser shots per site for a stationary target, the deposition rate decreased to a steady-state value [19]. This work was carried out at laser fluences of 1.5, 2.6 and 7.1 J/cm^2 and the deposition rate was measured by replacing a water-cooled quartz-crystal microbalance with the substrate holder. It was also found that the deposition rate for a target with density equal to 92% of a single-crystal was only 20% lower than that for a target of 55% density.

The YBaCuO films are believed to be formed by an island growth mechanism [21]. Island formation has been found to proceed via a screw dislocation resulting in spiral growth [22]. It has been shown that at a lower deposition rate, coalescence will be incomplete, thus producing "pinholes" in the film, while at higher rates coalescence will be complete but misoriented grains or "outgrowths" will nucleate. By choosing the deposition rate at the appropriate oxygen partial pressure and substrate temperature (usually ≈200 mTorr and ≈750°C) such that film coalescence is just complete smooth *c*-axis oriented films can be grown.

Norton et al. [23] made use of a "vicinal" MgO surface which consisted of (001) terraces tilted at an angle to the original (001) oriented substrate surface. The x-ray diffraction pattern of a YBaCuO layer grown on such a structure revealed that only the (001) peaks of YBaCuO were present and there were no traces of the MgO peak which indicated that the film was highly oriented with its *c-axis* normal to the substrate rather than the vicinal surface and that the lattice parameter and crystal structure of the substrate does not control the growth mechanism. The growth of YBaCuO on a vicinal surface was investigated further by using (001) $SrTiO_3$ instead of MgO [24]. The x-ray diffraction pattern of this structure revealed very weak traces of *c*-axis orientation and obviously no trace of the $SrTiO_3$ peak which indicated that this time the film grew with the *c*-axis normal to the $SrTiO_3$ vicinal plane and that film growth was dependent on the crystal properties of the substrate. This could have been further confirmed by offsetting the θ plane of the diffractometer by the tilt angle which in this case was 3°. Both the MgO peak and the (001) YBaCuO peaks should have been present in this case.

Oxygen incorporation:

$YBa_2Cu_3O_{7-\delta}$ thin films deposited in vacuum at room temperature are non-crystalline and have an oxygen content close to 6 ($\delta \approx 1$) [17]. A post-deposition anneal in air or oxygen is therefore required to stabilize the $YBa_2Cu_3O_{7-\delta}$ tetragonal phase ($\delta < 0.5$). At high substrate temperatures used during *in-situ* growth (≈750°C) another major obstacle to good film formation is the oxygen out-diffusion which makes the necessity for an oxygen ambient even more crucial. However the presence of oxygen has a number of effects on the ablation mechanism a few of which are outlined briefly in this section.

The time of flight (TOF) distributions under high ablation fluence can be controlled by changing the oxygen pressure. Using an ArF laser with an energy density above 2.2 J/cm^2, Okada et al. [25] observed a twin-peak distribution for the Ba atom while ablating a $YBa_2Cu_3O_{7-\delta}$ pellet under vacuum. The two peaks correspond to low and high velocity components. As the oxygen pressure increased, the slower velocity components were rapidly quenched while the faster velocity components were less affected by the presence of the oxygen gas.

The pressure of background oxygen was found to greatly influence the velocity distribution of ejected particles [26]. The velocities of atomic species remained quite constant from high vacuum to an oxygen ambient pressure of about 0.01 mbar and decreased rapidly beyond, whereas the velocities of diatomic species such as YO or BaO decreased regularly with the oxygen pressure. It was also found that in vacuum, the velocity as well as angular distributions of the various species were somewhat different [27,28]. Such spatial and temporal separation of the atoms in the plume is detrimental to large-area uniform film distribution. However the effect of having an ambient oxygen background was found to homogenize the atomic velocities, probably as a result of the large number of background collisions. Hence the presence of an ambient oxygen background plays an important role in the hydrodynamics as well as in providing more oxygen atoms for *in-situ* grown films.

The exact O_2 pressure depends on the specific system and the laser wavelength used. It was found that shorter-wavelength lasers such as ArF will optimise at lower O_2 pressures than longer-wavelength lasers such as KrF or XeCl [29]. The pressure cannot be too high, otherwise the laser plume will be quenched and the deposition rate will be intolerably low.

Apart from reducing the out-diffusion of oxygen, *in-situ* deposition of HTSC films at low substrate temperatures (less than 600°C) can make the process more practical to integrate with semiconductor technology. A number of methods have been utilized to achieve successful depositions at lower substrate temperatures. If instead of plain oxygen a more reactive oxidizing agent is used, less of it should be required to supply the oxygen necessary for HTSC films. It has been demonstrated that the use of highly oxidizing gases such as ozone (MBE-YBCO) [30], N_2O (PLD-YBCO) [31,32] and NO_2 (MBE-BSSCO) [33,34] can redefine the optimum growth parameters towards lower pressures and lower temperatures.

The major role of oxygen is due to its incorporation into the surface of the film rather than the reaction between oxygen and the plasma. It was found that better films were produced if an oxygen jet was pointed towards the substrate [35]. Substrate temperatures as low as 600°C could be used without post-annealing.

By applying a voltage of 300V on a ring electrode placed between the $YBa_2Cu_3O_{7-\delta}$ target and the substrate, Witanachchi et al. [36] managed to reduce the required substrate temperature to 400°C without post-annealing. A dc discharge was formed which enhanced the production of O_2^+ ions and thus increased the oxygen content of the deposited film.

Target -substrate distance:

There is a strong correlation between the oxygen pressure, P_{O_2}, and the target-substrate distance, D, as well as the strong correlation between P_{O_2} and substrate temperature, T_s for obtaining high quality $YBa_2Cu_3O_{7-\delta}$ films by PLD. Kim and Kwok [37] studied this dependence using an ArF laser with an energy density of 3 J/cm^2. Figure 4.7 shows the optimum P_{O_2} for obtaining the best T_c and R(100)/R(300) for films deposited at 680°C at six different values of D. This figure can be used in conjunction with the P_{O_2} - T_s phase diagram in designing the various deposition parameters.

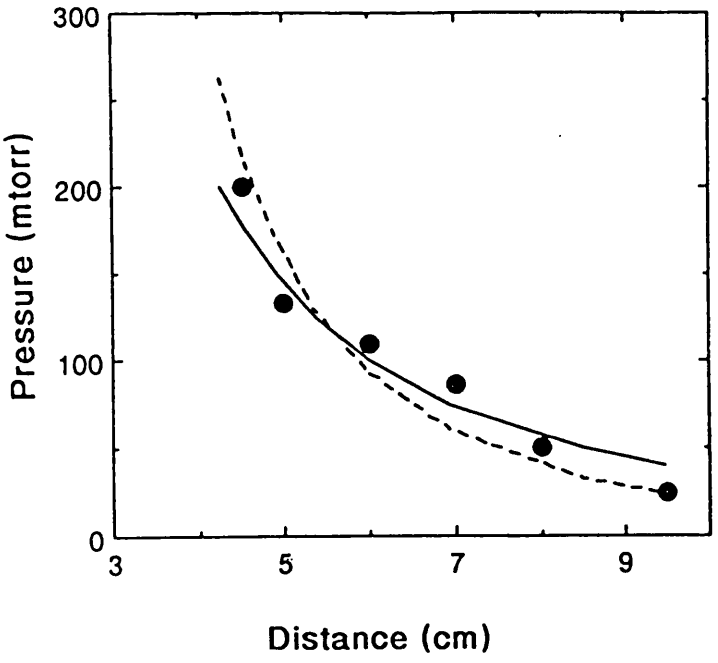

Figure 4.7 *Optimal oxygen partial pressure, P_{O_2} as a function of target-substrate distance, D. Solid line: $P_{O_2} x D^2$ = const. Dotted line: $P_{O_2} x D^3$ = const. [37].*

The reason for an optimal distance has been argued to be due to the velocities of various species in the laser plume attaining a value whereby a decent flux of moderately energetic ions and atoms can produce good quality films. Near the target the velocities higher than 10^6 cm/s are present which are reduced as a function of D due to collisions with O_2. These energetic ions and atoms can cause damage to the film if the substrate is too close to the target (for example the kinetic energy of Ba at 1.5×10^6 cm/s is 160 eV, which can cause sputtering damage to the substrate). On the other hand, if the substrate is too far away, the deposition rate will be too low and surface activation by moderately energetic ions and atoms will not be available. The "blast wave model" [60] was used to quantify the *P-D* scaling relationship. This model describes the propagation of a shock wave caused by explosive release of energy, through background gas. After a time t, the distance of which the shock-front propagates depends on the pressure. Best films are always obtained at a certain optimal value of shock-front velocity (obtained from dD/dt) regardless of P. P is related to D as:

$$PD^2 = \text{const.} \quad \text{(for low pressure of } \approx 100 \text{ mTorr)} \qquad (4.14)$$

$$PD^3 = \text{const.} \quad \text{(for high pressure of } >> 100 \text{ mTorr)} \qquad (4.15)$$

It can be seen from figure 47 that both equations fit the data reasonably well, although eqn 4.14 is a slightly better fit.

Substrate preparation:

The transport properties and morphology of HTSC thin films can be affected by the substrate quality and preparation. Grain boundaries, twins, polish scratches and residual chemicals can all contribute to lowering the quality of these films [38,39]. It is therefore essential that substrates with high crystal quality are employed.

As discussed the initial stages of YBaCuO growth is believed to proceed via an island growth mechanism. Moeckly et al. [40] have suggested that it is highly favourable for these islands to nucleate at the edge of steps formed on the surface of the MgO substrate. They investigated the effect of substrate preparation by using mechanically polished MgO substrates which prior to YBaCuO film deposition were either, chemically cleaned, chemically polished in a hot phosphoric acid etch, or heated in air or oxygen to 1100-1200°C for 12-24 hr. The process of annealing in air or oxygen was believed to form a

high density of atomic steps on the substrate surface. Both the transport properties and the crystal quality of the films were shown to improve as the substrate preparation was moved from mechanically polished to chemically polished to annealing in air or oxygen. Awaji et al. [42] also obtained an improvement in the quality of their sputter deposited YBaCuO films grown on pre-deposited oxygen annealed MgO substrates. The annealing treatment was believed to remove the contamination created by crystal cleavage and water vapour. The treatment was found to be more effective for films of very low thickness (5 nm).

4.5 General requirements for thin film deposition

The requirements for device-quality thin films can be summarized as follows:

i) A high T_c:
It is necessary to grow the films with the appropriate composition in the correct crystal phase [14]. The superconducting film must have a high T_c layer right up to the interface to within the ζ of the material [42].

ii) A small transition width ΔT between the normal and superconducting states:
The film has to enter the superconducting state over a narrow temperature range. This is particularly important in the case of multi-phase superconducting systems such as, BSCCO or TBCCO [14].

iii) A high critical current J_c:
The presence of defects in the crystal structure or features such as grain boundaries in the microstructure introduced during the deposition could reduce this requirement [14]. The large anisotropy in electrical conductivity requires a perfect orientation of the *c*-axis perpendicular to the substrate, and perfect alignment of the *a*- and *b*-axes of the orthorhombic phase (*a*-axis if tetragonal) [43]. The slow growth rate in the *c*-direction leads to a platelet morphology of the HTSC oxides [43]. However, in constructing devices based on the Josephson effect, a long coherence length, ζ, is considered to be advantageous [14]. The value of ζ_a (31 Å [42]) is large compared to the *a*- and *b*-axes

lattice constants (3.83 Å and 3.89 Å respectively in the case of $YBa_2Cu_3O_7$ [43]) whereas ζ_c is small (4.3 Å [42]) compared to the *c*-axis lattice constant (11.69 Å in the case of $YBa_2Cu_3O_7$ [43]), hence it would be insensitive to a modest amount of disorder expected at the interfaces.

iv) A smooth film surface:
It is crucial to have films with with smooth superconducting surfaces, in order to delineate micron and submicron features and to fabricate junction devices consisting of superconducting layers sandwitching an insulating or normal metal [14].

v) Sharp interfaces between films, and film and substrate:
This property requires that little interdiffusion or chemical reaction take place, since these could lower the T_c in such materials [14].

Despite the fact that there are phases with T_c greater than 100 K most work has concentrated on the fabrication of the YBCO compound for which a T_c of ≈90 K is readily obtained. For both BSCCO and TBCCO it is difficult to obtain a pure, high T_c (2223) phase without inclusion of the lower T_c phases. However, the oxygen content in YBCO is critical and its phase transformations can introduce undesirable effects [43]. Also YBCO may lose O_2 over long periods of time in the presence of humidity which can be prevented by encapsulation.

The HTSC-substrate combination needs to meet the following requirements [43]:

(a) Lattice match: since the superconducting current is highly anisotropic and is maximum in the *a-b* plane, then the a plane of the substrate should be as close as possible to the value of 3.8 or $\sqrt{2}$x3.8 = 5.4 Å.

(b) Chemical stability: in order to minimize unwanted chemical reactions between the substrate and the HTSC oxide. The best T_c and J_c results have been obtained with $SrTiO_3$ substrates (a=3.904 Å [44]) which are very lossy for microwave applications. $LaAlO_3$ (a=3.788 Å [44]) has lower microwave losses; however, it undergoes a phase transformation at 450°C which introduces crystalline defects in the substrate. MgO, with

a relatively bad lattice match (a =4.211 Å [45]), seems to give good quality films with nearly all HTSC oxides.

Thin films of HTSC can be formed either *in-situ* by depositing the films directly in the orthorhombic or tetragonal phase at a certain temperature in an oxygen ambient (followed by an *in-situ* anneal in a reducing atmosphere in the case of NCCO), or by depositing the film in some random phase at a relatively low temperature followed by a high temperature anneal (higher than in an *in-situ* deposition) in oxygen (followed by annealing in a reducing atmosphere in the case of NCCO) - *ex-situ* growth. From a technological point of view, in order to produce sharp interfaces, and minimize film-substrate interaction and stresses in the film, a low temperature process is preferred.

4.6 Deposition of HTSC on silicon

It is desirable to form good quality HTSC films on substrates such as silicon, rather than oxide single-crystal substrates such as MgO, $LaAlO_3$ or $SrTiO_3$ due to their high cost and restricted substrate size. The main problem in using silicon is the redistribution of elements due to chemical interactions and the possibility of interdiffusion of detrimental impurities between the film and the substrate during any high temperature annealing process [46]. Three methods can minimise these effects:
(i) The growth of thicker films.
(ii) A reduction in the processing temperature by using either *in-situ* deposition or rapid thermal annealing.
(iii) The use of a buffer layer between the film and the substrate.

The growth of thicker YBCO films directly on silicon has resulted in superconductors with transport properties similar to that of bulk samples, i.e. high T_c of ≈90 K but low J_c of a few hundred A/cm^2 at 77 K [47]. The *in-situ* growth of YBCO films directly on silicon at low temperatures has resulted in films with T_c in the 85 K region and J_c of less than 5x10^4 A/cm^2[47].

Growth of HTSC thin films on silicon using an intermediate buffer layer has by far given the best results with properties similar to that of films on the more popular oxide

substrates. However, it has been suggested, that the values of critical current density, J_c are generally low unless buffer layers with high crystalline perfection are used [47]. Table 4.2 lists some of the properties of a number of materials, which need to be considered in choosing the correct substrate or buffer layer.

Table 4.2 *Crystal and thermal properties of a number of materials used in HTSC thin film processing.*

Material	Lattice parameter (001) plane (Å)	Thermal expansion coefficient ($x10^{-6}/K$)	% Lattice mismatch with Si (room temp.)
Si	5.43	3.0	
MgO	4.2	13.5	9.4 (110)
YSZ	5.10-5.16	10.4	5.0-6.0 (100)
$SrTiO_3$	3.90	9.5	1.6 (110)
$MgAl_2O_4$	8.11	7.4	5.6 (110)
$BaZrO_3$	4.19	7.8	9.3 (110)
$LaAlO_3$	3.79	10.0	1.3 (110)
$NdGaO_3$	3.86	8.0	<0.1 (110)
CeO_2	5.42	11.6	0.18 (100)
CaF_2	5.40		0.6 (100)
PrO_2	5.47		0.73 (100)
$PbTiO_3$	3.96	-16.0 (below 490°C)	<0.1 (110)
		25.0 (above 490°C)	
$BaTiO_3$	3.99	14.0	3.9 (110)
ITO		10.0	
$YBa_2Cu_3O_7$	3.82, 3.88	12.0	<0.1 (110)

It can be seen from the above discussion that interdiffusion and chemical reaction at the interface of Si and YBaCuO, and for that matter any HTSC, lead to a reduction in J_c. Buffer layers with flat surfaces and high crystalline perfection are favoured, since they essentially form the substrate for the growth of HTSC thin films. Both the HTSC/buffer layer and the buffer layer/Si would therefore need to meet the requirements necessary for

HTSC-substrate combination. It has been suggested that the value of J_c can be enhanced if buffer layers with high crystalline perfection are used [47]. Table 4.3 lists a number of YBaCuO/buffer layer/Si combinations with their resulting T_c and J_c, and the method of deposition used.

Table 4.3 *YBaCuO/buffer layer/Si combinations with their resulting T_c and J_c, and method of deposition used.*

Buffer layer	T_c (K)	J_c (A/cm^2)	Deposition method	Reference
$BaTiO_3/MgAl_2O_4$	87	$6x10^4$ (77 K)	PLD/r.f.magnetron/CVD	[48]
CaF_2	72	N/A	PLD/MBE	[49]
CeO_2	87	$1.5x10^5$ (77K)	PLD	[50]
$CoSi_2$	91	N/A	PLD	[51]
In_2O_3	81	N/A	d.c.magnetron	[52]
Indium tin oxide	68	$2.5x10^3$ (4.2 K)	ion-beam sputtering	[53]
$MgO/BaTiO_3$	83.5	$6.7x10^5$ (77 K)	PLD	[54]
RuO_2	79	$5x10^3$ (60K)	r.f.magetron sputtering	[55]
$SrTiO_3$	73	N/A	e-beam	[56]
Yttrium Stabilized zirconia (YSZ)	89	$1x10^6$ (77 K)	PLD/e-beam	[57]
YSZ	88	$2x10^5$ (77 K)	PLD	[58]
ZrO_2/SiO_2	83	N/A	e-beam evaporation	[59]

4.7 Summary

Superconductivity and the properties associated with the traditional low temperature superconductors were introduced in the beginning of this chapter. This was complemented with a simple outline of the classical BCS theory. The newly discovered perovskite based high temperature superconductors, HTSC, were briefly discussed in terms of the common features in their tetragonal or orthorhombic crystal structures. The

importance of the average copper valence in dictating whether the charge carriers are positively charged holes or negatively charged electrons was explained. Although paired species are known to exist in these materials, the mechanism responsible for their formation has not yet been fully explained.

Pulsed laser deposition of HTSC thin films was described mainly with reference to YBaCuO. Lasers with wavelengths in the u.v. region are preferred due to the low absorption length of HTSCs at short wave lengths. The YBaCuO films are believed to be formed by an island growth mechanism in which an optimum deposition rate at the appropriate oxygen pressure and substrate temperature would reduce the problem of incomplete coalescence resulting from low deposition rates, and misoriented grains resulting from high deposition rates. A post-deposition anneal in air or oxygen is crucial in stabilizing the YBaCuO tetragonal phase. The presence of an oxygen partial pressure exists at a given substrate temperature. This can be further optimised to render the best values by adjusting the distance between the target and the substrate. The quality of the HTSC films can also be affected by the substrate quality and preparation.

For a device-quality HTSC thin film, the substrate and the superconducting layer need to be lattice matched and any difference in their thermal expansion coefficient has to be minimal. In order to grow HTSC films on substrates such as silicon, the use of an intermediate buffer layer is by far the best solution to minimize the effect of chemical interaction between the film and the substrate during a high temperature annealing process.

References

[1] A.C.Rose-Innes and E.H.Rhoderick, *"Introduction to Superconductivity"*, second edition, Pergammon Press, U.K.,(1978).

[2] R.Dalven, *"Introduction to Applied Solid State Physics"*, Chapter 8, second edition, Plenum Press, (1990).

[3] D.R.Tiley and J.Tiley, *"Superfluidity and Superconductivity"*, Chapter 6, third edition, Adam Hilger, (1990).

[4] G.Burns, *"High-Temperature Superconductivity"*, Academic Press, USA, (1992).

[5] see for example, *"High Temperature Superconductivity"*, edited by D.P.Tunstall and W.Barford, Adam Hilger, (1991).

[6] J.G.Bednorz and K.A.Müller, *Z. Phys. B*, **64**, p189, (1986).

[7] A.Schilling, M.Cantoni, J.D.Guo and H.R.Ott, *Nature*, **363**, p56, (1993).

[8] A.A.Broyles, E.Teller and B.G.Wilson, *J. of Supercon.*, **3**, 2, p161, (1990).

[9] J.M.Tarascon, L.H.Greene, J.Clayhold, B.G.Bagley, G.W.Hull, S.M.D'Egidio, P.F.Miceli, Z.Z.Wang, T.W.Jing, E.Wang, D.Brawner and N.P.Ong, *Phys. Rev. B*, **40**, 7, p4494, (1989).

[10] R.J.Cava, *Scientific American*, **7**, p24, (1990).

[11] Y.Tokura, H.Takagi and S.Uchida, *Nature*, **337**, p345, (1989).

[12] M.G.Smith, A.Manthiram, J.Zhou, J.B.Goodenough and J.T.Markert, *Nature*, **351**, p549, (1991).

[13] S.Hoen, W.N.Creager, L.C.Bourne, M.F.Crommie, T.W.Barber III, M.L.Cohen, A.Zetti, L.Bernardez and J.Kinney, *Phys. Rev. B*, **39**, p2269, (1989).

[14] F.Beech and I.W.Boyd, in *"Photochemical Processing of Electronic Materials"*, edited by I.W.Boyd & R.B.Jackman, Academic Press, New York, p387, (1991).

[15] L.Lyon, B.R.Weinberger, G.C.Peterson and H.A.Krasinski, *Appl. Phys. Lett.*, **52**, p2450, (1988).

[16] G.Koren, A.Gupta, R.J.Baseman, M.I.Lutwyche and R.B.Laibowitz, *Appl. Phys. Lett.*, **55**, p2450, (1989).

[17] X.D.Wu, S.R.Foltyn, R.C.Dye, A.R.Garcia, N.S.Nogar and R.E. Muenchausen, *Thin Solid Films*, **218**, p310, (1992).

[18] X.D.Wu, R.E.Muenchausen, S.Foltyn, R.C.Estler, R.C.Dye, A.R.Garcia, N.S.Nogar, P.England, R.Ramesh, D.M.Hwang, T.S.Ravi, C.C.Chang, T.Venkatesan, X.X.Xi, Q.Li and A.Inam, *Appl. Phys. Lett.*, **57**, p523, (1990).

[19] S.R.Foltyn, R.C.Dye, E.Peterson, K.M.Hubbard, K.C.Ott, R.C.Estler, W.Hutchinson, R.E.Muenchausen, and X.D.Wu, *Appl. Phys. Lett.*, **59**, p594, (1991).

[20] T.Venkatesan, X.D.Wu, R.Muenchausen and A.Pique, *MRS Bulletin*, **2**, p54, (1992).

[21] C.C.Chang, X.D.Wu, R.Ramesh, X.X.Xi, T.S.Ravi, T.Venkatesan, D.M.Hwang, D.M.Hwang, R.E.Muenchausen, S.Foltyn and N.S.Nogar, *Appl. Phys. Lett.*, **57**, p1814, (1990).

[22] M.Hawley, I.D.Raistrick, J.G.Beery and R.J.Houlton, *Science*, **251**, p1587, (1991).

[23] M.G.Norton, B.H.Moeckly, C.B.Carter and R.A.Buhrman, *J. Crys. Growth*, **114**, p258, (1991).

[24] M.Kamei, H.Takahashi, S.Fujino and T.Morishita, *Physica C*, **199**, p425, (1992).

[25] T.Okada, N.Shibamaru, Y.Nakayama and M.Maeda, *Appl. Phys. Lett.*, **60**, p941, (1992).

[26] C.H.Chen, R.C.Phillips and P.W.Morrison, *Thin Solid Films*, **218**, p291, (1992).

[27] J.P.Zheng, Q.Y.Ying, S.Witanachchi, Z.Q.Huang, D.T.Shaw and H.S.Kwok, *Appl. Phys. Lett.*, **54**, 10, p954, (1989).

[28] T.Venkatesan, X.D.Wu, A.Inam and J.B.Wachtman, *Appl. Phys. Lett.*, **52**, 14, p1193, (1988).

[29] H.S.Kwok, *Thin Solid Films*, **218**, p277, (1992).

[30] B.R.Johnson, K.M.Beauchamp, T.Wang, J,X.Liu, K.M.McGreer, J.C.Wan, Y.J.Zhang, M.Tuominen, M.L.McCartney and A.M.Goldman, *Appl. Phys. Lett.*, **56**, p1911, (1990).

[31] G.Koren, A.Gupta and R.J.Baseman, *Appl. Phys. Lett.*, **54**, p1920, (1989).

[32] P.Schwab, D.Baüerle, *Physica C*, **182**, 1-3, p103, (1991).

[33] M.Kawai, S.Watanabe and T.Hanada, *J. Vac. Sci. Technol. A*, **8**, p4106, (1990).

[34] M.Kawai, S.Watanabe and T.Hanada, *J. Cryst. Growth*, **112**, p745, (1991).

[35] A.Inam, M.S.Hedge, W.D.Wu, T.Venkatesan, P.England, P.F.Miceli, E.W.Chase, C.C.Chang, J.M.Tarascon and J.B.Wachtman, *Appl. Phys. Lett.*, **53**, 908, (1988).

[36] S.Witanachchi, H.S.Kwok, X.W.Wang and D.T.Shaw, *Appl. Phys. Lett.*, **53**, p234, (1988).

[37] H.S.Kim and H.S.Kwok, *Appl. Phys. Lett.*, **61**, 18, p2235, (1992).

[38] M.Schieber and Y.Ariel, *Appl. Phys. Lett.*, **61**, 8, p970, (1992).

[39] Z.Barkay, D.Racah, E.Grünbaum and G.Deutcher, *J. Appl. Phys.*, **73**, 11, p7585, (1993).

[40] B.H.Moeckly, S.E.Russek, D.K.Lathrop, R.A.Buhrman, J.Li and J.W.Mayer, *Appl. Phys. Lett.*, **57**, 16, p1687, (1990).

[41] T.Awaji, K.Sakura, Y.Sakaguchi and T.Kobayashi, *Jpn. J. Appl. Phys.*, **31**, pL642, (1992).

[42] T.Venkatesan, X.D.Wu, A.Inam, M.S.Hedge, E.W.Chase, C.C.Chang, P.England, D.M.Hwang, R.Krchnaveh, J.B.Wachtman, W.L.McLean, R.Levi-Setti, J.Chabala and Y.L.Wang, *"Chemistry of High Temperature Superconductors II"*, (ed. D.Nelson and T.F.George) ACS Symp. Ser., 377, (1988).

[43] M.Schieber, *J. Crystal Growth*, **109**, p401, (1991).

[44] F.S.Galasso, *"Perovskites and High T_c Superconductors"*, Chapter II, Gordon & Breach Science, 1990.

[45] D.K.Fork, F.A.Ponce, J.C.Tranontana and T.H.Geballo, *Appl. Phys. Lett.*, **58**, 20, p2294, (1991).

[46] K.Harada, N.Fujimori and S.Yazu, *Jpn. J. Appl. Phys.*, **27**, 8, p1524, (1988).

[47] A.Mogro-Campero, *Supercon. Sci. Tech.*, **3**, p155, (1990).

[48] D.M.Hwang, R.Ramesh, C.Y.Chen, X.D.Wu, A.Inam, M.S.Hedge, B.Wilkens, C.C.Chang, L.Nazar, T.Venkatesan, S.Miura, S.Matsubara, Y.Miyasaka and N.Shohata, *J. Appl. Phys.*, **68**, 4, p1772, (1990).

[49] A.N.Tiwari, S.Blunier, H.Zogg, P.Lerch, F.Marcenat and P.Martinoli, *J. Appl. Phys.*, **71**, 10, p5095, (1992).

[50] L.Luo, W.D.Wu, R.C.Dye, R.E.Muenchausen, S.R.Foltyn, C.J.Maggiore, Y.Coulter, and T.Inoue, *Appl. Phys. Lett.*, **59**, 16, pL2043, (1991).

[51] A.Kumar and J.Narayan, *Appl. Phys. Lett.*, **59**, 14, p1785, (1991).

[52] Y.Zeng, Z.Zhang, W.Luo, N.Yang, Y.Cai and X.Shen, *Thin Solid Films*, **214**, p235, (1992).

[53] B.J.Kellet, J.H.James, A.Gauzzi, B.Dwir, D.Pavuna and F.K.Reinhart, *Appl. Phys. Lett.*, **57**, 11, p1146, (1990).

[54] D.K.Fork, F.A.Ponce, J.C.Tramontana and T.H.Geballe, *Appl. Phys. Lett.*, **58**, 20, p2294, (1991).

[55] Q.X.Jia and W.A.Anderson, *Appl. Phys. Lett.*, **57**, 3, p304, (1990).

[56] H.Ishiwara, N.Tsuji, H.Mori and H.Nohira, *Appl. Phys. Lett.*, **61**, 12, p1459, (1992).

[57] A.Lubig, C.Buchal, J.Schubert, C.Copeti, D.Guggi, C.L.Jia and B.Stritzker, *J. Appl. Phys.*, **71**, 11, p5560, (1992).

[58] R.D.Vispute, S.M.Kanetkar, S.B.Ogale, K.C.Rajkumar, A.Madhukar, N.Parikh and B.Patnaik, *Physica C*, **199**, p59, (1992).

[59] A.Mogro-Campero and L.G.Turner, *Appl. Phys. Lett.*, **52**, 14, p1185, (1988).

[60] D.B.Geohegan, *Appl. Phys. Lett.*, **60**, 22, p2732, (1992).

Chapter 5

Experimental Procedure

In this chapter the experimental set-up for thin film deposition using PLD is described. Detailed treatment of the characterization techniques used during the course of this project is beyond the scope of this thesis and only a brief description is given. The interested reader may refer to the references given.

5.1 Experimental set-up for thin film deposition

Two experimental set-ups for PLD of thin films were constructed and used during the course of this project one of which was employed for depositions using a Q-switched frequency doubled Nd:YAG laser (532 nm) and the other was dedicated to depositions using a KrF excimer laser (248 nm). Apart from the type of laser, appropriate optics and substrate heater, both systems were basically similar in design and set-up. This was shown in figure 3.1.

The deposition set-up consisted of a vacuum chamber which could be pumped down to pressures of $\approx 1 \times 10^{-6}$ mbar using a turbo-molecular pump. The walls of the chamber were degased by heating them up using a halogen lamp mounted inside the chamber which also helped to reduce the amount of water vapour, the main constituent at vacuum pressures of $\approx 10^{-6}$ mbar. A reactive gas could be let in through a needle valve. The target (pellet of superconducting or dielectric material) was held using three adjustable screws inside a holder which was connected to a motor and rotated at 5 rpm. The distance between the target and substrate could be varied by moving either of them to and fro. The laser was guided to the vacuum cell via a series of mirrors, and a lens was used through which the beam was focused and defocused onto the target surface.

The Nd:YAG laser (Quantel, model YG 580) could deliver pulses with 4 ns duration (FWHM) and an energy of ≈1 J which was reduced by the aid of neutral density filters. The repetition rate could be set to 10 Hz, 5 Hz, 2 Hz or single pulses (controlled manually). The excimer laser (Lambda Physic, model LPX 300) could deliver pulses with 20 ns duration (FWHM) and an energy of ≈1 J. Laser conditions such as energy and repetition rate (1-10 Hz) could be altered on a computer program menu.

Two types of substrate heaters were used, a home-made one and a commercial one. The home-made substrate heater, shown in figure 5.1, consisted of a ceramic material (pyrophylite) which was initially machinable but was hardened when fired at a high temperature (≈1000°C). The heating wire (FeCrAlY) was inserted through the grooves machined in the substrate holder, and covered with alumina cement. FeCrAlY has the property that once fired its surface oxidizes without affecting the inner core of the wire. This substrate holder could be heated up to 800°C in oxygen atmosphere (≈10^{-1} mbar), however it had the disadvantage that it kept burning out after two or three depositions at high temperatures and high oxygen pressures (≈800°C, ≈10^{-1} mbar).

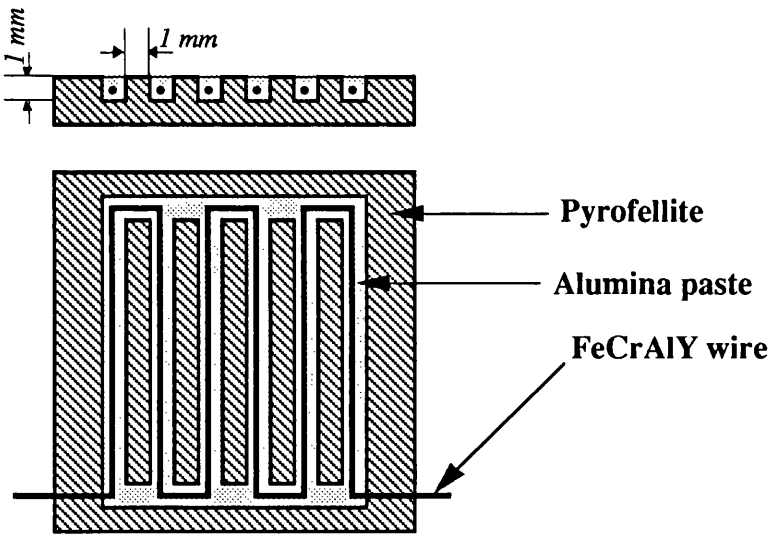

Figure 5.1 *Cross-sectional front and top views of the home-made substrate heater.*

The commercial silicon nitride substrate heater could be heated up to 900°C under high oxygen pressures, eg. ≈4x10^{-1} mbar. This heater also degraded -realised by an increase

in its electrical resistance - when subjected to high temperatures and oxygen pressures but its lifetime was considerably longer than the home-made one. Since depositions at high oxygen pressures were mainly carried out using the excimer laser, eg. in the *in-situ* deposition of superconducting materials, the home-made substrate heater was used in the set-up using the Nd:YAG laser and the commercial substrate heater was employed in the set-up using the excimer laser.

5.2 Characterization techniques

5.2.1 X-ray diffraction

The determination of exact inter-atomic distances and bond angles for inorganic solids is carried out mainly by x-ray diffraction [1].

The x-rays are generated by bombarding a metal source, usually Cu, Mo, or Co, with an electron beam emitted from a heated element. This will ionize electrons from the K-shell of the source atoms, and x-rays are emitted as the resultant vacancies are filled by electrons from the L or M shells which in turn gives rise to intense K_α and K_β lines. The wavelength of the characteristic emissions, λ, decreases with the increasing atomic number of the source element.

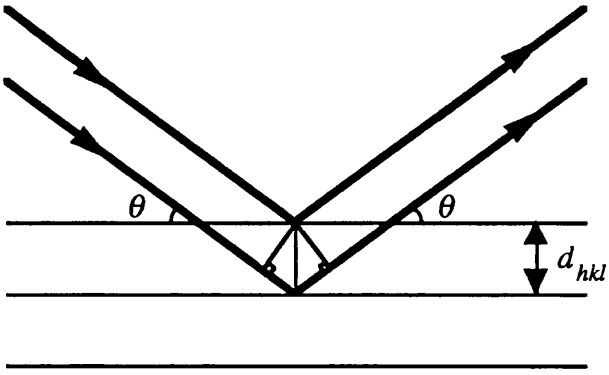

Figure 5.2 Bragg reflection from crystal planes with spacing d_{hkl}.

X-rays are scattered by their interaction with atomic electrons, and interference takes place between x-rays scattered from different parts of an atom. As a result the scattering power (also known as scattering factor) decreases with increasing scattering angle, 2θ. Scattering form a crystal can be described in terms of reflection from a set of lattice planes as shown in figure 5.2. For constructive interference,

$$n\lambda=2d_{hkl}\sin\theta \qquad (5.1)$$

where n is the scattering order number associated with respective planes, d_{hkl} is the distance between planes and θ is the angle of incidence. This is known as the *Bragg* equation, and it represents the condition for diffraction to take place. The relationship between d_{hkl}, lattice constants (a,b,c) and Miller indecies (h,k,l) for an orthorhombic crystal structure is given by,

$$\frac{h^2}{a^2}+\frac{k^2}{b^2}+\frac{l^2}{c^2}=\frac{1}{d_{hkl}^2} \qquad (5.2)$$

Exact values of d-spacing obtained from an x-ray powder pattern of a compound, and the estimated line intensities can be compared with those listed in the Powder Diffraction File, to provide a typical fingerprint which can be used in qualitative analysis. Quantitative analysis of mixtures can also be made by comparing the intensities of characteristic lines from each phase; standards are usually required. The powder data obtained from the diffraction pattern however does not yield enough information to give a complete structure determination. For example although lattice parameters can be calculated, bond lengths cannot be determined.

In a centred cell, reflections from certain planes will be absent because atoms in one motif will scatter exactly out of phase with atoms in another. The intensity, I_{hkl} of reflection from a plane *hkl* may be greater than the intensity from another plane since,

$$I_{hkl} \propto F^2_{hkl} \qquad (5.3)$$

where F_{hkl} is the structure factor, which represents the amplitude (and phase) of scattering by the several atoms in the unit cell.

5.2.2 Rietveld Refinement

This method initiated by Rietveld [2] is used to determine the detailed structural information from powders from the XRD pattern by using a least-squares refinement process which minimizes the difference between the observed and the calculated profiles, rather than the individual reflections. This is discussed in detail in section 7.2.3.

5.2.3 Microscopy

In this section the various microscopy techniques used during the course of this project are briefly described. This includes scanning electron microscopy, SEM, used to study the surface morphology of the samples, transmission electron microscopy, TEM, used to examine the interface between the CeO_2 thin film and Si substrate in fine details and also to study the crystal orientation of a particulate and/or a smooth surface by selective area diffraction, and electron-probe micro-analysis, EPMA, used to identify the various constituents of the sample and to measure their relative composition.

5.2.3.a Electron - sample interactions

In all the techniques mentioned below, the sample is bombarded with electrons which are generated by thermionic emission from a cathode filament (often tungsten) and 'monochromated' by an accelerating voltage of 10-100 keV (depending on which technique is used). The condenser lenses produce a fine, parallel beam of electrons that when incident on the sample results in a range of interactions, some of which are summarized in figure 5.3. The electrons are scattered by the atoms in the sample and as with x-rays there is sharp fall-off of scattering power with $\sin\theta/\lambda$. Also the scattering factor increases with atomic number. The various forms of emissions shown in figure 5.3 provide the basis for different microscopy techniques [3] or analysis methods, some of which are briefly described below.

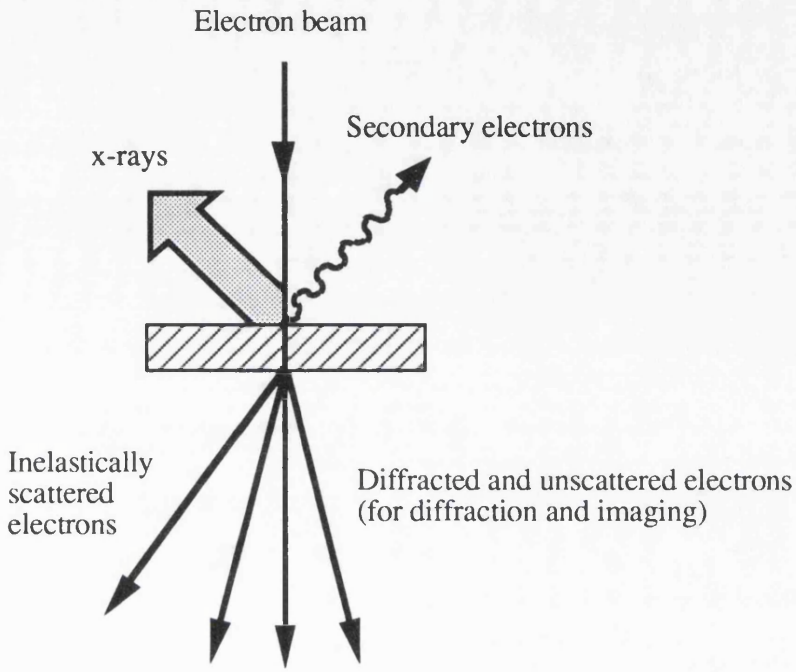

Figure 5.3 *The interaction of an electron beam with a sample.*

5.2.3.b Scanning electron microscopy, SEM

The low-energy (< 50 eV) secondary electrons from the surface of the sample forms the basis for this type of microscopy. The electron beam is focused to a small probe, ≈20 Å in diameter, and may be rastered across the sample using scanning coils. An image is displayed on a cathode ray tube, CRT, which is collected from the secondary electrons detected above the sample. Various parts of the sample result in secondary electrons of different intensity which in turn form the brighter or darker images on the CRT with a resolution of better than 5 nm. This scanning image is particularly useful for examining the morphology of the sample surface.

5.2.3.c Transmission electron microscopy, TEM

The diffracted and unscattered electrons that are transmitted through the sample shown in figure 5.3, form a diffraction pattern which can be transformed directly into an image using magnetic lenses. Either the diffraction pattern or the image can be projected on to a viewing screen as shown in figure 5.4. By appropriately orienting the sample, crystal

diffraction patterns, similar in appearance to zero-level x-ray precession photographs [4] can be obtained.

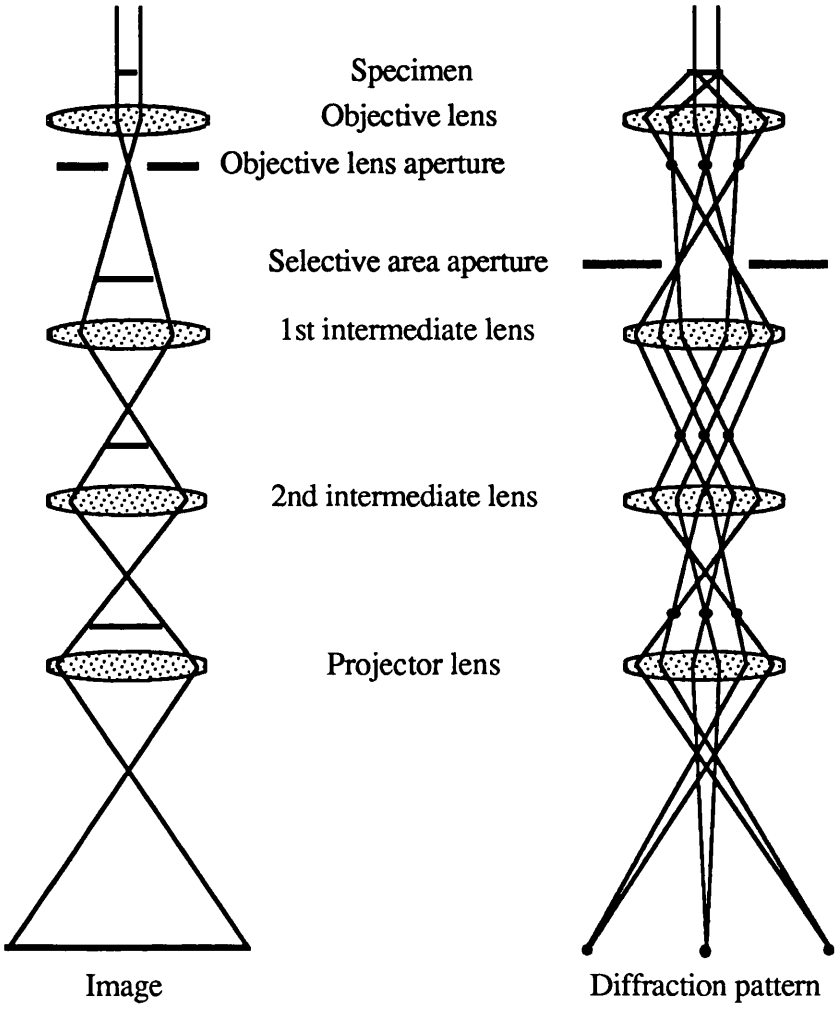

Figure 5.4 *Generation of image and diffraction pattern in a transmission electron microscope.*

Images with atomic resolution are possible with a powerful microscope. The resolving power is dependent upon the wavelength and the quality of the objective lens and the image is sensitive to sample thickness and the focusing conditions. A great deal of care is thus required in preparing the samples, since they need to be thinned down to ≈ 1 μm thickness or less. TEM is ideal for studying defects at interfaces, and in the selective area diffraction patterning mode the crystal structure of a small area with sub-micron dimensions can be examined.

5.2.3.d Electron-probe micro-analysis (EPMA)

In this technique [5] an electron beam is finely focused on to the sample to generate an x-ray spectrum with lines of different intensities at different wavelengths or photon energies. The presence of individual elements in a sample can be identified from the corresponding wavelength (or photon energy) and their concentration can be estimated from the intensity of the line at that wavelength (or photon energy).

In *qualitative* analysis the x-ray spectrum is recorded with either a "wavelength-dispersive" (w.d.) or an "energy-dispersive" (e.d.) spectrometer. In a w.d. spectrometer a diffracting crystal is used which acts as a monochromator, selecting one wavelength at a time, depending on the angle of incidence of the x-rays. The pulses from the detector are counted and amplified using electronic circuitry within the spectrometer. In an e.d. spectrometer solid-state x-ray detectors are employed which record the whole spectrum simultaneously. The pulse heights produced in the detector are sorted according to x-ray energy. Although the e.d. technique has the advantage that it is a much quicker compared to the w.d. method, the resolving power obtainable is substantially inferior. In both techniques certain instrumental corrections such as the continuous background x-ray spectrum are subtracted from the measured line intensity to provide a more accurate value.

In *quantitative* analysis the intensities of the x-ray lines are compared with those from standards with known composition. To take account of the various factors concerning the relationship between intensity and composition 'ZAF corrections' are applied which comprise the correction factors due to absorption of x-rays, fluorescence by other x-ray lines and background, and electron backscattering and 'stopping power' of the sample (both functions of atomic number).

In EMPA the generation of high resolution electron images are not as important as they are in SEM or TEM, however in recent years e.d. spectrometers have been introduced in scanning and transmission electron microscopes turning them into analytical instruments.

5.2.4 Resistance - temperature measurements

These measurements were carried out at GEC Hirst Research Laboratories, London. This involved cooling the sample in a cryostat at a preset rate and measuring its resistance each time using the linear four point probe method. The value of the applied current was adjusted according to the surface resistance of the sample and whether a positive or negative change in resistance with temperature was expected. Gold tipped probes were employed which gently pressed the sample in position, and conductive paint was applied at their point of contact. The cooling rate was set by adjusting the rate at which the sample probe was inserted into a liquid helium dewar.

References

[1] C.Giacovazzo, in *"Fundamentals of Crystallography"*, edited by C.Giacovazzo, Oxford University Press, (1992).

[2] H.M.Rietveld, *J. Appl. Cryst.*, **2**, p65, (1969).

[3] P.J.Goodhugh and F.J.Humphreys, *"Electron Microscopy and Analysis"*, second edition, Taylor & Francis, London, (1975).

[4] A.R.West, *"Solid State Chemistry and its applications"*, fourth edition, Wiley, UK, (1990).

[5] S.J.B.Reed, *"Electron Microprobe Analysis"*, second edition, Cambridge University Press, (1993).

Chapter 6

Growth of Cerium Oxide Thin Films by Pulsed Laser Deposition

In this chapter a systematic optimisation of the parameters governing the growth of CeO_2 by PLD is undertaken and deposition using a frequency doubled Nd:YAG operating at 532 nm, and a KrF excimer laser operating at 248 nm are compared. It is important from a technological view point that a buffer layer is flat and of high crystalline perfection. This is the prime objective for the variations of the parameters investigated in this project. In addition the feasibility of changing the lattice constant via doping and the use of CeO_2 in multilayer structures is demonstrated.

6.1 Introduction

The use of buffer layers between a deposited HTSC thin film and the silicon substrate has recently become a subject of intensive research. The high processing temperatures often result in interdiffusion between the HTSC film and Si producing a non-sharp intermixed interface and leading to the degradation of material properties.

Cerium oxide, CeO_2, is an electrical insulator with the fluorite (CaF_2) crystal structure, as shown in figure 6.1. The unit cell depicted shows eightfold (cubic) coordination of Ce atoms by eight oxygen atoms and fourfold coordination of O atoms by four Ce atoms. The structure can be viewed as a cube which can be divided into eight smaller cubes. There is a Ce atom at centre of each alternate cube and oxygen atoms in every corner. It can also be viewed as an fcc lattice of Ce where all the tetrahedral interstice are occupied by oxygen atoms.

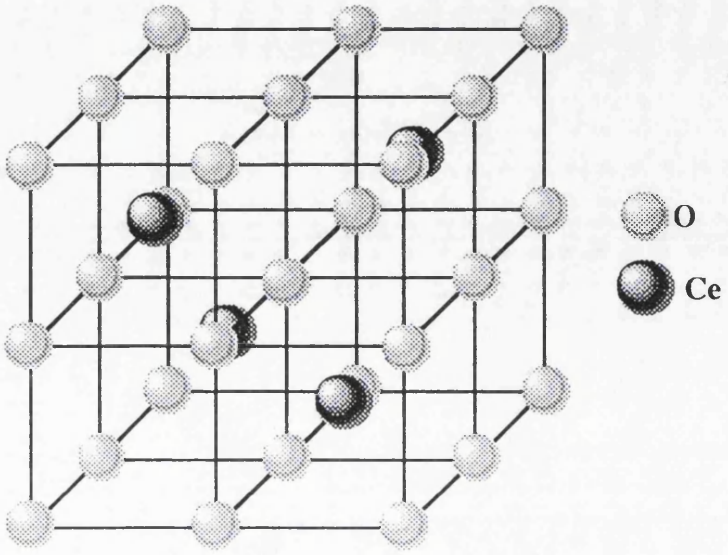

Figure 6.1 The CaF_2 structure of CeO_2.

The material is stable even at a very high temperature; x in CeO_x is higher than 1.99 at 1000°C under 7.6×10^{-9} Torr of oxygen [1]. Its lattice constant, a, of 5.411 Å [2] which is close to that of silicon (the misfit factor, $\Delta a/a$, being only 0.35%). It also closely lattice matches some HTSCs such as BiSrCaCuO ($a \approx b \approx 5.4$ Å [3]) and PbSrYCaCuO ($a \approx b \approx 5.4$ Å [4]) in their a-b planes. Furthermore there are no inter-mixing problems which makes it a suitable candidate for use as a buffer layer between the HTSC thin films and the silicon substrate. At first sight in certain HTSCs such as $YBa_2Cu_3O_{7-\delta}$ it appears that there is a large lattice mismatch ($a \approx 3.8$ Å, $b \approx 3.9$ Å for YBaCuO resulting in mismatches of ≈30% and ≈28% respectively). However, by simply rotating the unit cell 45° in the basal plane, the mismatch will only be 0.16% along the a-axis and 1.7% along the b-axis.

6.2 Thin film growth of CeO_2 (by other groups)

CeO_2 thin films have been grown using a variety of deposition techniques. Pulsed laser deposition (PLD) of CeO_2 has been performed using excimer lasers operating at 193 nm [1,16-18], 248 nm [6], 308 nm [7] as well as the frequency doubled Nd:YAG laser at 532 nm [8]. Other competitive techniques include sputtering [10-12], thermal evaporation [14], MOCVD [15], e-beam evaporation [19-24] and ion assisted e-beam evaporation [25,26].

6.2.1 Growth by PLD

Koinuma et al. [16] were the first group to grow CeO_2 thin films by PLD. An ArF excimer laser (193 nm, 2 Hz, energy density of 1 J/cm^2) was used to deposit the films on single crystals of Si(111) at a substrate temperature of 650°C and an oxygen partial pressure of < $1x10^{-7}$ Torr. Partial reduction of Ce^{4+} to Ce^{3+} by silicon within the initial two to three CeO_x ($1.5 < x < 2.0$) layers was detected by using x-ray photoelectron spectroscopy, XPS, however beyond these layers film growth was stoichiometric. This group also studied the growth of CeO_2 on Si with and without the removal of the native oxide [1]. Growth in the [110] or [111] direction resulted when Si(100) or Si(111) respectively was used with the native oxide removed before deposition. By using reflection high energy electron diffraction, RHEED, it was found that only the growth on Si(111) was epitaxial. When the native oxide was not removed, growth in the [111] direction resulted. Further work by the same group [17] demonstrated the epitaxial growth of CeO_2(100) on Si(100) using an intermediate layer of $SrTiO_3$(100).

Wu et al. [2] using a XeCl excimer laser (308 nm, 20 Hz, energy density of 2 J/cm^2) deposited epitaxial films of CeO_2 on $LaAlO_3$(100) single crystal substrates at an oxygen partial pressure, P_{O_2}, of 150 mTorr and a substrate temperature, T_s, of 750°C resulting in films oriented in the [100] direction. At low P_{O_2}, mixed (111) and (100) orientations were obtained. Using the same P_{O_2} and T_s, CeO_2 thin films were also prepared on (1$\underline{1}$02) sapphire growing in a preferred [100] orientation [6]. By employing a KrF excimer laser (248 nm, 10 Hz, energy density of 3 J/cm^2), Denhoff and McCaffrey [6] also deposited CeO_2 thin films on (1$\underline{1}$02) sapphire at a P_{O_2} of 200 mTorr and a T_s of >720°C resulting in (100) oriented films.

Sánchez et al. [18] also used an ArF excimer laser (193 nm, 10 Hz, energy density of 2 J/cm^2) to grow CeO_2 thin films on Si(100), however, although they followed the normal procedure of chemically cleaning and heating up the substrate to remove the native oxide before deposition, their films were (111) oriented. It should be noted that despite using an oxide removal process when preparing their substrates, they do not actually claim to have removed the native oxide.

6.2.2 Growth by other techniques

The epitaxial layer growth of CeO_2 on Si was first reported by Inoue et al. [19]. They used e-beam evaporation of hot pressed CeO_2 tablets to grow films on Si(100) and Si(111) substrates (native oxide removed) held at 800°C at a P_{O_2} of $8x10^{-6}$ Torr. Characterization of the films using RHEED and Rutherford backscattering, RBS, showed the CeO_2 layers on Si(111) to be highly crystalline , whereas films grown on Si(100) displayed a large amount of defects, especially at the interface. They also found that the minimum temperature for epitaxial growth on Si(111) could be as low as 200°C [20]. The growth orientation was found to be similar to the films grown using PLD i.e. CeO_2(111) on Si(111) and CeO_2(110) on Si(100) [21]. Observations from cross-sectional high resolution transmission electron microscopy, X-HRTEM, also revealed the existence of an amorphous layer of ≈60Å thickness between the CeO_2 film and Si(100). Furthermore a high density of defects were observed in the CeO_2 layer near the interface. The crystal quality of CeO_2(110) layers grown on Si(100) was found to improve significantly when the substrates used were cut with an off-axis of 0.17° [22].

Sputtering was also used to grow CeO_2 thin films [10-12]. Wang et al. [11] used on-axis dc magnetron sputtering to grow (100) oriented CeO_2 buffer layers between $YBa_2Cu_3O_{7-\delta}$ and sapphire. The best films were deposited at a T_s of 850°C and a pressure of 10^{-1} Torr consisting of Ar and O_2 at a ratio of 4:1. A post-deposition heat treatment (30 min at 900°C in 1 atm of O_2) improved the surface morphology (surface roughness of < 3Å) and crystallinity, especially for films grown under non-optimal conditions.

Chemical techniques have also been used to deposit CeO_2 thin films. Dahmen et al. [15] grew CeO_2 thin films on quartz, sapphire , MgO(100) and Si(100) by MOCVD. The films were oriented preferentially in the [100] direction (regardless of which substrate was used) when no oxygen was introduced into the chamber, and polycrystalline in the presence of oxygen. The (100) film orientation on Si(100) was in contrast to the (110) orientation obtained using physical deposition techniques.

6.3 Thin film growth Of CeO_2 (at UCL)

The vacuum deposition system described in section 5.1 was used to deposit the films. The substrates used in this study were single crystal wafers of Si(100) and Si(111), Corning glass 7059, and sapphire (1$\underline{1}$02). Prior to deposition the substrates were degreased using successive acetone and methanol rinses, and dried with nitrogen gas. The native oxide was not removed from the silicon substrates and thus a clean oxide-free surface was not presented to the ablation plume. The target to substrate distance was fixed at ≈4 cm. Depositions using a frequency doubled Nd:YAG laser (532 nm) with a pulse duration of 4 ns at 5 Hz, and a KrF excimer laser (248 nm) with a pulse duration of 20 ns at 5 Hz were investigated. Unless mentioned otherwise the lasers were focused onto the rotating target (5 rpm) producing an energy density of ≈3.5 J/cm^2. The angle between the incident laser beam and normal to the target was ≈25°. The target surface was smoothened prior to deposition using an emery paper, followed by blowing the surface with nitrogen to remove residual particles.

Targets were made in the form of pellets, 13 mm in diameter, by cold pressing fine CeO_2 (99.99%) powder under a pressure of 4 tons. The pellets were then placed in a furnace at room temperature and heated up at a rate of 3°C/min to 1100°C. They were left at that temperature for ≈6 hrs and cooled down to room temperature at a rate of 3°C/min resulting in a hard but slightly brittle pellet which was off-white in colour.

Films were characterized using x-ray diffraction, XRD, scanning electron microscopy, SEM, and transmission electron microscopy, TEM. XRD measurements were carried out at the Department of Crystallography, Birkbeck College, and a Cu K_α source ($K_{\alpha 1}$: λ =1.5406 Å, $K_{\alpha 2}$: λ =1.5444 Å, K_β: λ =1.3922 Å) was used during the measurements.

6.3.1 Effect of oxygen partial pressure, P_{O_2}

Thin films of CeO_2 were grown on both Si(100) and Si(111) single crystal wafers at a constant T_s of 500°C but with the P_{O_2} as a variable. The film thickness was maintained at ≈2000 Å. The results obtained for films deposited using either a frequency doubled Nd:YAG laser (532 nm) or a KrF excimer laser (248 nm) are presented and compared below.

(a) Thin film deposition at 532 nm:

The x-ray diffraction (XRD) patterns of films grown on Si (100) at different oxygen pressures are shown in figure 6.2.

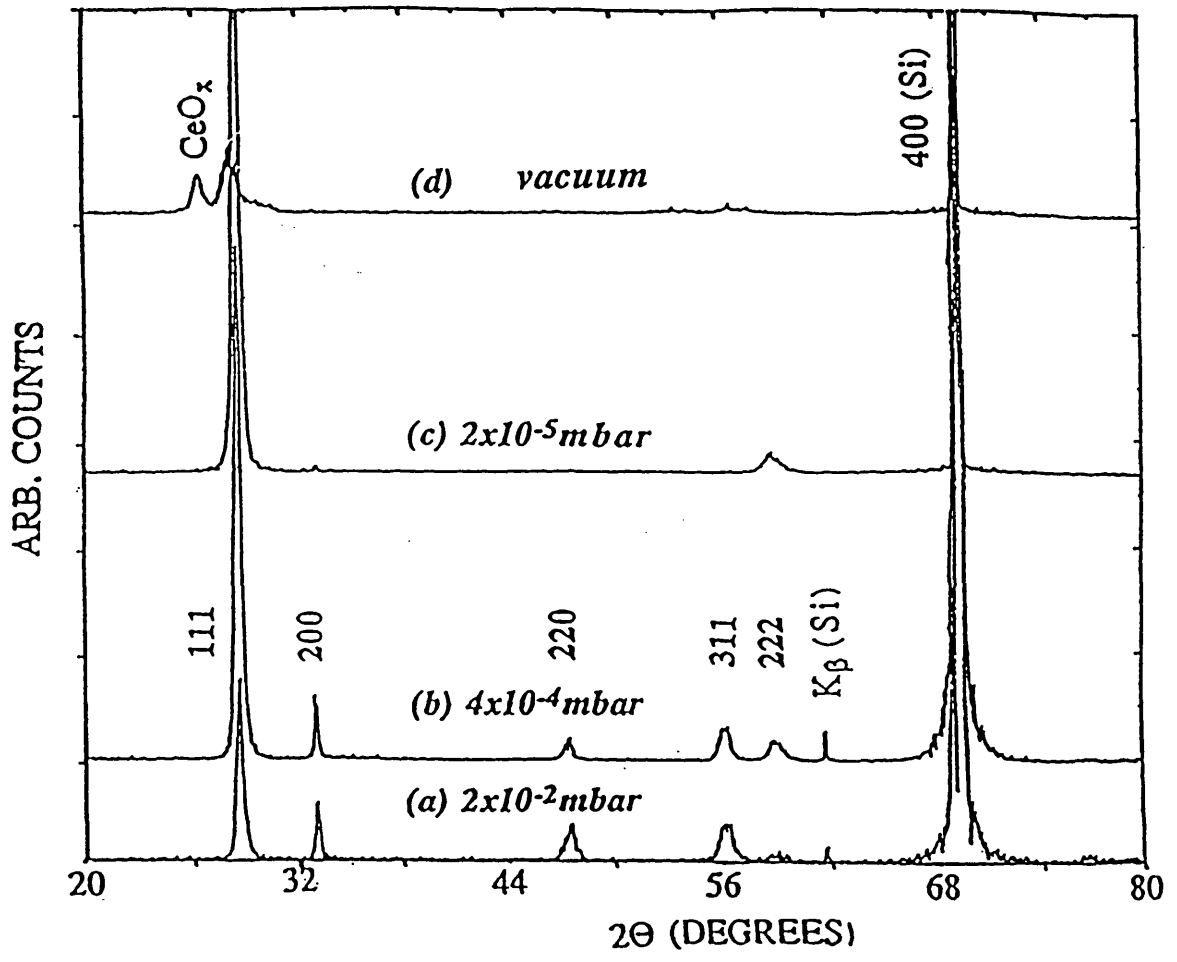

Figure 6.2 *XRD patterns of CeO_2 films grown on Si(100) using the Nd:YAG laser (532 nm), at a fixed T_s of 500°C under different P_{O_2}.*

As can be seen for a high P_{O_2} ($\approx 10^{-4}$ mbar) all the diffraction peaks corresponding to polycrystalline CeO_2 are present (JCPDS No. 34-394). As P_{O_2} is reduced, the ratio of the [111] peak counts to the other peaks rises until at $\approx 2 \times 10^{-5}$ mbar only the [111] and [222] peaks remain. At a P_{O_2} of $\approx 10^{-1}$ mbar no peaks apart from the Si peak were observed in the diffraction pattern indicating deposition of an amorphous film. Similar results were obtained for films grown on Si (111) as shown in fig 6.3.

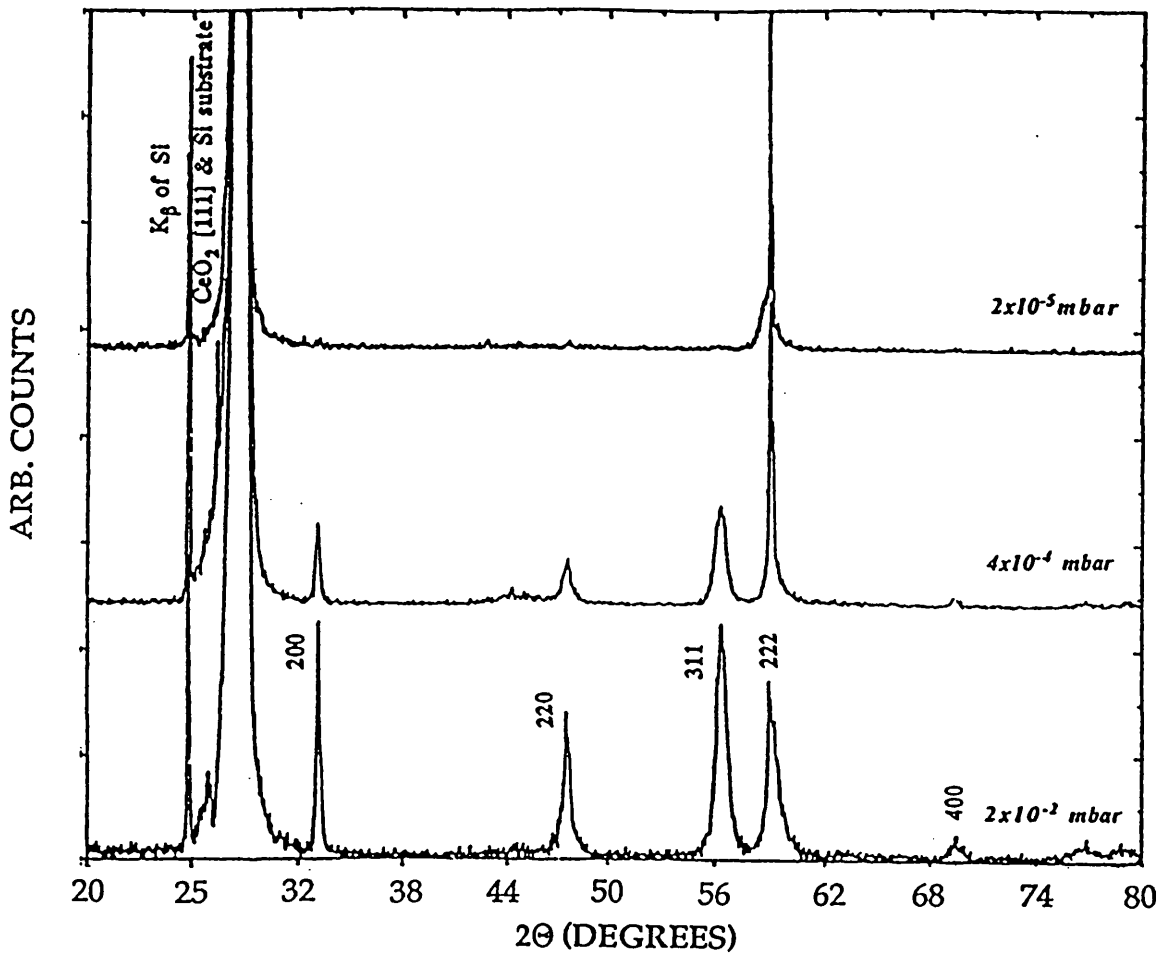

Figure 6.3 XRD patterns of CeO_2 films grown on Si(111) using the Nd:YAG laser (532 nm), at a fixed T_s of 500°C under different P_{O_2}.

Deposition at a vacuum pressure of $4x10^{-6}$ mbar and without the introduction of oxygen resulted in other XRD peaks which were more likely to be suboxides of CeO_x ($1.5 \leq x < 2$), such as Ce_2O_3, Ce_6O_{11}, etc., as shown in figure 6.2. At this pressure the amount of oxygen is negligible and the main sources of residual gas are water vapour and ammonia [28]. The ablated region on the target surface developed a metallic grey colour which indicated a loss of oxygen. This was confirmed by the fact that at a higher P_{O_2} the colour was lighter - at a P_{O_2} of $\approx 10^{-1}$ mbar the ring hardly changed in colour. The evaporated material therefore appears to be initially short of oxygen and it is only after reacting with oxygen 'en-route' to the substrate that it transforms into its original stoichiometric form. Thus a partial pressure of oxygen appears to be necessary, although it should be low enough to promote growth in the [111] direction.

The scanning electron micrographs of the surface of the films deposited on Si(100) at $4x10^{-4}$ mbar and $2x10^{-5}$ mbar are shown in fig 6.4. As can be seen the density of particulates decreases significantly at lower pressures which when comparing to the XRD patterns shown previously suggests a polycrystalline nature for the particulates and a preferred (111) orientation for the flat region (this was further confirmed using selective area diffraction during TEM studies, described in section 6.3.8).

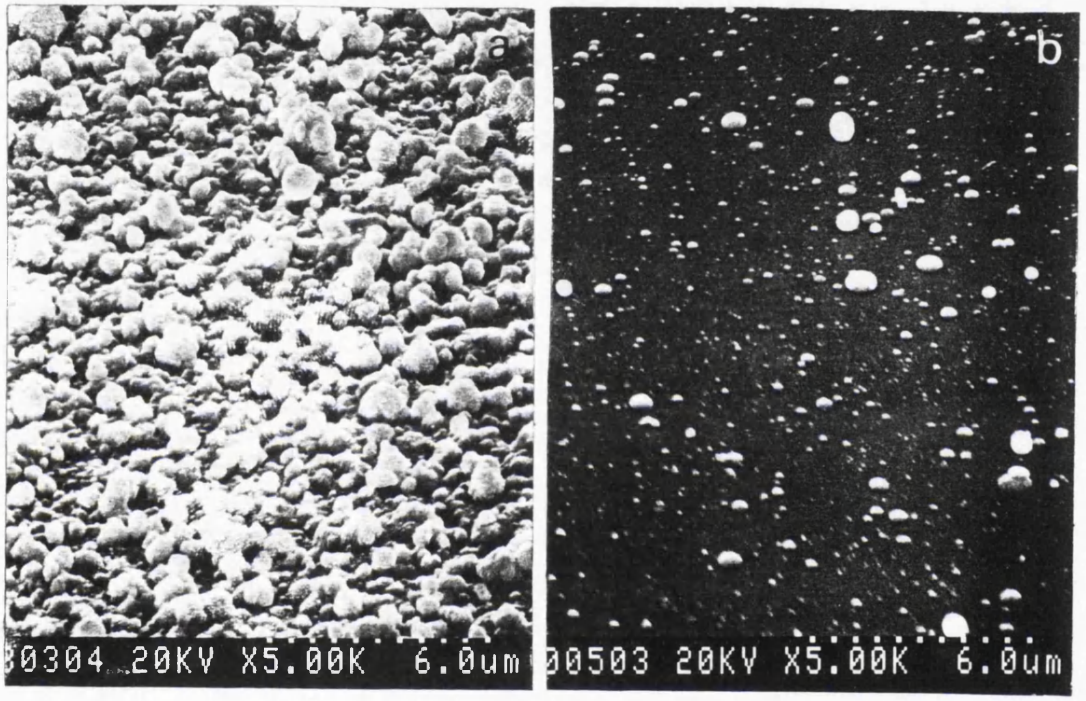

Figure 6.4 *SEM micrographs of CeO_2 films grown on Si(100) using the Nd:YAG laser (532 nm), at a T_s of 500°C and a P_{O_2} of: a) $4x10^{-4}$ mbar, and b) $2x10^{-5}$ mbar.*

The ablated ejecta contain 'round chunks' of material, 1-2 μm in diameter, knocked off the target which when deposited on the substrate deteriorate the surface morphology. Due to their large sizes the reason for the production of these particles is likely to be laser-target interaction (see section 3.4). At a P_{O_2} $>10^{-4}$ mbar, a local build-up of pressure is developed in the plasma which seems to increase the flux of these chunks, resulting in a film covered with particulates, and displaying a polycrystalline, powder like, XRD pattern. At lower pressures the reduced number of particulates results in an increase in the ratio of the [111] peak compared to the other peaks.

(b) Thin film deposition at 248 nm:

The XRD patterns of all the films displayed preferential growth in the [111] direction which is in contrast to the films produced using the Nd:YAG laser, and interestingly deposition under a vacuum pressure of $\approx 6 \times 10^{-6}$ mbar resulted in a [111] oriented film with no traces of suboxides. However, as can be seen in figure 6.5, the crystallinity of the films was enhanced with decreasing P_{O_2}. This is shown in terms of the average full width at half maximum (FWHM) of the [111] peak from the XRD θ–2θ pattern which was determined using the Split-Pearson $\underline{V}$ curve-fitting technique. In this method the peak is fitted into a shape which is *split* into left and right halves that can be adjusted separately to be partly Gaussian and partly Lorentzian. The value for FWHM is obtained for a peak by assuming one half of the complete peak shape to be either the left half or the right half of the measured peak and thus two values are obtained. Throughout this thesis the average of these two values are quoted to provide an indication of film crystallinity. A narrow peak is an indication of high film texturing with large area grains in the case of a polycrystalline (a columnar growth is assumed).

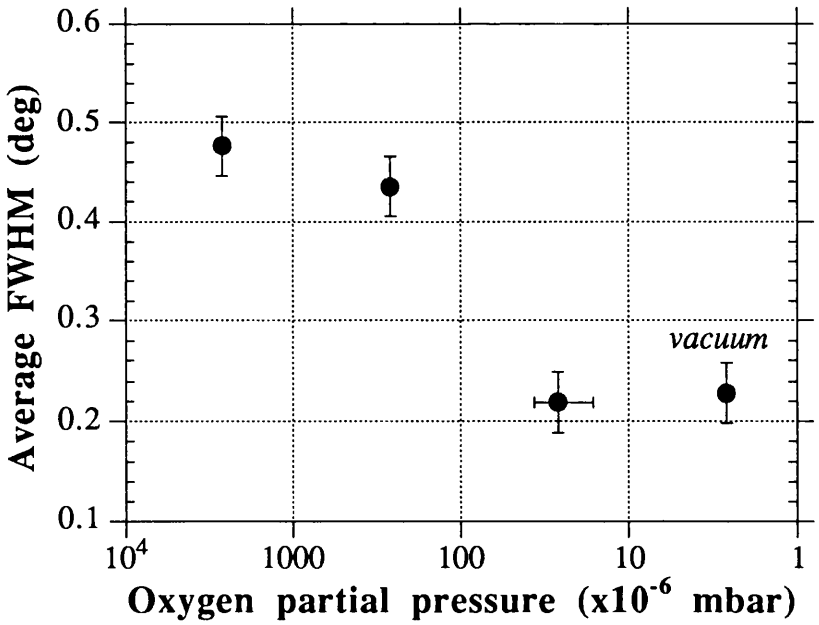

Figure 6.5 *Average FWHM (111-peak) vs P_{O_2} for CeO_2 films deposited at a constant T_s of 500°C using a KrF excimer laser (248 nm).*

The ablated region of the target again attained a metallic grey colour following deposition in vacuum or low P_{O_2}, and became lighter in colour at higher oxygen pressures. However, after a few days exposure to air it developed a much fainter colour which indicated regain of some of the lost oxygen. This is in contrary to ablation with the Nd:YAG laser whereby the dark metallic region remains intact after a few days exposure to air, indicating a higher oxygen loss.

The SEM micrograph of a film deposited at a T_s of 500°C and a P_{O_2} of $2x10^{-5}$ mbar using the excimer laser (248 nm), is shown in figure 6.6b and is compared with a film deposited under the same conditions but using the Nd:YAG laser (532 nm) shown in figure 6.6a. As can be seen the density of particulates on the film surface is decreased significantly in the case of 248 nm radiation.

(a) *(b)*

Figure 6.6 *SEM micrographs of CeO_2 films deposited on Si(100) using: (a) a frequency doubled Nd:YAG laser (532 nm), and (b) a KrF excimer laser (248 nm).*

As briefly discussed in section 3.4 the laser absorption depth is higher and thus the peak temperature reached is deeper into the target when the Nd:YAG laser (532 nm) is used compared to the case in which an excimer laser (248 nm) is employed. The higher absorption depth can lead to sub-surface boiling with a recoil pressure which can eject 'chunks' of material from the target and deposit them on to the substrate and therefore deteriorate the film surface morphology. Under irradiation at 248 nm the laser absorption depth is much lower and the ablation process takes place close to the surface of the target resulting in a much smaller number of particulates being ejected. The density of these particulates are still low enough that even at high oxygen pressures the XRD pattern displays (111) orientation. However, the presence of a few particulates strongly suggests the existence of a minute quantity of polycrystalline material.

The ablated region on the target suggested a lower oxygen loss in the case of excimer laser radiation which is again believed to be due to the ablation process taking place close to the target surface. Under a vacuum pressure of $\approx 6 \times 10^{-6}$ mbar, the amount of oxygen present (water vapour could also act as an oxidizing agent) seems to be sufficient for the oxygen-deficient CeO_x species ejected from the target to regain their stoichiometry and result in (111) oriented films with no suboxides. Koinuma et al. employed a P_{O_2} of $\approx 1 \times 10^{-8}$ mbar over a base pressure of $\approx 1 \times 10^{-10}$ mbar to deposit thin films of CeO_2 [16].

6.3.2 Effect of substrate temperature, T_s

Thin films of CeO_2 were deposited on Si(100) at a fixed P_{O_2} of 2×10^{-5} mbar and at T_ss in the range 250 to 650°C using either the Nd:YAG (532 nm) or the excimer (248 nm) laser. The thickness of these films were between 2000 and 2500 Å. The XRD patterns of all the films revealed preferential growth in the [111] direction, however as shown in figure 6.7 the average XRD-FWHM decreased with increasing T_s indicating improved crystallinity at higher temperatures. As can be seen apart from a slightly sharper peaks at higher temperatures (>500°C) there appears to be no major difference whether 532 nm or 248 nm radiation is used. Depositions at room temperature resulted in amorphous films.

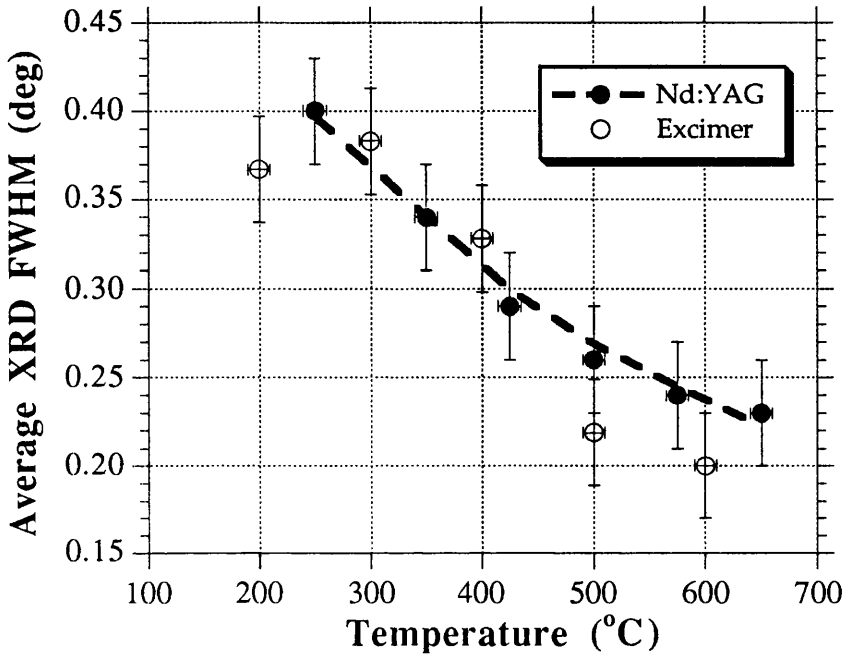

Figure 6.7 *Average XRD-FWHM (111-peak) vs. substrate temperature for CeO_2 films grown on Si(100) at a P_{O_2} of $2x10^{-5}$ mbar using the frequency doubled Nd:YAG laser (532 nm) or the KrF excimer laser (248 nm).*

An increase in T_s leads to a rise in adatom mobility which in turn causes an increase in grain size. This effect manifests itself as a reduction in FWHM of the XRD peak(s).

6.3.3 Variation of crystallinity with film thickness

CeO_2 films with various thickness were grown on Si(100) at a P_{O_2} of $2x10^{-5}$ mbar and a T_s of 500°C using the Nd:YAG laser (532 nm). Film thickness was measured using the talystep - a fine mechanical stylus that was moved across a sharp step created between the deposited and the non-deposited regions. As can be seen in figure 6.8 the [111] peak count becomes more intense and the average XRD-FWHM (111-peak) decreases with increasing film thickness. For a polycrystalline specimen the FWHM is dependent upon the mean crystallite size as well as the imperfections prevailing in the lattice. Also the combined effects of a number of instrumental and physical factors broaden the "pure" diffraction line profile.

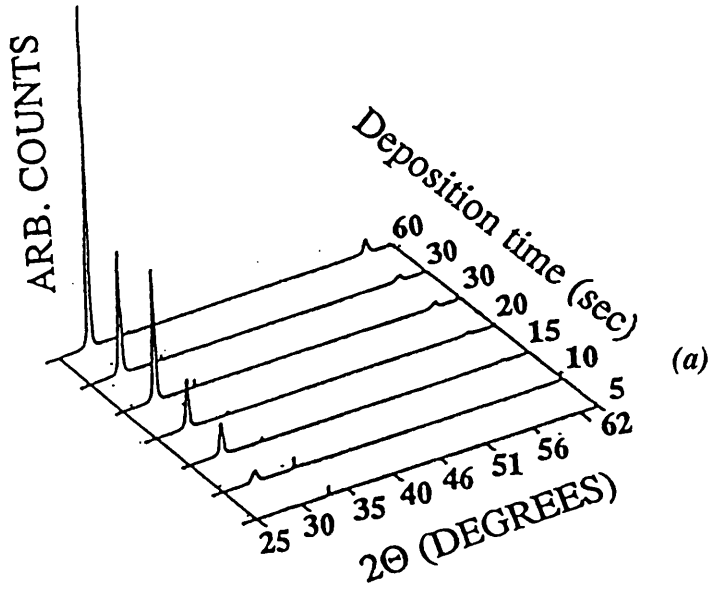

(a)

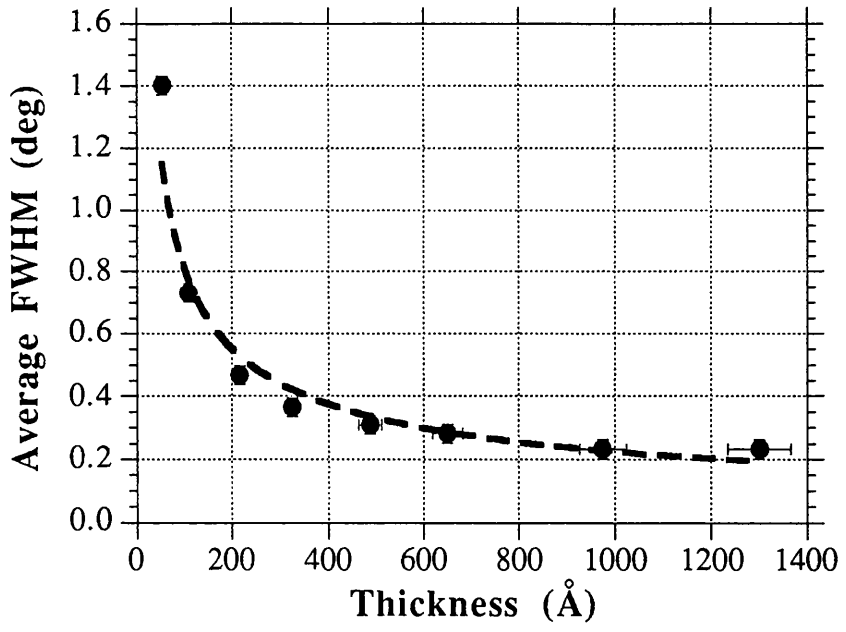

(b)

Figure 6.8 *(a) XRD patterns of CeO_2 films grown on Si(100) for different deposition time (film thicknesses) using the Nd:YAG laser and (b) variation of average XRD FWHM (111-peak) for the films in (a) vs film thickness.*

The classical Scherrer's equation relates the size of a crystallite with no lattice imperfection to the FWHM in the form:

$$L = K\lambda / \beta\cos\theta \qquad (6.1)$$

where L is the mean dimension of the crystallite, β the FWHM, λ the wavelength of the radiation source (for CuKα it is ≈1.54 Å),θ the peak position, and K a constant usually equal to 0.89. For 200Å and a 100Å size crystals, the corresponding valuesof FWHM are ≈0.4° and ≈0.8° repectively which are close to the data shown in figure 6.7. Thus it seems that the reduction in FWHM with increasing film thickness is mainly due to an increase in crystallite size.

The results were the same whether Si(100) or Si(111) substrates were used. However, it should be noted that since the native oxide was not removed in either case the effective growth surfaces were similar. To confirm this, CeO_2 films with different

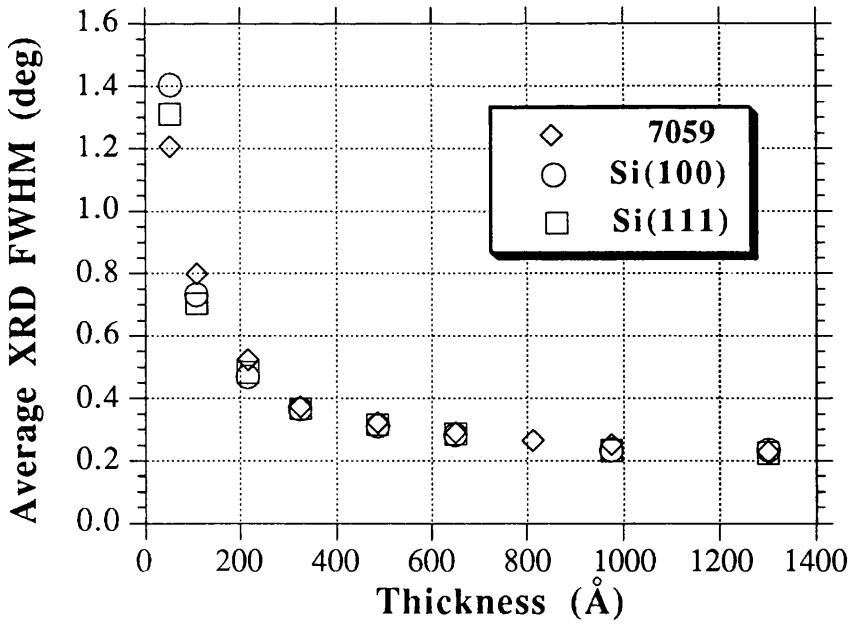

Figure 6.9 *Average XRD FWHM (111-peak) for CeO_2 films grown on Corning 7059 glass substrate at a P_{O_2} of $2x10^{-5}$ mbar and a T_s of 500°C. These are compared with the data for growth on Si(100) and Si(111).*

thickness were grown on Corning 7059 glass substrates to remove any possible crystalline substrate effect, and again growth in the preferential [111] direction was obtained. The effect of reduced average FWHM with increasing thickness is shown in figure 6.9 for films deposited on Corning 7059 glass, and compared to that of Si(100) and Si(111). The values of thickness for films deposited on Si(111) and glass were taken by assuming that they would be similar to the values for films deposited on Si(100) for the same deposition time.

6.3.4 Why preferential orientation?

The reason for the preferential (111) film orientation on Si covered with the native oxide as opposed to the (110) orientation observed for films grown on cleaned Si(100) has been argued to be chemical rather than crystallographic in nature [1]. The central concept of this argument is when Ce-O species approach a silicon substrate covered with the oxide layer the Ce as opposed to the oxygen of CeO_2 is preferentially attracted and bonded to surface oxygens. The 2-dimensional Ce atom population is highest in the (111) plane: $2.31/a^2$ for (111), $2.00/a^2$ for (001), and $1.41/a^2$ for (110) where a is the lattice constant of CeO_2. The higher Coulombic interaction between Ce and oxygen should favour the CeO_2 (111) growth on oxidized silicon. Due to the coverage with oxide layer, the silicon lattice has little effect on the arrangement of CeO_2.

6.3.5 Effect of laser fluence

The effect of laser fluence on deposition rate and surface morphology was investigated by depositing CeO_2 films on Si(100) at a P_{O_2} of $2\text{x}10^{-5}$ mbar and a T_S of 500°C using both the Nd:YAG laser (532 nm) and the excimer laser (248 nm). Laser energy was attenuated by selecting the desired energy on the control menu when using the excimer laser, and neutral density filters were used when the Nd:YAG laser was employed. The deposition time was reduced with increasing laser energy density in order to keep the film thickness approximately constant. The spot size was $\approx$0.05 cm^2 (2.5 mm diameter) in the case of Nd:YAG laser and $\approx$0.03 cm^2 (1 mm x 3 mm) when the excimer laser was used.

(a) Effect on deposition rate:

The effect of laser fluence on deposition rate is shown in figures 6.10a and 6.10b.

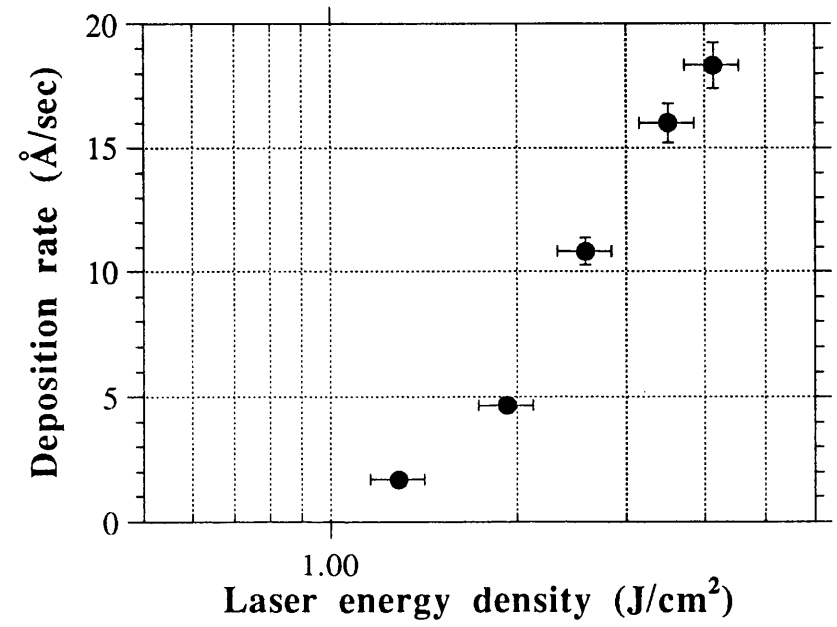

(a)

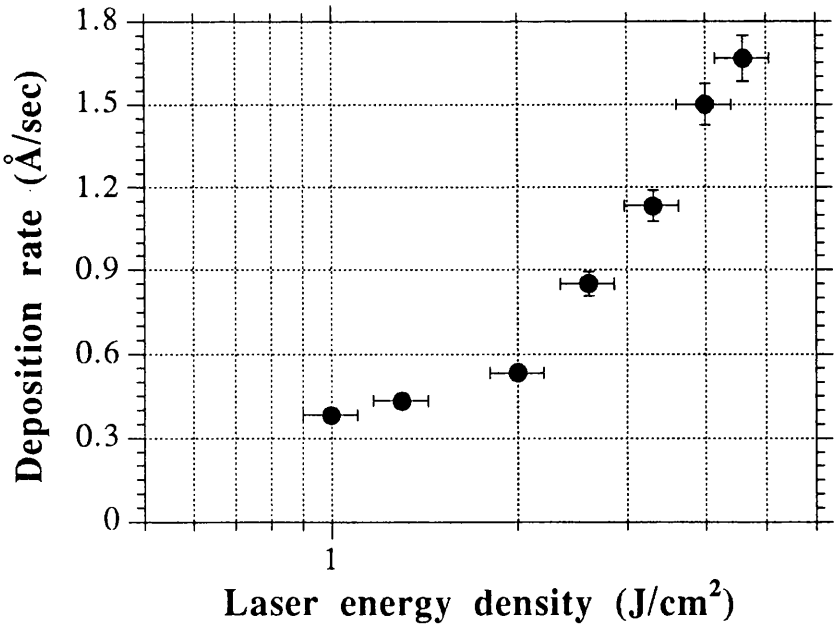

(b)

Figure 6.10 *Effect of variations in laser energy density on deposition rate when (a) a frequency doubled Nd:YAG laser (532 nm), or (b) a KrF excimer laser (248 nm) is used.*

As can be seen the deposition rate varies in proportion to the logarithm of laser energy density, particularly beyond ≈2 J/cm^2. This is in agreement with the discussion in section 3.2b in which at medium laser energy densities material removal is believed to enter a phase whereby a $\cos^n\theta$ profile and a more stoichiometric transfer of material (in the case of multi-component materials) is obtained. Foltyn et al. [29] while measuring the deposition rate from a YBaCuO target irradiated with an excimer laser (308 nm) at different fluences found the rate to decrease to a steady-state value after a certain number of pulses which increased with laser fluence. Interestingly the steady-state deposition rate was found to increase *linearly* with fluence.

The deposition rate in the case of 532 nm radiation is almost an order of magnitude higher than the deposition rate when 248 nm radiation is used. This increase is partly due to the smaller spot size and also due to the process of evaporation/ablation occurring in a much smaller volume on the target when the excimer laser is used.

(b) Effect on surface morphology:

The effect of laser fluence variations on surface morphology was examined for films deposited using the Nd:YAG and excimer lasers. As can be seen in figure 6.11, for radiation at 532 nm an increase in laser energy density had the effect of reducing the density of smaller (< 1 μm diameter) particulates. The density of larger size particles (> 1 μm diameter) is generally believed to increase with increasing laser fluence [30]. In a detailed treatment by Zherikhin et al. [31], the appearance and increase of these particles occurred beyond a threshold fluence which in the case of a YBaCuO target irradiated by an excimer laser at 308 nm was ≈3.5 J/cm^2. The density of smaller type particles was believed to be due to parameters such as T_s or P_{O_2}. A reason for no appreciable difference in the number of larger type particles in the case of CeO_2 could therefore be that even at 4 J/cm^2 the threshold value was not reached.

The appearance of these particles is believed to be due to the laser irradiating a non-polished surface - this is discussed in more detail in section 6.3.6. Since both the substrate temperature and the oxygen pressure were the same throughout the fluence range, the increase in the density of smaller type particles is believed to be due to the increase in deposition time associated with a reduced laser energy density.

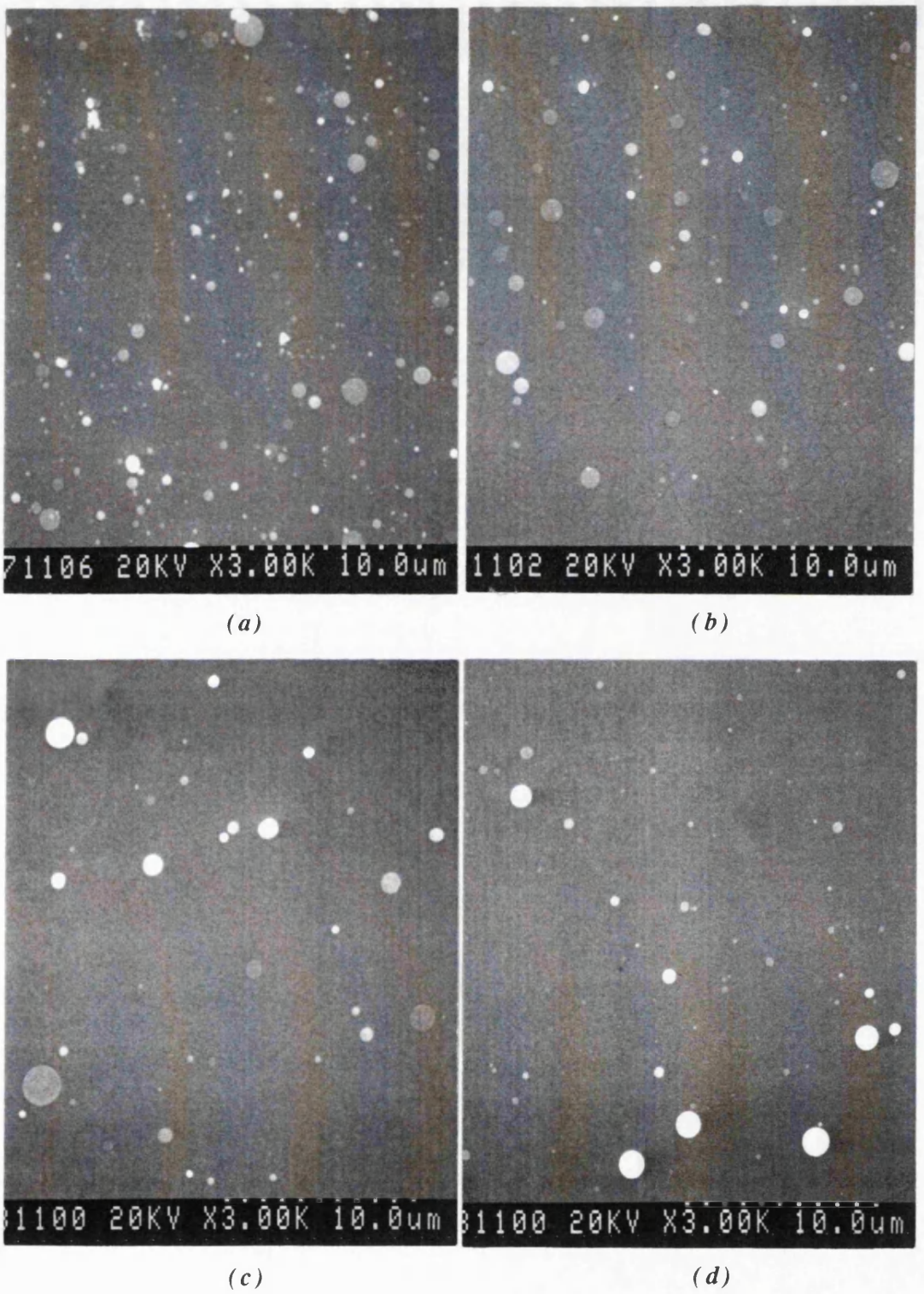

Figure 6.11 *Effect of laser energy density variations on surface morphology for films deposited using the Nd:YAG laser (532 nm). The laser was focused onto the target to generate an energy density of:*
(a) ≈1.6 J/cm², (b) ≈2.5 J/cm², (c) ≈3.2 J/cm², and (d) ≈4.1 J/cm².

The effect of varying the laser energy density using the excimer laser at 248 nm is shown in figure 6.12. As can be seen at ≈1.3 J/cm^2, the film surface contains a number of smaller type particles together with surface defects such as voids. (The square patch in the middle is due to beam focusing). At ≈2 J/cm^2 the density of particles is reduced. Further increase in laser energy density does not seem to make a dramatic change in surface morphology. The absence of larger type particles is more likely to be due to laser - target interaction.

As discussed in section 6.3.1b at a lower wavelength of 248 nm, laser irradiation is absorbed in a region close to the surface of the target, which means that any problems associated with sub-surface boiling can be avoided. Also this would ensure that the laser always encounters a relatively flat surface (c.f. irradiation at 532 nm) - this will also be discussed in a greater length in the next section.

6.3.6 Effect of polishing the target surface

The effect of polishing the target surface prior to deposition was studied by examining the surface morphology of three films deposited for 10 seconds (less than one target rotation) from targets that were polished (not ablated), ablated for 12 seconds (one target rotation), and ablated for 180 seconds (15 target rotations). These were done using the Nd:YAG (532 nm) laser and the excimer (248 nm) laser. It should be noted that polishing the target surface in this case refers to removing the ablated region by rubbing it against an emery paper to produce a smooth surface.

(a) Effect of 532 nm radiation:

The surface morphology of the films is shown in figures 6.13, a, b, and c, and the corresponding density of particulates with different sizes, appearing on their surfaces is summarized in table 6.1.

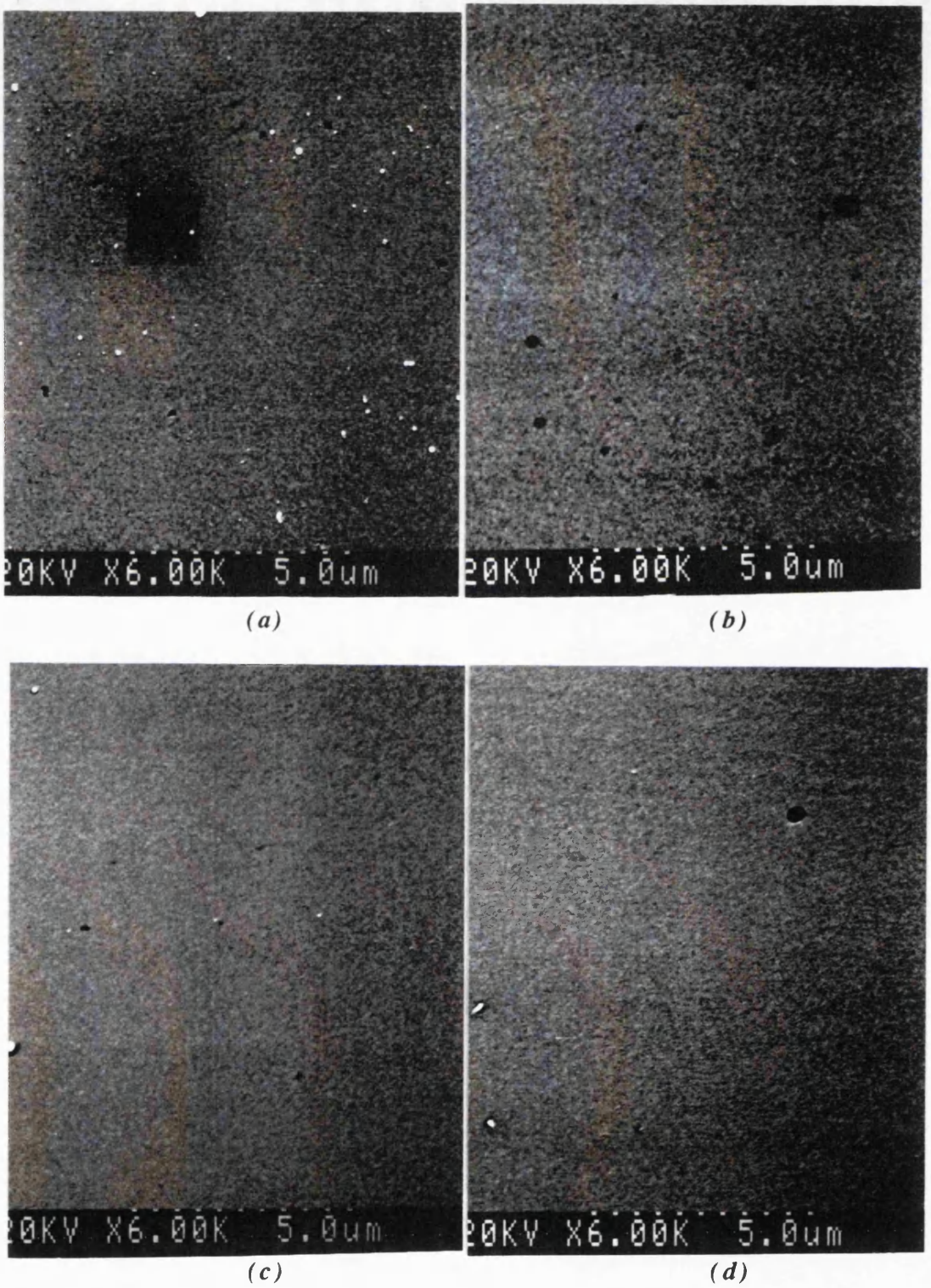

(a) *(b)*

(c) *(d)*

Figure 6.12 *Effect of laser energy density variations on surface morphology for films deposited using the excimer laser (248 nm). The laser was focused on to the target to generate an energy density of:*
(a) ≈1.3 J/cm², (b) ≈2 J/cm², (c) ≈3.3 J/cm², and (d) ≈4.6 J/cm².

Table 6.1 *Effect of target polishing prior to deposition, on the surface morphology of the CeO_2 films. The number of particulates are per 65 μm x 52 μm square.*

Period of target ablation prior to deposition (sec)	No. of particulates larger than 1 μm in diameter	No. of particulates between 0.5 and 1μm in diameter	No. of particulates less than 1μm in diameter
180	32	37	132
12	7	26	156
none	none	40	177

As can be seen although the total number particulates did not change significantly in any of the cases, the density of larger type particulates (>1 μm diameter) decreased to nil with target surface polishing.

As mentioned in section 3.4, according to Strikovsky et al. [32] the particulates appearing on the surface of laser deposited YBaCuO films can be classified into three types namely, the smaller size (0.02-0.1 μm diameter), the medium size (0.2-0.4 μm diameter), and the larger size (1-5 μm diameter) particulates which are caused by the material growth mode, vapour condensation at a distance away from the target, and laser-target interaction respectively. In the case of this project if the size of particulates can also be classified into smaller type (< 0.5 μm diameter), medium type (0.5-1 μm diameter) and larger type (>1 μm diameter), then by comparing the growth of CeO_2 to that of YBaCuO and by neglecting the slight dissimilarity in size of the CeO_2 and YBaCuO particulates of the same type, it seems from table 6.2 that by depositing from a polished surface the formation of larger type particulates can be avoided. However, it should be noted that although a polished target surface could result in a film with lower number of particulates with sizes >1 μm diameter, deposition from a target rotating at 5 rpm means that only in the first 12 seconds the laser would encounter a polished surface. A deposition time of 12 seconds corresponds to a thin film with a thickness that would result in a large FWHM, thus lower crystal quality. An ideal but not practical case would be to use a multiple target holder and to move from one target to another.

(a) *(b)* *(c)*

Figure 6.13 *SEM micrograph of CeO_2 thin film surfaces deposited for 12 sec on Si (100) using the Nd:YAG laser (532 nm) from: (a) a polished target, (b) a target pre-ablated for 12 sec (1 rev), and (c) a target pre-ablated for 180 sec (5 revs')*

(b) Effect of 248 nm radiation:

The surface morphology of the films is shown in figure 6.14. Contrary to the previous case, pre-ablating the target seems to have been beneficial in producing a film with less number of particulates on its surface. This can be explained by the SEM micrographs of target surfaces irradiated by the Nd:YAG and the excimer lasers and compared with a non-radiated target surface, as shown in figure 6.15. As can be seen the fact that a polished surface yields a better surface morphology still holds, however the ablated target surface is much smoother (more polished) than the 'hand polished' region. It should be noted however that a more elaborate polishing process (c.f. single crystal polishing) should result in a surface which could be as smooth if not smoother than that of a pre-ablated target.

A rough surface has the effect that the laser radiation can penetrate deeper into the target and therefore a higher number of particulates can be ejected. Radiation at 532 nm results in the laser beam penetrating deep into the target due to the relatively long absorption length ($\alpha \approx 10^4$ cm^{-1} [36]) which can lead to melting and formation of pin-holes on the target surface. The target surface should therefore be polished prior to any ablation. However, at 248 nm since ablation of the target takes place closer to the surface due to a low absorption length ($\alpha \approx 10^5$ cm^{-1} [36]), the target surface becomes smoother when ablated. By placing a shutter a short distance (few mm) away from the substrate the target can be pre-ablated prior to deposition without breaking the vacuum.

6.3.7 Post-deposition cooling rate

Due to the difference in the linear thermal expansion coefficients of Si (2.6×10^{-6}) and CeO_2 (11.6×10^{-6} [8]), micro-cracks tend to develop in 'thick' films cooled down at a fast rate as shown in figure 6.16. The formation of micro-cracks may be avoided by either growing another intermediate buffer layer(s) with its'(their) linear thermal expansion coefficient(s) being between those of Si and CeO_2, or by lowering the film thickness and the cooling rate. We have observed that a cooling rate of 5°C/min for a film thickness of < 2000 Å is sufficient to avoid the formation of micro-cracks.

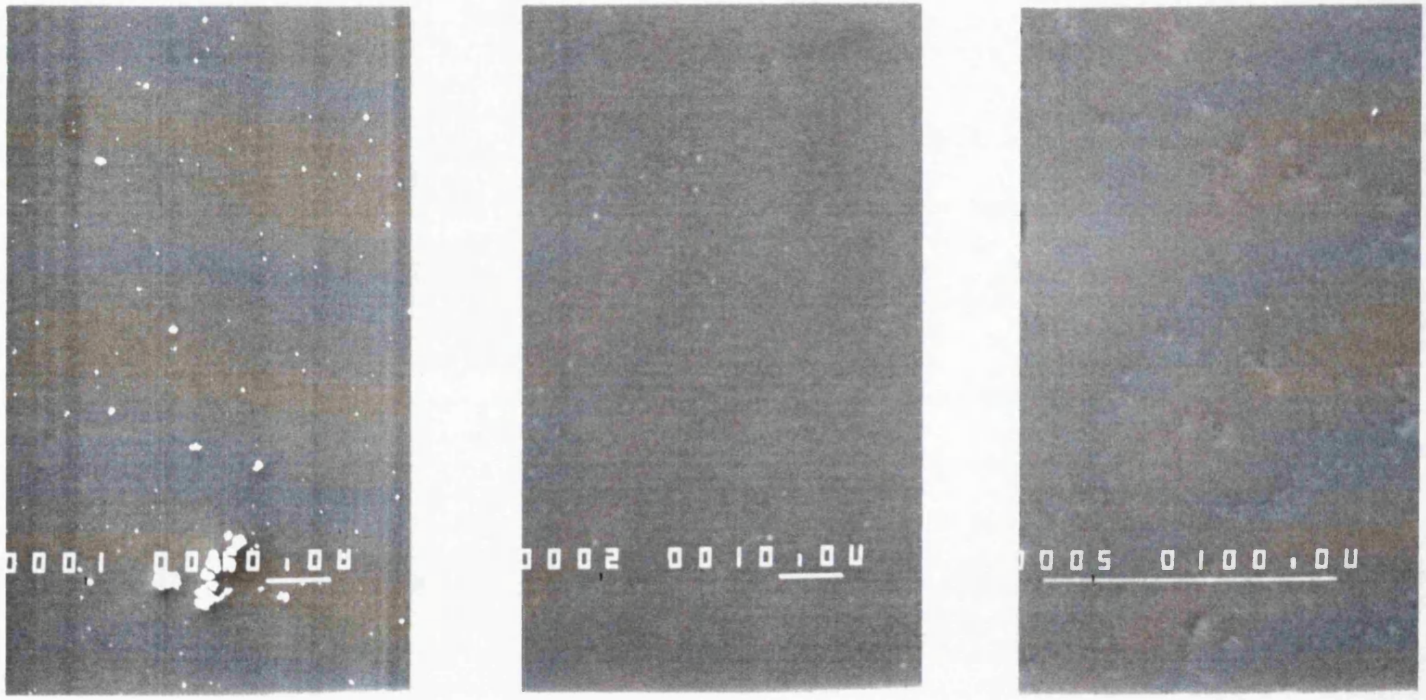

(a) (b) (c)

Figure 6.14 *SEM micrograph of CeO_2 thin film surfaces deposited for 12 sec on Si (100) using the excimer laser (248 nm) from: (a) a polished target, (b) a target pre-ablated for 12 sec (1 rev), and (c) a target pre-ablated for 180 sec (5 revs')*

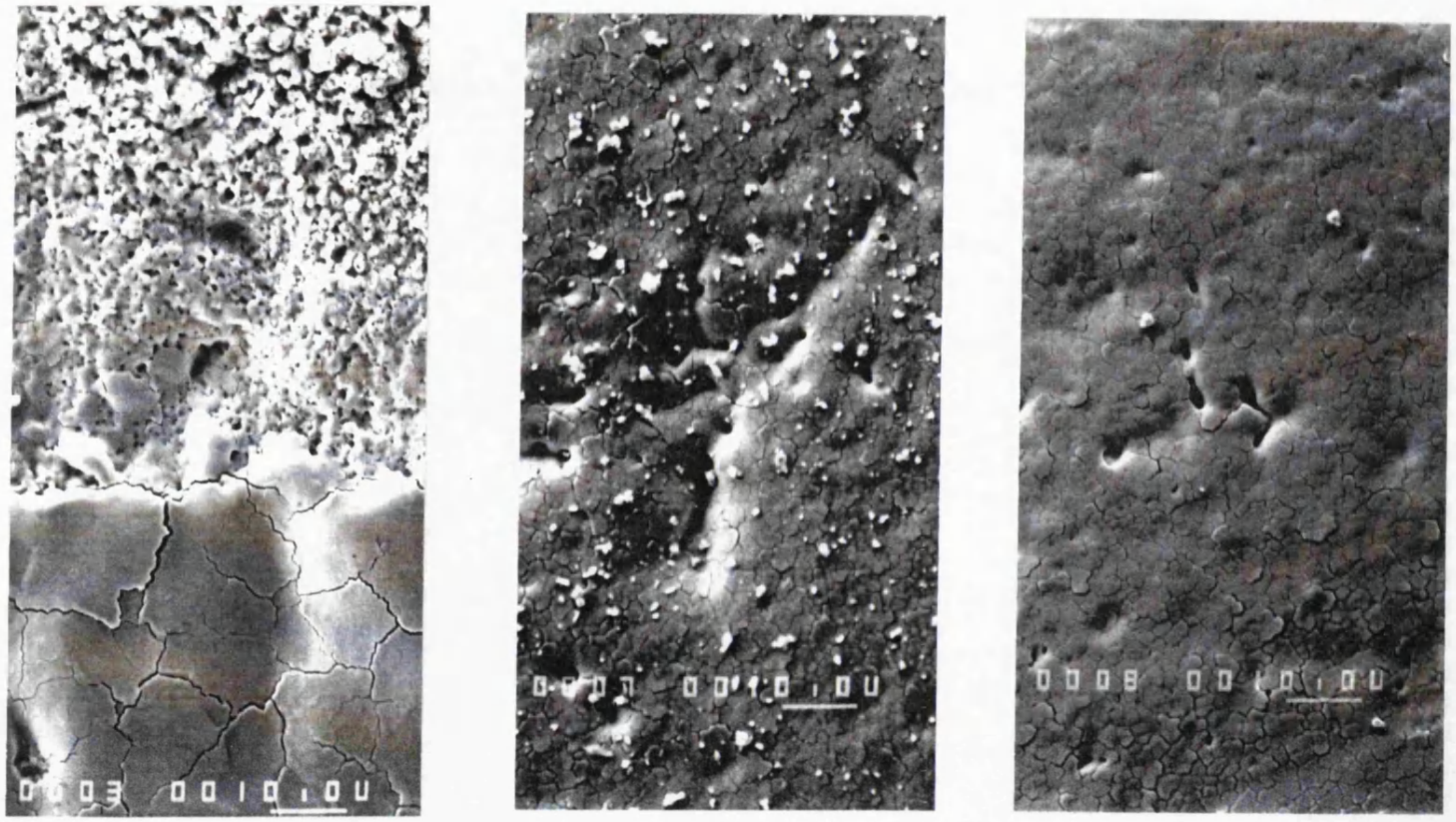

(a) (b) (c)

Figure 6.15 *SEM micrograph of: (a) the border between the non-ablated and the excimer ablated target surface, (b) target ablated using the frequency doubled Nd:YAG laser (532 nm), and (c) target ablated using the KrF excimer laser (248 nm).*

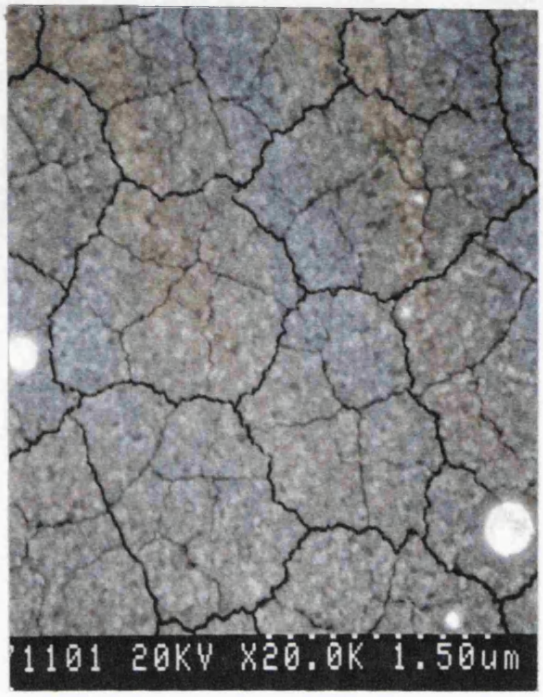

Figure 6.16 *SEM micrograph of a CeO_2/Si(100) cooled down at a fast rate.*

6.3.8 TEM studies

The crystal structure and grain size of the particulates and the flat regions on the surface of a CeO_2 film grown on Si(100) using the Nd:YAG laser were examined by TEM. Sample preparation and microscopy were carried out by Dr. E. Beithel, Department of Material Science and Metallurgy, University of Cambridge. The plan-view specimens were made by using an ultrasonic drill to prepare 3 mm diameter discs of the wafer, which were mechanically ground and polished from the substrate side to a thickness of ≈100 nm. An argon ion mill was then used to remove some of the CeO_2 until the CeO_2/Si interface was very close to the surface (within ≈50 nm, judged by the interference colour). Finally the samples were milled from the Si side until perforated. The result is a sample where the electron transparent area contains the CeO_2/Si interface. Figure 6.17 shows the cross-sectional view of a typical sample at very low magnification. It can be seen clearly that some of the spherical particulates appear to have been nucleated within the main CeO_2 layer while others stand on top of the surface.

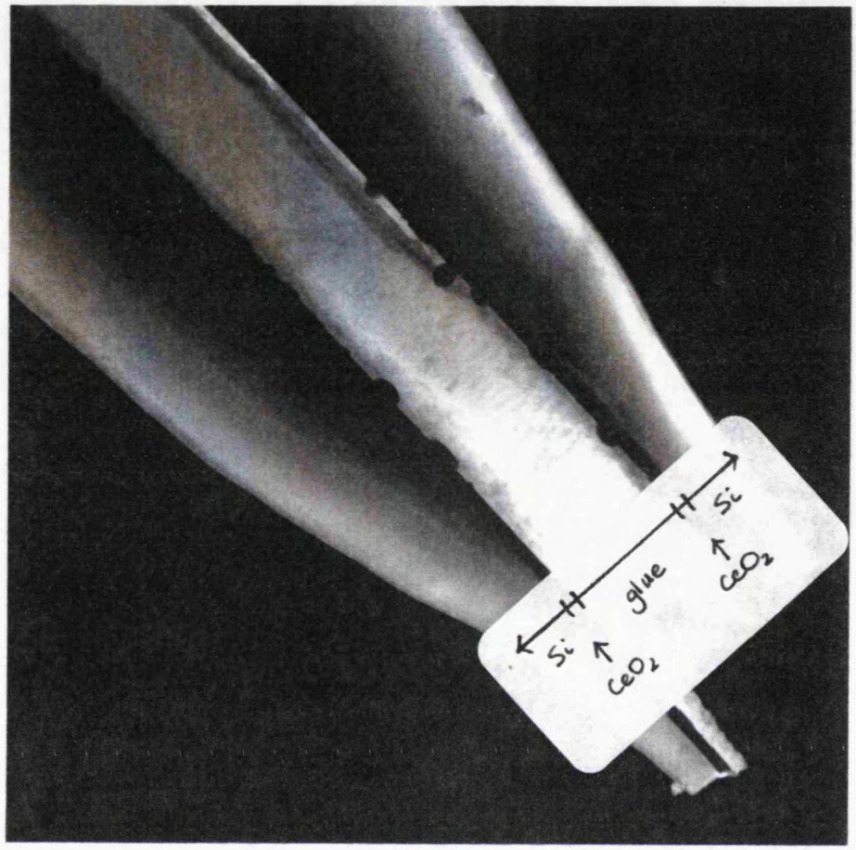

Figure 6.17 *Cross-sectional view of two sections of a CeO_2/Si sample glued together, showing the particulates at the top surface of the layers.*

The diffraction patterns from the flat part of the layer and from one of these particulates (figure 6.18a and figure 6.18b) show that the flat parts of the film possess a pronounced texture with <111> CeO_2 parallel to the [100] silicon wafer normal, whereas the particulates have no particular preferred orientation. An electron diffraction pattern gives an undistorted picture of the reciprocal lattice and is related inversely to the size and shape of the unit cell. Thus the distances between pairs of spots are inversely proportional to the corresponding distances in the actual crystal. The centre of the pattern, corresponds to the position of the straightthrough, undiffracted beam of radiation - the 000 beam. In figure 6.18a, an interpretation of the electron diffraction pattern is as follows: the concentric diffraction pattern rings from the 220, 422, and 440 reflections, and the absence of all the intermediate rings indicate a strong <111> texture (these set of planes are orthogonal to the (111) plane - dot product equals zero). The position of the spots resembles that of silicon due the cubic

crystal structure and the almost identical lattice constant of CeO_2. The formation of ring patterns is due to the small crystal grain sizes in the flat part of the film; the ion - milling process is also believed to cause such ring patterns. (The arcs which are not concentric around the 000 beam are caused by double diffraction from the underlying silicon reflections - since the scattering efficiency of electrons is high, the diffracted beams are strong and can effectively become the incident beam which can be diffracted by another set of lattice planes).

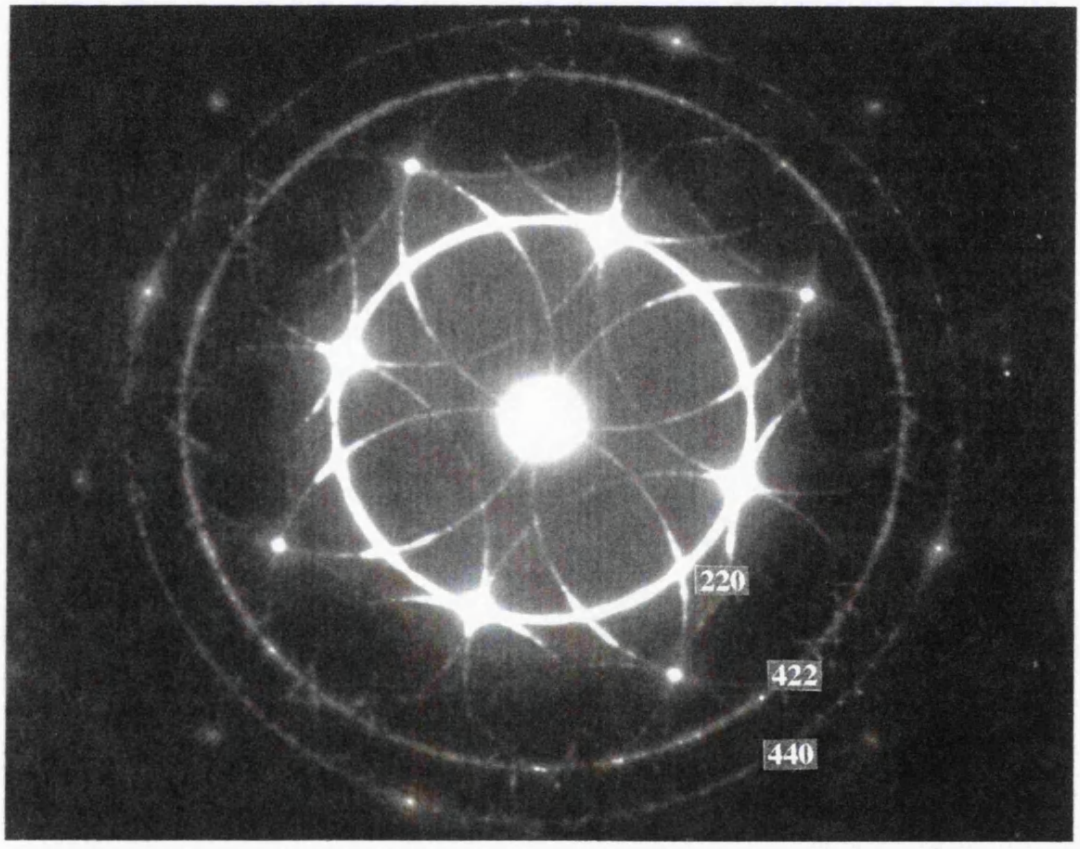

Figure 6.18a *Selected area diffraction pattern from a flat region between the particulates.*

In the diffraction pattern from one of the spherical particles, shown in figure 6.18b, all the expected diffraction rings are present (111, 200, 220, 311, 222, 400 etc.) indicating no preferred orientation. The rings are broken up because of the larger grain size (i.e. fewer grains diffracting).

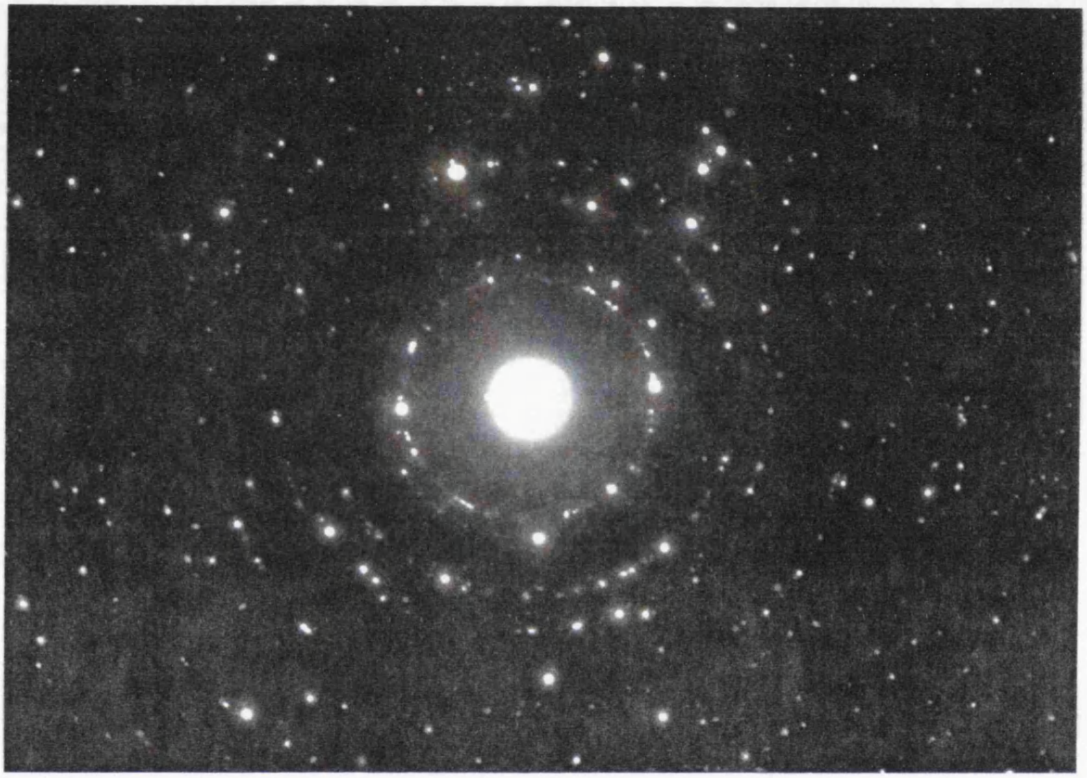

Figure 6.18b *Selected area diffraction pattern from a particulate.*

The size of the grains have been estimated from the dark field images shown in figures 6.19 a&b to be 100-200 nm in a particulate and ≈25 nm in the flat region.

A lattice image at the interface of a CeO_2/Si(100) film grown using the excimer laser is shown in figure 6.20. Sample preparation and microscopy was carried out by Dr.Y.Li, Department of Material Science and Metallurgy, Imperial College of Science and Technology, London. As can be seen two kinds of very thin amorphous layers formed at the interface, with the dark layer at the CeO_2 side and the bright one at the Si side. This suggests that there are more Ce atoms in the dark layer and more Si atoms in the bright layer, since Ce atom is much heavier than Si atom. Thus during the initial stages of growth an amorphous CeO_2 (or CeO_x) seems to have formed on top of the native oxide. As growth proceeded the structure developed into a highly ordered pattern.

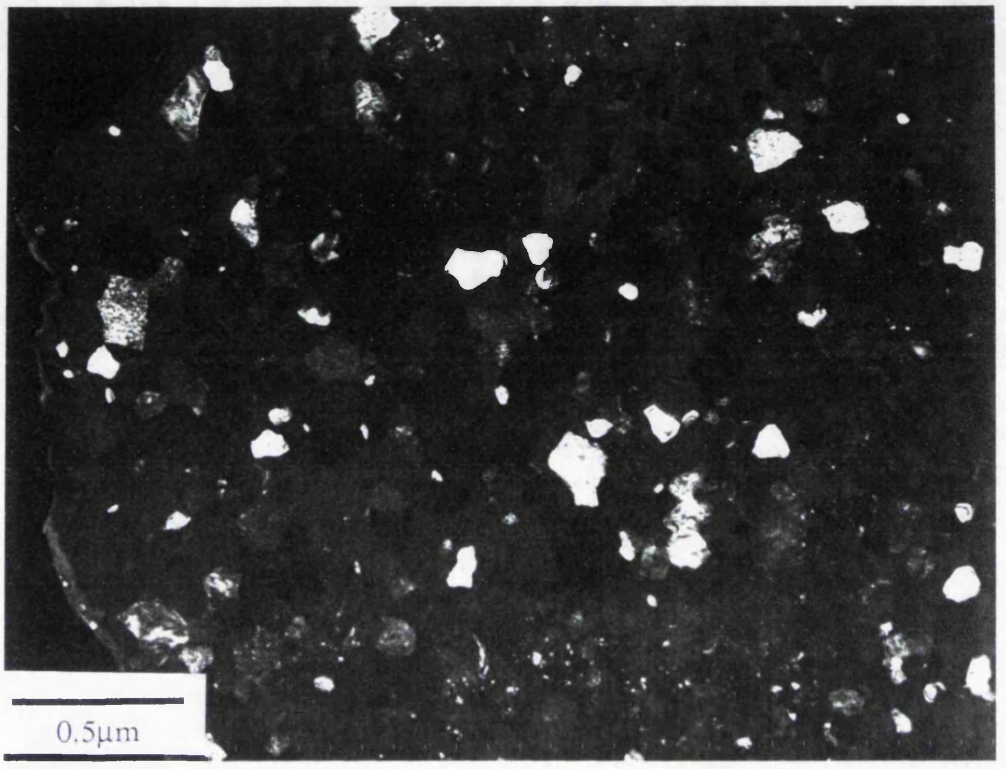

(a)

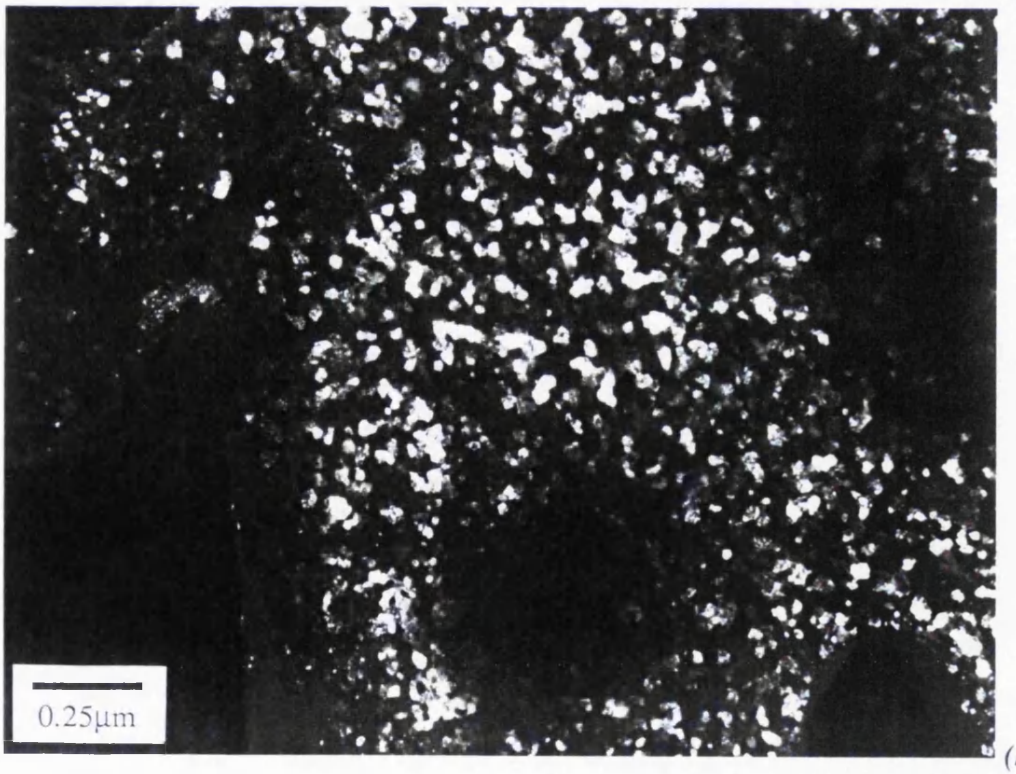

(b)

Figure 6.19 *(a) Dark field image of a particulate. The much smaller grain size outside the particulate is just visible at the edges of the micrograph. (b) Equivalent dark field image of an area between the particulates, showing the reduced grain size.*

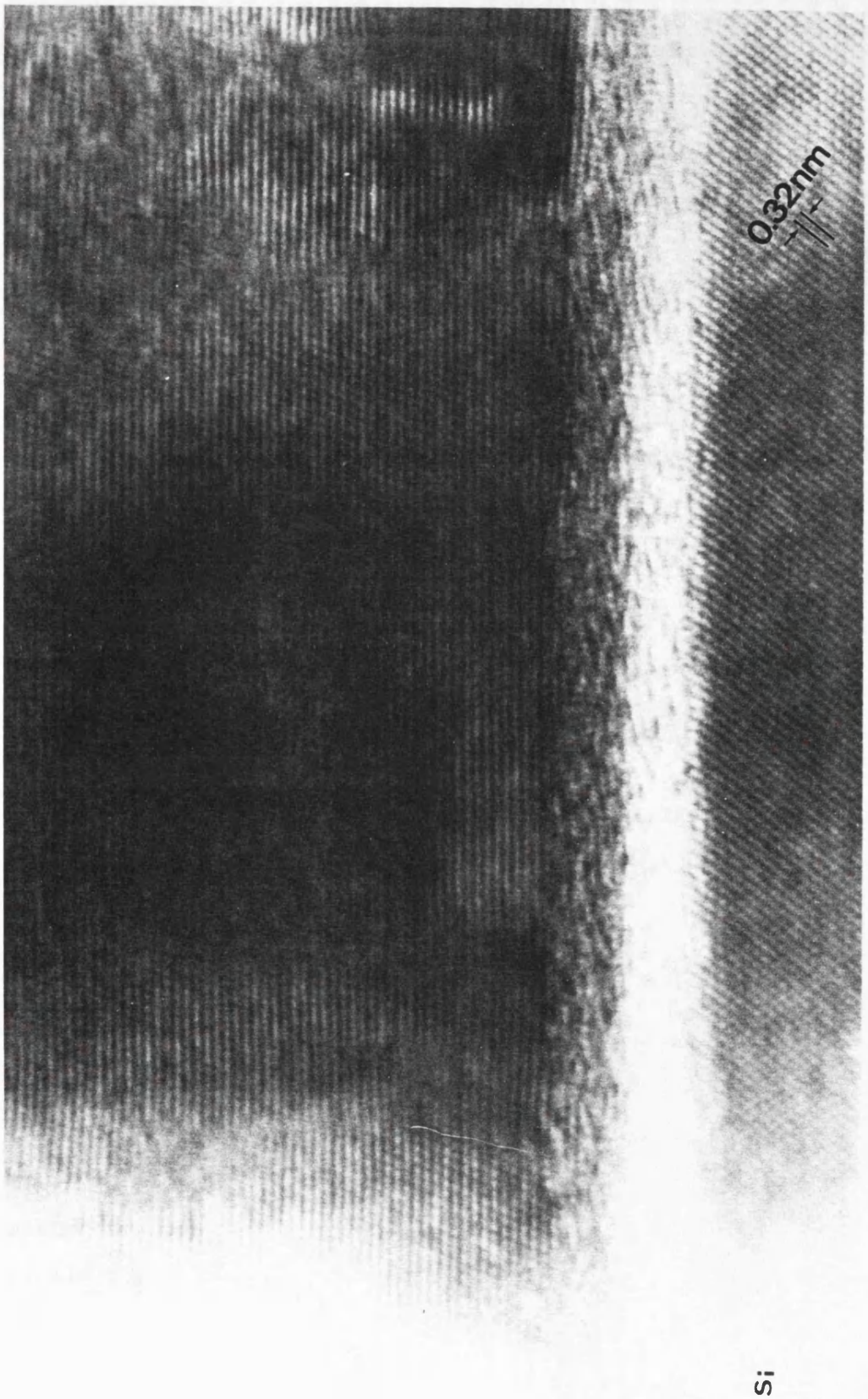

***Figure 6.20** TEM lattice image of the CeO_2/Si(100) interface.*

6.3.9 Growth on sapphire substrates

Microwave applications of HTSC require the fabrication of large-area thin films on appropriate substrate materials. Substrates such as $SrTiO_3$, $LaAlO_3$, $NdGaO_3$ or $CaNdAlO_4$ each have their advantages and drawbacks [34]. $SrTiO_3$ for example has a large dielectric constant which is >300. $LaAlO_3$, the commonly used material for microwave applications has a relatively low dielectric constant of 15-25, however, there is the problem of twinning which can develop during a cubic-rhombohedral phase transition at ≈500°C.

Sapphire has an excellent potential of becoming a common substrate for microwave devices based on HTSC. The low dielectric constant of 8-11, good mechanical strength, and above all availability in large sizes with perfect polish at a comparably low cost makes it a highly desirable candidate. However in growing HTSC films on sapphire the problem of interdiffusion at the interface exists which means that there is a need for a suitable buffer layer such as CeO_2.

Thin films of CeO_2 were grown on (1$\underline{1}$02) Al_2O_3 (*R*-cut sapphire) substrates using two separate conditions. One was to grow the film using the same deposition parameters for most CeO_2/Si samples i.e. P_{O_2} of ≈$2x10^{-5}$ mbar and T_s of ≈500°C. The other was to deposit the film at a P_{O_2} of $2x10^{-1}$ mbar and a T_s of 650°C. The XRD patterns for both films are shown in figures 6.23 a&b. It can be seen that by depositing at high P_{O_2} and high T_s, growth in the [200] direction can be achieved. These results compare well with the results of Denhoff et al. [6] and Holstein et al. [7] whereby T_s and P_{O_2} of, 750°C at 150 mTorr, and, 740°C at 200 mTorr respectively were employed. This suggests two different growth mechanisms. It is likely that at the lower T_s and much lower P_{O_2}, the growth mechanism is similar to growth on an amorphous oxide resulting in a (111) oriented film, i.e. a chemical rather than a crystallographic growth mechanism. However, at the higher T_s and much higher P_{O_2}, the growth mechanism can be of a crystallographic rather than a chemical nature.

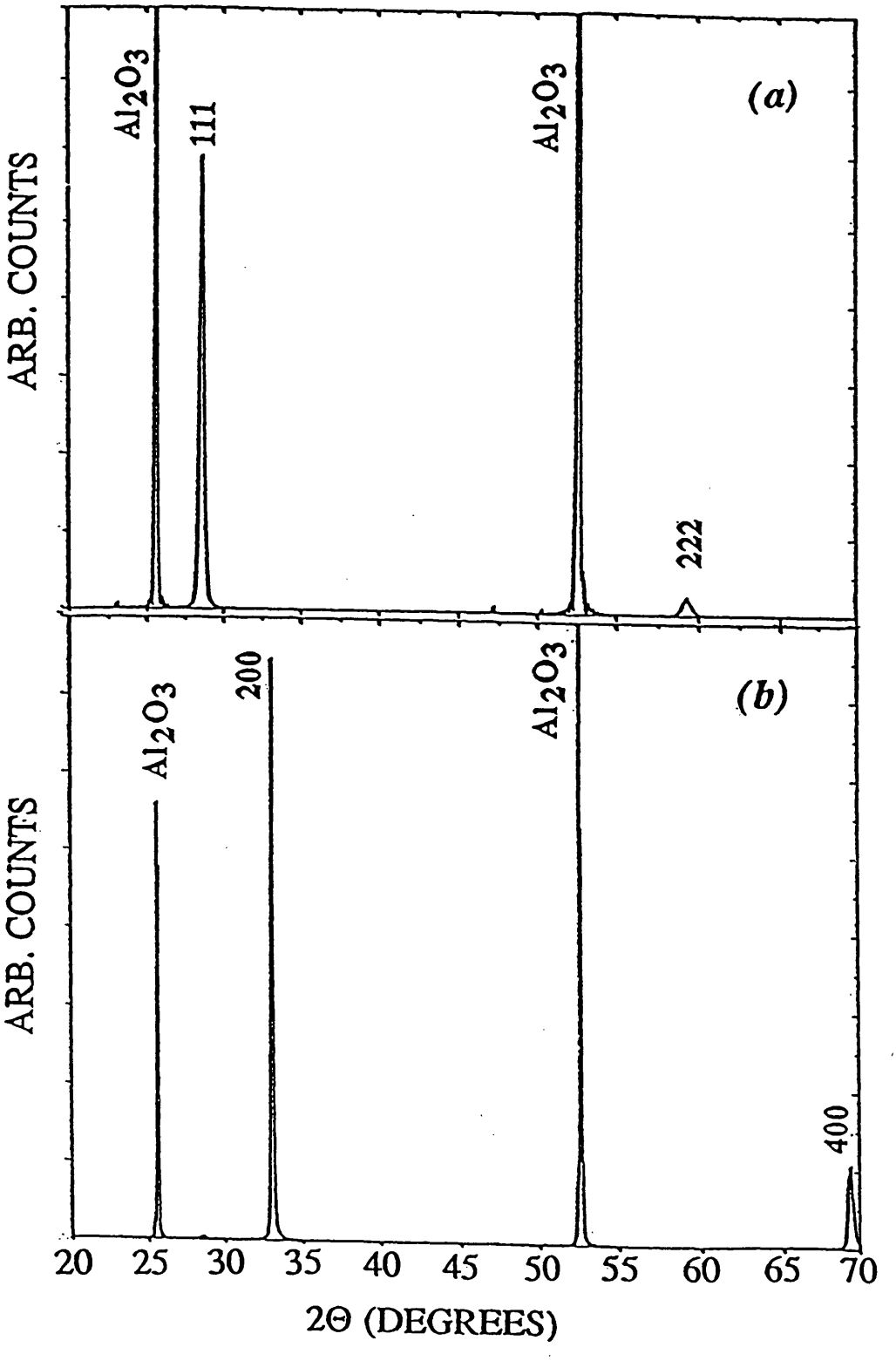

Figure 6.23 *XRD patterns of CeO_2 films grown on sapphire at: (a) P_{O_2} of $2x10^{-5}$ mbar, T_s of 500°C and (b) P_{O_2} of $2x10^{-1}$ mbar, T_s of 650°C.*

6.3.10 La added CeO_2

To enable optimum matching of superconducting films with semiconductors such as silicon, several criteria must be considered in the use of buffer layers. Not only must they act to limit atomic interdiffusion, but they must be capable of sustaining any lattice mismatch and thermal expansion characteristics between the layers. In this respect it would be desirable to engineer the lattice constant to ensure near perfect matching over a specific temperature range with the underlying substrate as well as the superconducting material deposited over the buffer layer. If no unique material is available the next best option would involve growth of a graded stack of layers starting with the substrate matching properties and ending with the superconductor fitting features. In this case pure CeO_2 already has a very close lattice matching with silicon. Depending upon the superconducting lattice parameters one then proceeds up or down in lattice constant, ending with a layer which is closely matched with the final active material to be deposited. This can be achieved by doping the CeO_2 with elements such as La or Y to increase or decrease the lattice constant.

By employing the usual deposition conditions for depositing CeO_2 on Si and glass, bilayers of CeO_2 and La doped CeO_2 were grown on Si(100). The CeO_2:La layer was deposited from a target with composition, 40% La_2O_3 and 60% CeO_2. The thicknesses of the films were ≈2000 Å each, as measured by the talystep. An XRD pattern of this bilayer is shown in figure 6.24. As can be seen both layers are highly oriented resulting in lattice constants of 5.41 Å for the CeO_2 layer and 5.55 Å for the CeO_2:La layer.

6.3.11 $YBa_2C_3O_{7-\delta}/CeO_2/Si$ multilayer system

Thin films of $YBa_2C_3O_{7-\delta}$ were deposited on CeO_2/Si(100) substrates under a P_{O_2} of ≈2.5×10^{-1} mbar and a T_s of 750°C by PLD. The KrF excimer laser was used during the growth of YBaCuO and CeO_2 films. Immediately after the deposition the sample was cooled down to ≈650°C in ≈5 min and the P_{O_2} was raised to >10^2 mbar. This was followed by cooling down at a rate of ≈10°/min to 400°C and switching off the heater.

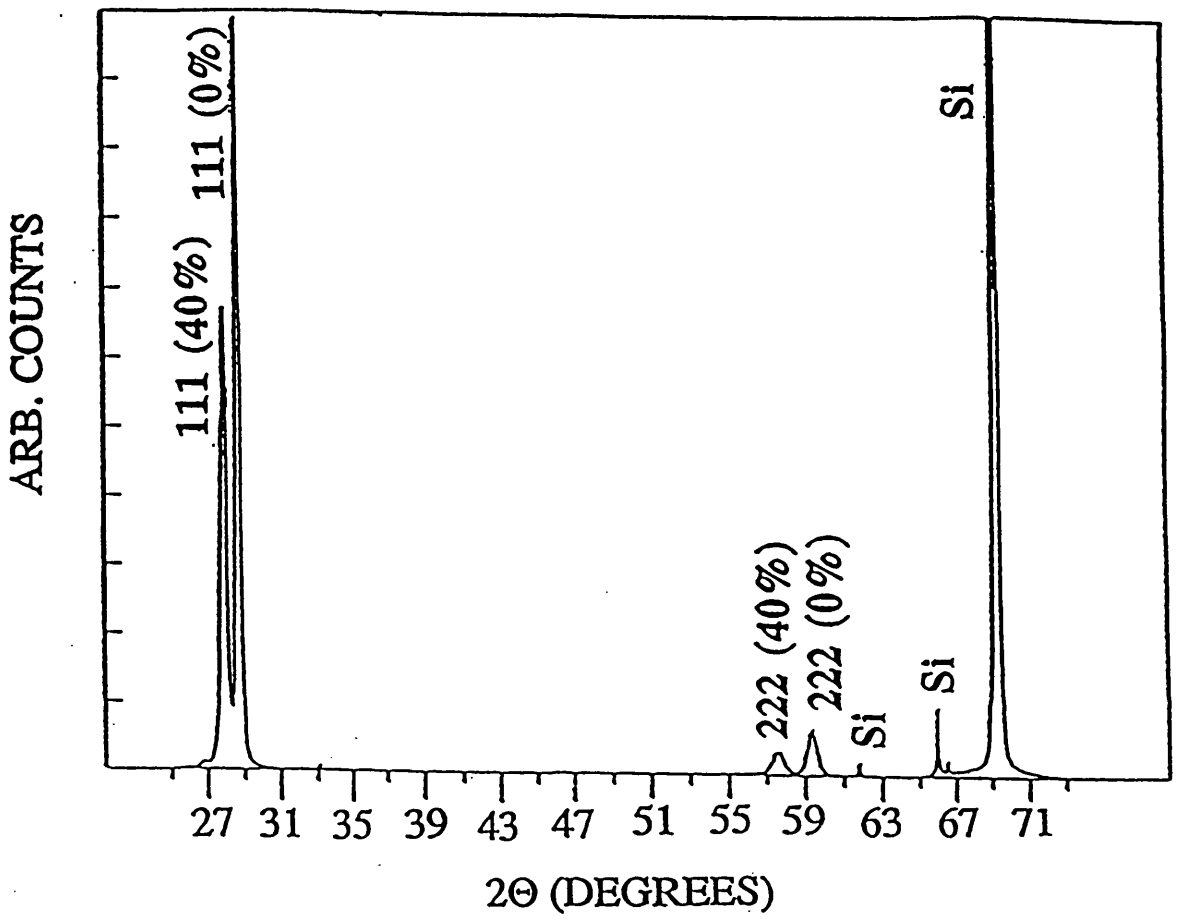

Figure 6.24 XRD pattern of a CeO_2:La/CeO_2/Si bilayer system.

For depositing both the CeO_2 and the $YBa_2C_3O_{7-\delta}$ layers a KrF excimer laser operating at 248 nm with a pulse duration of 20 ns at 5 Hz was used which was focused onto the targets to give an energy density of 3 J/cm^2. The thicknesses of the CeO_2 and the $YBa_2C_3O_{7-\delta}$ layers were measured to be ≈2000 Å and ≈1500 Å respectively. An XRD pattern of this multilayer is presented in figure 6.25. As can be seen the film shows *c*-axis orientation with the peaks of both $YBa_2C_3O_{7-\delta}$ and CeO_2 being quiet sharp and distinct.

The resistance vs. temperature profile of this multilayer is shown in figure 6.26. A $T_{c(onset)}$ of ≈78 K and a $T_{c(0)}$ of ≈40 Kwere obtained which are not as high as the ones generally obtained for $YBa_2C_3O_{7-\delta}$ grown on MgO or other single crystal oxides, and the best T_c reported in literature for growth using intermediate buffer oxides. By fine-tuning the deposition parameters for the growth of $YBa_2C_3O_{7-\delta}$ on CeO_2/Si, a T_c close to 90 K should be possible.

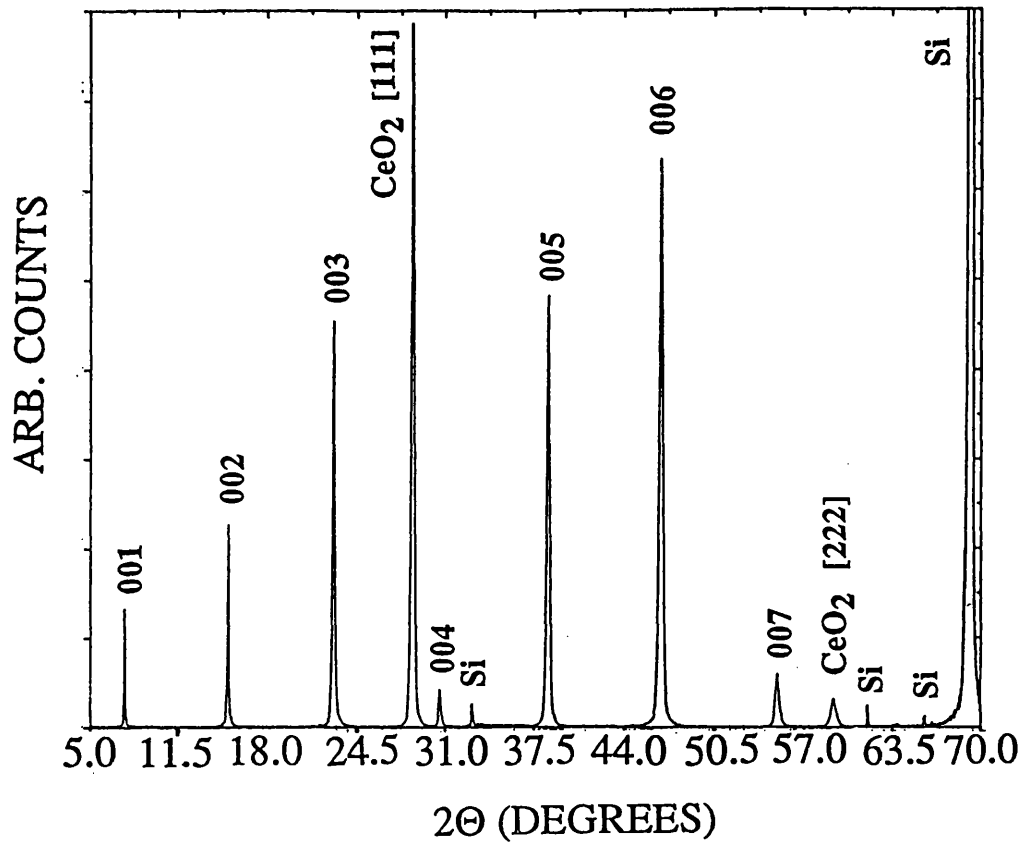

Figure 6.25 XRD pattern of a $YBa_2Cu_3O_{7-\delta}$ film grown on CeO_2/Si.

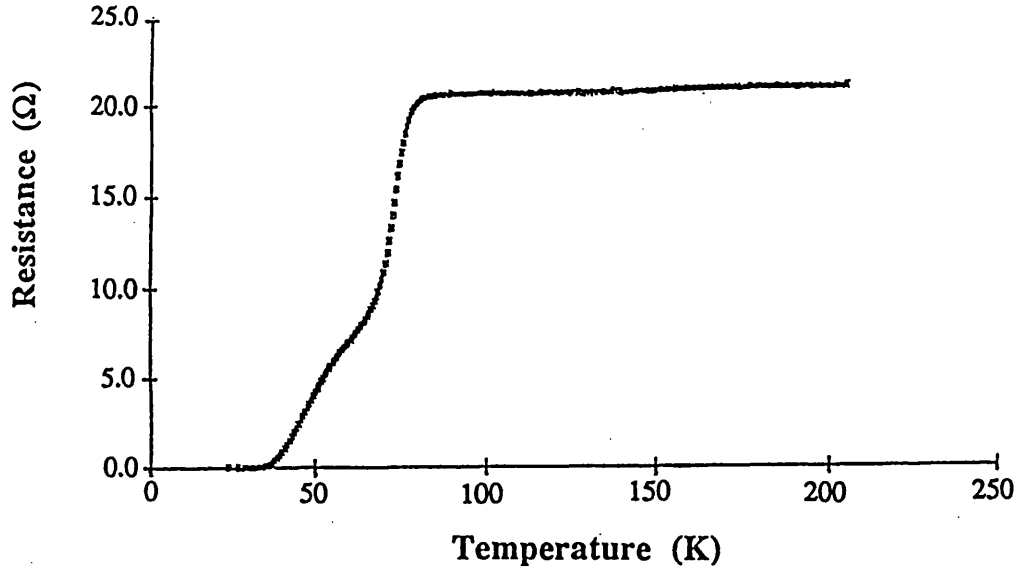

Figure 6.26 Resistance vs. temperature characteristic of the $YBa_2Cu_3O_{7-\delta}$ film grown on CeO_2/Si.

6.3.12 BiSrCaCuO/CeO_2/Si multilayer system

Thin films of BiSrCaCuO were deposited on CeO_2/Si(100) substrates at room temperature under a base pressure of $\approx 1 \times 10^{-4}$ mbar by PLD from a BiSrCaCuO (2223 phase) target. The sample was then annealed in a tube furnace at $\approx$ 850°C in air for 15 min. The BiSrCaCuO and CeO_2 layers were deposited using either the Nd:YAG laser, or the excimer laser. The BiSrCaCuO films were grown by Mr. A.Sajjadi, Department of Electronic & Electrical Engineering, UCL, when the Nd:YAG laser was used, and Dr. F.Beech, (same department), UCL, when the excimer laser was employed.

As can be seen in the XRD pattern of figure 6.27a the growth of BiSrCaCuO on CeO_2/Si resulted in intermixing of the two layers when the Nd:YAG laser was used. However, when the excimer laser was employed a totally different growth profile was obtained as shown in figure 6.27b. This time there was no sign of intermixing, but the XRD pattern displayed a highly *c*-axis oriented BiSrCaCuO film with some of the peaks missing.

The first case can be compared with the work of Chin et al. [23] whereby e-beam evaporation and *in-situ* dc sputtering were used to grow the CeO_2 and the BiSrCaCuO films respectively. Their results from XRD and Auger depth profiling studies suggested that Ce gets diffused into the BiSrCaCuO film even at temperatures as low as 580°C.

Missing XRD peaks in *c*-axis oriented films of BiSrCaCuO have also been observed by Ranno et al. [35]. A frequency tripled Nd:YAG laser operating at 354 nm was used to grow the films *in-situ* on MgO (100) single crystals from targets with compositions $Bi_4Sr_3Ca_3Cu_4O_y$ and $Bi_2Sr_2Ca_1Cu_2O_y$. Depending on the growth conditions, thin films of the 2201 phase, the 2212 phase or a combination of the two could be obtained. When a combination of two phases was grown missing XRD peaks were observed which were attributed to the intermixing of both phases known as intergrowth. When the number of CuO_2 planes increases in a BiSrCaCuO unit cell the number of XRD peaks for the same 2θ range also increases. In the case of intergrowth of the *A* phase and *B* phase, if the (00*i*) XRD peak in the pure *A* phase

is close to a (00*j*) XRD peak of the pure *B* phase, the resulting peak is less shifted and broadened, and it remains intense. However, if the (00*i*) peak is far from the (00*j*) peak, the resulting peak is shifted and broadened with the intensity diminishing down to zero.

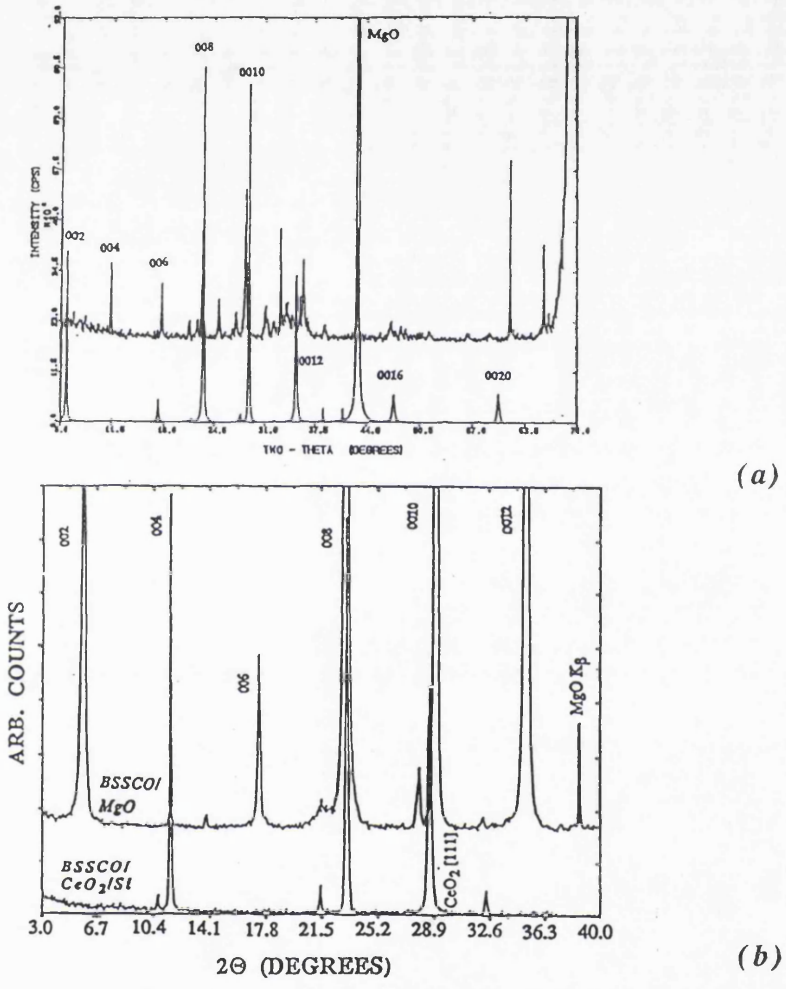

Figure 6.27 *XRD patterns for the BiSrCaCuO/CeO_2 /Si multilayer: (a) when a Nd:YAG laser (532 nm) is used, and (b) when an excimer laser (248 nm) is used.*

6.4 Superconducting multilayer systems grown by other groups

This work was performed independently of the several groups who reported the growth of CeO_2 films during the execution of this project. The suitability of CeO_2 as an intermediate buffer layer between various superconducting films and different substrates has been demonstrated by a number of groups, a summary of which is presented in table 6.2.

***Table 6.2** Superconducting multilayer systems using CeO_2 as an intermediate buffer layer.*

Multilayer system	$T_{c(0)}$ (K)	J_c (A/cm^2)	Reference
$YBa_2Cu_3O_{7-\delta}$ (c-axis) / $CeO_2(00n)$ / $LaAlO_3$	90	5.9×10^6	2
$YBa_2Cu_3O_{7-\delta}$ (a-axis) / CeO_2 (110) / Si(100)	87	1.5×10^5	9
$YBa_2Cu_3O_{7-\delta}$ (c-axis) / CeO_2(111) /Si(100)	84	–	18
$YBa_2Cu_3O_{7-\delta}$ (a-axis) / $CeO_2(00n)$ / sapphire	88	1.3×10^6	6
$YBa_2Cu_3O_{7-\delta}$ (c-axis) / $CeO_2(00n)$ / sapphire	87	–	11
$YBa_2Cu_3O_{7-\delta}$/ $CeO_2(00n)$ / $SrTiO_3(00n)$ /MgO (00n)	86	–	27
BiSrCaCuO (01n) / CeO_2 (220) / MgO(110)	50	–	12
$Tl_2Ba_2CaCu_2O_8$ (c-axis) / $CeO_2(00n)$ / sapphire	98	2.8×10^5	7

6.5 Conclusion

A number of parameters involved in the PLD growth of CeO_2 thin films on substrates of Si(100), Si(111), Corning glass 7059 and sapphire ($1\underline{1}02$), using a frequency doubled Nd:YAG laser (532 nm) and a KrF excimer laser (248 nm) were investigated. Since the native oxide was not removed from the Si surfaces, growth on these substrates were essentially similar and resembled that on Corning glass 7059.

A partial pressure of oxygen is necessary when the Nd:YAG laser is used to avoid the formation of suboxides. However, the amount must be low enough ($< 5\times10^{-5}$ mbar) to reduce the density of particulates on the film surface. When the excimer laser is employed the base vacuum pressure of $\approx1\times10^{-6}$ mbar is sufficient to supply the necessary amount of oxygen to preserve stoichiometry, and a decreasing P_{O_2} enhances

the crystal quality of the films. Deposition using the lower wavelength of 248 nm results in a much reduced density of particulates. High substrate temperatures of >500°C are beneficial in increasing the crystal quality. During the growth of CeO_2 an amorphous layer of CeO_x ($1 < x < 2$) is initially formed (within 50-60 Å) which is gradually developed into a highly oriented CeO_2 structure. A low laser energy density (< 2 J/cm) results in a linear dependence of deposition rate with laser fluence, while at higher laser energy densities a logarithmic dependence is obtained. A transition from the linear to logarithmic regime results in a reduced density of voids and particulates on the surface of the film. Deposition from a target with a smooth and flat surface was shown to reduce the density of particulates on the film surface, and particularly in the case of ablation using the Nd:YAG laser the density of larger particles (>1 μm) could be reduced to zero. However, a target pre-ablated with the Nd:YAG laser had a rougher surface when compared to a non-ablated target, while a target pre-ablated with the excimer laser generated a flatter surface. The deposition of CeO_2 thin films on sapphire at a P_{O_2} of $2x10^{-5}$ mbar and a T_s of 500°C resulted in a (111) oriented film while a P_{O_2} of $2x10^{-1}$ mbar and a T_s of 650°C resulted in a film that was (200) oriented. The lattice constant of CeO_2 can be modified by the addition of elements such as La or Y. This was done by depositing a film from a target with composition: 60% CeO_2 and 40% La_2O_3, on top of an undoped CeO_2 film. Deposition of YBaCuO thin films on CeO_2/Si resulted in a *c-axis* oriented film with no apparent traces of interdiffusion (an Auger or secondary ion mass spectroscopy depth profiling can be carried out to confirm this). A T_c of only ≈78 K was obtained which can be improved by optimising the growth of YBaCuO. The growth of BiSrCaCuO on CeO_2/Si resulted in intermixing when the Nd:YAG laser was used for the deposition of HTSC and buffer layers. A highly *c*-axis oriented BiSrCaCuO film with some missing peaks resulted when the excimer laser was used to deposit the HTSC and the buffer layers.

References

[1] M.Yoshimoto, H.Nagata, T.Tsukahara and H.Koinuma, *Jpn. J. of Appl. Phys.*, **29**, 7, pL1199, (1990).

[2] X.D.Wu, R.C.Dye, R.E.Muenchausen, S.R.Foltyn, M.Maley, A.D.Rollet, A.R.Garcia and N.S.Nogar, *Appl. Phys. Lett.*, **58**, 19, pL2165, (1991).

[3] M.Schieber, *J. Crystal Growth*, **109**, p401, (1991).

[4] R.J.Cava, B.Batlogg, J.J.Krajewlski, *Nature*, **336**, p211, (1988).

[5] A.G.Frangoul, K.B.Sundaram and P.F.Wahid, *J. Vac. Sci. Technol. B*, **9**, 1, p181, (1991).

[6] M.W.Denhoff and J.P.McCaffrey, *J. Appl. Phys.*, **70**, p3986, (1991).

[7] W.L.Holstein, L.A.Parisi, D.W.Face, X.D.Wu, S.R.Foltyn and R.E.Muenchausen, *Appl. Phys. Lett.*, **61**, 8, pL982, (1992).

[8] S.Amirhaghi, F.Beech, V.Craciun, A.Sajjadi, M.Vickers, S.Tarling, P.Barnes and I.W.Boyd, *Proceedings of the MRS Conference*, San Fransisco 1992.

[9] L.Luo, X.D.Wu, R.C.Dye, R.E. Muenchausen, S.R.Foltyn, Y.Coulter, C.J.Maggiore and T.Inoue, *Appl. Phys. Lett.*, **59**, 16, pL2043, (1991).

[10] R.G.Schwab, R.A.Steiner, G.Mages and H.J.Beie, *Thin Solid Films*, 207, p283, (1992).

[11] F.Wang and R.Wördenweber, to be published in *Thin Solid Films*.

[12] J.Tanimura, K.Juroda, M.Kataoka, O.Wada, T.Takami, K.Kojima and T.Ogama, *Jpn. J. Appl. Phys.*, **32**, 2B, part 2, pL254, (1993).

[13] M.Ozawa, M.Kimura and A.Isogai, *J. of Mat. Science*, **26**, p4818, (1991).

[14] A.G.Frangoul, K.B.Sundaram and P.F.Wahid, *J. Vac. Sci. Technol. B*, **9**, 1, p181, (1991).

[15] K.H.Dahmen, M.Becht and T.Gerfin, *Proceedings on High Temp. Superconductor Thin Films, EMRS Conference*, Strasbourg, France p715 (1991),.

[16] H.Koinuma, H.Nagata, T.Ysukahara, S.Gonda and M.Yoshimoto, *Appl. Phys. Lett.*, **58**, 18 pL2027, (1991).

[17] H.Nagata, T.Tsukahara, S.Gonda, M. Yoshimoto and H.Koinuma, *Jpn. J. of Appl. Phys.*, **30**, 6B, pL1136, (1991).

[18] F.Sánchez, M.Varela, X.Queralt, M.V.Garcia-Cuenca, R.Aguiar and J.L.Morenza, *Physica C*, 195, p47, (1992).

[19] T.Inoue, Y.Yamamoto, S.Koyama, S.Suzuki and Y.Ueda, *Appl. Phys. Lett.*, **56**, 14, p1332, (1990).

[20] T.Inuoe, M.Osonoe, H.Tohda, M.Hiramatsu, Y.Yamamoto, A.Yamanaka and T.Nakayama, *J. Appl. Phys.*, **69**, 12, p8313, (1991).

[21] T.Inoue, T.Ohsuna, L,Luo, X.D.Wu, C.J.Maggiore, Y.Yamamato, Y.Sakurai and J.Chang, *Appl. Phys. Lett.* **59**, 27, p3604, (1991).

[22] T.Inoue, T.Ohsuna, Y.Yamada, K.Wakamatsu, Y.Itoh, T.Nozawa, E.Sasaki, Y.Yamamoto and Y.Sakurai, *Jpn. J. Appl. Phys.* **31**, pL1736, (1992).

[23] T.S.Chin, J.Y.Huang. L.H.Perng, T.W.Huang, S.J.Yang and S.E.Hsu, *Physica C*, 192, p154, (1992).

[24] G.Atanassov, R.Thielsch and D.Popov, *Thin Solid Films*, 223, p288, (1993).

[25] M.S.Al-Robaee, M.G.Krishna, K.N.Rao and S.Mohan, *J. Vac. Sci. Tech. A*, **9**, 6, p3048, (1991).

[26] M.S.Al-Robaee, K.N.Rao and S.Mohan, *J. Appl. Phys.*, **71**, 5, p2380, (1992).

[27] D.Youm and S.Lee, *IEEE Trans. Appl. Supercon.*, **3**, 1, p1065, (1993).

[28] N.Harris, "*Modern Vacuum Practice*", McGraw Hill (UK), p66, (1989).

[29] S.R.Foltyn, R.C.Dye, K.C.Ott, E.Peterson, K.M.Hubbard, W.Hutchinson, R.E.Muenchausen, R.C.Estler and X.D.Wu, *Appl. Phys. Lett.*, **59**, 5, p592, (1991).

[30] J.Flokstra, R.P.Ijsselsteijn and J.W.M.Higenkamp, *Thin Solid Films*, **218**, p304, (1992).

[31] A.Zherikhin, V.Bagratashvili, V.Burimov, E.Sobol, G.Shibnii and A.Sviridov, *Physica C*, **198**, p341, (1992).

[32] M.D.Strikovsky, E.B.Klyuenkov, S.V.Gaponov, J.Schubert and C.A.Copetti, *Appl. Phys. Lett.*, **63**, 8, p1146, (1993).

[33] O.Madelung (editor), "*Landolt-Bornstein New Sreies*", **17b**, Springer Verlag, New York, (1982).

[34] K.H.Young, G.V.Negrete, M.M.Eddy, J.Z.Sun, T.W.James, McD.Robinson and E.J.Smith, *Thin Solid Films*, **206**, p116, (1991).

[35] L.Ranno, D.Martínez-García, J.Pierriére and Barboux, *Physical Review*, **48**, 18, p13945, (1993).

[36] to our knowledge there is surprisingly no published data on the absorption coefficient of CeO_2, however, preliminary results of V.Cracuin et al. (Dept. of Elec. Eng., UCL) have indicated the value of α to be close to that of ZnO at 248 nm and 532 nm.

Chapter 7

Growth of $Nd_{2-x}Ce_xCuO_{4-y}$ Thin Films by Pulsed Laser Deposition

The basic properties of the electron-doped superconductor, $Nd_{2-x}Ce_xCuO_{4-y}$, are discussed in the initial part of this chapter. This is followed by outlining the preparation of this material in bulk form and discussing the detailed analysis of these materials using Rietveld refinement of powder diffraction data. The *ex-situ* and *in-situ* growth of thin films of $Nd_{2-x}Ce_xCuO_{4-y}$ are presented and discussed. These films were probed using resistance-temperature measurements, x-ray diffraction, energy dispersive x-ray analysis and electron-probe micro-analysis in order to fully characterise this intriguing material.

7.1 Properties of $Nd_{2-x}Ce_xCuO_{4-y}$

The parent materials Ln_2CuO_4 (Ln=Nd, Pr, Sm) have a tetragonal T' phase structure containing CuO_2 planes in which the copper ions are surrounded by a square planar arrangement of oxygen ions. This is significantly different to materials based on La_2CuO_4 which also exist in an orthorhombic T phase structure (below ≈500 K) and contain CuO_2 planes. However, in this case the copper ions are surrounded by octahedral arrangement of oxygen ions. The T and T' structures of La_2CuO_4 and Nd_2CuO_4 are shown in figure 7.1.

This family of materials can be rendered *n*-type by chemically reducing the Cu (i.e. doping the system with electrons) using a two step procedure:
(1) the replacement of the trivalent (Ln) by the tetravalent ions (Ce or Th),
and
(2) an associated removal of excess oxygen [1].

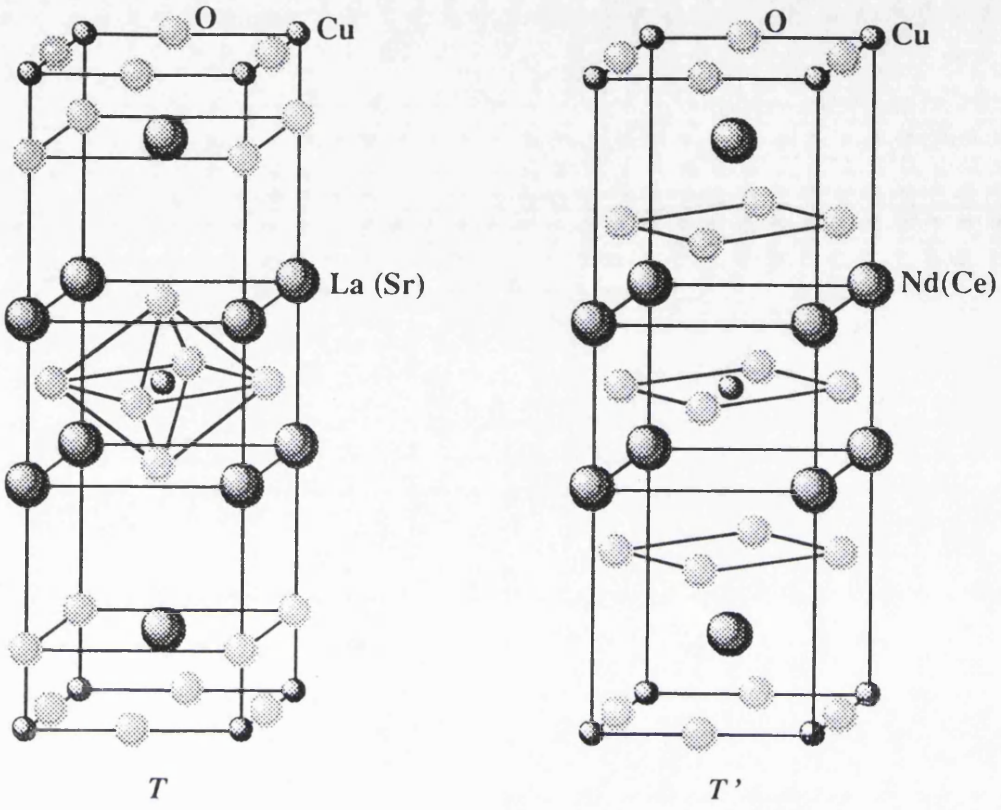

Figure 7.1 *The T and T' structures of $La(Sr)_2CuO_4$ and $Nd(Ce)_2CuO_4$.*

The nature of the charge carrier was confirmed by Hall measurements showing negative Hall coefficients both at 300 K and 80 K [1]. The system becomes superconducting upon cooling with the maximum T_c of 24 K being obtained in the case of $Nd_{1.85}Ce_{0.15}CuO_{4-y}$. This value is only comparable to those of the old low temperature superconducting alloys (Nb_3Ge, $T_c \approx 23$ K). However, these materials are of interest since whilst they contain the ubiquitous CuO_2 planes common to cuprate superconductors, the planes contain a different Cu-O co-ordination environment to that normally encountered, and in addition the carriers are electrons (*n*-type) and not holes (*p*-type). These differences suggests that $Ln_{2-x}Ce_xCuO_{4-y}$ should be investigated so as to shed more light on the inter-relation between the electrical and structural properties of the cuprate perovskites.

An interesting feature of these materials is that superconductivity can be generated from the parent Ln_2CuO_4 by substituting Ga or In for Cu [2], and F for O [3]. Thus it

appears that CuO_2 planes can be doped with electrons, rendering the Ln_2CuO_4 parent compounds metallic and superconducting, by substituting electron donor elements at sites within as well as outside the CuO_2 planes. This result is somewhat surprising since in all the other cuprate superconductors the introduction of a foreign atom on the Cu-O planes always results in the destruction of the superconductivity.

However, in many other respects the doping results in changes that are similar to those observed for the other cuprate systems. In the parent materials the Cu^{2+} magnetic moments are observed to order antiferromagnetically below ≈250 K (the Neél temperature) [4]. Increasing the concentration x of Ce or Th is believed to introduce more electrons into the CuO_2 planes, producing an insulator-metal transition, suppressing the Cu^{2+} antiferromagnetism, and yielding superconductivity with maximum T_c and maximum flux expulsion at x ≈0.15 [4]. The temperature-dopant concentration phase diagrams for the hole doped $La_{2-x}Sr_xCuO_4$ and electron doped $Nd_{2-x}Ce_xCuO_{4-y}$ systems is shown in figure 7.2.

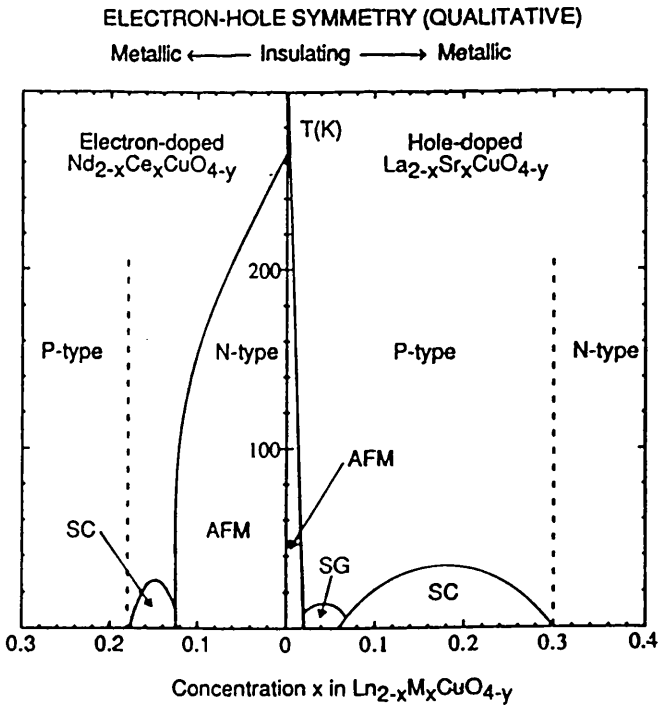

***Figure 7.2** Temperature-dopant concentration, (T-x), phase diagram for hole-doped $La_{2-x}Sr_xCuO_{4-y}$ and electron-doped $Nd_{2-x}Ce_xCuO_{4-y}$ systems. (AFM=anti-ferromagnetic phase, SG=spin glass, SC=superconducting phase) [4].*

As can be seen the gross behaviour of the two systems is broadly similar. However, one key point that should be stressed is the considerably narrower concentration range over which superconductivity occurs in $Nd_{2-x}Ce_xCuO_{4-y}$. It has been suggested that this narrow range may be ascribed to the persistence of the Cu-Cu antiferromagnetic correlations to much higher doping concentrations in the $Nd_{2-x}Ce_xCuO_{4-y}$ system than in $La_{2-x}Sr_xCuO_4$ [4].

A requirement towards the understanding of the doping mechanism in *n*-type superconductors, is the acquisition of information about the valence state of the dopant ion. A number of measurements have indicated the average valent nature of the Ce dopant ions. For example by calculating the values for the unit volume cell, *v*, from x-ray diffraction results for different concentrations of Ce, and estimating the values of *v* for $Nd_{2-x}Ce^{3+}{}_xCuO_4$ and $Nd_{2-x}Ce^{4+}{}_xCuO_4$, Hor et al. [5] found that the Ce dopant in $Nd_{2-x}Ce_xCuO_4$ appears in a valence state between 3+ and 4+. Additional information on this problem was presented by Huang et al. [6] who by calculating the slope from the variation of the *c*-axis lattice constant with Ce concentration and comparing them to the cases with Ce^{3+} and Ce^{4+}, estimated the average valence of the Ce ions to be 3.84 with an associated average ionic radius of 0.993 Å (c.f r =1.143 Å for Ce^{3+} and r =0.97 Å for Ce^{4+}).

A study which is of direct practical interest to the investigations in this chapter is that performed by Idemato et al. [7] who carried out chemical analysis on samples of $Nd_{1.85}Ce_{0.15}CuO_{4-y}$ annealed at different partial pressures of oxygen and different temperatures. The results of which, shown in figure 7.3 and table 7.1, offer us an insight into the annealing conditions for the growth of *ex-situ* films. In the figure, line 1 with symbols ∇ represents the melting points, and line 2 with symbols Δ gives the chemical stability limit above which the material decomposes. As can be seen in the table the Ce valence remains effectively constant within experimental error. However, the Cu valence is highly dependent on both parameters. Super-conductivity appeared when the average Cu valence was below 1.84.

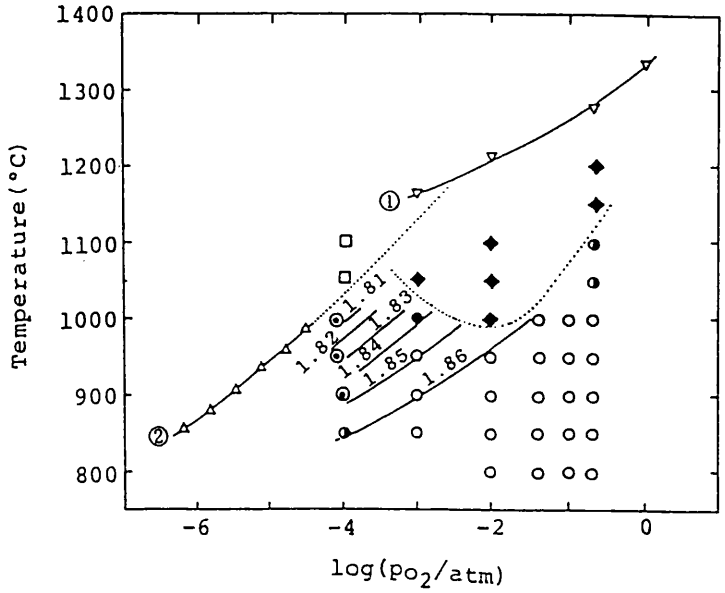

Figure 7.3 *T-log P_{O_2} diagram of $Nd_{2-x}Ce_xCuO_{4-y}$ [7].*

Table 7.1 *Annealing conditions and the average valence of Ce and Cu in $Nd_{2-x}Ce_xCuO_{4-y}$ [7].*

Annealing conditions		Time	Valence	Valence	4-δ
Temperature (°C)	Oxygen partial pressure (atm)	(h)	of Ce	of Cu	
1000	$10^{-4.1}$	48	3.84	1.803	3.965
950	$10^{-4.1}$	42	3.85	1.816	3.972
900	$10^{-4.0}$	84	3.86	1.836	3.978
1050	$10^{-3.0}$	36	3.84	1.830	3.978
1000	$10^{-3.0}$	36	3.85	1.840	3.984
850	$10^{-4.0}$	84	3.87	1.847	3.989
1100	$2x10^{-1}$	36	3.86	1.858	3.994
1050	$2x10^{-1}$	36	3.84	1.865	3.996
600	$2x10^{-1}$	24	3.87	1.874	4.002

To further clarify the situation with regard to the doping process, some information on the valence state of Cu is also necessary. X-ray photoemission spectroscopic studies (XPS) performed on polycrystalline samples have reflected the expected increase in the amount of Cu^{1+} and the decrease in the amount of Cu^{2+} with Ce substitution and reduction, which creates the electron doping on the Cu sites [8]. The fractions of Cu^{1+}

were estimated to be proportional to x in $Nd_{2-x}Ce_xCuO_{4-y}$ in the region up to x =0.2, where Ce reaches its solubility limit. Ishii et al. [8] estimated the average value for the Cu valence to be 2-x-2y. An interesting comparison can be made at this point by reference to the work of Kohiki et al. [9] who applied XPS techniques to thin films of $Nd_{1.85}Ce_{0.15}CuO_{4-y}$. In this case they found the Cu valence for a reduced c-axis oriented *thin film* to be uniquely 1+. This conclusion was supported by the observation from the O1*s* spectra, that only the O_1- state existed in this film (Cu^{2+}-$O^{2-} \rightarrow Cu^{1+}$ - O^{1-}).

These results highlight the crucial role that the method of sample preparation has on determining the measured properties. The reason for such differences in properties have been attributed to compositional inhomogeneities and also to possible ordering of oxygen defects/interstitials in ceramic samples [10,11]. Thus it is imperative when attempting to assess the work performed in this material system to consider the thermal history and synthetic route used in the sample preparation.

Another clear example of the need for caution when interpreting data can be seen by considering the normal state electrical properties of these materials. Reported data on the normal state ceramic samples indicate an increase in resistivity with a decrease in temperature (semiconducting behaviour). In addition the Meissner fractions are rather low (< 20%), particularly for samples prepared by solid state reaction [10]. This contrasts with single crystals and epitaxial thin films in which resistivity decreases with a decrease in temperature and Meissner fractions in excess of 50% have been obtained [10]. The normal state *ab*-plane resistivity is however distinct as it shows a T_2-like temperature dependence rather than the usual linear behaviour. Figures 7.4 and 7.5 show the resistivity versus temperature characteristics of ceramic and single crystal samples of $Nd_{1.85}Ce_{0.15}CuO_{4-y}$.

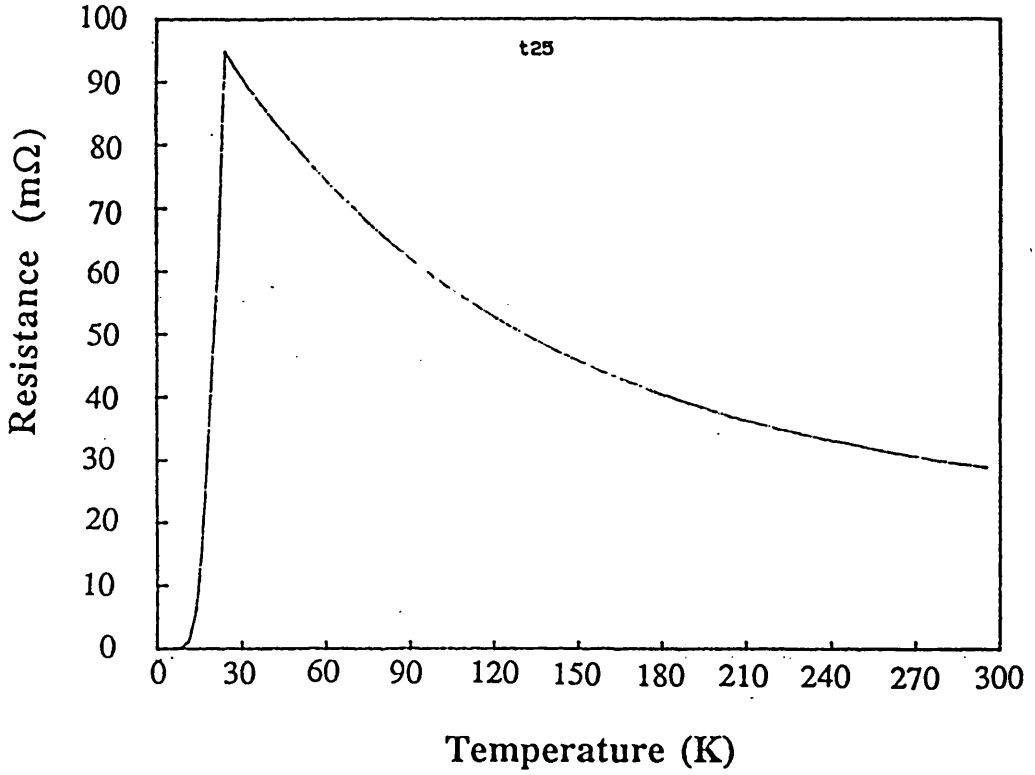

Figure 7.4 Resistivity vs. temperature characteristics of a CERAMIC sample of $Nd_{1.85}Ce_{0.15}CuO_{4-y}$.

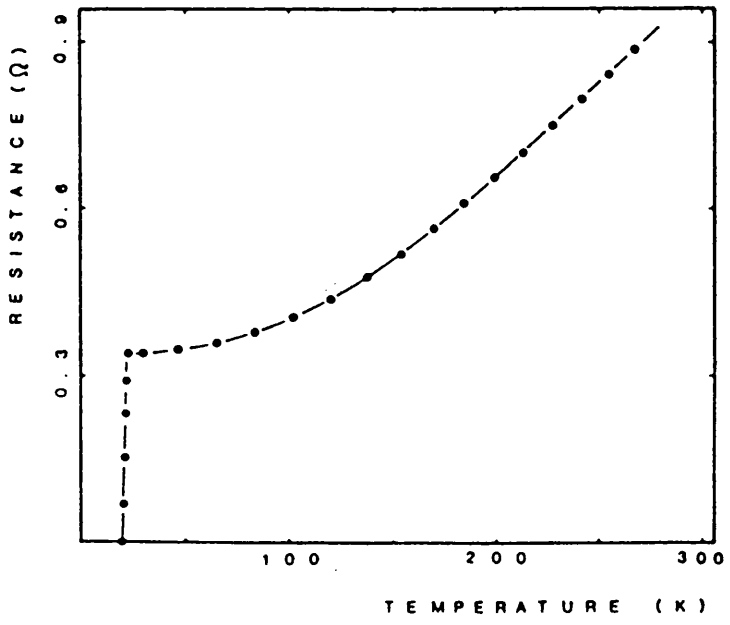

***Figure 7.5** Resistivity vs. temperature characteristics of a SINGLE CRYSTAL sample of $Nd_{1.85}Ce_{0.15}CuO_{4-y}$ [12].*

7.2 PLD of $Nd_{2-x}Ce_xCuO_{4-y}$ (results)

7.2.1 Target preparation and characterization

(a) $Nd_{2-x}Ce_xCuO_{4-y}$ target preparation:

Initial samples were prepared by simply mixing the correct stoichiometric amounts of CuO, Nd_2O_3 and CeO_2 and firing the ground mixture in air at 900°C for 24 hrs and two subsequent firing at 1050°C in air for 15 hrs with intermediate regrinds. This method produces apparently single phase materials that unfortunately displayed poor superconducting properties in that a wide transition into the superconducting state was observed. The resistance vs. temperature characteristics of a typical film using this method is shown in the insert of figure 7.6.

The main difficulty in preparing bulk ceramics of this material is obtaining a homogeneous Ce distribution; the reason being that the energy required to break the strong Ce-O bond results in very slow diffusion of this cation throughout the host Nd_2CuO_4 lattice even over very long reaction times (5-10 days) at usual furnace temperatures (≈1050°C) [13].

In order to circumvent this problem the procedure used by López-Morales et al. [13] was adopted in preparing the targets. In this approach a two-step procedure is used where a stable Nd-Ce-oxide is initially formed. The details of the method are as follows:

(1)- The compound $NdCeO_{3.5}$ is formed by grinding and mixing the correct molar amounts of Nd_2O_3 and CeO_2, followed by a heat treatment at 1400°C for ≈48 hrs in air. This assures the complete reaction of all CeO_2.

(2)- The product is then reground and mixed with molar amounts of additional Nd_2O_3 as well as CuO to achieve the desired target composition.

(3)- This mixture is fired at 980°C for ≈24 hrs in flowing oxygen.

(4)- The product is then reground, formed into a pellet (13 mm in diameter), and sintered at 1050°C, with several repetitions for a total period of ≈48 hrs, again in flowing oxygen.

(5)- The pellet is again reground and a portion of it is set aside for powder XRD analysis. The two portions are formed into pellets again and sintered for ≈24 hrs in flowing oxygen.

(6)- The 'non-XRD' pellet is annealed at 980°C for ≈30 hrs in flowing argon.

(7) Finally, the sample is rapidly quenched (≈1 min) to room temperature in flowing argon.

(b) $Nd_{2-x}Ce_xCuO_4$ target characterization

Pellets of $Nd_{2-x}Ce_xCuO_4$ with Ce concentration, $0 \leq x \leq 0.19$, were prepared by the above route and their resistance vs. temperature behaviour was characterized using four point probe resistance measurements. Superconductivity was observed in samples with Ce composition in the range of $0.12 < x < 0.19$. Figure 7.6 shows the characteristic of a bulk pellet with composition $Nd_{1.85}Ce_{0.15}CuO_4$.

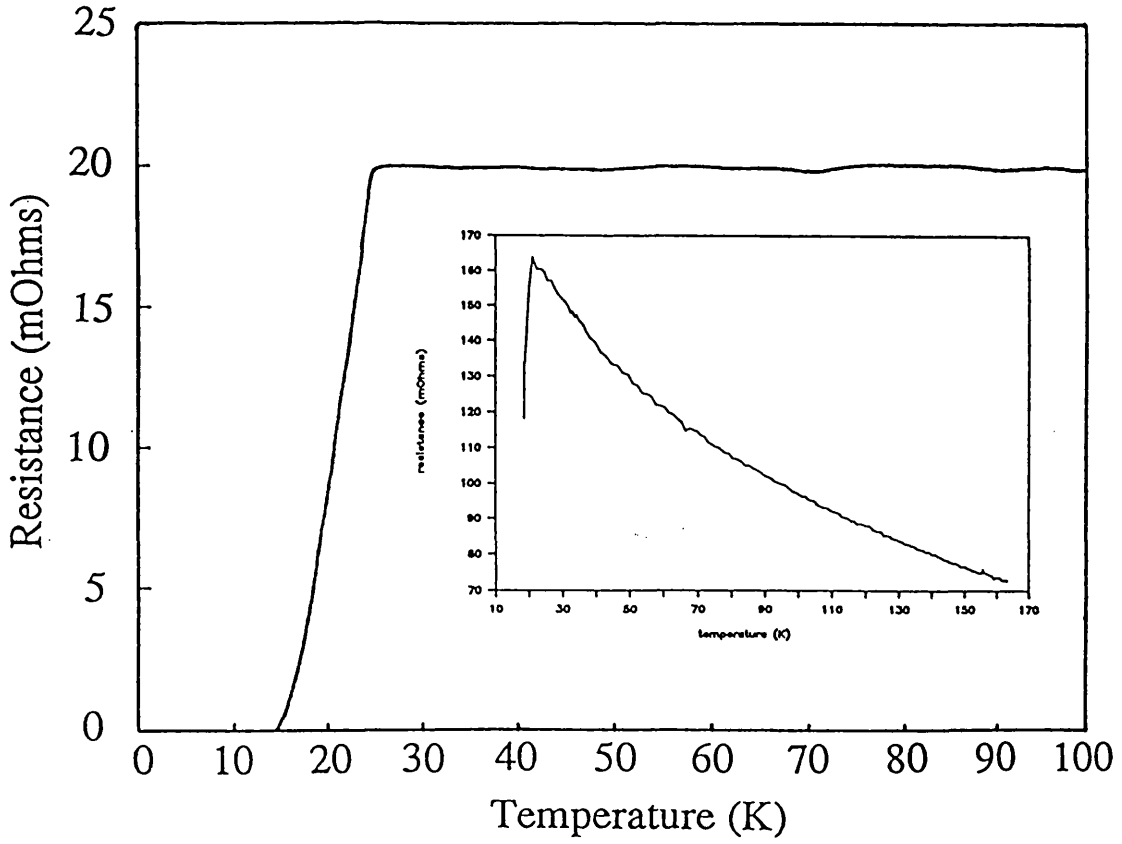

Figure 7.6 *Resistance vs. temperature characteristics of a $Nd_{1.85}Ce_{0.15}CuO_{4-y}$ bulk pellet prepared using the López-Morales et al. [13] method. Shown in the insert is the characteristics of a pellet prepared using the older method.*

As can be seen the $T_{c(onset)}$ and $T_{c(0)}$ are 24 K and 14 K respectively. The powder XRD pattern of this sample is shown in figure 7.7. This was carried out at the Department of Geology, UCL, and a Co source ($K_{\alpha 1}$: λ=1.78896 Å, $K_{\alpha 2}$: λ=1.79285 Å) was used during the measurement.

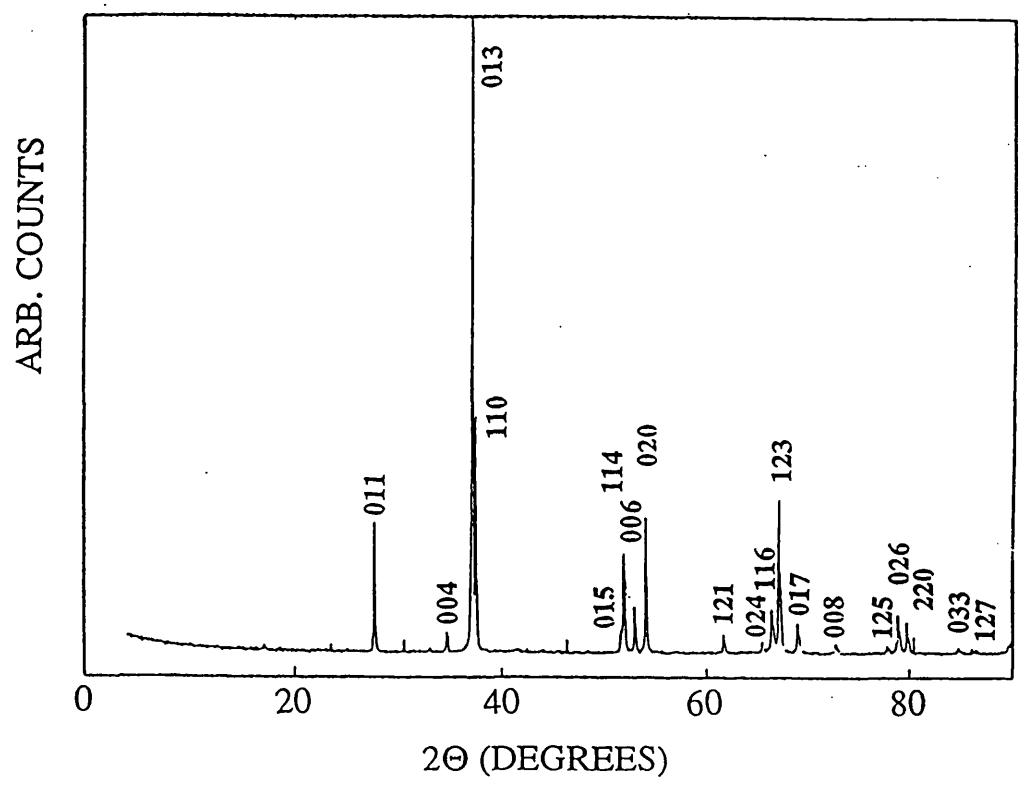

***Figure 7.7** X-ray diffraction pattern of a bulk pellet of $Nd_{1.85}Ce_{0.15}CuO_4$.*

The aim in this section is to fully characterize the pellets produced as targets for ablation. This is obviously a key objective since as previously discussed there is a narrow range of Ce stoichiometry which is compatible with the production of a homogeneous superconducting sample. One area where we would like to obtain information on concerns the possibility of any Ce segregation since Ce is a slow diffusant in Nd_2CuO_4. A secondary objective is to gain information on the variation of the *a*- and *c*- lattice parameters with Ce concentration and thus produce a comprehensive composition vs. lattice parameter map for easy identification of stoichiometry. Since we are working with powders the only method to obtain such structural information is the Rietveld refinement of XRD data.

7.2.2 Rietveld Refinement

(a) The technique:

The analysis of an x-ray diffraction pattern can be conveniently subdivided into two separate tasks. The first operation consists of assigning an *hkl* value for each particular reflection (indexing the pattern). The second operation consists of determining the area under the peak. This intensity can then be used in a structural analysis in which structural parameters, such as position of the atoms, site occupancy and temperature factors are varied via the use of least-squares procedures. This procedure is relatively facile provided that the individual reflections are well separated in 2θ (with respect to the resolution of the measuring diffractometer). Unfortunately this is only true for very simple high symmetry systems such as CeO_2, and for most materials of technological interest overlap of the individual reflections to form composite peaks occurs. The question then arises of how to distribute the area of the composite peak between the individual peaks creating the composite entity. One possibility is to simply assign the intensity in an arbitrary manner but this would be generally impossible since such a mode of operation presupposes a detailed understanding of the structure under investigation.

The problem has been addressed in an elegant manner in the work of Rietveld [14]. In this technique the problem is circumvented by refining the pattern as a whole rather than considering individual Bragg reflections. The intensity of each measured point of the diffraction pattern is included as an observation, y_i (obs), and compared with the corresponding intensity, y_i (calc), calculated via reference to a structural model. The last point is of some importance since it should be stressed that this technique is a refinement process and not an *ab-initio* structural determination technique. The key requirement for a successful application of the refinement process is the derivation of an accurate description for the shape of the individual peaks which can then be used to create the composite peak. The shape of a diffraction peak depends on several parameters such as the radiation source, the wavelength distribution in the primary beam selected by a monochromator crystal, the beam characteristics as dictated by the slits and collimator arrangements, and the detector system. The choices for peak-shape

functions are generally, Gaussian, Lorentzian, or a combination of both. The analytical expressions for these peak shapes contain variable parameters that allow their application over a range of diffraction conditions. The full width at half maximum of a peak, FWHM, and the background intensity are usually considered to vary with scattering angle.

The application of the Rietveld technique in order to obtain detailed structural information is generally a two step process. In the first stages of a refinement the intensity at any point *i* is calculated by the program from a series of given structural information obtained from the model. In the second stage these intensities are manipulated via conventional least-squares techniques. In this case however the structural analysis is performed by not only the variation of structural parameters but also the peak shape parameters and also some diffractometer parameters (such as the zero point). In the final refinement all the parameters are varied simultaneously.

The model may be refined by minimizing using a least-square process the residual,

$$M = \sum_i w_i [y_i(obs) - \frac{1}{c} y_i(calc)]^2 \qquad (7.1)$$

where w_i is given by,

$$(w_i)^{-1} = (\sigma_i)^2 = (\sigma_{ip})^2 + (\sigma_{ib})^2 \qquad (7.2)$$

σ_{ip} is the standard deviation associated with the peak, σ_{ib} is that associated with the background intensity, and c is the overall scale factor. y_i (calc) is the sum of the contributions from neighbouring Bragg reflections and from the background.

The goodness of profile fit is measured by [15],

$$R = \left[\frac{\sum_i w_i [y_i(obs) - \frac{1}{c} y_i(calc)]^2}{\sum_i w_i y_i^2(obs)} \right]^{1/2} \qquad (7.3)$$

For good experimental data the *R* value is expected to be around one percent. The profile analysis of the full diffraction pattern is often used to refine peak positions and peak heights for each reflection. From them lattice parameters are calculated and refined. Peaks generated by the overlapping of more reflections are deconvoluted and integrated intensities of individual *hkl* are calculated, together with their standard deviations and their correlations.

(b) Experimental conditions:

The samples of $Nd_{2-x}Ce_xCuO_4$ were synthesised using the method outlined earlier and were annealed in oxygen, ground, and pressed into a pellet on several occasions.

The experimental set-up used was kindly provided by Dr. I.Wood, Department of Geology, UCL, who also collaborated in the analysis of the data. It consisted of a standard Philips PW 1050 vertical powder goniometer. The radiation used was from an Iron filtered Co K_α source (K_{α_1}: λ=1.78896 Å, K_{α_2}: λ=1.79285 Å) and the beam was processed via a divergence / receiving / antiscatter slit assembly. All data points were collected at room temperature between 2θ angles 3 to 80° in steps of 0.01°. The region between 3 and 25° was excluded from the refinement due to the non-linear background. The data was analysed using the program LHPM 1 written by Wiles and Young [16] and updated by Howard and Hill [17]. The form factors used for the elements were standard non-ionized values taken from table 2.2B, *"International Tables for X-ray Crystallography"*, vol. IV (Kynoch Press). In all refinements the peak shape was approximated using a pseudo-Voigt function which is a mixture of Gaussian and Lorentzian profiles. The model used in the refinement was taken from the work of E.F.Paulus et al. [18]. It should be noted that in the case of this investigation an oxygen stoichiometry of 4 was assumed. It is not believed that this would bias the results since compared with the heavy scattering cations, the amount of scattering by the light scattering extra oxygen fraction will be insignificant. In the final refinement all structural and refinement parameters were refined until all calculated (shift / e.s.d.) were < 0.1. In all cases the refinement proceeded smoothly to good final R-factor with χ (R/R_{exp}) values of the order of 1.4 being routinely obtained. In all refinements no significant (>3 σ) deviation from the inputted Ce stoichiometry was observed and this coupled with no observable extraneous peaks led to the conclusion

that the Ce concentration is in fact the expected synthetic value. Refinements were performed in which whilst the overall occupancy of the mixed occupancy site was observed the relative starting occupancies were inputted at values far different from the correct ones. In all cases the refinement of the site occupancy restored the expected synthetic values.

A second major objective of this study was to produce a comprehensive composition vs. lattice parameter map for easy identification of stoichiometry. This information is conveyed in table 7.2 and figure 7.8. For comparison purposes we have included in table 7.2 the data of Paulus et al. at compositions for which they have reported data.

Table 7.2 *Effect of variation in Ce concentration on the lattice constants. The values in italic correspond to reference [18].*

Ce concentration (x)	a-lattice constant (Å)	c-lattice constant (Å)
0.00	3.9433(1)	12.1609(5)
0.05	3.9444(1) *3.9435(2)*	12.1316(4) *12.1272(10)*
0.10	3.9451(1) *3.9435(3)*	12.1098(4) *12.1048(12)*
0.13	3.9455(1)	12.0936(4)
0.135	3.9459(1)	12.0846(5)
0.14	3.9464(1)	12.0794(5)
0.15	3.9463(1) *3.9457(2)*	12.0797(4) *12.0764(9)*
0.16	3.9463(1)	12.0771(4)
0.165	3.9463(1)	12.0767(4)
0.175	3.9464(1)	12.0757(5)
0.18	3.9463(1)	12.0746(5)
0.19	3.9466(1)	12.0738(5)

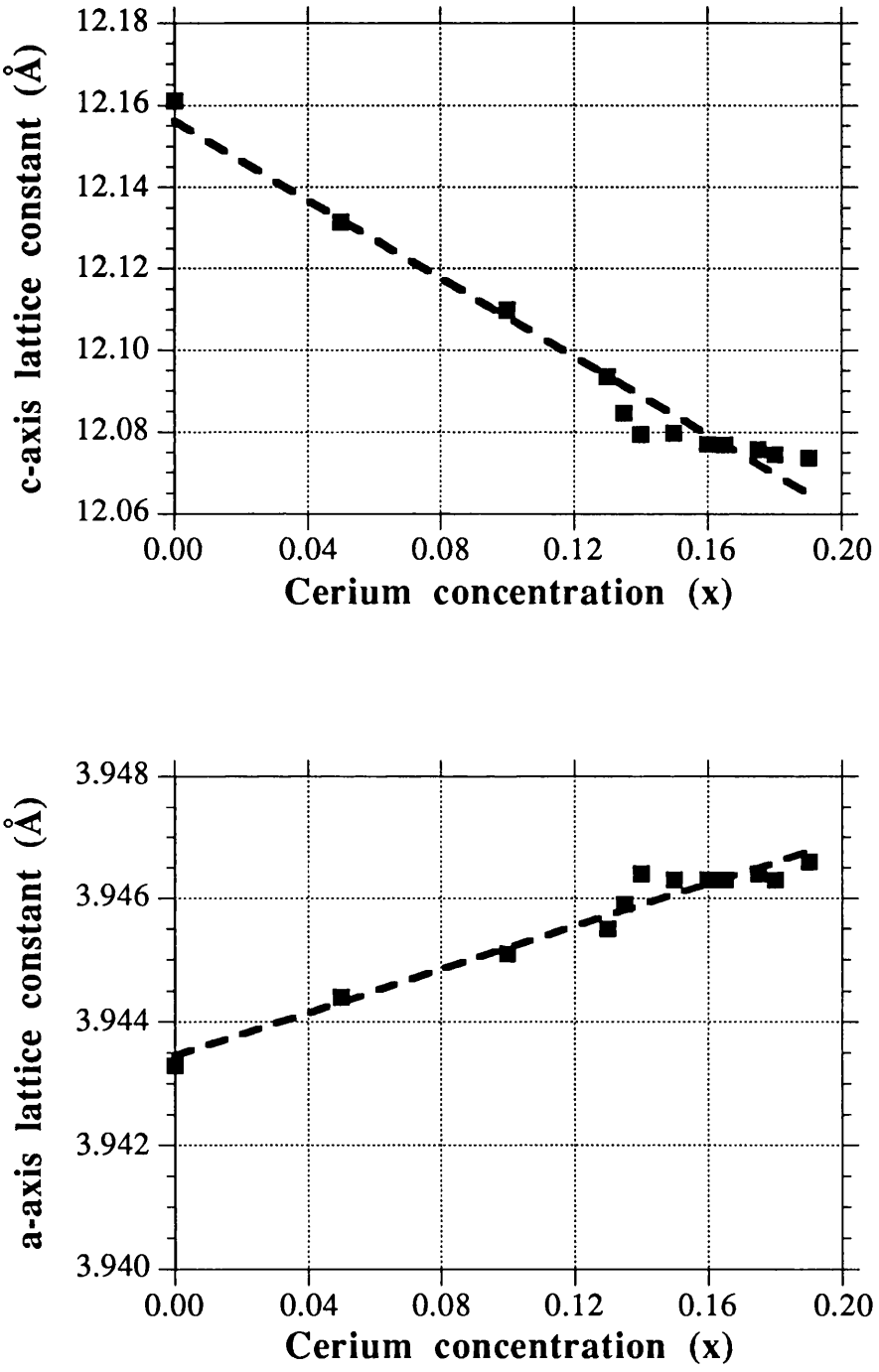

Figure 7.8 *a- and c-axis lattice constants vs. Ce concentration, x, after Rietveld refinement performed on XRD patterns of $Nd_{2-x}Ce_xCuO_4$ powders. For clarity the error bars listed in table 7.2 are omitted.*

7.2.3 Thin film growth of $Nd_{1.85}Ce_{0.15}CuO_{4-y}$

The basic conditions for all the thin films grown in the following sections were similar and so for clarity the basic experimental configuration is outlined at this point. The films were deposited on single crystal substrates of MgO(100), from a rotating target with composition $Nd_{1.85}Ce_{0.15}CuO_{4-y}$. Depositions were made using either the frequency doubled Nd:YAG laser operating at 532 nm with a pulse duration of 4 ns at 5 Hz or the KrF excimer laser operating at 248 nm with a pulse duration of 20 ns at 5 Hz. The experimental set-up for thin film deposition was described earlier in section 5.1. The distance between the target and substrate was kept at ≈4 cm and the angle between the incident laser beam and the normal to the target was 25°. The target was smoothened prior to deposition using an emery paper, followed by blowing the surface with nitrogen to remove residual particles. The substrates were degreased in acetone and methanol prior to deposition. In this section both the *ex-situ* and *in-situ* growth of $Nd_{1.85}Ce_{0.15}CuO_{4-y}$ thin films are described. Energy dispersive x-ray analysis, EDX, electron-probe micro-analysis, EPMA, x-ray diffraction, XRD, and resistance-temperature measurements were carried out to characterize the samples.

7.2.3.a Film stoichiometry

Before proceeding to the actual film growth it is essential to analyse the chemical composition of the as-deposited films to check for stoichiometric transfer of material from target to substrate. This is important due to the narrow range of Ce concentration for which superconductivity occurs.

(a) Stoichiometry deposited using the Nd:YAG laser:

Films were deposited under vacuum at different laser energy densities (varied by the aid of neutral density filters) and the resulting chemical compositions were investigated using EDX. The values, displayed in figure 7.9, are the average of measurements performed at four different points on the sample.

It is difficult to make definitive statements about the relative stoichiometry produced under these conditions since unfortunately the EDX technique is prone to large errors. These errors can range as high as 10%, thus in reference to figure 7.9 natural caution only permits us to state that over the range of laser energy densities shown, there seems to be an excess of Nd and Ce and a shortage of Cu in these films. However, the 10% error would easily cross over the ideal values which have been taken by normalizing the total atomic percentages of cations to 100, resulting in the ratios: Nd 61.67%, Ce 5%, and Cu 33.33% in the case of $Nd_{1.85}Ce_{0.15}CuO_{4-y}$. Due to the narrow range of Ce concentration required for these materials to superconduct a more sensitive technique is necessary.

(b) Stoichiometry deposited using the excimer laser:

To check the chemical composition, a series of films were grown using the excimer laser at different laser fluences under vacuum and under an oxygen partial pressure, P_{O_2}, of $4x10^{-1}$ mbar. A JOEL JXA - 8600 EPMA Spectrometer operating in the wavelength dispersive mode was used to probe the stoichiometry of these samples. The results of these investigations are displayed in figure 7.11. The values were taken from four different points on the sample and the average is shown in these graphs. This technique is expected to be more accurate than EDX, since it analyses each element separately rather than simultaneously as in the case of EDX analysis. This is particularly useful in differentiating between elements with close atomic numbers such as Nd and Ce. By referring to figure 7.11 it therefore seems that in the films grown under vacuum there are significant deviations away from the ideal values across all laser fluences. In contrast, the addition of an oxygen partial pressure to the deposition conditions results in atomic percentages for Nd, Ce and Cu that approach the desired value and error bars of 5% (not shown here to avoid confusion) would easily cross over the ideal case. Thus the key result arising from the above analysis is that at laser fluences in the region of 1 to 4 J/cm^2 the introduction of oxygen allows reasonable stoichiometric transfer between the target and substrate.

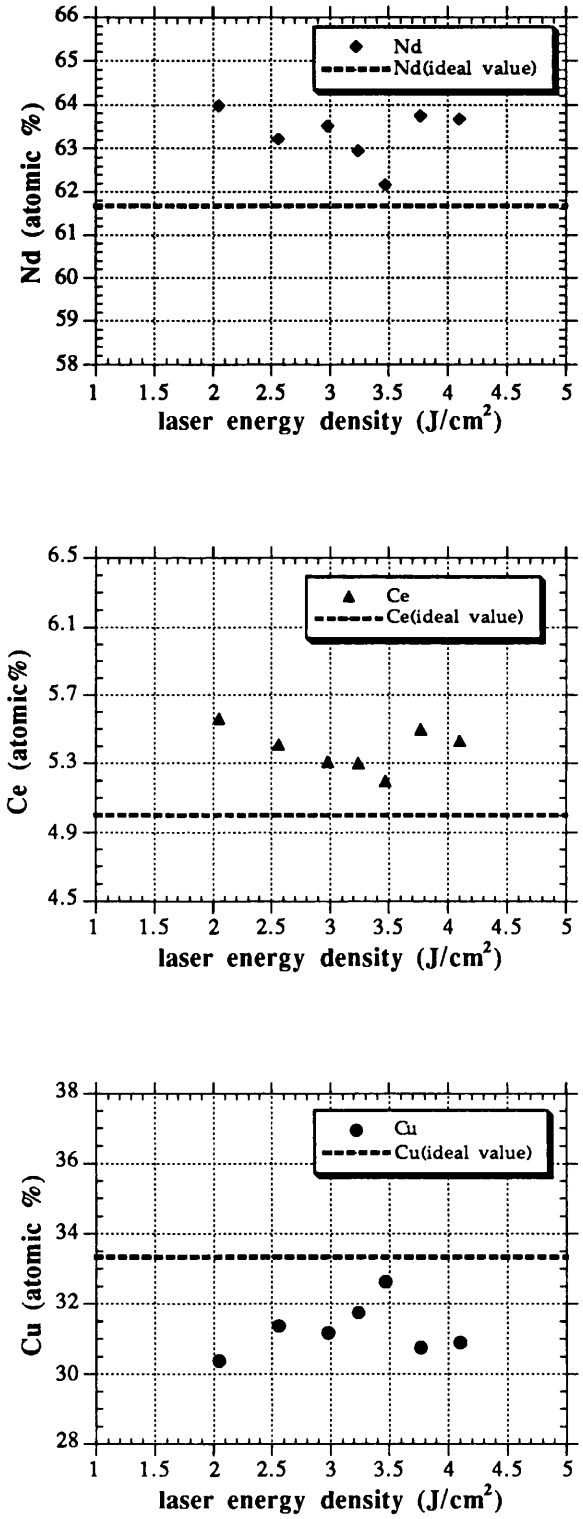

Figure 7.9 *Atomic % of Nd, Ce and Cu in films deposited in vacuum at different fluences from a target of $Nd_{1.85}Ce_{0.15}CuO_{4-y}$, using the Nd:YAG laser (532 nm).*

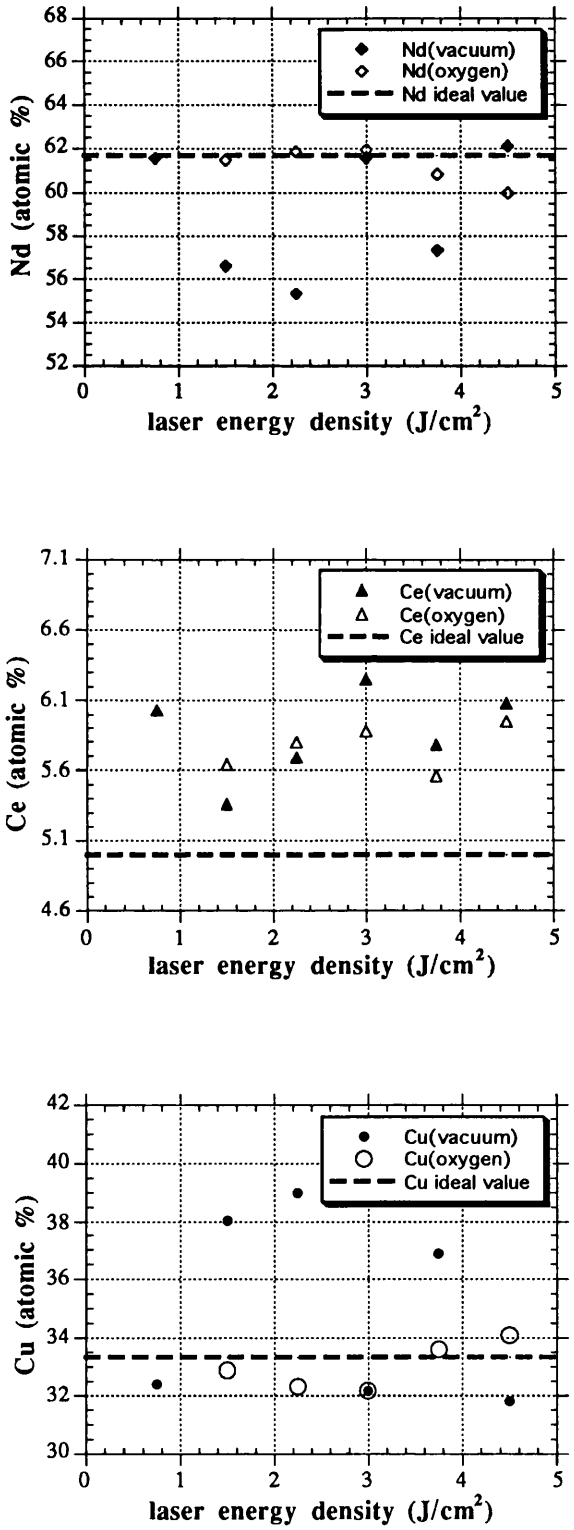

Figure 7.10 *Atomic % of Nd, Ce and Cu in films deposited in vacuum or in a P_{O_2} of $2x10^{-1}$ mbar at different fluences from a target of $Nd_{1.85}Ce_{0.15}CuO_{4-y}$, using the excimer laser (248 nm).*

7.2.3.b Ex-situ growth of $Nd_{1.85}Ce_{0.15}CuO_{4-y}$ thin films

A two part strategy was adopted to the *ex-situ* growth of films in that it was intended in step (a) to obtain *c*-axis oriented stoichiometric films that are then in step (b) reduced to create superconductivity.

(a) Growth using the Nd:YAG laser:

The deposition conditions used were those outlined in the previous section with the laser delivering an energy density of $3J/cm^2$ and the deposition occurring on substrates held at room temperature at a P_{O_2} of $4x10^{-1}$ mbar. The XRD pattern of a typical film grown by depositing from a target of $Nd_{1.85}Ce_{0.15}CuO_{4-y}$, followed by annealing at 1050°C in oxygen for 45 min is shown in figure 7.10.

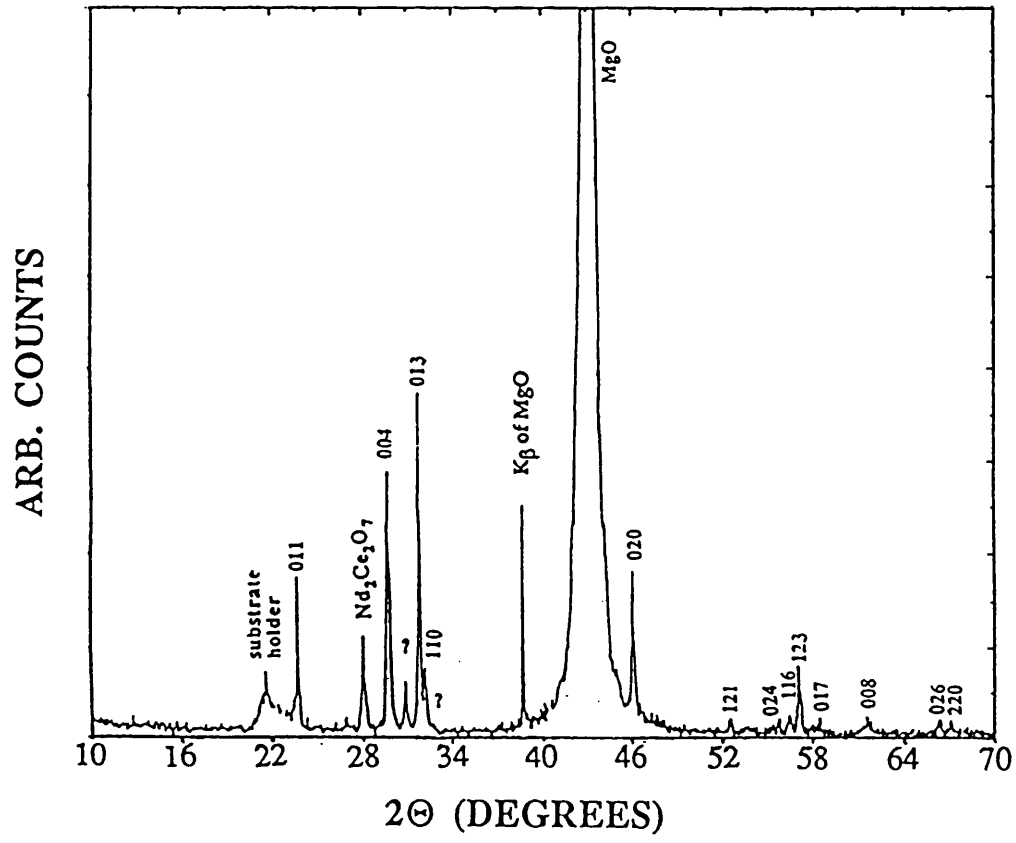

Figure 7.10 *XRD pattern of a $Nd_{2-x}Ce_xCuO_4$ film deposited using the Nd:YAG laser after a 45 min anneal in oxygen.*

This was carried out at the Department of Crystallography, Birkbeck College, and a Cu K_α source ($K_{\alpha1}$: λ=1.5406 Å, $K_{\alpha2}$: λ=1.5444 Å, K_β: λ=1.3922 Å) was used during the measurement.

As can be seen apart from the peaks expected for the desired phase, there are a number of other peaks indicating the presence of impurities in this sample. Two of the peaks seem to be due to $Nd_2Ce_2O_7$ (JCPDS No: 28-267), but the other peak does not correspond to any reflection of the standard combinations of Nd_2O_3 and CeO_2 and CuO in the JCPDS files. The presence of these peaks may be attributed to a solid solution of Nd_2O_3 and CeO_2. However, there would need to be large changes in the relative intensities of the reflections for this scenario to be correct. Such a solid solution has also been invoked by Horwitz et al. [20] to explain unidentified reflections in their XRD patterns. It must be pointed out that to date no such solid solution has been isolated in phase equilibria studies. Thus the identity of this peak remains an intriguing problem which will require further detail study. It should be noted that the existence of Nd_2CeO_7 is consistent with the excess Nd_2O_3 and CeO_2 observed in the EDX stoichiometry studies.

(b) Growth using the excimer laser:

The deposition conditions used were those outlined in the previous section with the laser delivering an energy density of 3 J/cm^2 and the deposition occurring on room temperature substrates at a background pressure of $2x10^{-1}$ mbar.

In figure 7.11 the XRD patterns of the deposited films after they have been annealed in oxygen are shown. Again a Cu K_α source was used during the XRD measurements. The peaks are normalized with respect to the [006] peak. The films were annealed for different periods of time under oxygen. When comparing the film (excimer) annealed for 45 min to the one in figure 7.10, it can be seen that the impurity peaks are greatly reduced. The patterns show that as the annealing time is lowered from 90 min to 30 min the impurity peaks are suppressed resulting in a single phase, although poly-crystalline film of $Nd_{2-x}Ce_xCuO_4$.

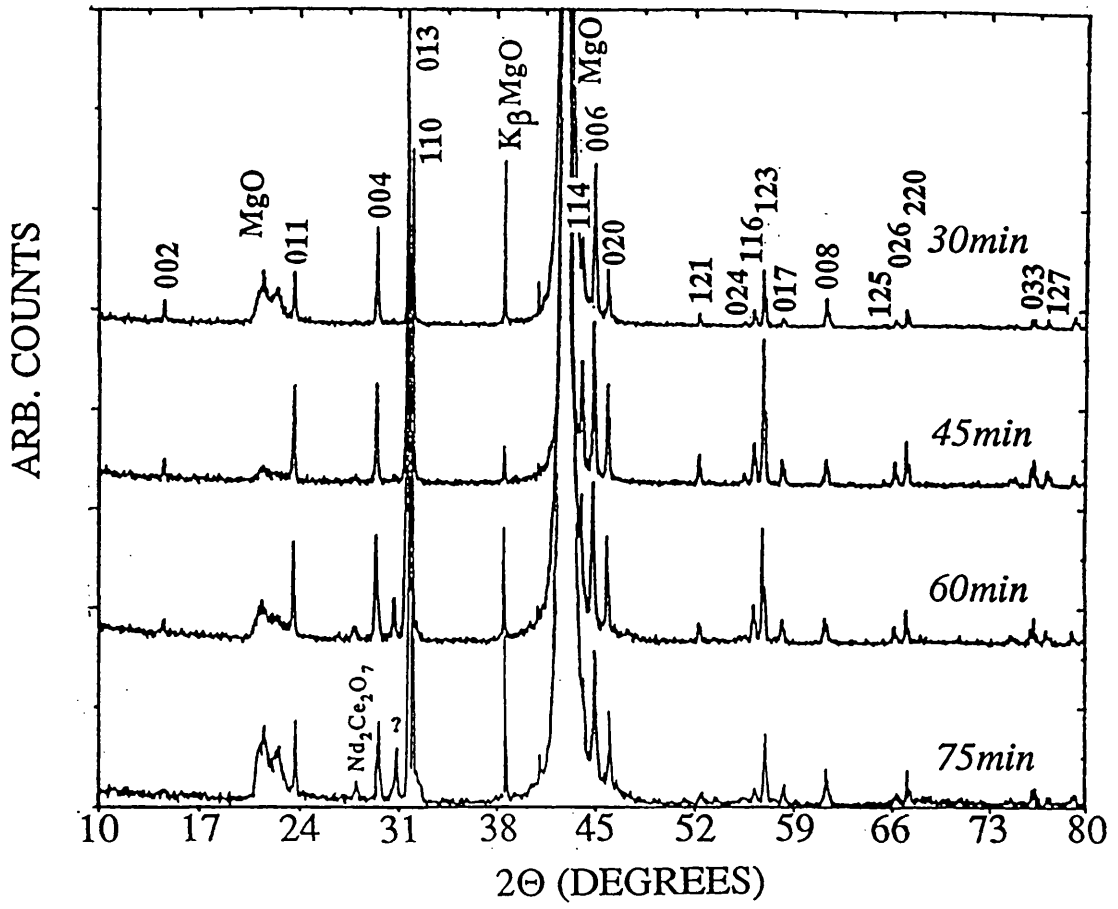

Figure 7.11 *XRD patterns of $Nd_{1.85}Ce_{0.15}CuO_4$ films after annealing in oxygen at 1040°C for different periods of time. All the films were ≈5000Å thick.*

The next objective is obviously to produce oriented films and to this effect films with different thickness were grown in order to study their effect on crystal ordering. It can be seen from figure 7.12 that as the thickness was lowered, the film became more textured until at ≈2000 Å only small traces of non-00*n* peaks were apparent. A high 00*n* orientation meant that the film was highly textured with the *c*-axis perpendicular to the substrate surface.

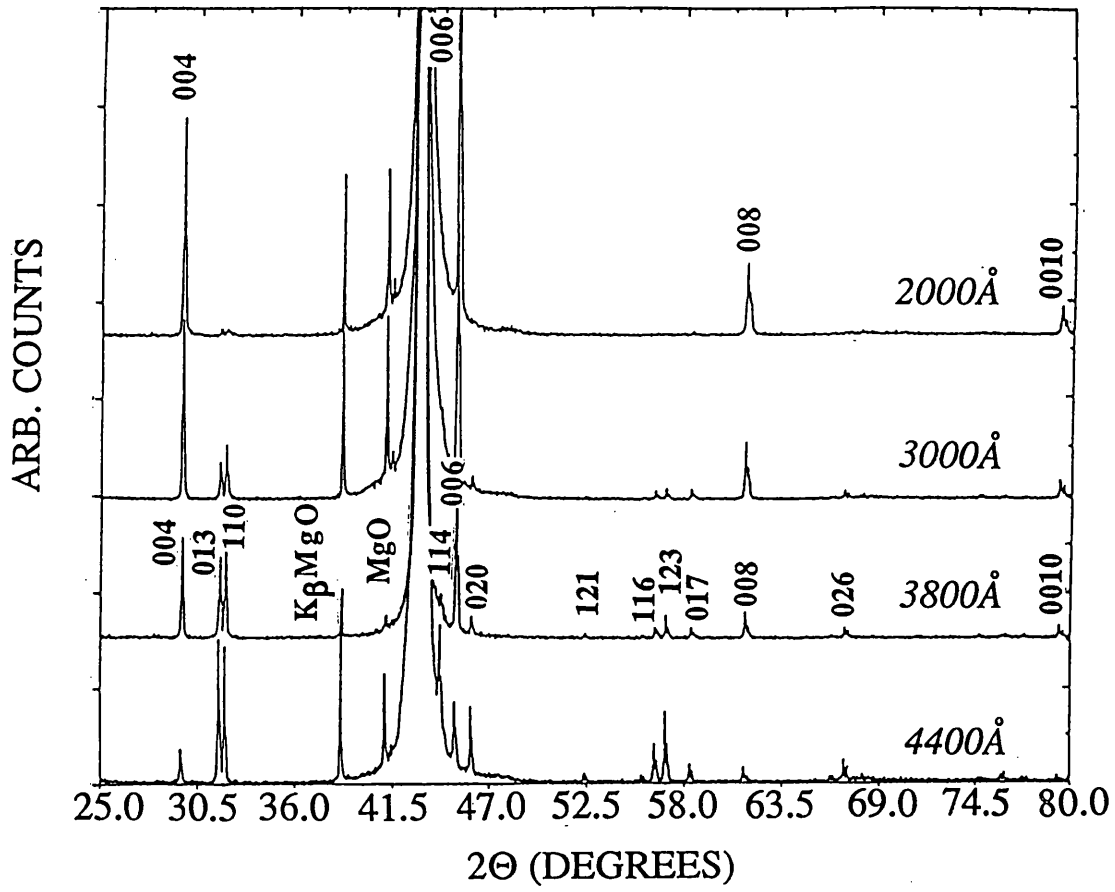

Figure 7.12 *XRD patterns of $Nd_{1.85}Ce_{0.15}CuO_4$ films with different thickness. All as-deposited films were annealed in oxygen at 1040°C for 30 min.*

A longer term objective of this study is the *in-situ* growth of films and obviously a shorter annealing time is preferred. A series of experiments were performed in order to investigate the lower limit of the annealing time and as shown in figure 7.13 high quality *c*-axis oriented films are possible with an anneal of only 3 1/2 min.

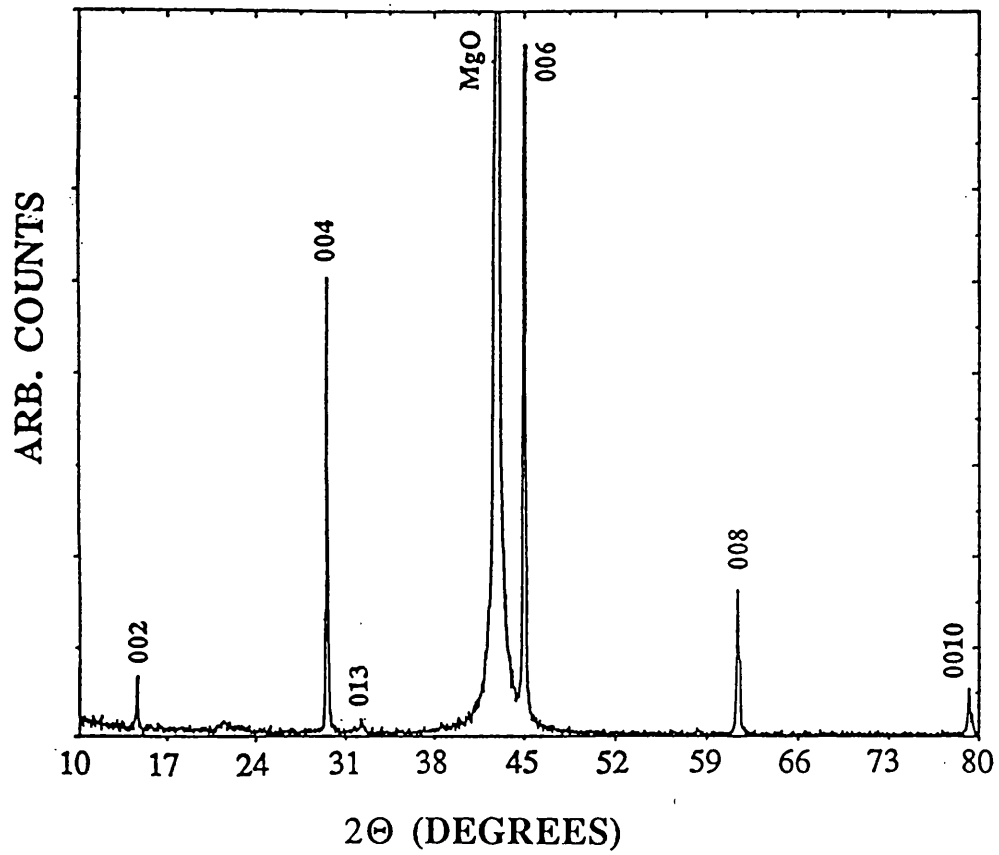

Figure 7.13 *XRD pattern of an ex-situ grown $Nd_{1.85}Ce_{0.15}CuO_4$ film post-annealed in oxygen for 3 1/2 min. The film was ≈1500 Å thick.*

Having produced a highly *c*-axis oriented single phase film the next step is to render it superconducting by post-annealing in argon, in order to effect the reduction. The post-annealing temperature or time are crucial during the reduction process. There is a critical trade off between the temperature and partial pressure of oxygen which dictates that either the film changes oxidation states or decomposes into a multi-phase mixture. Experiments were performed in which films were annealed under flowing argon for periods of time between 5 min and 1.5 hrs. As can be seen in figure 7.14 a reduction in argon does not result in any decomposition and only seems to alter the crystal ordering to a minor extent.

The resistance vs. temperature characteristic of the reduced films were measured using the four point probe technique. The films did not possess any superconducting characteristics and in fact displayed semiconducting behaviour at all temperatures down to 12 K as is shown in figure 7.15.

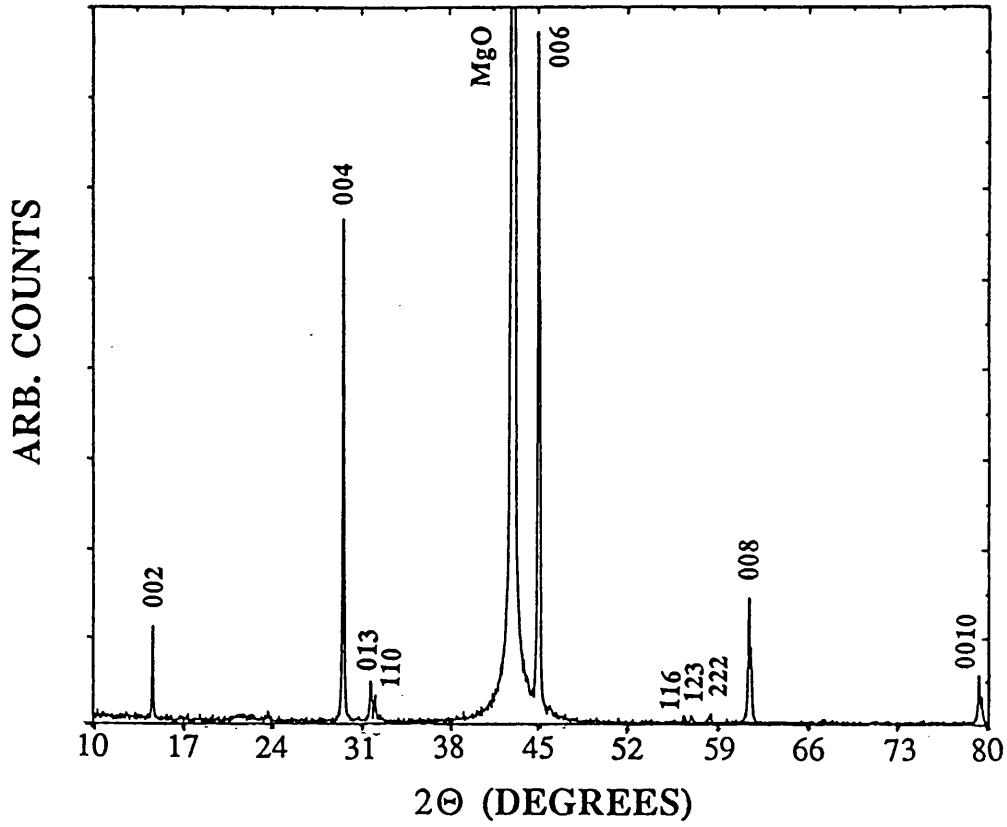

Figure 7.14 *XRD pattern of an ex-situ grown $Nd_{1.85}Ce_{0.15}CuO_{4-y}$ film after annealing in flowing argon at 900°C for 45 min.*

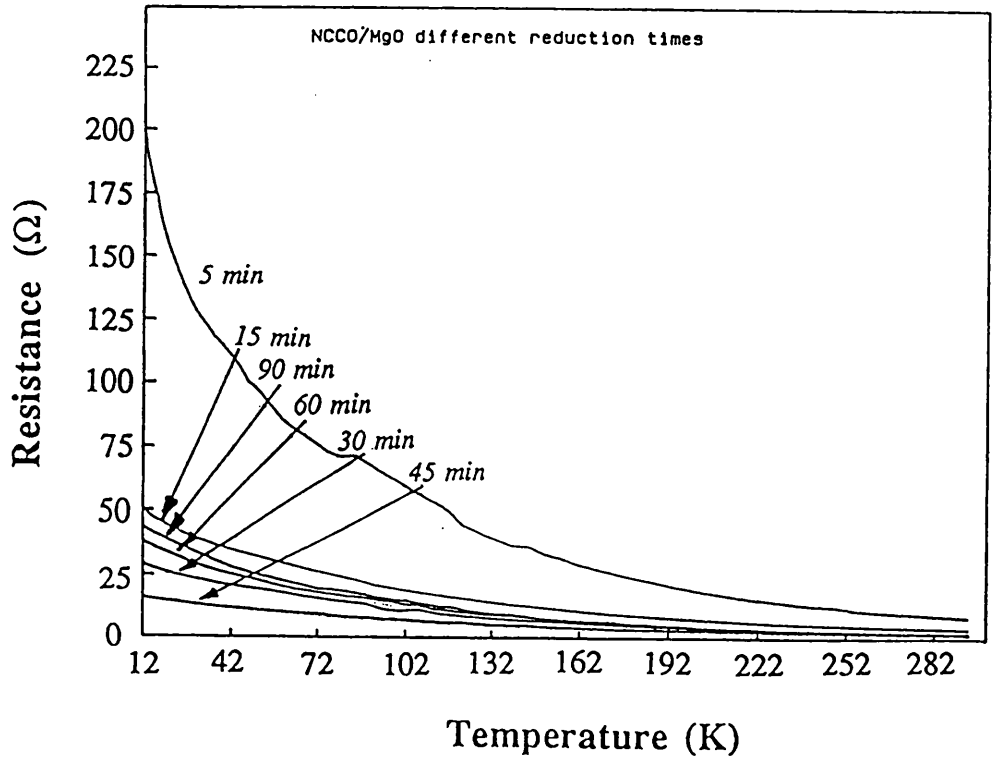

Figure 7.15 *Resistance vs. temperature characteristics of ex-situ grown $Nd_{1.85}Ce_{0.15}CuO_{4-y}$ films annealed for different periods of time in flowing argon.*

It is not clear at the moment why superconducting films are not produced. The problem of the concentration of the Ce may be one reason. If films within the narrow range of Ce stoichiometry that create superconductivity are not produced then obviously films with semiconducting behaviour are obtained. Such a deficiency could be due either to a non-stoichiometric transfer of the material during the ablation process or alternatively in the subsequent heat treatments Ce is locked into alternative phases.

7.2.3.c *In-situ* growth of $Nd_{1.85}Ce_{0.15}CuO_{4-y}$ thin films

The basic experimental configuration was that discussed in an earlier section. However, it should be noted that *in-situ* growth of $Nd_{1.85}Ce_{0.15}CuO_{4-y}$ films was carried out using the excimer laser only. As a benchmark for *in-situ* film growth, a film of the parent Nd_2CuO_4 material was initially deposited. The conditions used were a T_s of 700°C and a P_{O_2} of $4x10^{-1}$ mbar. Following deposition the sample was cooled down under the same P_{O_2} at 20°C/min to 300°C and the heater was then switched off. A *c*-axis oriented film was obtained. Having successfully grown the parent material the growth of the doped material from a target of $Nd_{1.85}Ce_{0.15}CuO_{4-y}$ was attempted. A T_c of 800°C was maintained during deposition and by consideration of the results obtained in the stoichiometric transfer section the choice of background partial pressure and laser energy density were rationalized to be $4x10^{-1}$ mbar and 4 J/cm^2 respectively. It should be noted that these values are in agreement with the conditions used by Gupta et al. [19], Horwitz et al. [20] and Lu et al. [21] as can be consulted by reference to table 7.3. A deposition time of 30 min resulted in films which were ≈1200 Å thick.

Following the same post-annealing regime as that used in the case of Nd_2CuO_4 the sample was cooled to 300°C under the same P_{O_2} at a rate of ≈20°C/min and the heater was then switched off. However, in this case these conditions resulted in a transparent film whose XRD pattern consisted of low intensity unindexable peaks. It was found that an *in-situ* post-deposition annealing treatment at the same T_s and P_{O_2}, prior to sample cooling solved this problem. An annealing treatment for 20 min resulted in films that were single phase and highly *c*-axis oriented. As shown in the section on Rietveld refinement by replacing a fraction of the Nd atoms with Ce in the parent Nd_2CuO_4, a reduction in the *c*-axis lattice constant is obtained. This results in a shift of the XRD peaks as shown in figure 7.16. The XRD patterns of the Nd_2CuO_4 film and the Ce doped film were refined using a least-square method. Due to the high *c*-

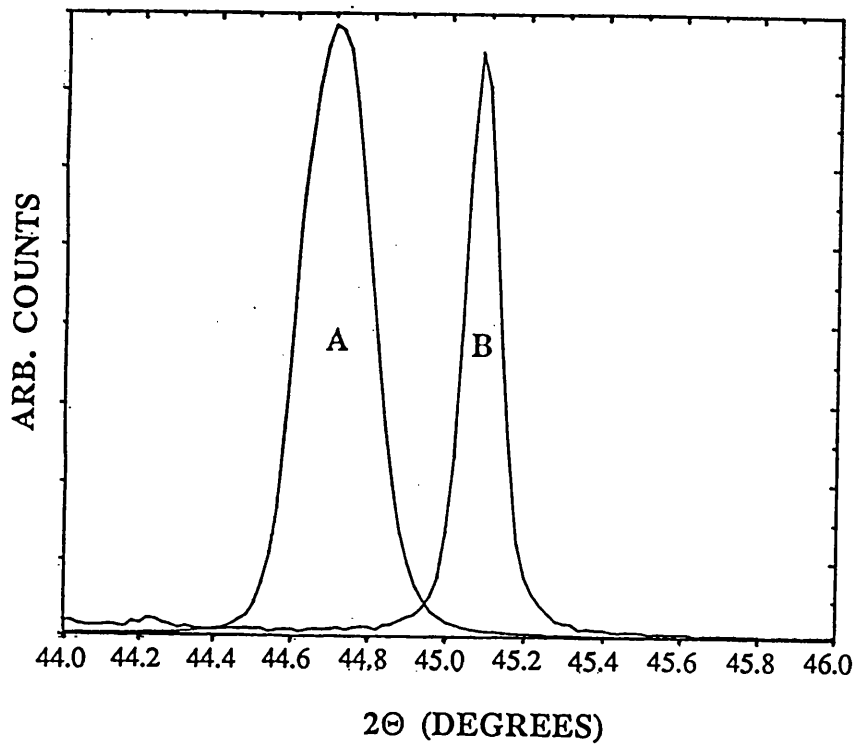

***Figure 7.16** XRD [006] peak of an in-situ grown film deposited from a target of : A - Nd_2CuO_4, and B - $Nd_{1.85}Ce_{0.15}CuO_{4-y}$.*

axis orientation, the value for the *a*-axis lattice constant was kept constant. The initial values of *a*- and *c*-axis lattice constants for Nd_2CuO_4 and $Nd_{1.85}Ce_{0.15}CuO_4$ were taken from the JCPDS file No 24-777 and table 7.2 respectively. The resulting values of *c*-axis lattice constant were 12.157(3) Å for Nd_2CuO_4 which compares well with the JCPDS value of 12.1595 Å, and 12.074(6) Å for $Nd_{2-x}Ce_xCuO_4$. By taking the standard deviation ($\pm 1\sigma$) into account the resulting lattice parameter range when referred to table 7.2, indicates a corresponding stoichiometry range of $0.14 \leq x \leq 2.0$. This figure in conjunction with the results from EPMA studies lead us to conclude that films with a stoichiometry consistent with the production of superconducting samples could be grown. Thus the key result of this section is that highly *c*-axis oriented film with the correct stoichiometric range could successfully be grown.

The next stage was to anneal the film in a reducing atmosphere. The method used by Lu et al. [21] was adopted whereby the samples were cooled down to ≈600°C and kept under vacuum for a period of time which depended upon the film thickness. This was followed by switching off the substrate heater to rapidly cool down the sample. For a 5000 Å thick film, Lu et al. found an annealing time of 4 hrs to produce the best

results. This meant that a shorter annealing time was required in the case of this project where the film thickness was ≈1200 Å. A series of experiments were performed in which the *in-situ* grown films were annealed under a vacuum of $1x10^{-3}$ mbar at 600°C for times varying between 45 and 105 min.

The reduction step did not seem to decompose or alter the film crystal orientation. However, although the reduced films were much more conductive at room temperature than the non-reduced ones, the resistance-temperature characteristics, shown in figure 7.17 did not reveal any sign of superconductivity and similar to the case of *ex-situ* growth displayed a semiconducting behaviour. Also deposition from targets with lower and higher Ce content, i.e. $Nd_{1.86}Ce_{0.14}CuO_{4-y}$ and $Nd_{1.84}Ce_{0.16}CuO_{4-y}$ did not improve the situation.

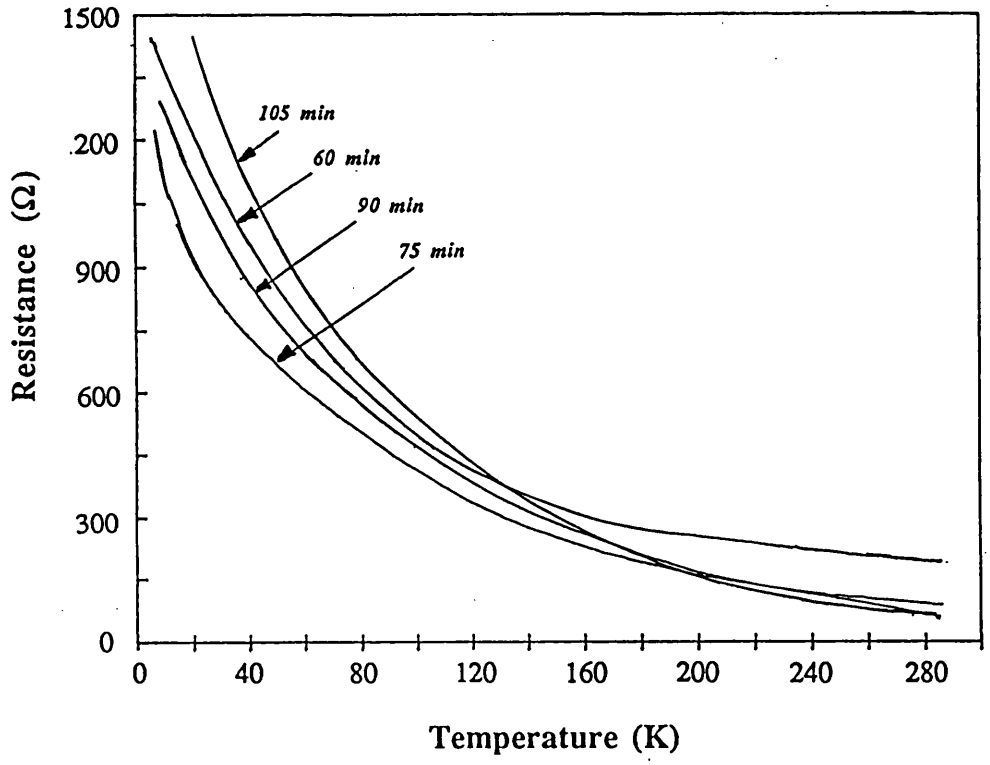

Figure 7.17 *Resistance vs temperature characteristics of in-situ grown films of $Nd_{1.85}Ce_{0.15}CuO_{4-y}$ annealed at 600°C under a vacuum pressure of ≈$1x10^{-3}$ mbar for periods of time varying between 45 and 105 min, following a post-anneal for 20 min at deposition temperature and pressure. The behaviour for a 45 min anneal was an order of magnitude more resistive and is therefore not shown here.*

Table 7.4 *Experimental conditions of research groups who succeeded in growing* $Nd_{1.85}Ce_{0.15}CuO_{4-y}$ *superconducting films by PLD.*

Group	Laser used	Laser conditions	substrate used	T_s (^oC)	Type and pressure of reactive gas during deposition	temperature and period of annealing in vacuum (^oC, min)	$T_{c\,(onset)}$, $T_{c\,(0)}$ (K)
Gupta et al [19]	Nd:YAG (355 nm)	4.5 Hz, 3.5 J/cm^2	$SrTiO_3$	780	O_2, 2 x 10^{-1} mbar	780, 45	21, 20
Horwitz et al [20]	excimer (248 nm)	5 Hz, 2 J/cm^2	$SrTiO_3$, MgO	900	O_2, 3 x 10^{-1} mbar	cooled down from 900 to 300^{o}C in 40 min	15, 11
Lu et al [21]	excimer (308 nm)	2 Hz, 2J/cm^2	$SrTiO_3$	780	O_2, 4 x 10^{-1} mbar	600, 240	21, 19
Kussmaul et al (Gupta) [22]	Nd:YAG (355 nm)	4 Hz, 3.5 J/cm^2	$SrTiO_3$	820	N_2O, 3.2 x 10^{-1} mbar	820, 30	20, 18.5
Mao et al [23] (Venkatesan)	excimer (248 nm)	10 Hz,	$SrTiO_3$, $LaAlO_3$	800	N_2O, 3 x 10^{-1} mbar	800, 10	23, 22.4

As discussed in the previous sections considerable inroads were made into the initial objective of growing $Nd_{1.85}Ce_{0.15}CuO_{4-y}$. Unfortunately whilst highly *c*-axis oriented single phase films could be grown, superconductivity could not be achieved in any film. The experimental conditions of the groups of Gupta et al., Horwitz et al., and Lu et al. who have successfully grown superconducting films are listed in table 7.4. As can be seen the conditions used by these groups do not vary in any major respect from those used in this thesis. In addition the ablation targets were fully characterized and hence it is not believed that they have caused any problem. The first possible deficiency that must be addressed concerns the correct transfer of stoichiometry from target to the films. The elucidation of the film stoichiometry is a tricky operation due to the difficulty in differentiating between Nd and Ce. There is no single technique that can deliver an unequivocal answer to this problem and hence this problem has been addressed via the application of both EPMA and lattice parameter mapping techniques. A consistent picture emerges from these studies in the sense that both techniques indicate that even if exact stoichiometric transfer has not been achieved the film composition is still within the boundaries that are consistent with the generation of superconductivity. The second possible deficiency concerns the oxidation states of Ce and Cu which are also key players in creation of superconductivity. Further reference to table 7.4 shows that the choice of conditions was again sensible and within the range used by groups. It should be noted at this point that a number of other groups also experienced difficulty in rendering the films superconducting. Results equivalent to those discussed in this chapter have been reported by Leppavouri et al. [24]. In additional discussions with A.Gupta and T.Venkatesan it became clear that films grown in oxygen displayed variable quality and only when the growth medium was changed to the more oxidizing N_2O reproducible results were obtained. Unfortunately time constraints meant that the growth of films using the above conditions with N_2O as the background gas was not attempted.

7.3 Conclusion

In the beginning of this chapter the structure and basic properties of $Nd_{2-x}Ce_xCuO_{4-y}$ were outlined. Bulk superconducting pellets of this material were prepared and characterized, and the effect of variations in Ce concentration on the lattice parameters was investigated using XRD and Rietveld refinement. Thin films of $Nd_{2-x}Ce_xCuO_4$

were *ex-situ* grown using either the frequency doubled Nd:YAG laser (532 nm) or the KrF excimer laser (248 nm). However only deposition using the excimer laser resulted in a single phase film, which was comparable with the results obtained from stoichiometric studies. By reducing the film thickness from ≈5000 Å to ≈2000 Å, highly *c*-axis oriented film were obtained. Unfortunately the films were not superconducting after a post anneal in argon for different periods of time. Highly *c*-axis oriented single phase films were *in-situ* grown at a P_{O_2} of $4x10^{-1}$ mbar and a T_s of 800°C by from a target of $Nd_{1.85}Ce_{0.15}CuO_{4-y}$. By least-square refining the XRD pattern of a typical film the resulting lattice parameter range indicated the chemical composition to fall within the range required to generate superconductivity. However, this was not realised when the films were post-annealed in vacuum at 600°C for various periods of time. This has been attributed to the oxidation states of Ce and Cu which are not easily controllable using oxygen as the growth medium. A more oxidizing agent such as N_2O is believed to alleviate this problem.

References:

[1] Y.Tokura, H.Takagi and S.Uchida, *Nature*, **337**, p345, (1989).

[2] I.Felner, U.Yaron,Y.Yeshurun,E.R.Yacobi and Y,Wolfus, *Phys. Rev. B*, **40**, p11366, (1989).

[3] A.C.W.P.James, S.M.Zahurak and D.W.Murphy, *Nature*, **338**, p240, (1989).

[4] M.B.Maple, *MRS Bulletin*, **6**, p60, (1990).

[5] P.H.Hor, Y.Y.Xue, Y.Y.Sun, Y.C.Tao, Z.J.Huang, W.Rabalais and C.W.Chu, *Physica C*, **159**, p629, (1989).

[6] T.C.Huang, E.Moran, A.I.Nazzal, J.B.Torrance and P.W.Wang, *Physica C*, **159**, p625, (1989).

[7] Y.Idemoto, K.Fueki and T.Shinbo, *Physica C*, **166**, p513, (1990).

[8] H.Ishii, T.Koshizawa, H.Kataura, T.Hanyu, H.Takai, K.Mizoguchi, K.Kume, I.Shiozaki, S.Yamaguchi, *Jpn. J. Appl. Phys.*, **28**, 11, pL1952, (1989).

[9] S.Kohiki, J.Kawai, T.Kamada, S.Hayashi, H.Adachi, K.Setsune and K.Wasa, *Physica C*, **166**, p437, (1990).

[10] A.C.W.P.James, D.W.Murphy, R.M.Fleming, D.J.Werder, S.M.Zahurak, C.H.Chen, J.Chiang, , B.Batlogg and L.F.Shneemeyer, *Mat. Res. Soc. Symp. Proc.*, **169**, p177, (1990).

[11] J.G.Lee, K.V.Ramanujachary and M.Greenblatt, *Mat. Res. Soc. Symp. Proc.* **169**, p181, (1990).

[12] S.Pinõl, J.Fontcuberta, C.Miravitlles and D.McK.Paul, *Physica C*, **165**, p265, (1990).

[13] M.E.López-Morales, R.J.Savoy and P.M.Grant, *J. Mat. Res.*, **5**, 10, p2041, (1990).

[14] H.M.Rietveld, *J. Appl. Cryst.* , **2**, p65, (1969).

[15] C.Giacovazzo, in "*Fundamentals of Crystallography*", edited by C.Giacovazzo, Oxford University Press, (1992).

[16] D.B.Wiles and T.A.Young, *J. Appl. Cryst.* ,**14**, p149, (1981).

[17] C.J.Howard and R.J.Hill, *AAEC Report No. n112*, (1986).

[18] E.H.Paulus, I.Yehia, H.Fuess, J.Rodriguez, T.Vogt, J.Ströbel, M.Klauda and G.Saemann-Ischenko, *Solid State Comm.*, **73**, 11, p791, (1990).

[19] A.Gupta, G.Koren, C.C.Tsuei, A.Segmüller and T.R.McGuire, *Appl. Phys. Lett.*, **55**, 17, p1795, (1989).

[20] J.S.Horwitz, D.B.Chrisey, M.S.Osofsky, K.S.Grabowski and T.A.Vanderah, *Mat. Res. Soc. Symp. Proc.*, **191**, p223, (1990).

[21] Y.Lu, R.A.Hughes, T.Strach, T.Timusk, D.Poulin and J.S.Preston, *Physica C*, **197**, p75, (1992).

[22] A.Kussmaul, J.S.Moodera, P.M.Tedrow and A.Gupta, *Appl. Phys. Lett.*, **61**, 22, p2715, (1992).

[23] S.N.Mao, X.X.Xi, S.Bhattacharya, Qi Li, T.Venkatesan, J.L.Peng, J.Mao, R.L.Greene, D.H.Wu and S.M.Anlage, *Appl. Phys. Lett.*, **61**, 19, p2356, (1992).

[24] S.Leppavouri, University of Oulu, Finland, *Private Communication.*

Chapter 8

Growth of Zinc Oxide Thin Films by Pulsed Laser Deposition

In this chapter the *in-situ* growth of highly *c*-axis oriented ZnO thin films by PLD using the frequency doubled Nd:YAG laser (532 nm) and the KrF excimer laser (248 nm) is presented and discussed. The effect of basic deposition parameters such as laser wavelength and fluence, oxygen partial pressure, substrate temperature, and film thickness have on the crystal quality, surface morphology, deposition rate and lattice constant is demonstrated. Characterization techniques used, included x-ray diffraction, XRD, and scanning electron microscopy, SEM.

8.1 Introduction

Zinc oxide, ZnO, is a wide bandgap (Eg ≈3.2 eV) n-type semiconductor with a hexagonal wurtzite structure as shown in figure 8.1. The bonding characteristics are partially ionic, and the zinc atoms transfer some of their electrons to the oxygen atoms. Along the *c*-axis, the layer of zinc surface atoms tend to have a positive charge defining the [001] direction (often the notation [0001] is used), while the oxygen surface atoms tend to possess a negative charge defining the [00$\underline{1}$] direction (or the [000$\underline{1}$]). The values for lattice constant are *a*-axis =3.2495 Å and *c*-axis =5.2069 Å [1]. ZnO thin films are optically transparent in the visible region of the spectrum unless a stoichiometric imbalance of zinc and oxygen atoms exist, in which a hazy or milky colour can result. Its electrical properties can be modified by doping with group III elements such as In [2,3], Al [4-7], Ga [8], Li [9], B [10,11] or group IV elements such as Si, Ge, Ti, Zr ,Hf, Pb or Sn [12]. Due to its lower cost and better chemical durability compared to indium tin oxide (ITO), it is a potential candidate for use as a

transparent conductive oxide layer. When in a highly *c*-axis oriented thin film form, it exhibits high resistivity and large piezoelectric effect [13,14]. These qualities have attracted considerable interest in recent years with ZnO thin films being used in acoustoelectric devices [15], as a front electrode or a back reflector in solar cells [16,17], and gas sensors [18-20].

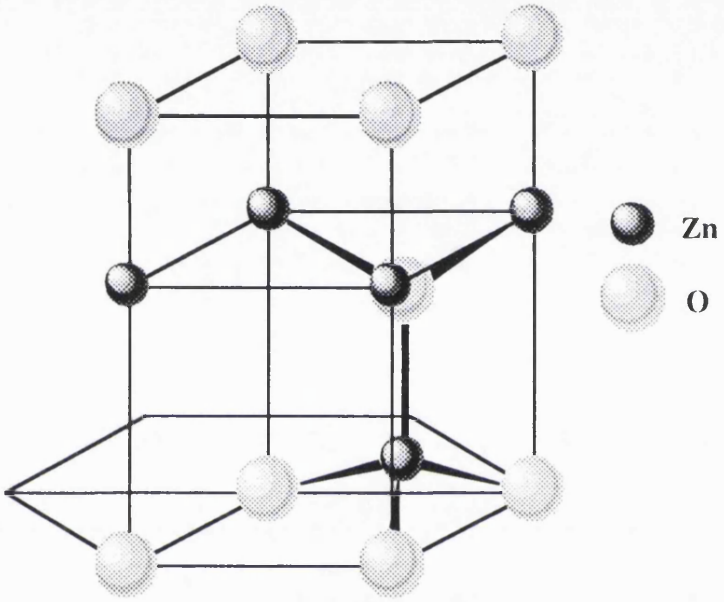

Figure 8.1 *The hexagonal wurtzite structure of ZnO. Note that the angle between the two sides is 120°.*

8.2 Thin film growth (other groups)

(a) Growth by PLD:

The first growth of ZnO thin films using PLD was reported by Sankur and Cheung [21]. A pulsed CO_2 laser operating at 10.6 μm was focused onto sintered ZnO targets thereby producing a power density of 10^4 W/cm^2. The substrates used were Si(100), Si(111), GaAs(100), GaAs(111), quartz, Corning glass 7059, sapphire (c-plane), gold or titanium films, and thermally grown SiO_2. The resulting films were *c*-axis (002) oriented with the crystallinity improving with decreased oxygen pressure, reduced deposition rate, and increased substrate temperature, T_s, in the range of 100 to 450°C. Annealing the as-grown films in air at temperatures $>T_s$ yielded stronger [002] peaks. The deposition rate was inversely proportional to growth temperature.

Maruyama et al. [22] grew thin films of ZnO on heated glass substrates at atmospheric pressure using a cw CO_2 laser. A stream of nitrogen gas was passed between the target and the substrate. The films were all *c*-axis oriented over a T_s range of 200-600°C, with small traces of the [103] peak apparent at T_s>350°C. The growth rate showed a maximum value of 20 nm/min at T_s=500°C and a nitrogen flow of 2 m/s.

To our knowledge Ianno et al. [23] are the only other group apart from UCL that are currently involved in the growth of ZnO thin films using PLD. In their article the growth of ZnO thin films on Si(100) substrates was studied as a function of laser wavelength. A Q-switched Nd:YAG laser operating at 1064 nm and 532 nm together with a KrF excimer laser operating at 248 nm were used. A fluence of 1.0 J/cm^2 and a frequency of 10 Hz were maintained in all cases. With 1064 nm radiation, a small Zn[101] peak was observed for a film deposited at room temperature. The film contained a high number of particles or "chunks" of material on the surface and was gray in colour. The Zn[101] peak disappeared for a scan of films deposited at 100, 200 and 300°C. Instead, weak, broad peaks of ZnO[101] and ZnO[002] were present, which indicated no texturing. At 532 nm, a small ZnO[101] peak was observed for a film deposited at room temperature. The films were transparent and contained a smaller number of particles on the surface. At T_s=100°C the [101] peak was more intense while at 200°C the [002] peak replaced the [101] peak, and finally at 300°C a stronger [002] peak with an XRD FWHM value of 0.899° was observed. The film deposited at 248 nm and room temperature revealed a small ZnO[002] peak. This film was colourless with a smooth and almost featureless surface. The crystallinity improved for a film deposited at 100°C resulting in a FWHM value of 0.477°. Further increase in temperature did not seem to improve this value. It was also found that film crystallinity improved with decreasing laser energy density with the FWHM reaching a value of 0.313° for a film deposited at room temperature using 248 nm radiation and a laser fluence of 0.5 J/cm^2.

(b) Growth by other techniques:

Sputtering is the most widely used technique for the growth of ZnO thin films. Although it is usually conducted in an Ar/O_2 ambient, sputtering in an Ar/H_2O medium has also been reported. The targets used are either sintered pellets of ZnO, or Zn metal,

although, ZnO targets are expected to provide better stoichiometry and thus improved crystallinity [27].

Tsuji et al. [24] used rf reactive sputtering of Zn metal to grow films of ZnO on Corning 7059 glass. For T_s>300°C films were mainly *c*-axis oriented. The growth rate increased with increasing oxygen concentration, O_c, and then decreased, with the maximum shifting towards higher values of O_c with increasing T_s. It was found that films with better stoichiometry and *c*-axis orientation displayed a lower conductivity. Films were optically opaque when deposited at room temperature and an O_c of less than 2%. However, for an O_c=2% the optical transmittance jumped to ≈90% and remained unchanged for higher concentrations. At T_s=200°C the transmittance was ≈90% and was nearly constant for low or high concentrations of oxygen.

Meng et al. [25] used reactive dc magnetron sputtering of Zn metal to grow ZnO films on Corning 7059 glass with no intentional heating. The deposition rate in their case was reduced with increasing oxygen pressure over almost the same range investigated by Tsuji et al. The excess oxygen causes a surface oxidation of the Zn target which usually reduces the sputtering yield and thus the deposition rate. It seems that oxidation occurs at a higher O_c when rf sputtering is used.

Nakada et al. [26] employed an H_2O/Ar ambient to grow ZnO thin films on glass-slide substrates by dc magnetron sputtering of a ZnO target. The results from SEM and XRD showed that as the H_2O partial pressure was increased the structure of the films was transformed from columnar to a film with a rough surface and large grains. The grain growth was proportional to T_s.

ZnO films deposited directly on GaAs substrates crumble easily and interdiffuse during post-deposition treatment. Kim and Mathur [27] overcame these problems by rf sputter depositing a layer of SiO_2 between ZnO and GaAs with no intentional heating. The film deposited on clean GaAs was *c*-axis oriented and had a better crystallinity than the film deposited on SiO_2/GaAs in which a weak [112] peak was observed in addition to (00*n*) peaks. However, a 10 min post-deposition anneal in forming gas (N_2/H_2) resulted in a *c*-axis oriented film with improved crystallinity, while the film on GaAs disintegrated completely.

As deposited films of ZnO suffer from the problem that when heated in air, their electrical resistance increases. For example the resistance can increase by over an order of magnitude when the films are annealed at 200°C for 2 hrs [28]. This is attributed to the chemisorption of oxygen at the grain boundaries thus creating acceptor states [28]. Using the technique of dual ion beam sputtering, Valentini et al. [28] showed that by introducing hydrogen in the assistance source gas, films of higher stability can be obtained, with the resistance hardly changing after 25 hr annealing in air at 200°C.

ZnO thin film have also been deposited by reactive thermal evaporation [29].This was carried out by evaporating $ZnCl_2$ in the presence of oxygen on heated quartz substrates.

Among the chemical techniques, metal-organic chemical vapour deposition is the most popular technique for the growth of ZnO thin films. Deposition has been conducted under both atmospheric [30] and low pressures [31].

8.3 PLD of ZnO thin films

8.3.1 Experimental

The process of ZnO target preparation was similar to that of CeO_2 discussed in chapter 6. Targets were made in the form of pellets, 13 mm in diameter, by cold pressing fine ZnO powder under a pressure of 3 tons/cm^2. The pellets were then heated up in a box furnace at a rate of 3°C/min to 1100°C. They were left at this temperature for ≈6hrs and cooled down to room temperature at a rate of 3°C/min resulting in a hard but brittle pellet which was light yellow in colour. Prior to each deposition, the target was polished followed by blowing the surface with nitrogen.

Single crystal Si(100) and Corning 7059 glass were used as substrates. The substrates were degreased in acetone and methanol and blown dry with nitrogen prior to deposition. The native oxide was not removed in the case of silicon substrates. The distance between the rotating target (5 rpm) and the substrate was kept at ≈4 cm.

A Q-switched frequency doubled Nd:YAG laser operating at 532 nm with a pulse duration of 4 ns at 5 Hz, or a KrF excimer laser operating at 248 nm with a pulse duration of 20 ns at 5 Hz were employed. The laser, Nd:YAG or excimer, was focused onto the target thereby producing an energy density of ≈3 J/cm^2 with the laser beam being incident at an angle of ≈25°.

8.3.2 Results

Thin films of ZnO were grown under various deposition conditions. However, for all the films that revealed any sign of crystallinity, the XRD patterns displayed (002) orientation, implying a textured structure with the *c*-axis perpendicular to the substrate. The XRD pattern of a typical film is shown in figure 8.2, in which only the [002] and the [004] peaks are present.

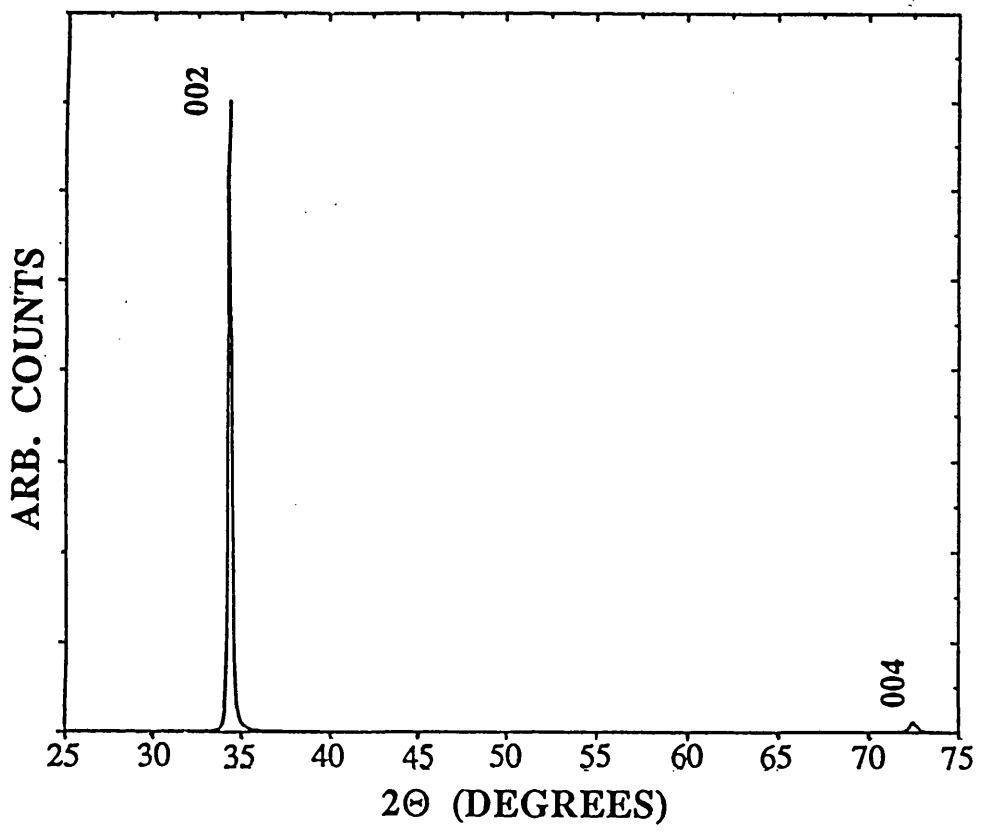

Figure 8.2 XRD pattern of a ZnO thin film deposited on glass using the frequency doubled Nd:YAG laser at a T_s of 250°C and a P_{O_2} of 2x10^{-5} mbar.

Throughout this chapter the crystal quality of the films is evaluated in terms of average full width at half maximum, FWHM, of the XRD peak, which in this case is the [002] peak. This value together with the peak position were obtained using the Split-Pearson V curve fitting technique described in section 6.3.1.

8.3.2.1 Effect of laser wavelength

The surface morphology of the ZnO films deposited at a T_s of 400°C and a P_{O_2} of $2x10^{-5}$ mbar on Si(100) using either the Nd:YAG laser or the the excimer laser is shown in the SEM micrographs of figures 8.3 - a&b.

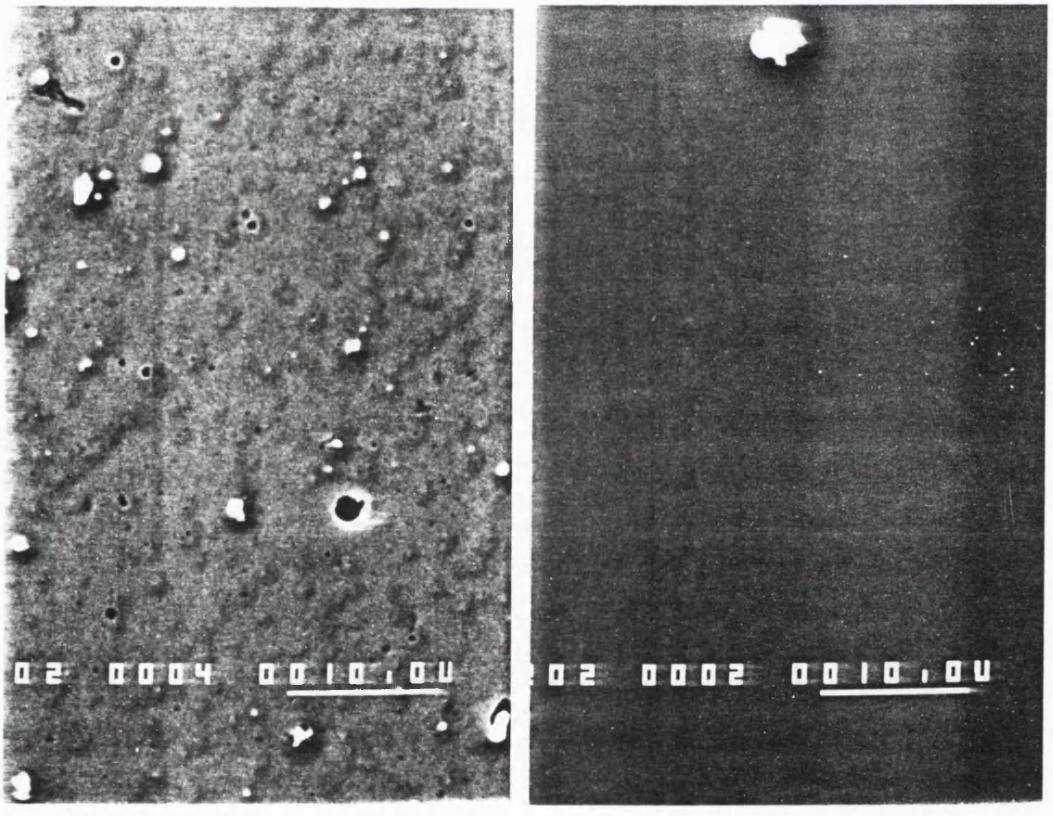

(a) *(b)*

Figure 8.3 *SEM micrographs of ZnO films deposited on Si(100) at a T_s of 400°C and a P_{O_2} of $2x10^{-5}$ mbar using: (a) a frequency doubled Nd:YAG laser (532 nm.) and (b) a KrF excimer laser (248 nm).*

Similar to the case of CeO_2 films grown by PLD, the density of particulates appearing on the film surface is reduced considerably using the excimer laser. Since the deposition conditions are identical, the formation of these particulates is more likely to be due to laser-target interaction or processes occurring within the plume. As mentioned in the case of CeO_2 the high density of particulates is believed to be a direct consequence of the much stronger optical absorption of the 248 nm radiation, $\alpha = 10^6$ cm^{-1}, which is below the absorption edge, whereas the 532 nm beam from the Nd:YAG laser penetrates much deeper into the bulk of the material, $\alpha = 10^5$ cm^{-1}. Temperature calculations for laser wavelengths of 532 nm and 248 nm have shown that when the surface reaches the melting temperature, the thermal gradient near the surface region is much steeper at 248 nm than at 532 nm [32]. Further support for this scenario is provided by the model of R.K.Singh et al. [33], which suggests that a small thermal gradient coupled with a low absorption coefficient can result in strong subsurface heating leading to micro-explosions once evaporation begins. Unfortunately the optical and thermo-physical constants of liquid ZnO are not as yet available to accurately verify the model predictions. Experimental evidence is provided by SEM investigations of the target surface before and after irradiation as is shown in figures 8.4 - a, b & c. As can be seen the surface of the pellet ablated by the excimer is smooth and flat (even smoother than the virgin surface), indicating that the ablation process was confined to a small depth, close to the the top surface, whereas the pellet hit by the Nd:YAG revealed a rough surface with cavity-like features.

While films deposited by the Nd:YAG laser exhibited a pale brown hue, those grown using the excimer laser were optically very clear and transparent. The visible transmittance (T) spectra of films deposited on glass by either laser, at a T_s of 300°C and a P_{O_2} of 2×10^{-5} mbar, are presented in figure 8.5. This was performed by using a Philips PU 8625 spectrometer, using a clean glass substrate as reference. The excimer laser deposited films in particular, have an average transmission higher than 80% in the visible region of the spectrum, as expected for undoped ZnO films [5,10, 24]. Both films exhibit a sharp cut-off at ≈380 nm.

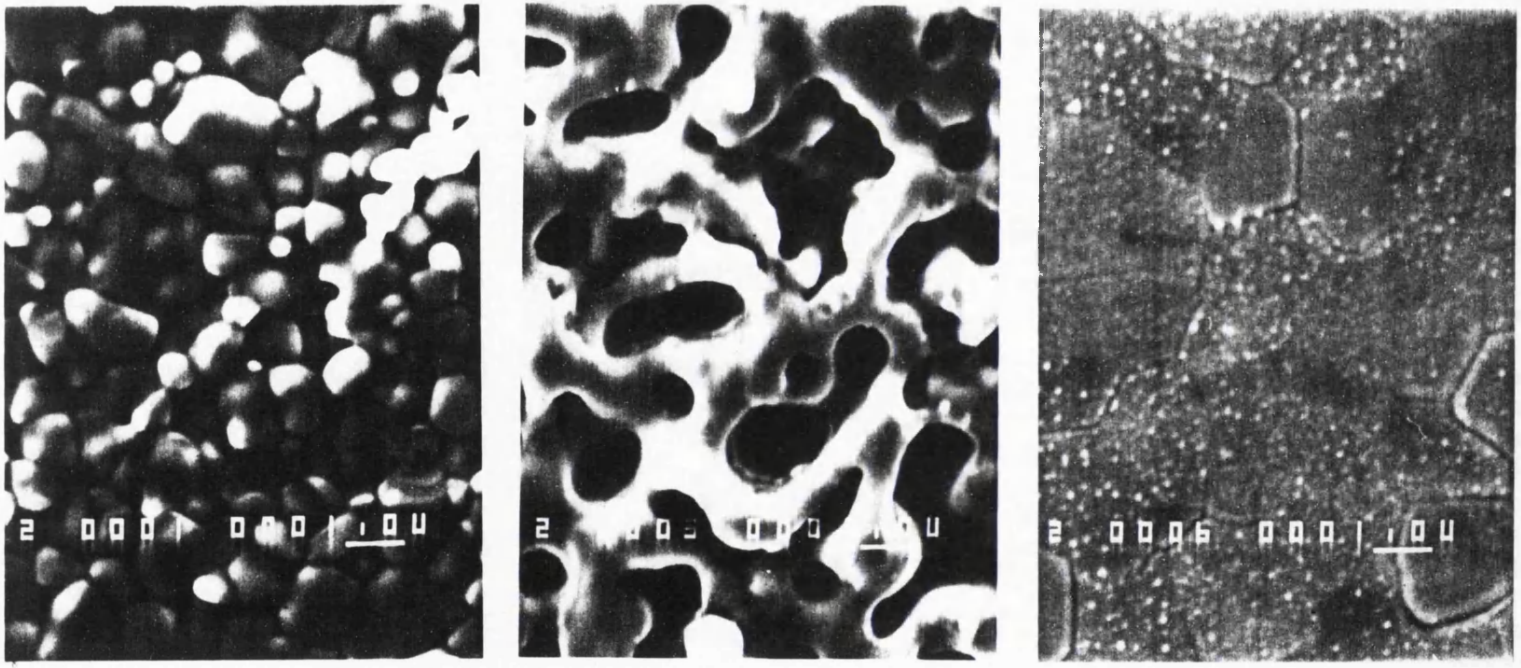

(a) (b) (c)

Figure 8.4. *SEM micrograph of ZnO target surfaces: (a) as prepared, (b) ablated using the frequency doubled Nd:YAG laser (532 nm), and (c) ablated using the KrF excimer laser (248 nm).*

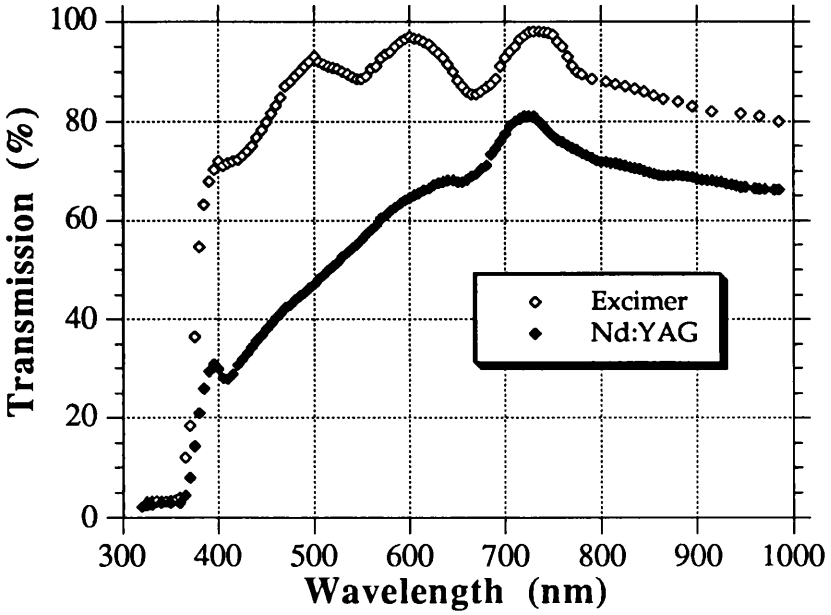

Figure 8.5 *Optical transmittance spectra of ZnO films deposited on glass using the frequency doubled Nd:YAG laser or the KrF excimer laser.*

8.3.2.2 Effect of oxygen partial pressure, P_{O_2}

Thin films of ZnO were grown on single crystal wafers of Si(100) at a fixed T_s of 400°C but under different P_{O_2}, using either the Nd:YAG laser (532 nm) or the excimer laser (248 nm). The films were ≈2000 Å thick. By varying the P_{O_2} the degree of texturing and the deposition rate were affected as discussed below. The error bars shown for the values of P_{O_2} do not take into account the instrumental error associated with the penning gauge which is typically ±50% [34].

(a) Effect on crystal quality:

The effect that varying the P_{O_2} has on film crystallinity and the in-built compressive stress is shown in figures 8.6 and 8.7. The key points to be noted concern the significant differences in the trends in the values of average FWHM and the 2θ peak position for films deposited using the Nd:YAG and the excimer lasers.

The values of average XRD FWHM for films deposited using the Nd:YAG laser were always higher than their counterparts for the excimer laser, as shown in figure 8.6. This implies that the structure of the films deposited using the excimer laser generally possess a much higher degree of texturing. The films displayed an improved texturing with decreasing oxygen pressure when the Nd:YAG laser was used. In contrast the value of average FWHM for the excimer laser deposited film remained essentially constant with perhaps a slight increase with decreasing pressure.

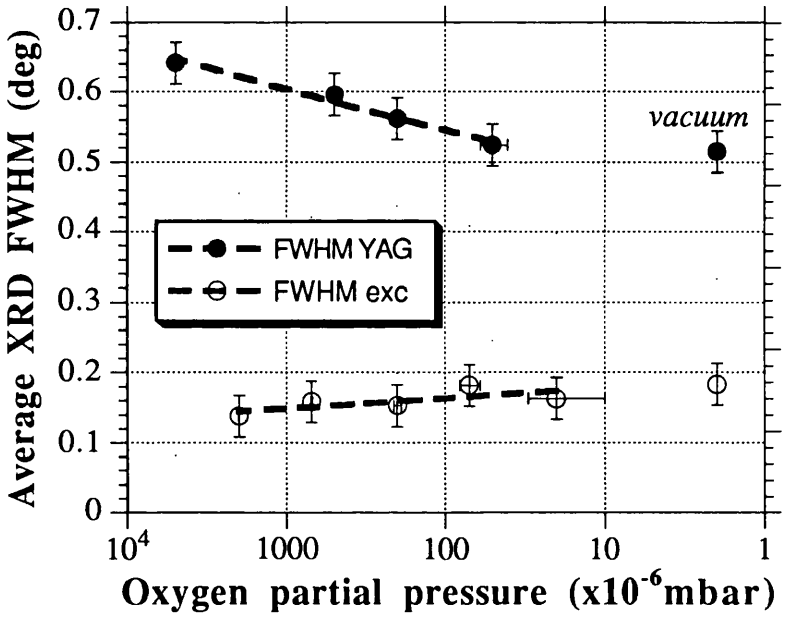

Figure 8.6 *Average XRD-FWHM of the [002] peak for ZnO thin films deposited on Si(100) at a T_s of 400°C but under different P_{O_2}.*

One possible explanation for the small increase in the average FWHM with decreasing P_{O_2} for films deposited using the excimer laser could be the formation of Zn interstitials and oxygen vacancies [24]. These defects have been invoked as donor-like defects in ZnO to explain the observed reduction in electrical resistivity. The existence of defects in the film leads to in-plane compressive stress and therefore a slight tilt in the crystal columns of the highly *c*-axis oriented film. A high P_{O_2} has the effect of compensating for these defects and thus relieving the built-in stress and reducing any

tilt in the crystallites. In the case of films deposited using the Nd:YAG laser no detailed study has been undertaken. However, as shown before there is a difference in the processes involved in ablation using these two wavelengths.

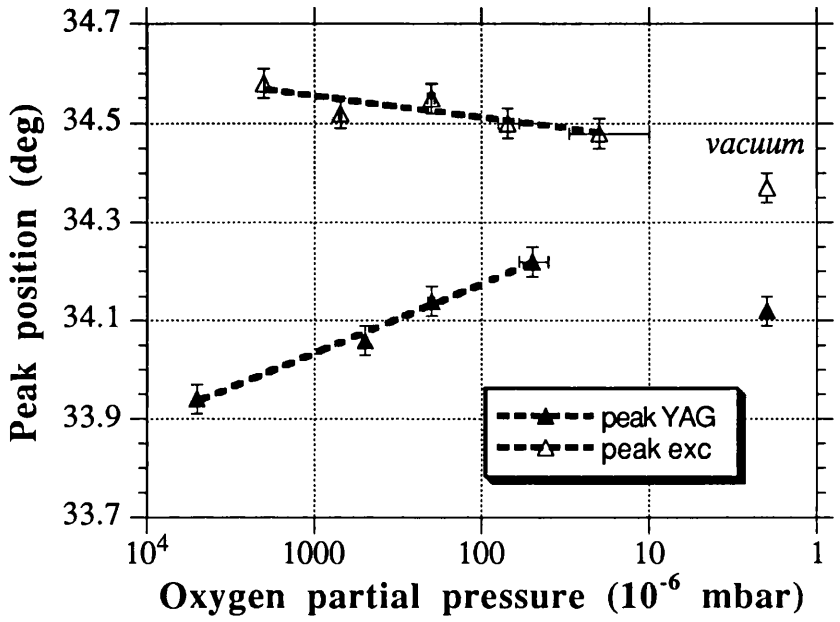

Figure 8.6 *Variation in [002] peak position for ZnO thin films deposited on Si(100) at a T_s of 400°C but under different P_{O_2}.*

As shown in figure 8.7, the position of the [002] peak for films deposited using the excimer laser are closer to those of the ZnO bulk value of 34.47°. The significant deviation from the ideal value observed for films grown using the Nd:YAG laser imply a higher degree of built-in compressive stress in these films. However, as can be seen the peak positions approach the bulk value with decreasing oxygen pressure. An examination of the values for peak positions for the excimer deposited films indicates that a high P_{O_2} actually results in deviation from the bulk value of 34.47° in a direction which implies an in-plane *expansion* rather than compression. These values are believed to be shifted upwards due to a difference in thermal expansion coefficient, TEC, between ZnO and Si (this is discussed in section 8.3.2.3). Thus the deposition of ZnO on a substrate with a similar TEC (eg. glass) under the same conditions would result in values of peak position that are all smaller than the bulk value but approaching it at high oxygen pressures.

(b) Effect on deposition rate:

This study was carried out for films deposited using the excimer laser only. As shown in figure 8.8 the deposition rate increases with P_{O_2}. This result may be rationalized using the model of Tsuji at al. [24] which suggests that the presence of Zn interstitials and O vacancies implies a film with excess Zn. In its limiting case a Zn atom which strikes an surface O forms a strong bond, while a Zn atom which hits surface Zn can reside for a limited time that decreases with increasing temperature. The deposition rate therefore increases with P_{O_2} since the evaporants encounter a substrate with better oxygen stoichiometry.

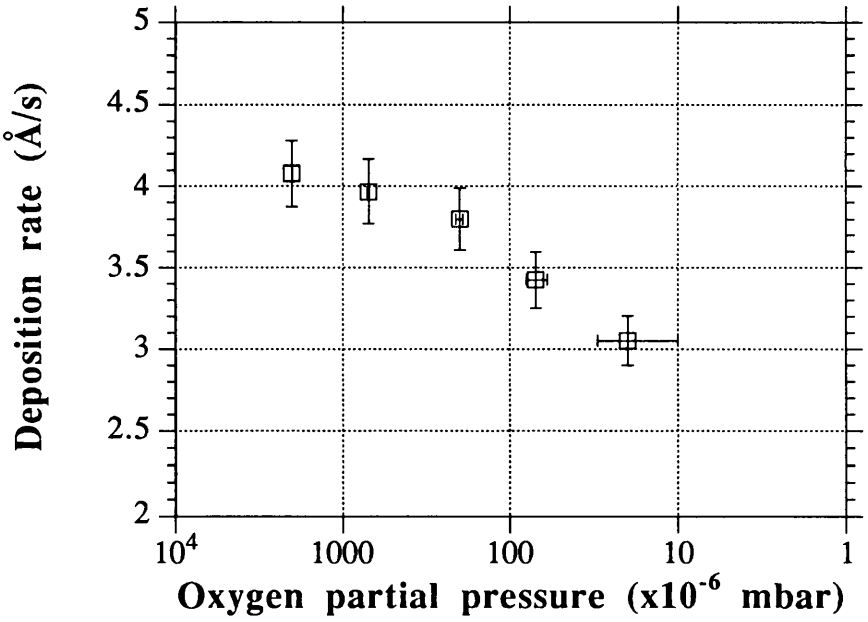

***Figure 8.8** Effect of variation in P_{O_2} on deposition rate for ZnO films deposited on Si(100) at a T_s of 400°C using the KrF excimer laser.*

8.3.2.3 Effect of substrate Temperature,T_s

Thin films of ZnO were grown on Si(100) at a constant P_{O_2} of $2x10^{-5}$ mbar but different T_s, using either the Nd:YAG laser (532 nm) or the excimer laser (248 nm). The films were ≈2000 Å thick and the XRD patterns revealed (002) oriented growth.

As can be seen from the curve fittings of figure 8.9 the crystallinity of the films improved with increasing T_s when either laser was used. Similar to the previous section whereby the effect of P_{O_2} variations was studied, the values of average FWHM for films deposited using the Nd:YAG laser were always higher than their comparable values obtained with the excimer laser.

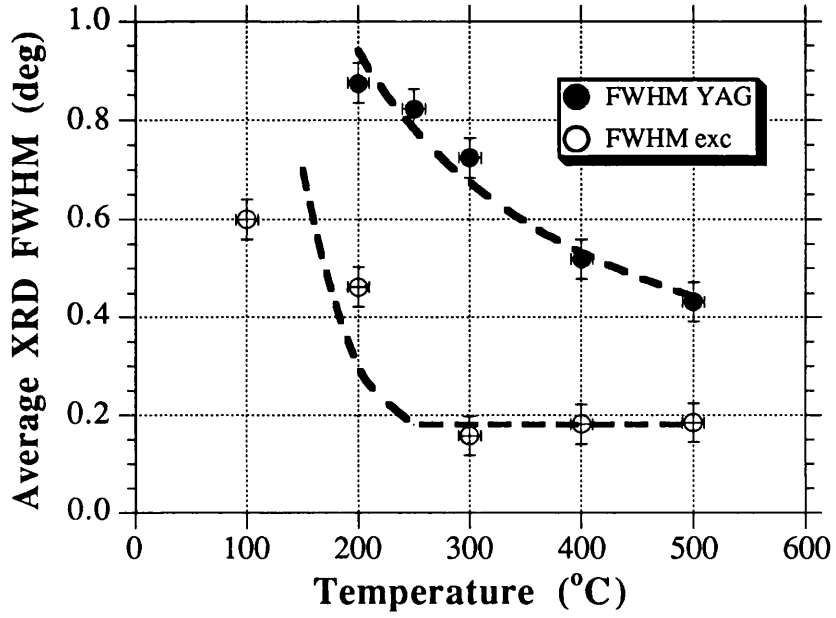

Figure 8.9 *Average XRD-FWHM of the [002] peak for ZnO thin films grown on Si(100) under a P_{O_2} of $2x10^{-5}$mbar and different T_s using either the frequency doubled Nd:YAG (532 nm) or the KrF excimer laser (248 nm).*

Film deposited at room temperature were amorphous with no peaks detected in their XRD pattern. An improvement in film crystallinity with increasing temperature is a behaviour observed in the growth of majority of films and is usually attributed to the increased adatom mobility at higher temperatures.

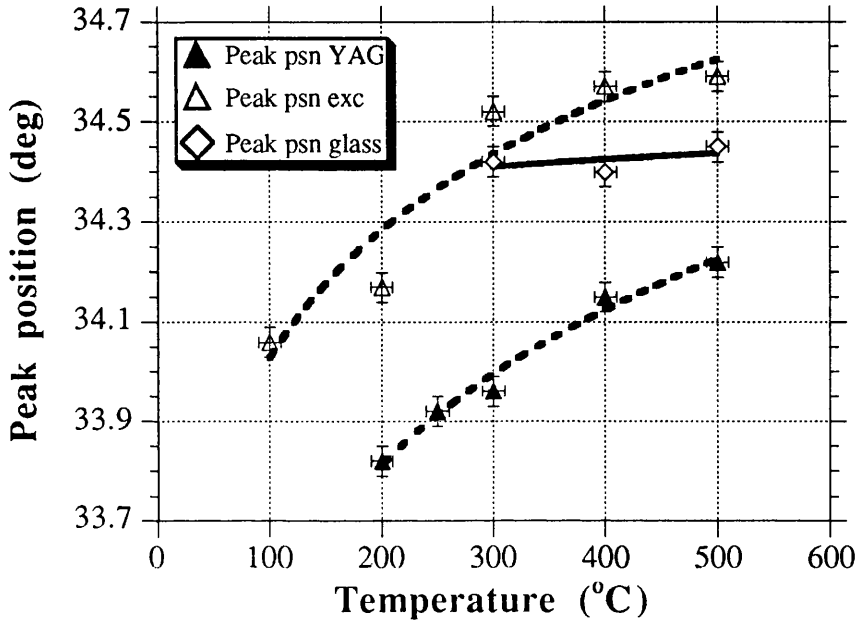

Figure 8.10 *The value of peak [002] position for ZnO thin films grown on Si(100) under a P_{O_2} of $2x10^{-5}$mbar and different T_s using either the frequency doubled Nd:YAG (532 nm) or the KrF excimer laser (248 nm). Solid line corresponds to variation in peak position for ZnO films deposited on glass using the excimer laser and under the same conditions.*

Two parameters, the FWHM and the position of the peak in 2θ, are considered here to quantify the quality of the films. The latter parameter is affected by the difference in the TECs of Si ($2.33x10^{-6}$/°C [34]) and ZnO ($4x10^{-6}$/°C [34])], and thus a film cooled down from a high temperature experiences tensile stress. The peak angular position at room temperature is therefore expected to increase from a near bulk value at a low T_s to higher values with rising T_s, implying a built-in expansion of the film. It can be seen in figure 8.10 that for films deposited using the excimer laser, this is indeed the case for $T_s \geq 300$°C. However, for a $T_s<300$°C, the behaviour is that of a film experiencing built-in compression. By examining the graph in figure 8.9, there seems to be a direct correlation between broadening of the [002] peak and built-in compression for films deposited at a $T_s<300$°C. An interpretation for this behaviour is that an increase in FWHM may be due to smaller grain sizes; this results in an increase

in the number of grains and grain-boundaries per unit area. Depending on how the lattice is interrupted at the grain-boundaries, the film may experience built-in compression. Hence, at a low T_s, the peak position depends on the inter-grain nature of the film due to the high number of small grains per unit area, while at a high T_s, it is intra-grain dependent. However, this would need further investigation, eg. using TEM studies.

The thin film deposition of ZnO on glass (TEC $\approx 4.5 \times 10^{-6}$/°C [34]) under the same conditions, also shown in figure 8.10 did not reveal any significant dependence of T_s on peak position.Thus it appears that matching the TECs is another key parameter for the growth of ZnO thin films.

8.3.2.4 Film Thickness

Thin films of ZnO of different thickness were deposited at a P_{O_2} of 2×10^{-5} mbar and a T_s of 400°C on glass substrates using the Nd:YAG laser. The XRD patterns of these films are presented in figure 8.11.

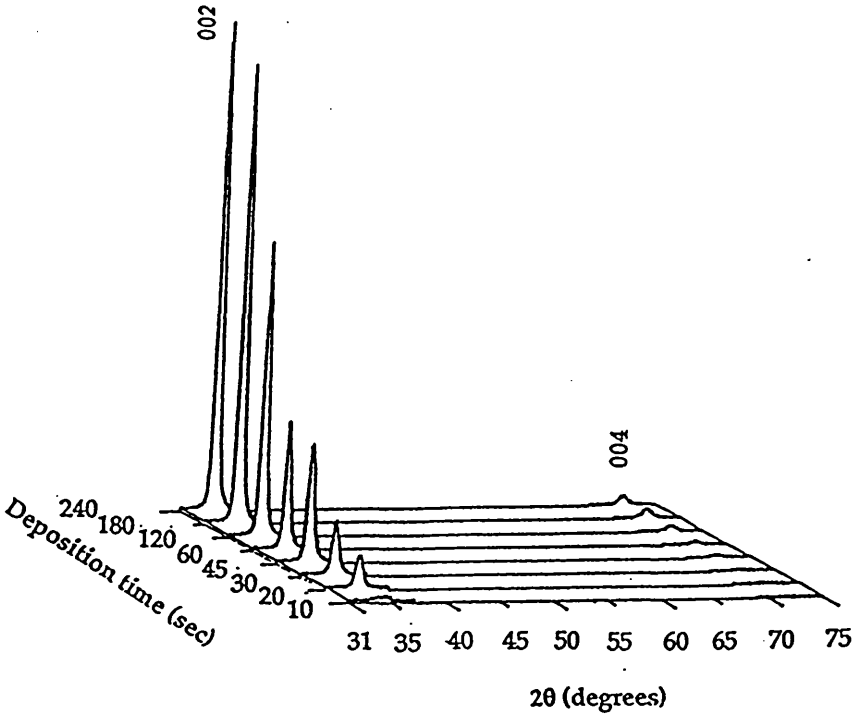

Figure 8.11 *XRD patterns of ZnO films deposited on glass for different deposition times at a T_s of 400°C and a P_{O_2} of 2×10^{-5} mbar using the frequency doubled Nd:YAG laser.*

It can be seen that even for the lowest thickness film (≈85 Å) only the [002] and the [004] reflections are present, indicating *c*-axis growth of ZnO to occur at the early stages of film growth. Similar to CeO_2 films, FWHM decreases with film thickness, especially up to ≈500 Å, and it remains practically unchanged for thicker films. Also there is a slow tendency for the [002] peak position to approach bulk value.

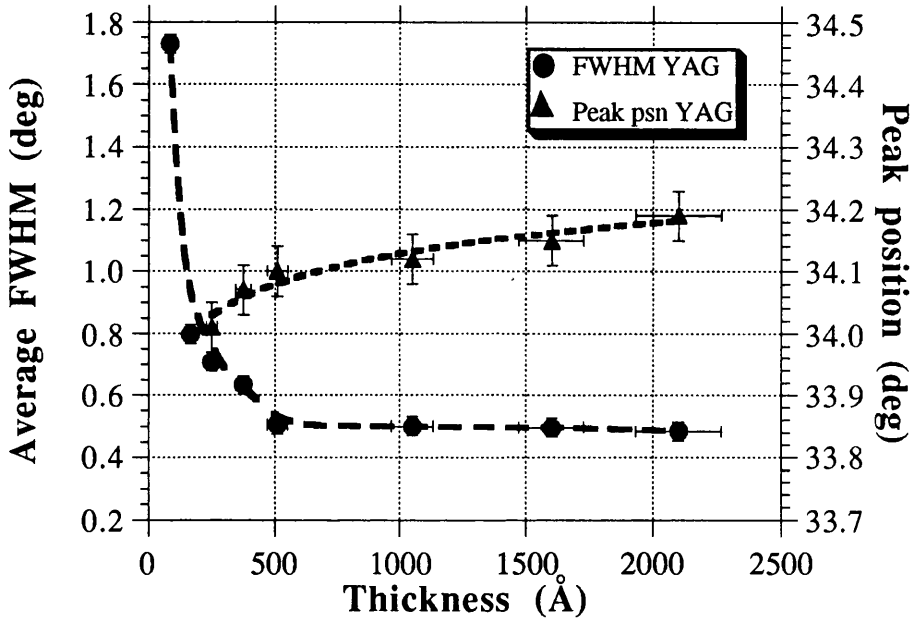

Figure 8.12 *(a) XRD patterns for ZnO films deposited at a T_s of 400°C and a P_{O_2} of $2x10^{-5}$ mbar using the frequency doubled Nd:YAG laser (532 nm) on glass for different deposition time, and (b) effect of film thickness on the average FWHM and the 2θ position of the [002] peak for the films shown in (a).*

8.3.2.5 Effect of laser fluence

The effect of laser fluence on crystal quality and deposition rate was investigated by depositing ZnO films on Si(100) at a P_{O_2} of $3x10^{-3}$ mbar and a T_s of 300°C using the excimer laser (248 nm). Laser fluence was attenuated by selecting the desired energy on the control menu, and the beam was focused on to the target to produce a spot size of ≈0.03 cm^2 (1 mm x 3 mm). The deposition time was reduced with increasing laser fluence in order to keep the film thickness nearly constant. However, all the films were over 1000 Å thick to avoid the increase in FWHM obtained at low film thickness.

rate had reached a steady-state value [36]. The steady-state value was reached after a number of pulses - this number increased with laser fluence.

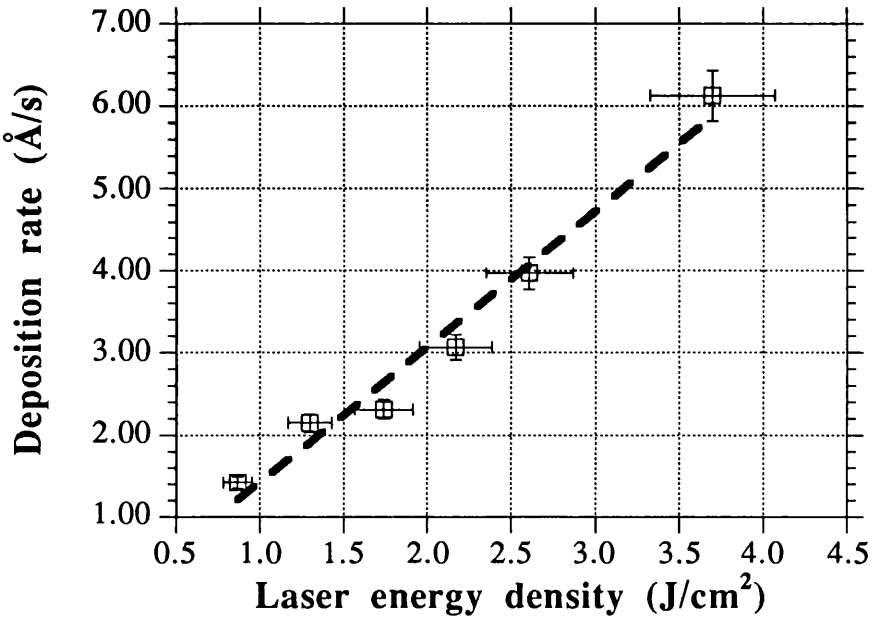

***Figure 8.14** Effect of laser fluence on deposition rate for ZnO films deposited on Si(100) at a P_{O_2} of 3x10^{-3} mbar and a T_s of 300°C, using the excimer laser.*

8.4 Conclusion

The objective of this thesis chapter was the isolation of a basic set of conditions for the growth of textured ZnO films. To this extent we were successful in that highly *c*-axis oriented thin films of ZnO were produced from ZnO targets using the PLD technique. Under identical deposition conditions, films grown using the KrF excimer laser were superior to the ones deposited by the frequency doubled Nd:YAG laser, as manifested by their smoother film surface, higher transmittance of over 80% in the visible region, higher degree of texturing, and a less built-in tensile-stress. This is attributed to the laser being absorbed close to the target surface when a short wavelength is utilized. Best results were obtained when a P_{O_2} of 3x10^{-3} mbar, a $T_s \geq 300$°C, a film thickness of greater than 500 Å, and a laser energy density of ≈3.5 J/cm^2 were employed. The quality of these films was monitored by reference to the average XRD FWHM and the

2θ peak position. The latter parameter was found to depend not only on the creation of defects in the film but also on a difference in thermal expansion coefficients between the film and substrate.

References

[1] A.R.West,"*Solid State Chemistry and its application*", fourth edition, Wiley, UK, (1990).

[2] R.P.Howson, G.W.Hall, G.W.Critchlow and D.E.Sykes, *Vacuum*, **43**, p169, (1992).

[3] M.L.Olvera, A.Maldonado, R.Asomoza, M.Konagai and M.Asomoza, *Thin Solid Films*, **229**, p196, (1993).

[4] A.Kuroyanagi, *Jpn. J. Appl. Phys.*, **28**, 2, p219, (1989).

[5] Y.Igasaki and H.Saito, *J. Appl. Phys.*, **7**, p3613, (1991).

[6] S.Ghosh, A.Sarkar, S.Chaudhari and A.K.Pal, *Vacuum*, **42**, p625, (1991).

[7] H.Sato, T.Minami, S.Takata, T.Mouri and N.Ogawa, *Thin Solid Films*, **220**, p327, (1992).

[8] S.Matsushima, D.Ikeda, K.Kobayashi and G.Okada, *Sensors and Actuators B*, **13-14**, p621, (1993).

[9] A.Valentini, F.Quaranta, M.Rossi and G.Battalgin, *J. Vac. Sci. Technol. A*, **9**, p286, (1991).

[10] W.Wenas, A.Yamada, K.Takahashi, M.Yoshino and M.Konagai, *J. Appl. Phys.*, **70**, 11, p7119, (1991).

[11] J.Hu and R.Gordon, *J. Electrochem. Soc.*, **139**, 7, p2014, (1992).

[12] H.Sato, T.Minami and S.Takata, *J. Vac. Sci. Technol. A*, **11**, 6, p2975, (1993).

[13] M.Kadota, T.Kasanami and M.Minakata, *Jpn. J. Appl. Phys.*, **31**, p3013, (1992).

[14] F.Hickernell, *IEEE Trans. Son. Ultrason.*, **SU-32**, p621, (1985).

[15] M.Kadota, T.Kasanami and M.Minakata, *Jpn. J. Appl. Phys.*, **32**, p2341, (1993).

[16] X.Yoo, A.Fahrenbruch and Bube, *J. Appl. Phys.*, **68**, 9, p4694, (1990).

[17] A.Banerjee, D.Wolf, J.Yang and S.Guha, *J. Appl. Phys.*, **70**, 3, p1692, (1991).

[18] A.Dutta, T.Chaudhuri and S.Basu, *Mat. Sci. Eng.*, **B14**, p31, (1992).

[19] S.Matsushima, D.Ikeda, K.Kobayashi and G.Okada, *Sensors and Actuators B*, **13-14**, p621, (1993).

[20] H.Nanto, H.Sokooshi and T.Kawai, *Sensors and Actuators B*, **13-14**, p715, (1993).

[21] H.Sankur and J.T.Cheung, *J. Vac. Sci. Technol. A*, **1**, p1806, (1983).

[22] K.Maruyama, S.Endo, G.Sasaki, K.Kamata, J.Nishino and K.Kuchitsu, *J. Mat. Sci. Lett.*, **11**, p1588, (1992).

[23] J.Ianno, L.McConville, N.Shaikh, S.Pittal and P.G.Snyder, *Thin Solid Films*, **220**, 92, (1992).

[24] N.Tsuji, H.Komiyama and K.Tanaka, *Jpn. J. Appl. Phys.*, **29**, p835, (1990).

[25] L.Meng, M.Andritschky and M.Santos, *Vacuum*, **44**, 2, p105, (1993).

[26] T.Nakada, Y.Ohkubo and A.Kunioka, *Jpn. J. Appl. Phys.*, **30**, 12A, p3344, (1991).

[27] H.K.Kim and M.Mathur, *J. Elec. Mat.*, **22**, 3, p267, (1993).

[28] A.Valentini, F.Quaranta, M.Penza and F.Rizzi, *J. Appl. Phys.*, **73**, 3, p1143, (1993).

[29] M.Jin and L.S.Ying, *Thin Solid Films*, **237**, p16, (1994).

[30] J.Hu and R.G.Gordon, *J. Appl. Phys.*, **71**, 2, p880, (1992).

[31] J.S.Kim, H.A.Mazouk and P.J.Reucroft, *Thin Solid Films*, **217**, p133, (1992).

[32] S.Amirhaghi, V.Craciun, D.Craciun, J.Elders and I.W.Boyd, *to be published in the Proceedings of the EMRS Conference*, Strasbourg, (1993).

[33] R.K.Singh, D.Bhattacharaya and J.Narayan, *Appl. Phys. Lett.*, **57**, p2022, (1990).

[34] N.Harris, *"Modern Vacuum Practice"*, McGraw Hill, UK, (1989).

[35] W.H.G.Horsthuis, *Thin Solid Films*, **137**, p185, (1986).

[36] S.R.Foltyn, R.C.Dye, K.C.Ott, E.Peterson, K.M.Hubbard, W.Hutchinson, R.E.Muenchausen, R.C.Estler and X.D.Wu, *Appl. Phys. Lett.*, **59**, 5, p592, (1991).

Chapter 9

Conclusions and Suggestions for Further Work

In this chapter the general conclusions and their implications are discussed by highlighting the key results obtained during the course of this research programme. This is followed by a number of suggestions given for further study of thin film growth mechanism, and their applications in electronic device technology.

9.1 Conclusions

9.1.1 Introductory chapters

We began with a brief discussion on thin film growth in order to provide a background information for the experimental work reported in this thesis. This was followed in the same chapter, by outlining a number of deposition methods at an introductory level for comparison with the PLD technique.

In chapter 3, PLD as a deposition technique was described. The advantages and disadvantages of this method were highlighted. The processes involved during laser - target interaction followed by plasma formation and expansion were discussed. This provided the physical understanding for the deposition technique upon which this work is centred. The generation of particles on the film surfaces grown by this technique were also discussed and a number of methods to minimize their generation were outlined. This was particularly useful since the problem of surface particles formed a major subject of investigation throughout chapter 6, and to some extend in chapter 8.

In chapter 4 the properties of the "traditional", and the relatively newly discovered, high temperature superconductors, HTSC, were highlighted. Thin film growth of HTSC by PLD was then discussed followed by an outline of the basic requirements for the growth of HTSC on single crystal oxide and silicon substrates. The need for intermediate buffer layers such as CeO_2 in the growth of HTSC on silicon were explained. This chapter thus supplied the introductory background to chapters 6 and 7.

Chapter 5 formed the final introductory chapter in which the experimental set-up and the characterization techniques used throughout this thesis were briefly described.

9.1.2 Result chapters

The growth of CeO_2 thin films by PLD was investigated in chapter 6. Si(100), Si(111), Corning glass 7059, and sapphire ($1\underline{1}02$) were used as substrates, with the native oxide not removed from the Si surfaces. A frequency doubled Nd:YAG laser (532 nm), or a KrF excimer laser (248 nm) were employed as laser sources. A low partial pressure of oxygen, P_{O_2} ($< 5x10^{-5}$ mbar) seems to be necessary during deposition to avoid the production of suboxides. However, in the case where the excimer laser is employed a base pressure of $\approx 1x10^{-6}$ mbar is sufficient to supply the necessary oxygen for stoichiometric deposition. Films deposited on amorphous oxide bases such as glass substrate, or Si covered with its native oxide, are (111) oriented with the crystallinity improving with decreasing P_{O_2} and increasing substrate temperature, T_s.

Results from TEM studies indicated the formation of an amorphous layer of CeO_2 during the initial stages of growth which gradually developed into a highly ordered structure. Also x-ray diffraction, XRD, measurements showed the crystallinity of the films to improve with increasing film thickness. The effect of laser energy on deposition rate followed a linear relationship for laser fluences of < 2 J /cm^2. At higher fluences a logarithmic dependence was observed. Deposition using the Nd:YAG laser resulted in the formation of high density of particulates on the film surface when compared to films deposited using the excimer laser. Results from selected area diffraction indicated a powder-like polycrystalline nature of these particulates. For films deposited at a high P_{O_2} ($> 1x10^{-4}$ mbar) using the Nd:YAG laser, the particulate density on the surface is so high

that the XRD pattern no longer displays a preferential orientation. Apart from using a laser source with a shorter wavelength, other ways to reduce the particulate density were deposition at fluences > 2J/cm^2 (logarithmic region on the deposition rate vs. fluence graph) and pre-ablating the target. Depending on whether film deposition was conducted at a low P_{O_2} (< 5x10^{-5} mbar) and a normal T_s (500°C), or a high P_{O_2} (2x10^{-1} mbar) and high T_s (650°C), CeO_2 thin films with either (111) orientation or (200) orientation were grown respectively, when a sapphire substrate was used.

The feasibility of altering the lattice constant was investigated via doping of CeO_2. Using the usual deposition conditions a La doped CeO_2 film was successfully grown from a target with composition: 60% CeO_2 and 40% La_2O_3 on a Si(100) substrate covered with a layer of undoped CeO_2 resulting in lattice constants of 5.41 Å for the undoped CeO_2 layer and 5.55 Å for the doped layer. A multilayer of $YBa_2Cu_3O_{7-\delta}/CeO_2/Si(100)$ was produced by *in-situ* growth of each layer, with the YBaCuO film being *c*-axis oriented. A T_c of only 78 K was obtained which can be improved by optimising the growth conditions of the YBaCuO layer. Multilayers of $BiSrCaCuO/CeO_2/Si(100)$ were *ex-situ* grown using both lasers. When the Nd:YAG laser was used, the growth of BiSrCaCuO on CeO_2/Si resulted in intermixing of the two layers. When the excimer laser was used a highly *c*-axis oriented BiSrCaCuO film with a number of missing peaks were obtained. This was attributed to the existence and inter-mixing of different phases in the BiSrCaCuO layer.

In chapter 7 the thin film growth of $Nd_{2-x}Ce_xCuO_{4-y}$ was presented. In this material superconductivity is achieved: (a) when the Ce concentration falls within a narrow range ($0.12< x <0.19$), and (b) when the 'correct amount' of oxygen is removed from the material. Before proceeding to actual thin film growth, the targets were fully characterized by preparing pellets with different Ce contents, to gain information on the possibility of any Ce segregation, and on the variation of lattice parameters with Ce concentration. This was carried out using XRD measurements and the Rietveld refinement of the resulting data. The thin films were then deposited from a target with composition, $Nd_{1.85}Ce_{0.15}CuO_{4-y}$. The chemical composition was first checked for films deposited using the frequency doubled Nd:YAG laser or the KrF excimer laser. Within the range of laser fluences examined, the deposition of films under a P_{O_2} of 4x10^{-1} mbar using the

excimer laser allowed reasonable stoichiometric transfer. The XRD measurements of *ex-situ* grown films revealed that only deposition using the excimer laser resulted in a single phase film. Highly *c*-axis oriented films were achieved by lowering the thickness of the *ex-situ* grown films from ≈5000 Å to ≈2000 Å. However, a post-annealing treatment in argon for different periods of time did not result in any superconducting characteristic.

The *in-situ* growth of $Nd_{1.85}Ce_{0.15}CuO_{4-y}$ films were performed using the excimer laser only. By depositing at a P_{O_2} of $4x10^{-1}$ mbar and a T_s of 800°C highly *c*-axis oriented single phase films were obtained. Least-square refinement of the XRD data indicated the resulting *c*-axis lattice constant range to fall within the range necessary to render the film superconducting. Unfortunately following a post-annealing treatment in vacuum at 600°C for various periods of time, superconductivity was not realised in these films. This is believed to be due to the oxidation states of Ce and Cu which are not easily controllable using oxygen as the growth medium. By using N_2O as the oxidizing agent a this problem should become easier to control.

In chapter 8, a preliminary study of the growth of ZnO thin films by PLD was presented. The objective was to obtain basic growth conditions that produce smooth and well textured films. Again both the frequency doubled Nd:YAG laser (532 nm) and the KrF excimer laser (248 nm) were used. However, under identical deposition conditions, films grown using the excimer laser were superior, as manifested by their smoother surface morphology, higher transmittance in the visible region,better crystallinity, and a less degree of built-in tensile stress. As with the growth of CeO_2 thin films this was due to the lower absorption length of ZnO at shorter wavelengths. By depositing films which were >500 Å thick, at a P_{O_2} of $3x10^{-1}$ mbar, a T_s ≥300°C, and a laser energy density of ≈3.5 J/cm^2, highly textured and smooth ZnO films with an average XRD FWHM as low as 0.14° were successfully grown.

The degree of stress in the ZnO films were investigated by studying the effects of variations in deposition parameters on the 2θ peak position. This value was found to depend on the difference in thermal expansion coefficients between the ZnO and the substrate material, as well as the presence of defects in the film.

9.2 Suggestions for further work

(a) Growth of CeO_2 thin films:

The optimum deposition parameters for the growth of highly oriented films with smooth surfaces were found to be, a short laser wavelength (in the u.v. region), a low P_{O_2} of $\leq 2x10^{-5}$ mbar, a T_s of $\geq 500^oC$, a deposition time corresponding to a film thickness of >500 Å, a laser fluence of $\geq$ 2 J/cm^2, and a pre-ablated target. Before proceeding to the next step which would obviously be the use of this film as an intermediate buffer layer between a high temperature superconductor thin film and a semiconductor such as Si, a series of studies can be made in order to understand the physics of ablation while depositing the films. One would be to measure the kinetic energy of species departing from the target using methods such as fast photography, or mass spectroscopy and time of flight measurements. The other would be to monitor the crystal formation and growth using *in-situ* reflective high energy electron diffraction, RHEED. In addition *in-situ* X-ray photo-electron spectroscopy, XPS measurements can provide information with regard to the binding between the constituent atoms in the film. Also removal of the native oxide and prevention of further oxide growth can be made easier under UHV conditions.and thus the growth of CeO_2 thin film on oxide free Si can also be studied.

From the engineering view point the growth of films from targets doped with Gd or Y, to increase or decrease the lattice constant can be further investigated. Inside the vacuum chamber, the use of a multiple target holder, and a shutter (positioned a few millimetres in front of the substrate), can speed up the process of multilayer thin film deposition. In the growth of the YBaCuO/CeO_2/Si system, the deposition conditions and any required *in-situ* post-annealing treatment of the YBaCuO layer has to be optimised to render superconducting films with T_cs of ≈90 K and critical current densities of ≈1x10^6 A/cm^2 (77 K).

(b) Growth of $Nd_{1.85}Ce_{0.15}CuO_{4-y}$ thin films:

Highly *c*-axis oriented single phase thin films of this material can now be reproducible grown and the film stoichiometry has been shown to fall within the range required for superconductivity to occur. The reason for the persistent non-superconducting behaviour

of these films has been attributed to the oxidation states of Cu and Ce. The growth of the films using strong oxidizing agents such as N_2O or ozone would be a sensible alternative to using oxygen as the growth medium. Also during discussions with T.Venkatesan, Department of Physics, University of Maryland, USA, the choice of substrate were found to be crucial in improving the quality of the superconducting films with Yttria-stabilized Zirconia delivering the best results. Also the *in-situ* techniques mentioned above can be used to study the film growth mechanism. *In-situ* RHEED can be used to monitor crystal growth prior to annealing in a reducing atmosphere, and *in-situ* XPS can be used to monitor the oxidation states of Cu and Ce.

(c) Growth of ZnO thin films:

Deposition using a short wavelength laser (in the u.v. region), a P_{O_2} of $3x10^{-3}$ mbar, a T_s of ≥300°C, a film thickness of >500 Å, and a laser fluence of ≈3.5 J/cm^2 formed the optimum conditions for the growth of *c*-axis oriented films with smooth surfaces. Again the use of different *in-situ* techniques such as mass spectrometry and time of flight measurements, RHEED and XPS can lead to a better understanding of the growth mechanism and provide technical evidence for a number of predictions that were believed to be the reason to some of the observations made during the growth of ZnO thin films.

The next stage would be the application of these films in the fabrication of electronic devices and to compare them with those made by other deposition techniques. One obvious application would be the use of ZnO thin films in solar cell technology. Being a prime candidate for use as a transparent conductive film, it would be reasonable to deposit films from ZnO targets doped with elements such as Al (say 1-5 %), under various P_{O_2}, and measure their resistivity and optical transmission. A simple photo-voltaic cell can then be fabricated by depsoiting a ZnO :Al layer on top of a p-type Si wafer. The characteristics of this structure can be measured in terms of the usual parameters defining a solar cell, such as the open circuit voltage, the short circuit current, and the fill factor under standard illumination levels. These can be compared with the results usually obtainable from using other physical deposition and chemical deposition techniques.